198024

NHTSA-98-3588-188

Evaluation of Motor Vehicle Fire Initiation and Propagation
Part 9: Propagation of a Rear-Underbody Gasoline Pool Fire in a 1998 Sport Utility Vehicle

Jeffrey Santrock
General Motors Corporation

ABSTRACT

This report describes a vehicle fire propagation test conducted pursuant to an agreement between GM and the United States Department of Transportation. This fire test was conducted on June 9, 1998. The test vehicle was a crash-tested 1998 Ford Explorer. In the crash test, this vehicle was stationary and was struck in the left rear (driver's side) by a moving barrier. The fuel system of the test vehicle did not leak at any time during the crash. Fluid was observed leaking from the filler tube of the test vehicle during a static roll test performed after the crash test. No fire was observed during this crash test, nor was there evidence of fire present in the test vehicle detected during an inspection of the test vehicle after the crash test. An artificial method of creating an underbody gasoline pool was used in this test. Gasoline was pumped continuously during this test from an external reservoir onto the ground under the rear of the test vehicle. The outlet of the artificial gasoline supply tube was near the rear inboard corner of the fuel tank in the test vehicle. The gasoline was ignited with a propane torch and allowed to burn until flames were observed spreading across the headlining panel in the test vehicle. Flames entered the passenger compartment through the window-opening in the left quarter panel, a seam opening between the rear compartment floor panel and the quarter panel behind the left rear wheelhouse, a seam opening between the rear compartment floor panel and the quarter panel in the right rear corner of the test vehicle, and a gap between the bottom of the rear lift gate and lift gate sill on the right side of the test vehicle. Fire suppression began at approximately 170 seconds after the gasoline was ignited.

DEPT. OF TRANSPORTATION
DOCKETS
02 OCT 22 AM 12:09

Appendicies

List of Figures

Report

List of Figures

Appendicies

List of Tables

Report

List of Tables

Appendicles

1 Introduction and Test Summary

The work described in this report was conducted by General Motors (GM) pursuant to an agreement between GM and the United states Department of Transportation. According to this agreement, GM and the National Highway Traffic Safety Administration (NHTSA) jointly developed fifteen separate vehicle fire safety research projects. One of these projects, entitled "Fire Initiation and Propagation Tests", involves conducting 1) vehicle crash tests to investigate potential ignition events that occur in vehicle crashes, and 2) subsequent vehicle fire tests to characterize fire propagation in these crash-tested vehicles. The vehicle models to be tested, and the crash- and fire-test methods to be used for Project B.3 are described in another report [1]. The objectives of the fire tests are:

- To determine the principal fire paths and time-lines for flame propagation into the passenger compartment under the test conditions;
- To identify which components burn and to measure the thermal environments around those components associated with their ignition under the test conditions; and
- To measure air temperatures, heat fluxes, and combustion gas concentrations in the passenger compartment under the test conditions.

These tests were conducted under carefully designed test conditions noted throughout this and other reports. They cannot be relied upon to predict the specific nature and characteristics of actual post-collision fires in the field.

The test vehicle was a 1997 Ford Explorer (VIN: 1FMDU34X6VUA99109). The test vehicle was crash tested on December 17, 1997 at the General Motors Proving Ground in Milford, Michigan [2]. In the crash test, this vehicle was stationary and was struck in the left rear (driver's side) by a moving barrier. The barrier had a deformable aluminum honeycomb face similar to that described in FMVSS214 [3]. The test vehicle parked with the brakes on. The test vehicle was positioned so that the longitudinal center-line of the test vehicle was parallel to the direction of motion (velocity vector) of the barrier and offset to the right so that approximately 70% of the barrier face overlapped the rear of the test vehicle. The barrier speed at impact was 84.4 km/h (52.4 mph). The mass of the test vehicle, including Anthropomorphic Test Devices and test instrumentation, was 2,249 kg (4,958lbs.). The mass of the barrier was 1370 kg (3020 lbs.). The maximum change in velocity of the test vehicle was 38 km/h (23.6 mph). The fuel system of the test vehicle did not leak at any time during the crash, but leaked during the static roll test performed after the crash test as specified in FMVSS301[4]. The leak was came from a tear in the hose connecting the filler to the fuel tank. A detailed description of this test can be found in another report [2].

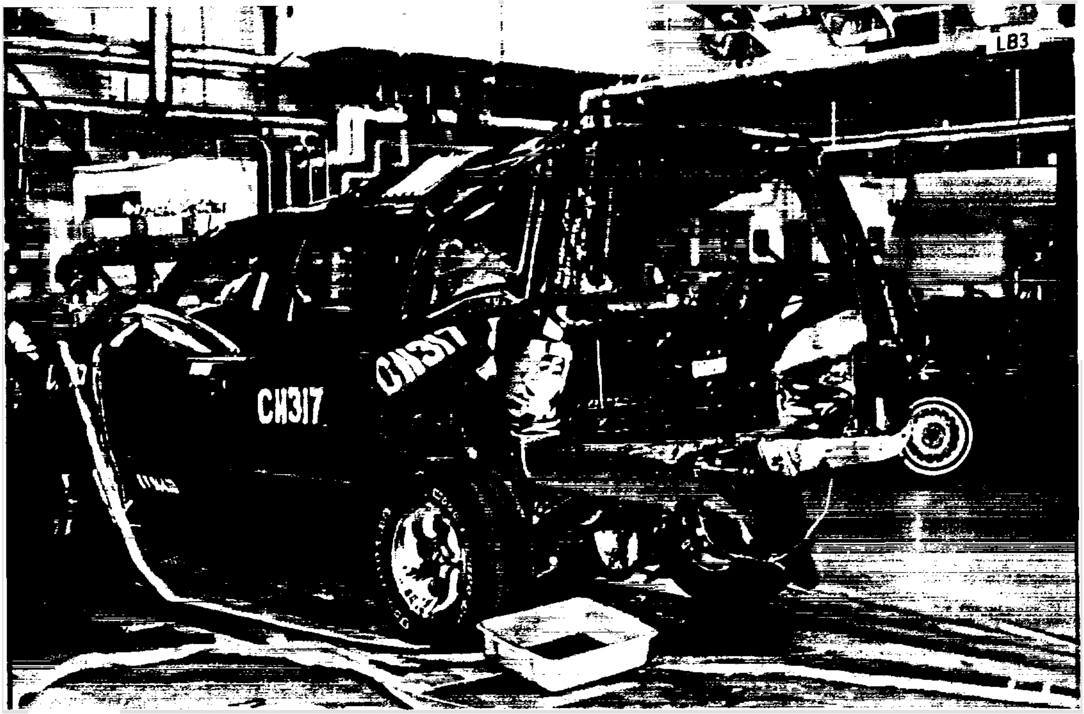

Figure 1. Fire Test F980609. Photograph of the test vehicle after the crash test.

Figure 1 is a photograph of the test vehicle after the crash test. The residual crush to the test vehicle was 550 mm on the left side of the test vehicle and 160 mm on the right side of the test vehicle. The left and right rear quarter glass panes and rear lift gate glass were broken in the crash test (Fig. 1). The right quarter interior trim finishing panel was broken, and the left quarter interior trim finishing panel was broken and dislodged (Fig. 2). The rear compartment floor pan panel and rear section of the roof were displaced upward relative to the front of the test vehicle (Fig's 1 and 2). The rear lift gate remained latched during and after the crash test (Fig. 1).

Potential fire paths into the occupant compartment observed during inspection of the test vehicle after the crash test included the window-openings in the left and right quarter panels (Fig. 1), the window opening in the rear lift gate (Fig. 1), gaps around the left rear door and door frame that were the result of deformation to the structure of the test vehicle during the crash test (Fig. 1), and four seam openings around the rear compartment floor panel. Figure 2 is a photograph of the rear compartment of the test vehicle after the crash test. The arrows in Figure 2 indicate the approximate locations of these seam openings: a seam opening between the rear compartment floor panel and the quarter panel behind the left rear wheelhouse (A); a seam opening between

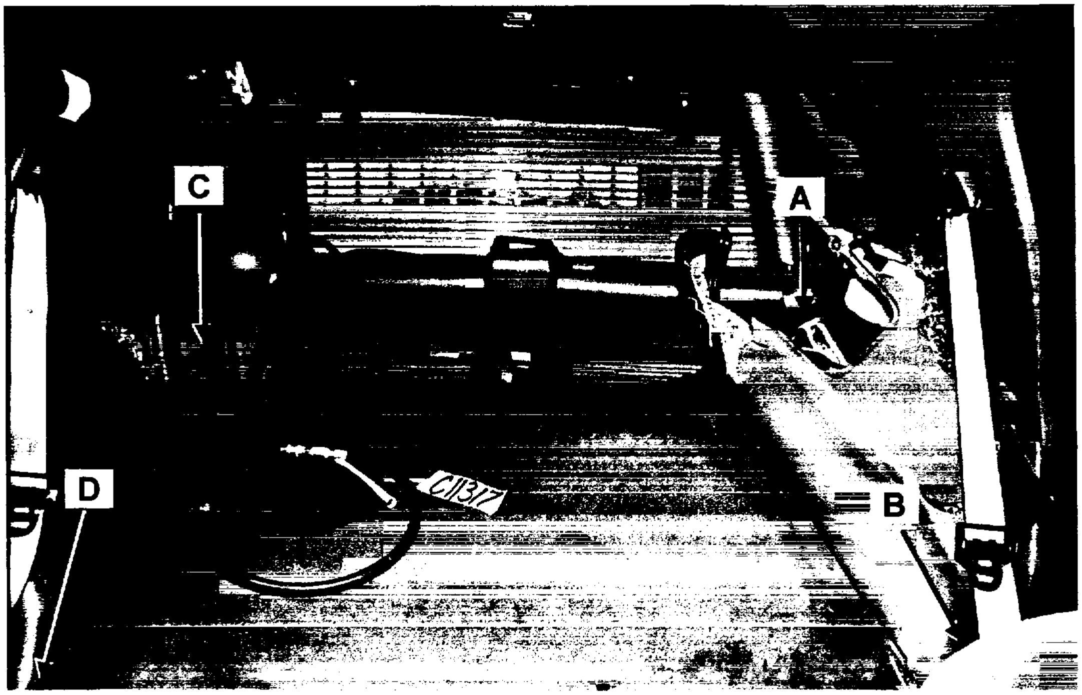

Figure 2. Fire Test F980609. Photograph of the rear interior of the test vehicle after the crash test. The arrows indicate the locations of seam openings noted in the test vehicle after the crash test.

the rear compartment floor panel and left wheelhouse at the kick-up behind the rear seat (B); a seam opening between the rear compartment floor panel and the quarter panel in the right rear corner of the test vehicle (C); and a seam opening between the rear compartment floor panel and right wheelhouse at the kick-up behind the rear seat (D). The seam opening between the rear compartment floor panel and the quarter panel behind the left rear wheelhouse is visible in Figure 2. The other seam openings were behind the interior trim panels and not visible in Figure 2.

The fire test described in this report was conducted on June 9, 1998 at the Factory Mutual Test Center in West Glocester, Rhode Island. The fire test was designed to study propagation of an under-body gasoline pool fire into the passenger compartment. Table 1 summarizes the timing of flame-spread into the passenger compartment along these pathways.

An artificial method of creating an underbody gasoline pool was used in this test. Gasoline was pumped from an external reservoir onto the ground under the rear of the test vehicle continuously during the fire test. The outlet of the artificial gasoline supply tube was near the rear inboard corner of the fuel tank in the test vehicle. The gasoline was ignited with a propane torch and allowed to burn until flames were observed spreading across the headlining panel in the test vehicle. Flames entered the passenger compartment through the window-opening in the left quarter panel, a seam opening between the rear compartment floor panel and the quarter panel behind the left rear wheelhouse, a seam opening between the rear compartment floor panel and the quarter panel in the right rear corner of the test vehicle, and a gap between the bottom of the rear lift gate and lift gate sill an the right side of the test vehicle. Fire suppression began at approximately 170 seconds after the gasoline was ignited.

Table 1

Summary of Fire Development during in Fire Test F980609

Time[1] (sec)	**Event**
-29	Start of gasoline flow
0	Gasoline under the test vehicle was ignited using a propane torch
10 – 15	Flames entered the left rear wheelhouse
10 – 20	Flames entered the right rear wheelhouse
30 – 60	Right rear tire started to burn
90 – 100	Edge of left interior quarter trim panel started to burn
120	Spare tire blew-out
120 – 125	Flames enter rear compartment through seam opening in rear left corner of the test vehicle
150 – 160	Fire plume started to spread along rear section of headlining panel
157	Rear left tire blew-out
170	Fire suppression began

[1] Time after ignition of the gasoline pool.

2 Vehicle Condition and Test Protocol

The crash-tested vehicle was prepared for the fire tests at the General Motors Research and Development Center (GM R&D Center) in Warren, Michigan, and shipped to the Factory Mutual Test Center in West Glocester, Rhode Island where this fire test was conducted. The test vehicle was returned to the GM R&D Center after the fire test, where it was systematically disassembled to permit closer inspection of the fire damage and identification of fire spread paths that were not obvious during the tests.

A description of the video cameras used during this test is in **APPENDIX A**. A description of the infrared cameras used in this test is in **APPENDIX B**. A description of the thermocouples installed in the test vehicle and data from these thermocouples are in **APPENDIX C**. A description of the aspirated thermocouples used in this test appears in **APPENDIX D**. Data was not collected from the aspirated thermocouples during this test because of an equipment malfunction. A description of the heat flux transducer/radiometer assemblies installed in the test vehicle and data from these devices are in **APPENDIX E**. Description of the pressure and airflow measurement equipment and analysis procedures, and data from these measurements are in **APPENDIX F**. Description of the Fire Products Collector (FPC) at the Factory Mutual Global Test Center and analysis procedures, and data from this device are in **APPENDIX G**. A description of the Fourier Transform Infrared Gas Analysis System used during this test and results from this device are in **APPENDIX H**. Descriptions of the Gas Chromatography/Mass Spectrometry equipment and analysis procedures, and the results of these analyses are in **APPENDIX I**. Descriptions of the particulate sampling equipment and analysis procedures, and the results of these analyses are in **APPENDIX J**.

The vehicle was placed in a rectangular steel pan (length = 25 ft., width = 15 ft., height = 4 in.) to prevent spilled and leaking automotive fluids from spreading in the test facility. This fluid containment pan was fabricated from two sheets of carbon steel. Angle-braces were welded to the under-side of the pan to keep it from flexing under the weight of the vehicle. The corners of the support frame rested on load cells. Mass loss was determined from data acquired from the load cells during the test.

A layer of fiberglass-reinforced cement construction board (DuraRock, USG Corporation) was placed on bottom of the fluid containment pan. A thin layer of sand was used to level the concrete board so that the grade of the surface measured from the center to the edges along the major and minor axes was no greater than 1%. The joints between boards were sealed with latex caulking.

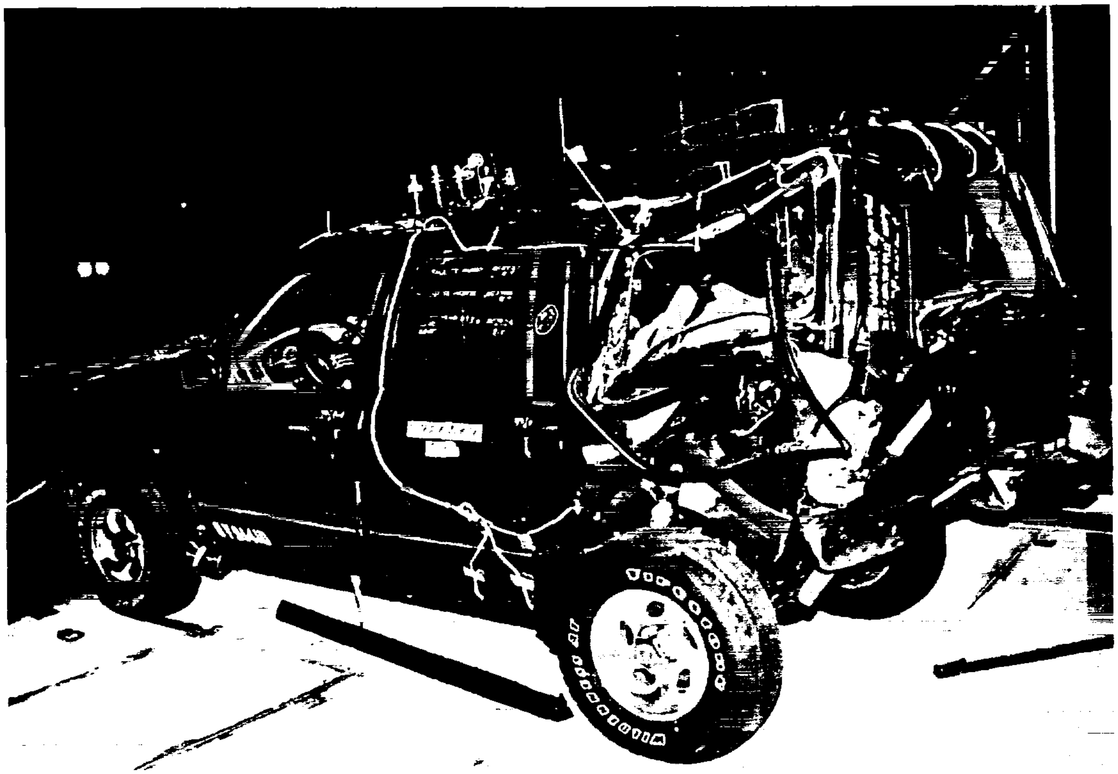

Figure 3. Fire Test F980609. Photograph of the test vehicle in the fluid containment pan before the fire test.

The test vehicle was placed in the center of the pan (Fig. 3). All doors were closed, and the door window glasses were raised to their fully closed position in each door. The left and right quarter window glasses and the rear lift gate glass, which were broken in the crash test, were not replaced for the fire test.

An air horn was sounded to signal three events during the test: (1) the start of gasoline flow, (2) ignition of the gasoline pool by a propane torch, and (3) the end of the test and start of fire suppression. The air horn was used to synchronize the data acquisition systems used in this test. The air horn was audible on the videotapes and infrared imaging systems. One channel of the data acquisition system for vehicle instrumentation monitored a normally open switch, which was depressed at each sounding. The real-time clock in the FTIR data system was synchronized to the real-time clock in the vehicle instrumentation data system.

Gasoline was delivered from a pressurized external receiver at a constant flow rate during this test. Technical personnel from the Building and Fire Research Laboratory of the National Institutes of Standards and Technologies designed, built, and operated the gasoline delivery system used in this test. Figure 4 shows a schematic diagram of the gasoline delivery system

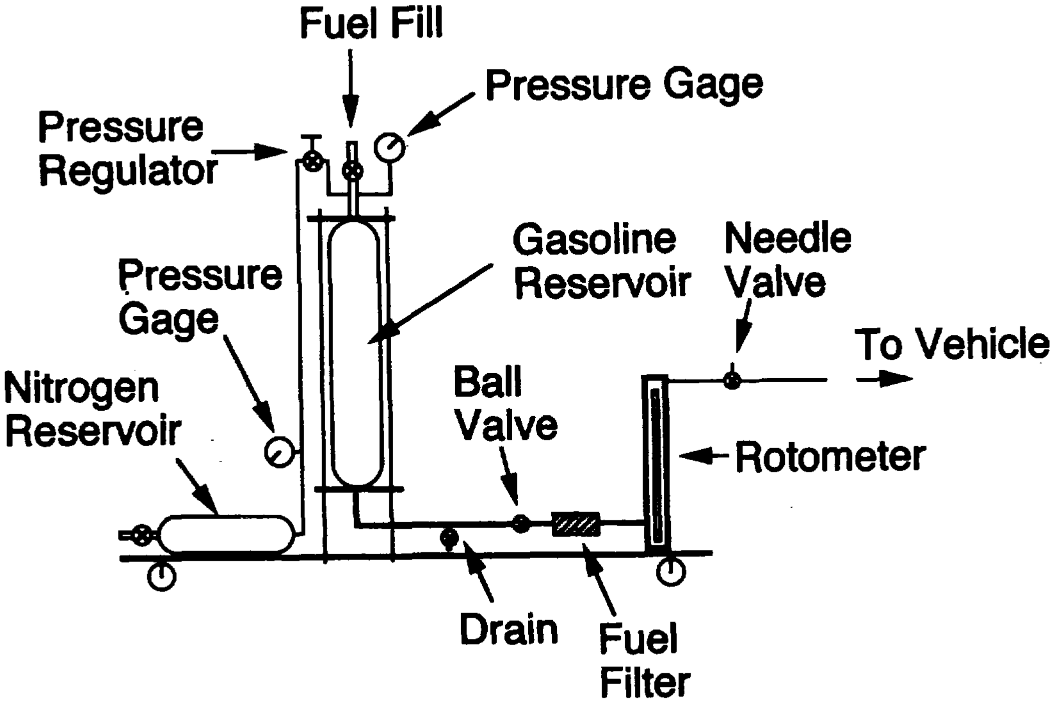

Figure 4. Fire Test F980609. Schematic diagram of the external gasoline reservoir and delivery system used to artificially supply gasoline to the test vehicle during this test.

used in this test. This system consisted of two stainless steel cylinders. One cylinder functioned as a fluid reservoir and had a capacity of 4 L, while the other cylinder functioned as a gas reservoir and had a capacity of 2 L. A pressure regulator in the line connecting the gas reservoir to the fluid reservoir controlled the head pressure in the fluid reservoir. The outlet line of the fluid reservoir contained a ball valve that was used to turn on and off the flow of gasoline during the test, a rotometer to indicate the flow of gasoline during the test, and a needle valve to control the flow of gasoline.

The outlet of the tube was located near the rear inboard corner of the fuel tank in the test vehicle. The outlet of the tube was fitted with a flow restrictor (i.d. = 0.125") to reduce vaporization of gasoline by maintaining some back-pressure in the delivery tube.

Gasoline (4 L) was added to a steel fluid reservoir (4 L). The gas reservoir was filled with dry nitrogen gas. The pressure regulator was adjusted to maintain a head pressure of 275 kPa (25.0 psi) in the fluid reservoir. Before the test, the delivery tube was purged with gasoline before the start of the test to eliminate air. The needle valve was adjusted to give a flow rate of approximately 750 ± 20 cm^3/min of gasoline[1]. A valve approximately 3 feet from the outlet of the gasoline delivery tube was mounted to the right outer quarter panel and opened to start the flow of gasoline during this test. The flow rate of gasoline through the delivery tube was determined from readings taken from the rotometer. The head pressure in the fluid reservoir and ball position in the rotometer was checked at 30 second intervals during the test to determine if the initial flow rate of gasoline had changed. The pressure regulator and needle valve were adjusted as necessary to maintain a constant flow rate of gasoline during the test.

The test was ended approximately 175 seconds after the gasoline pool under the test vehicle was ignited. A water mist was used to extinguish the flames after the flow of gasoline was stopped.

---

[1] A series of measurements was performed after this test to determine the flow rate of gasoline from the delivery system during this test. In this series of measurements, 4 L of gasoline was added to the reservoir and the pressure regulator was adjusted to maintain a head pressure of 275 kPa (25.0 psi) in the fluid reservoir. The rotometer was adjusted to match the readings recorded during the test. The volume flow rate of gasoline from the system was determined by collecting the effluent from the outlet in a graduated cylinder for a measured period of time.

3 Ignition

Figures 5 through 8 show a series of video stills from Cameras 1 through 4 at 1 second before ignition and about ½ second after ignition. Gasoline was allowed to flow onto the cement board surface under the test vehicle for approximately 30 seconds. The flow rate of liquid gasoline was maintained at 750 ± 20 cm^3/min throughout this test by manually adjusting the needle valve to keep a constant rotometer reading.

The shape of the gasoline pool on the cement board surface was not symmetrical. Liquid gasoline dripping from the rear axle differential housing onto the cement board spread out radially. A stream of liquid gasoline flowed toward the right rear wheel forming an elongated pool under the rear axle of the test vehicle (upper video stills, Fig.'s 5, 7, and 8). No attempt was made to estimate the flow rate of gasoline from the increase in pool size because of the irregular shape and depth of the pool.

A propane torch was used to ignite gasoline vapor above the liquid gasoline pool under the test vehicle approximately 30 seconds after the start of gasoline flow (lower video stills, Fig.'s 5 through 8). Ignition occurred near the rear axle differential housing. Blue flames (Fig.'s 5 through 8) spread concentrically from the point of ignition through gasoline vapor retained in the bottom of the fluid containment pan[2] after it had vaporized.

---

[2] The density of gasoline vapor is between 3 and 4, where $d_{AIR} = 1$ [5].

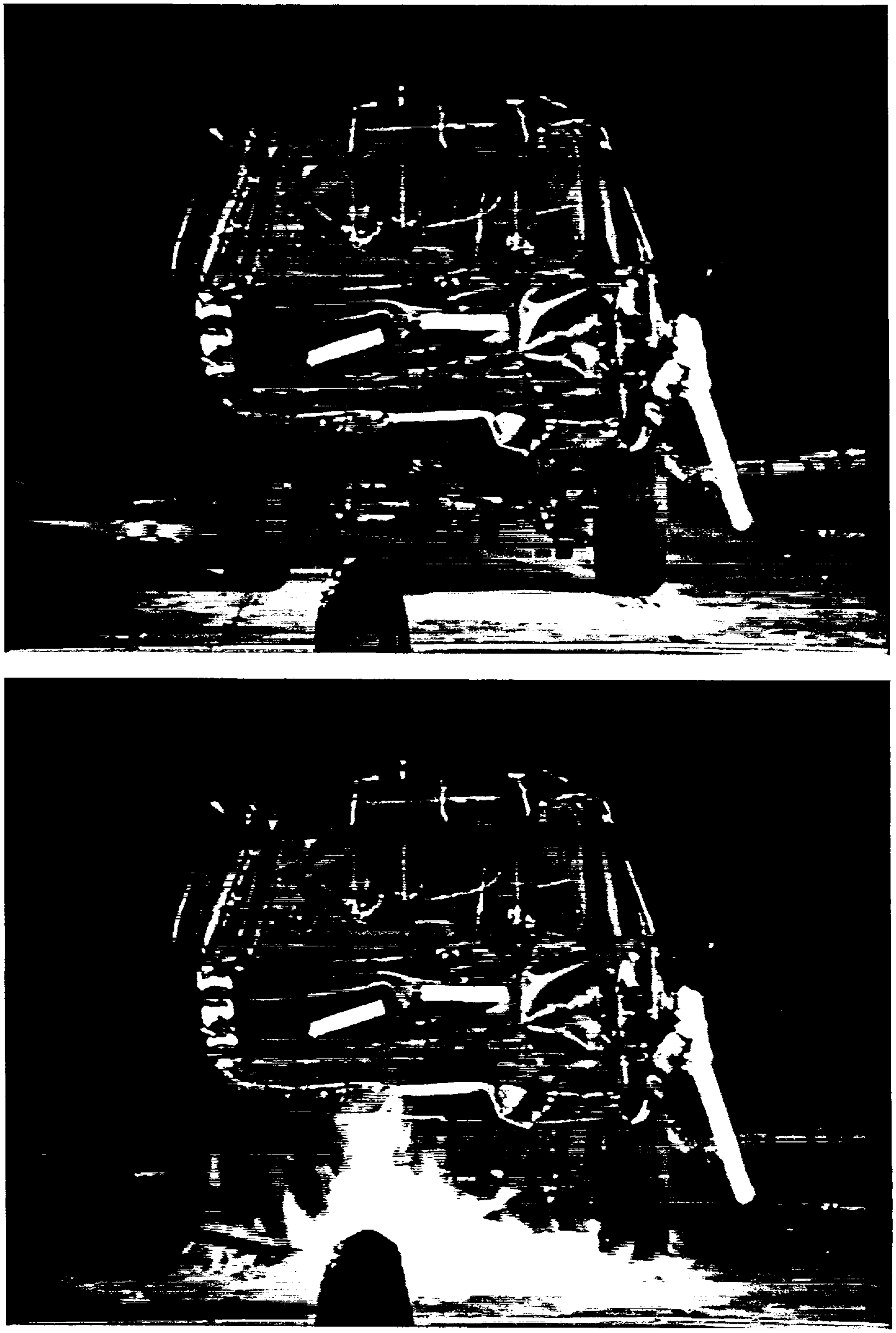

Figure 5. Fire Test F980609. Video stills from Camera 1 at 1 second before ignition (upper) and approximately ½ second after ignition (lower).

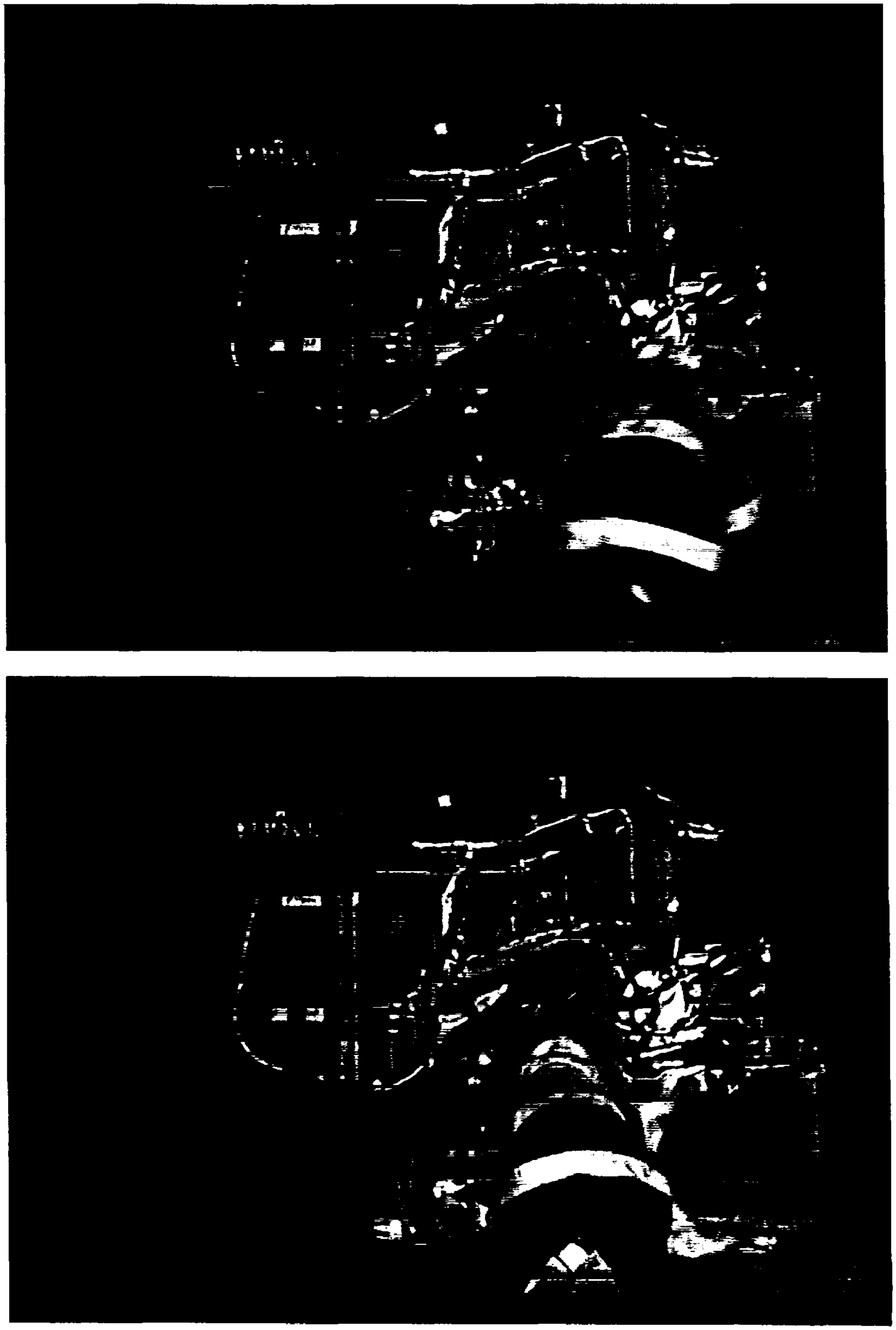

Figure 6. Fire Test F980609. Video stills from Camera 2 at 1 second before ignition (upper) and approximately ½ second after ignition (lower).

4 Behavior of the Underbody Gasoline Pool Fire in this Test

The distribution of flames on the test vehicle underbody was affected by the shape, dimensions, and location of the gasoline pool on the cement board relative to the test vehicle, the distance from the cement board to the vehicle underbody, and the shape of the test vehicle underbody. Figures 9 through 19 show a series of video stills from Cameras 5 and 6 at ½, 5, 25, 50, 75, 100, 120, 125, 150, 157, 162, and 170 seconds post-ignition. At the time of ignition, the width of the fire plume at the surface of the cement board was defined by the width of the gasoline pool, which contacted the inner side-wall of the rear right tire and extended to the left approximately 90 cm (Fig. 9). The distance between the inner side-walls of the rear tires was about 120 cm, so liquid gasoline did not contact the rear left tire at the time of ignition. The lateral extension of flames at the surface of the cement board did not change substantially from the time of ignition until about 120 seconds post-ignition (Fig.'s 10 through 14).

The shape of the vehicle underbody affected the distribution of flames on the test vehicle. The underbody of the rear compartment of the test vehicle contained the rear axle and differential housing, exhaust pipes down-stream from the muffler, the rear section of the fuel tank and fuel tank skid plate, the vapor recovery canister, and the spare tire. Vertical distances from the cement-board surface to the underbody were as follows: approximately 30 cm along the rear axle; approximately 20 cm at the center of the differential housing; 30 – 55 cm at the exhaust pipes; 15 – 20 cm at the rear of the fuel tank skid plate; 70 cm at the vapor recovery canister; approximately 35 cm at the front of the spare tire; and approximately 55 cm at the rear of the spare tire. The vertical distance between the cement-board surface and the floor pan was approximately 70 cm at the "kick-up" just behind the rear seat, approximately 90 cm on the right side of the test vehicle just forward of the rear bumper, and approximately 95 cm on the left of the test vehicle just forward of the rear bumper.

Flames extended upward between 70 and 90 cm during the first few seconds after ignition, contacting the rear axle, spare tire, exhaust pipe and floor pan to the right and left of the spare tire, and vapor recovery canister and floor pan to the left of the spare tire (Fig.'s 9 and 10). Flames spread laterally outward as they encountered these objects on the underbody of the test vehicle. Flame height increased uniformly over the next 120 seconds. Flames entered the left rear wheelhouse between 5 and 10 seconds post-ignition, and started to emerge sporadically from the top of the wheelhouse between 10 and 15 seconds post-ignition. Flames entered the right rear wheelhouse between 10 and 15 seconds post-ignition, and started to emerge sporadically from the top of the wheelhouse between 20 and 25 seconds post-ignition. Flames started to emerge sporadically behind the rear bumper by 5 seconds post-ignition.

Figure 9. Fire Test F980609. Video stills from Camera 6 (upper) and 5 (lower) at approximately ½ second after ignition.

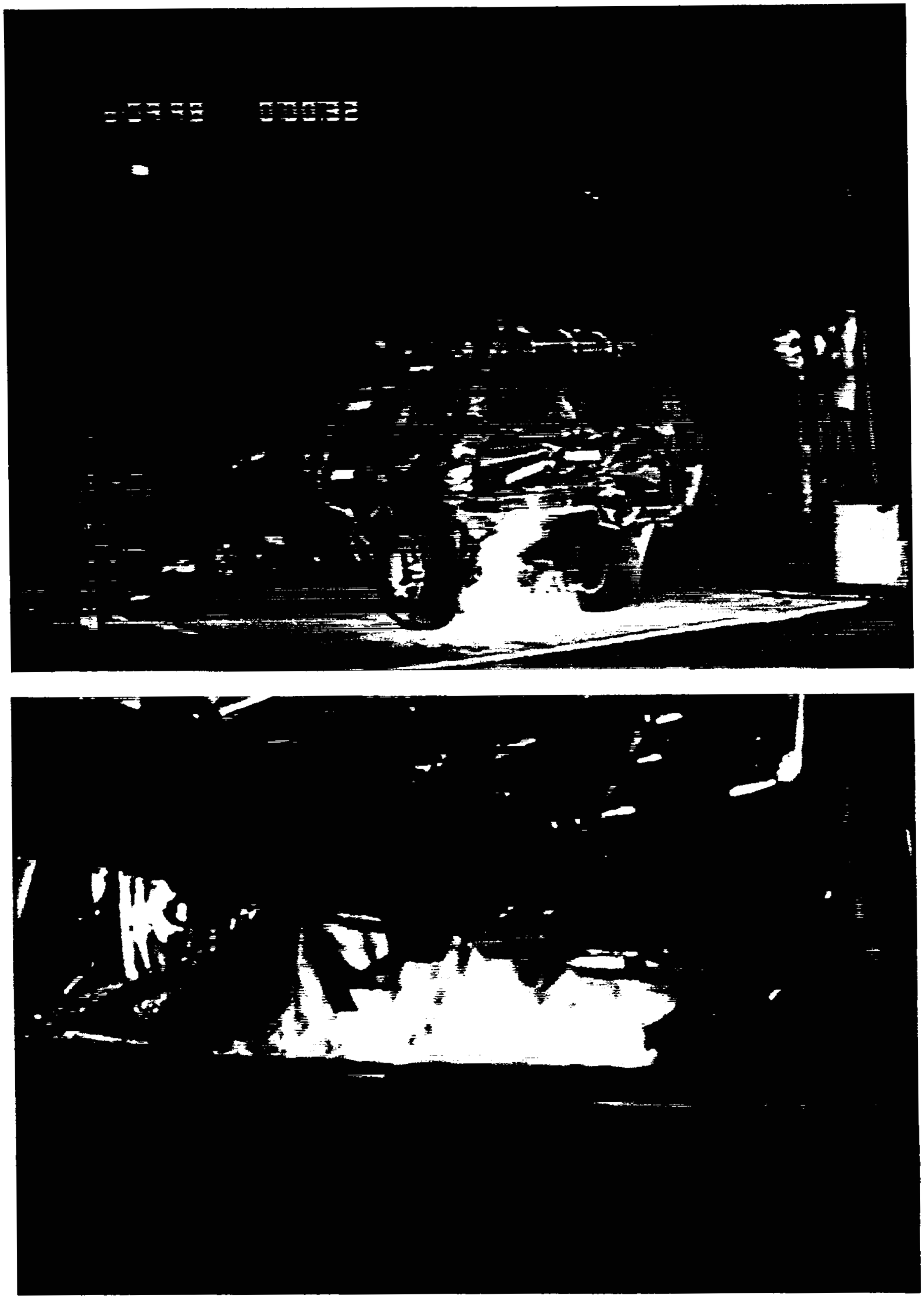

Figure 10. Fire Test F980609. Video stills from Video Cameras 6 (upper) and 5 (lower) at 5 seconds post-ignition.

Figure 11. Fire Test F980609. Video stills from Video Cameras 6 (upper) and 5 (lower) at 25 seconds post-ignition.

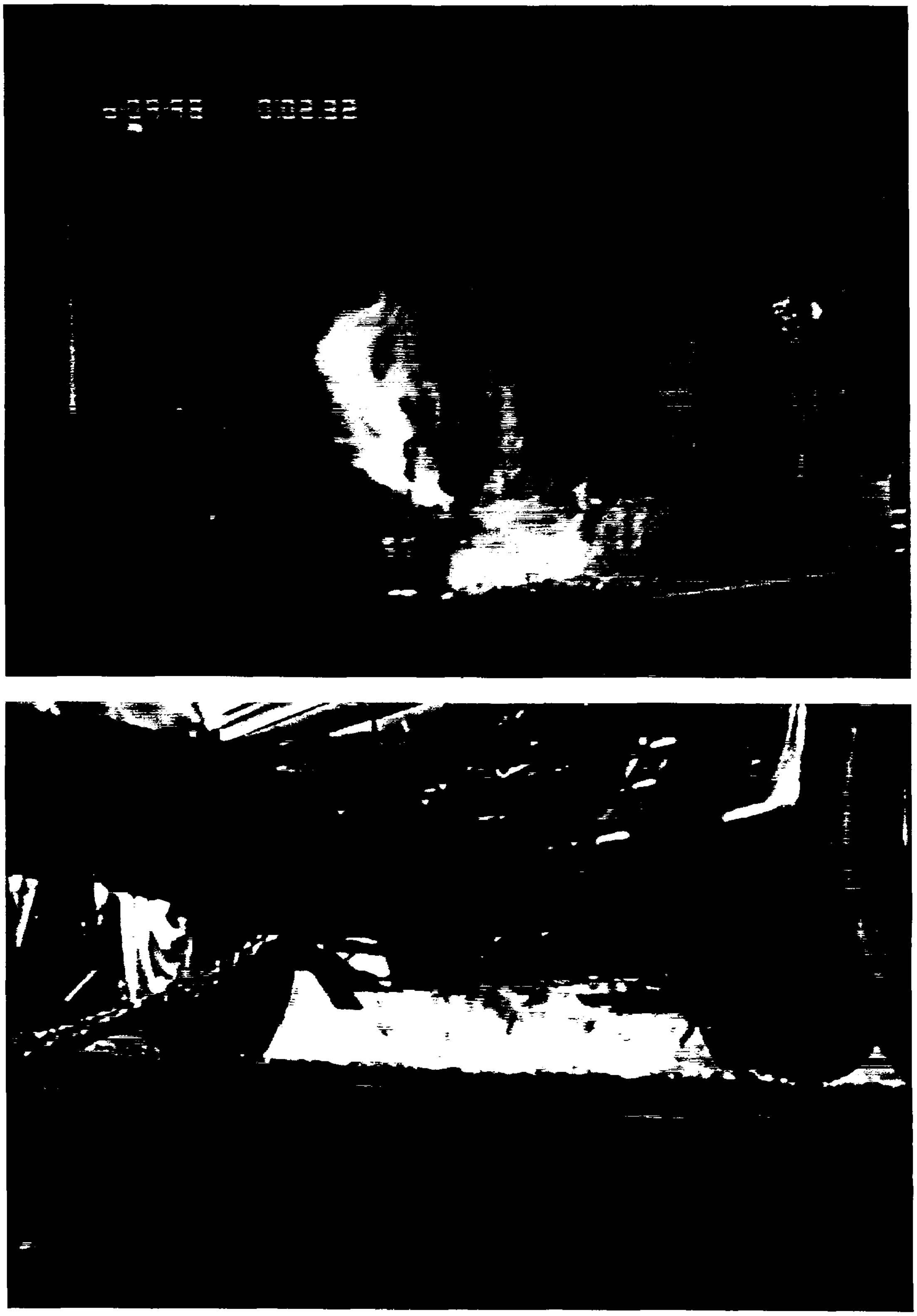

Figure 17. Fire Test F980609. Video stills from Video Cameras 6 (upper) and 5 (lower) at 125 seconds post-ignition.

The height of the fire plume emerging from the rear left wheelhouse was about 190 cm at 119 seconds post-ignition (Fig. 15). The spare tire blew out at about 120 seconds post-ignition, causing a transient increase in flame volume under, to the sides, and to the rear of the test vehicle (Fig. 16). The height of the fire plume emerging from the rear left wheelhouse decreased to approximately 165 at this time (Fig. 16). Inspection of the test vehicle after this fire test revealed that the side-wall of the spare tire facing downward was charred and contained a hole where it was pushed against the rear axle differential housing[3] (Fig. 20). The location and orientation of the hole indicated that air venting from the tire was directed downward onto the fluid containment pan and outward radially from under the rear of the test vehicle. The resulting transient increase in airflow over the surface of the gasoline pool had two effects: it increased ventilation under the test vehicle and it distributed a mixture of gasoline aerosol and vapor outward in the direction of airflow. These combined effects resulted in the transient increase in flame volume at 120 seconds post-ignition (Fig. 16).

The height of the fire plume emerging from the rear left wheelhouse decreased to about 140 cm at 125 seconds post-ignition and remained approximately constant until 157 seconds post-ignition (Fig.'s 17 through 19). The rear right tire blew out at approximately 157 seconds post-ignition

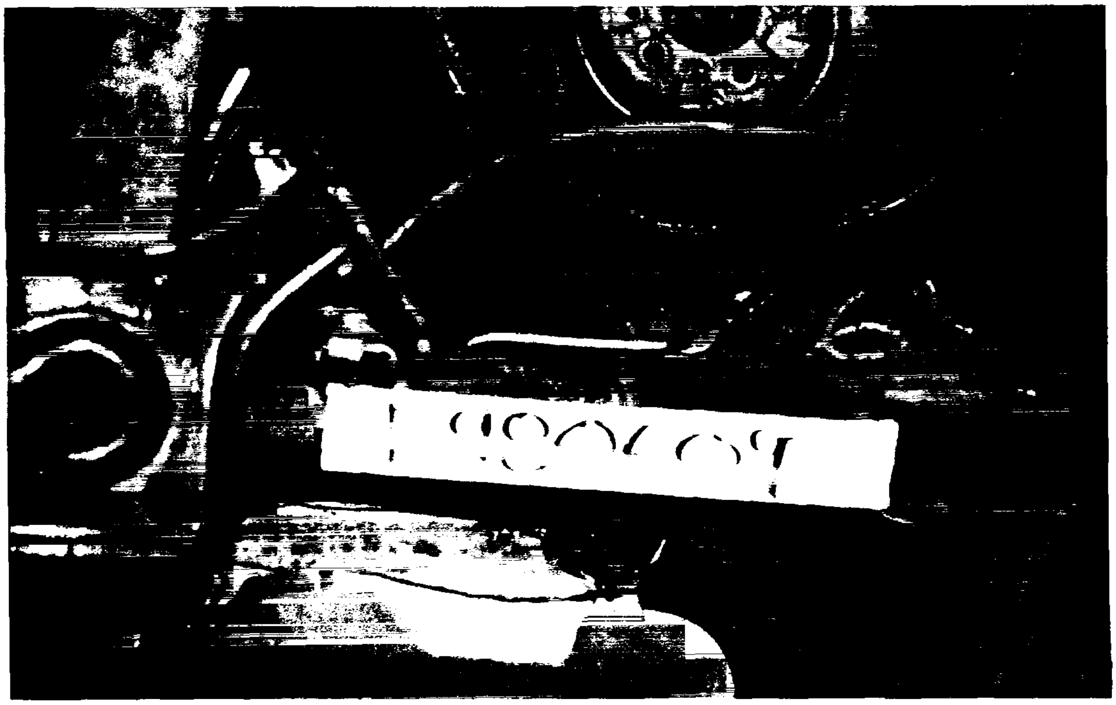

Figure 22. Fire Test F980609. Photograph of the spare tire and rear axle in the test vehicle after this fire test.

---

[3] The spare tire was pushed against the differential housing during the crash test.

(Fig. 20). A video still from Camera 1 at 50 seconds post-ignition shows that the inner side-wall and sections of the tread of the rear right tire burning (Fig. 23).

Figure 23. Fire Test F980609. Close-up of a Video Still from Camera 1 at 50 seconds post-ignition.

Inspection of the test vehicle after this test showed that the inner side-wall of the rear right tire was charred (Fig. 24). A hole was observed in the bottom section of the inner side-wall (Fig. 24). The location and orientation of the hole indicated that air venting from the rear right tire was directed to the left along the surface of the fluid containment pan. This transient increase in airflow over the surface of the gasoline pool resulted in the transient increase in flame volume to the left of the test vehicle observed at about 157 seconds post-ignition (Fig. 20). The inner side-wall of the rear left tire was charred, and sections of the tread contained an oily film (Fig. 24), indicating that sections of the rear left tire had ignited by the time this test was ended.

This area of the test vehicle was not visible in the videos recorded during this test. Isothermal contour plots were estimated from temperature data recorded from thermocouples located just below the floor panel in the rear compartment of the test vehicle. Figure 25 shows a series of

Figure 24. Fire Test F980609. Photograph of the area under the rear of the test vehicle after this fire test.

diagrams of the test vehicle with estimated isothermal contour plots of temperature profiles below the rear compartment floor panel at –10, 0, 25, 50, 75, 100, 120, 125, 150, 157, 162, and 170 seconds post-ignition.[4] The approximate distribution of flames under the test vehicle was indicated by isothermal contours with t ≥ 600°C.[5] This analysis indicates that flames were present below an area of the floor pan in the drive train tunnel just forward of the differential housing starting at about at about 50 seconds post-ignition. The area where estimated temperatures were greater than 600°C did not change substantially for the next 100 seconds. Estimated temperatures below the floor pan increased between 167 and 170 seconds post-ignition, which was coincident with the timing of the rear right tire blowing out. Temperatures > 600°C were recorded in the rear left wheelhouse sporadically starting at about 25 seconds post-ignition, and continuously from about 75 seconds post-ignition until the end of this test. Isothermal contours were not estimated for the rear right wheelhouse because no thermocouples were located in the rear right wheelhouse.

---

[4] Isothermal contours of the temperature below the rear compartment floor panel were estimated from the temperature data recorded from Thermocouples F5, F7, F9, F12, F14, F16, F18, F20, F22, F24, WW1, and WW6 using a three-dimensional interpolation algorithm available in SigmaPlot for Windows Version 4.00 [6]. This algorithm used an inverse distance method to interpolate temperature values for points on a uniformly spaced Cartesian grid from the [x,y,t] triple data from these thermocouples. Refer to **APPENDIX C** for the approximate locations of these thermocouples.

[5] As in previous reports, a value of 600°C was used in this report as the threshold to indicate the presence of flame.

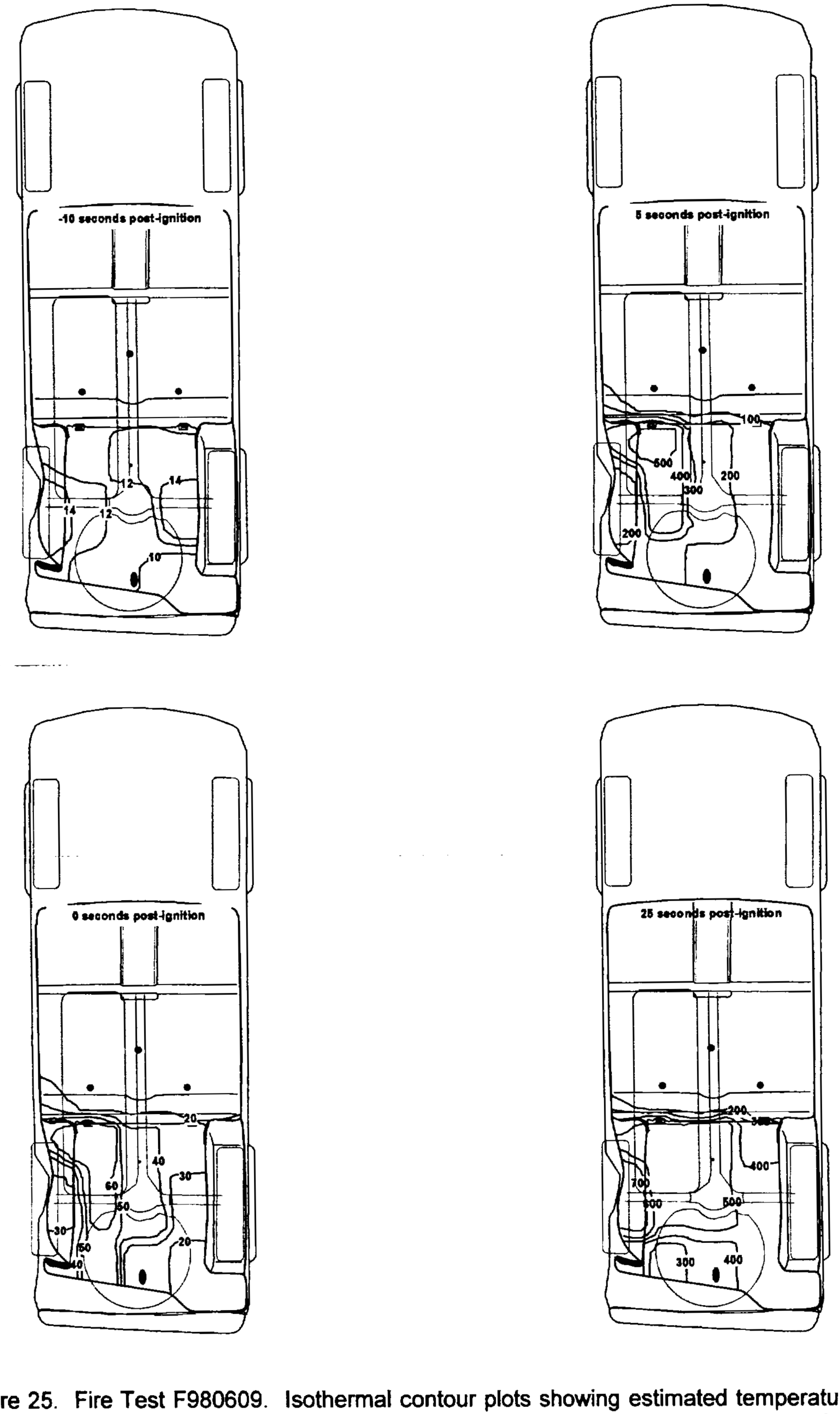
-10 seconds post-ignition

5 seconds post-ignition

0 seconds post-ignition

25 seconds post-ignition

Figure 25. Fire Test F980609. Isothermal contour plots showing estimated temperatures below the floor panel at –10, 0, 5, 25, 50, 75, 100, 120, 125, 150, 157, and 170 seconds post-ignition.

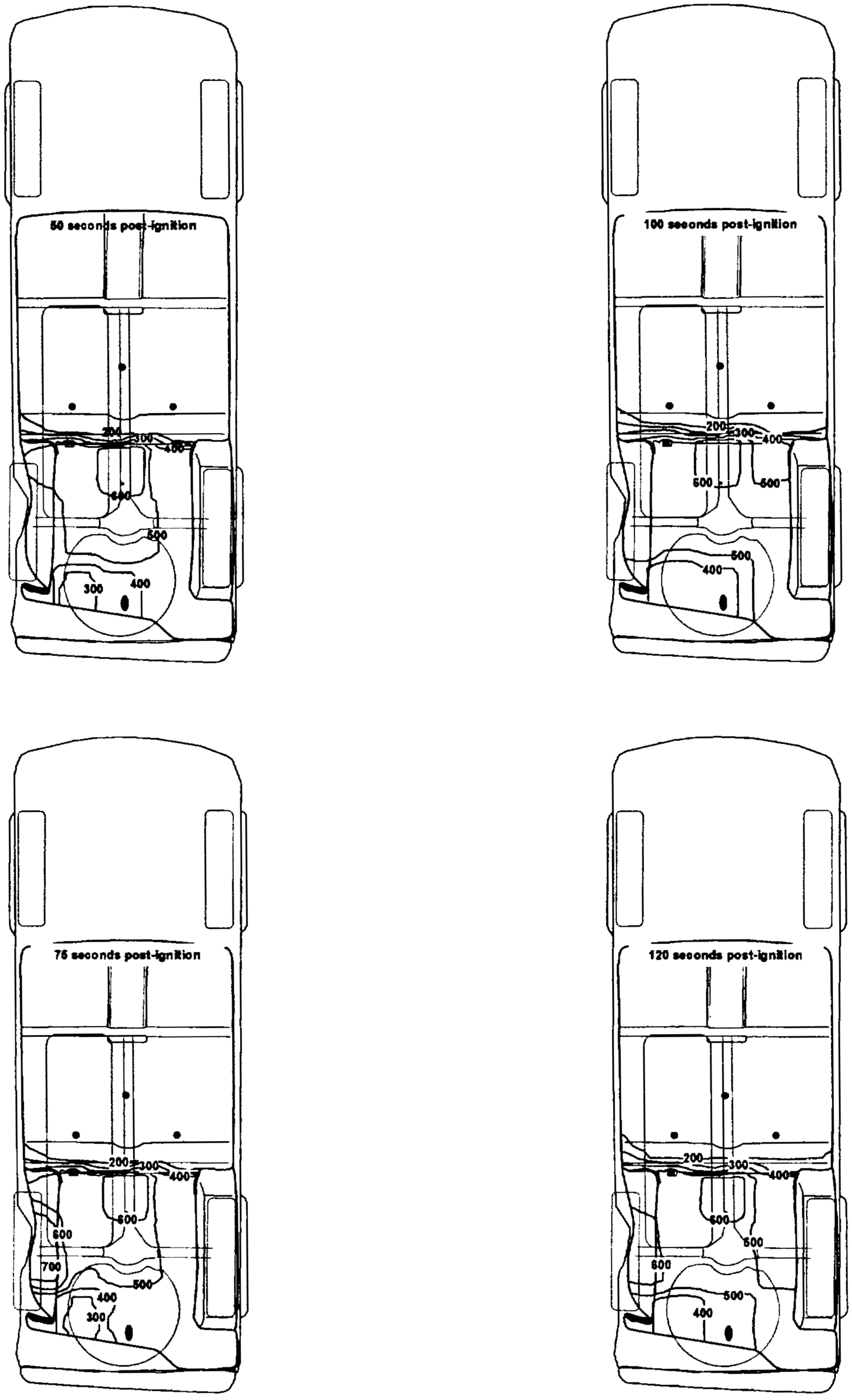

Figure 25, continued. Fire Test F980609. Isothermal contour plots showing estimated temperatures below the floor panel at –10, 0, 25, 50, 75, 100, 120, 125, 150, 157, 162, and 170 seconds post-ignition.

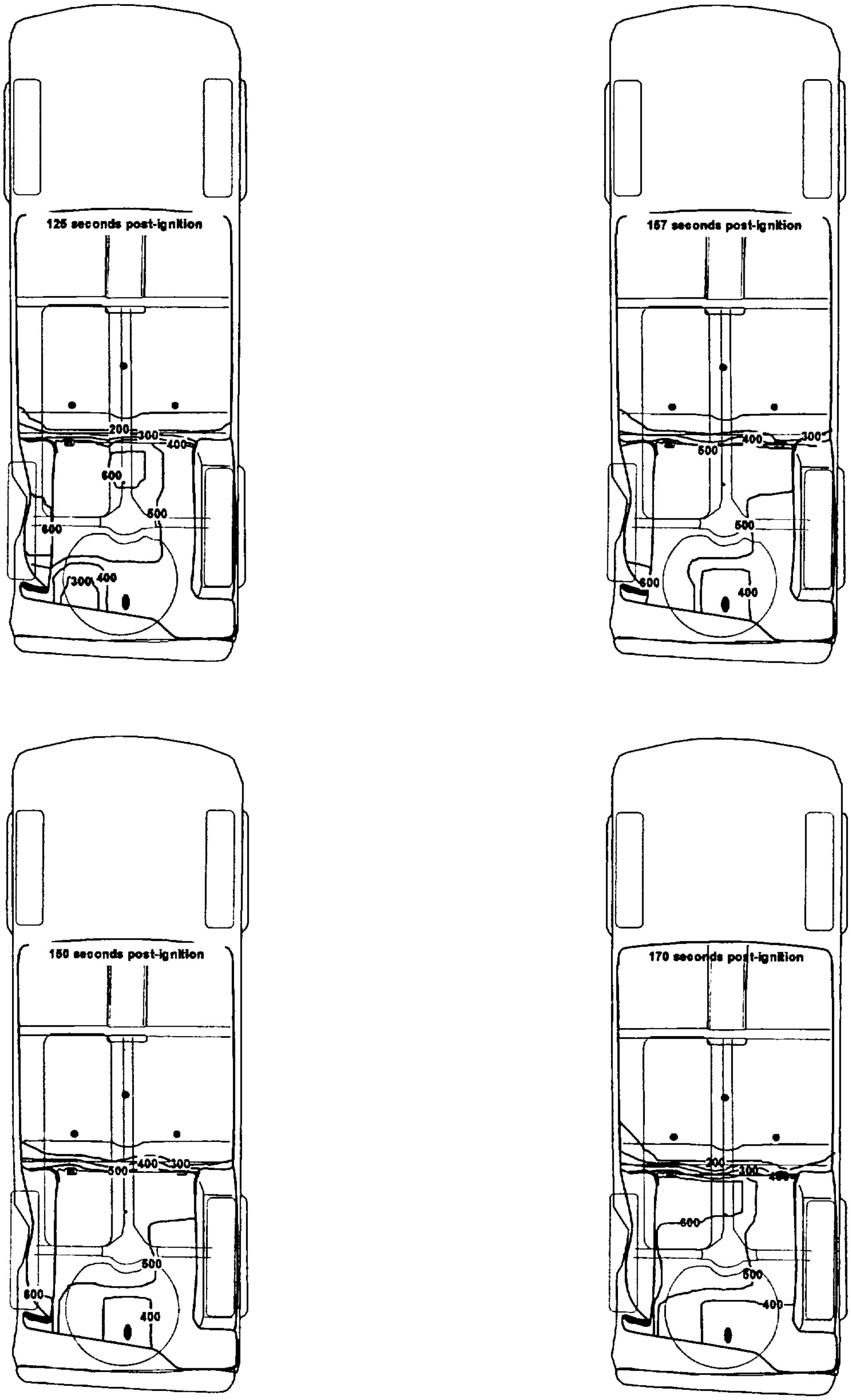

Figure 25, continued. Fire Test F980609. Isothermal contour plots showing estimated temperatures below the floor panel at –10, 0, 25, 50, 75, 100, 120, 125, 150, 157, 162, and 170 seconds post-ignition.

Components such as the fuel tank, spare tire, and exhaust system heat shields appear to have affected the distribution of heated gases and flames in the area just below the lower surface of the rear compartment floor panel. Figure 26 is a diagram of the test vehicle showing the approximate locations of crash-induced seam openings, floor pan plugs, fuel tank, the spare tire/wheel, rear axle and rear tires/wheels, and the exhaust system components.

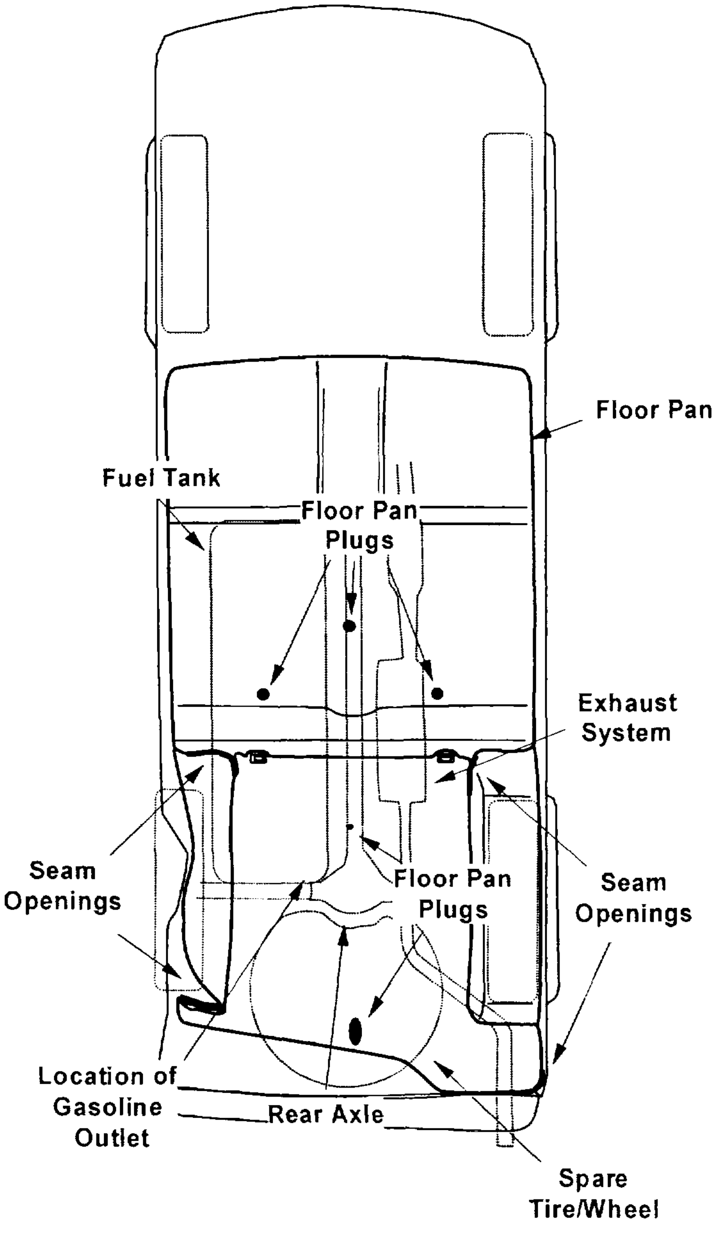

Figure 26. Fire Test F980609. Top view of the floor pan in the test showing the floor pan and the approximate locations of crash-induced seam openings, floor pan plugs, fuel tank, the spare tire/wheel, rear axle and rear tires/wheels, exhaust system components, and the gasoline outlet installed on the test vehicle for this test.

The estimated temperature profiles in Figure 26 indicate that heated gases and flames were not distributed along the lower surface of the rear compartment floor panel concentrically around the gasoline outlet, which was the approximate center of the gasoline pool. For example, estimated temperatures above the spare tire and exhaust system were 100 to 200°C lower than estimated temperatures above the rear of the fuel tank or in the left rear wheelhouse (Fig. 26). One possible explanation of this temperature difference is that the spare tire and exhaust system acted as physical obstacles shielding areas of the floor pan in the rear compartment from direct exposure to heated gases and flames. These and other underbody components also may have restricted airflow into the space just below the floor panel reducing ventilation and resulting in insufficient oxygen for combustion, which may explain the decrease in estimated temperatures below the floor pan between 125 and 150 seconds post-ignition.

5 Flame-Spread into the Passenger Compartment

The data presented in this section indicate that flame-spread into the passenger compartment progressed along a number of pathways simultaneously. The forward vertical and lower horizontal edges of the left quarter trim panel around the left quarter glass opening were ignited by the fire plume rising along the exterior of the left quarter panel. Flames spread into the rear compartment through a crash-induced seam opening at the rear of the left rear wheelhouse. Flames spread into the area behind the right quarter trim panel through a crash-induced seam opening at the rear right corner of the floor pan. Conduction through the floor pan resulted in ignition of the lower edge of the right rear quarter trim panel at the base of the rear right wheelhouse. Flames spread into the rear compartment under the bottom right edge of the lift gate. The following sections contain an analysis of the test data to determine the timing and locations of flame spread into the passenger compartment.

Figures 27 through 33 show a series of video stills from Cameras 1 and 4 and Infrared thermograms for IR3 and IR4 at 119, 120, 125, 150, 157, 158, and 170 seconds post-ignition. This sequence of video stills shows the approximate timing of flame-spread into the passenger compartment through a crash-induced seam opening at the rear of the left rear wheelhouse. Flames were not visible in the rear compartment in the area of the rear left wheelhouse earlier than 125 seconds post-ignition (Fig.'s 27 and 28). A fire plume was visible in the space above the left rear wheelhouse by 125 seconds post-ignition (Fig. 29), coincident with the timing of the spare tire blowing out, and appeared to contact the roof trim by about 150 seconds post-ignition (Fig. 30). By 157 seconds post-ignition, flames had spread laterally to the right along the rear of the roof trim panel, reaching the right side of the test vehicle (Fig. 31). The size of the fire plume above the left rear wheelhouse increased between 157 and 158 seconds post-ignition (Fig.'s 31 and 32), which coincided with the timing of the right rear tire blowing out (Fig. 31). A fire plume in the area of the right rear wheelhouse was visible by 170 seconds post-ignition (Fig. 33).

5.1 Flame-Spread through a Seam Opening in the Left Rear Wheelhouse and the Left Quarter Glass Opening, and Ignition of the Left Quarter Trim Panel

Data recorded from thermocouples and a heat flux transducer located in the rear compartment of the test vehicle indicated that flames spread into the rear compartment through a crash-induced seam opening between the rear compartment floor panel and the left rear wheelhouse panel between 140 and 160 seconds post-ignition. Figure 34 is a photograph of the left side of the rear compartment of the test vehicle after the crash test and before this fire test showing a crash-induced seam opening between the rear compartment floor panel and the left rear wheelhouse panel.

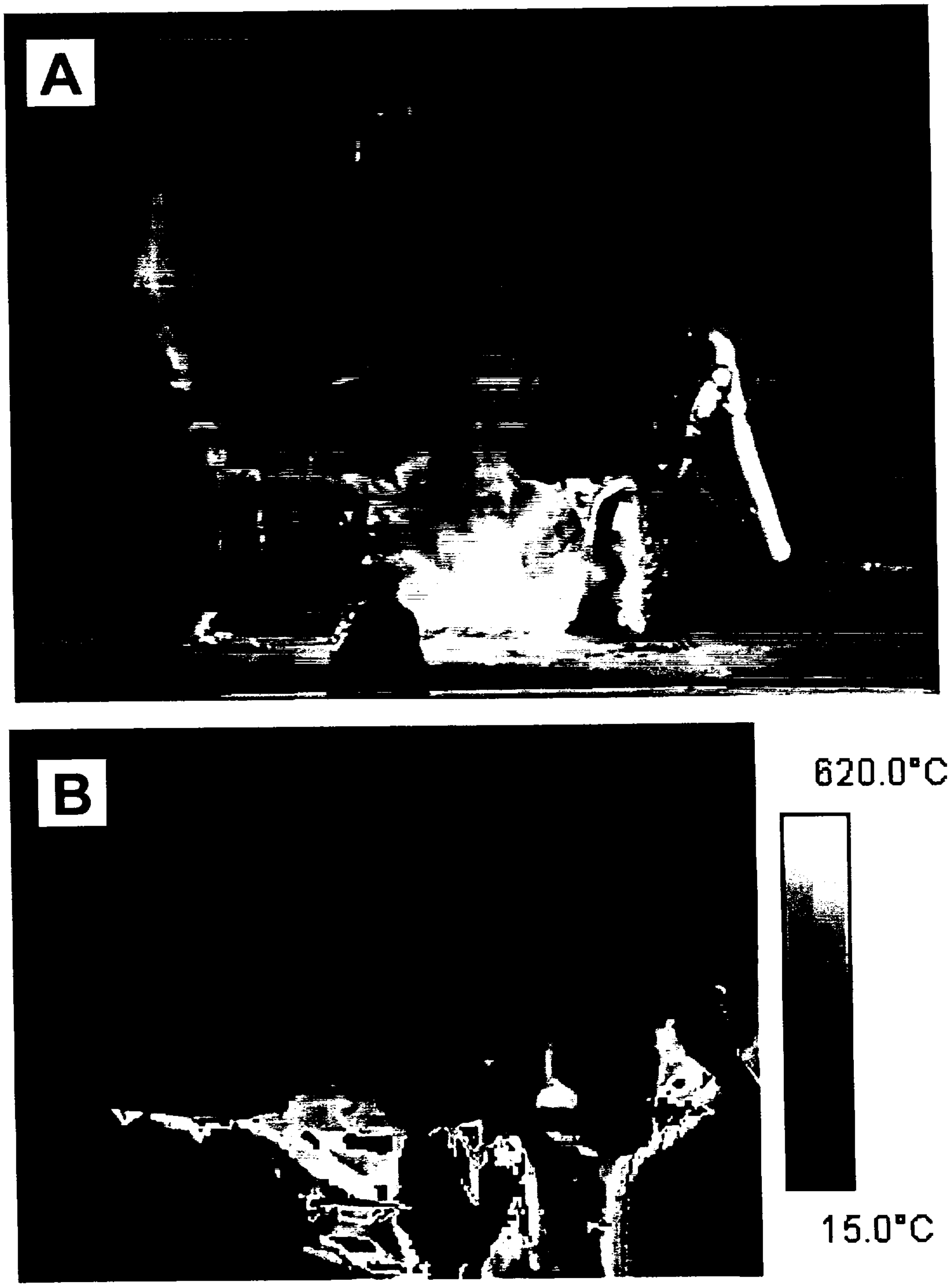

Figure 27. Fire Test F980609. Video still from Video Camera 1 (A), Infrared thermogram from IR3 (B), video still from Camera 4 (C), and Infrared thermogram from IR4 (D) at 119 seconds post-ignition.

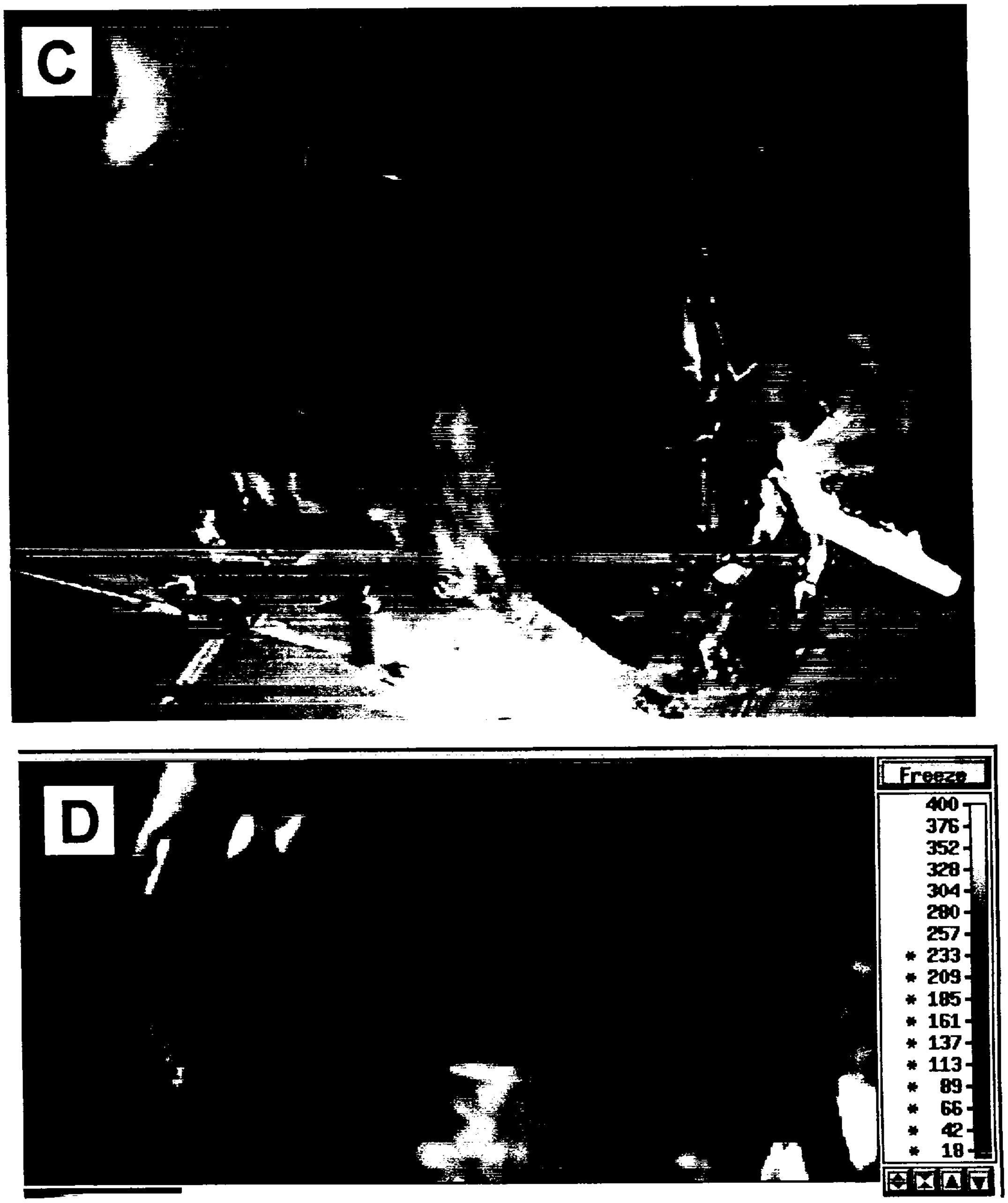

Figure 27, continued. Fire Test F980609. Video still from Video Camera 1 (A), Infrared thermogram from IR3 (B), video still from Camera 4 (C), and Infrared thermogram from IR4 (D) at 119 seconds post-ignition.

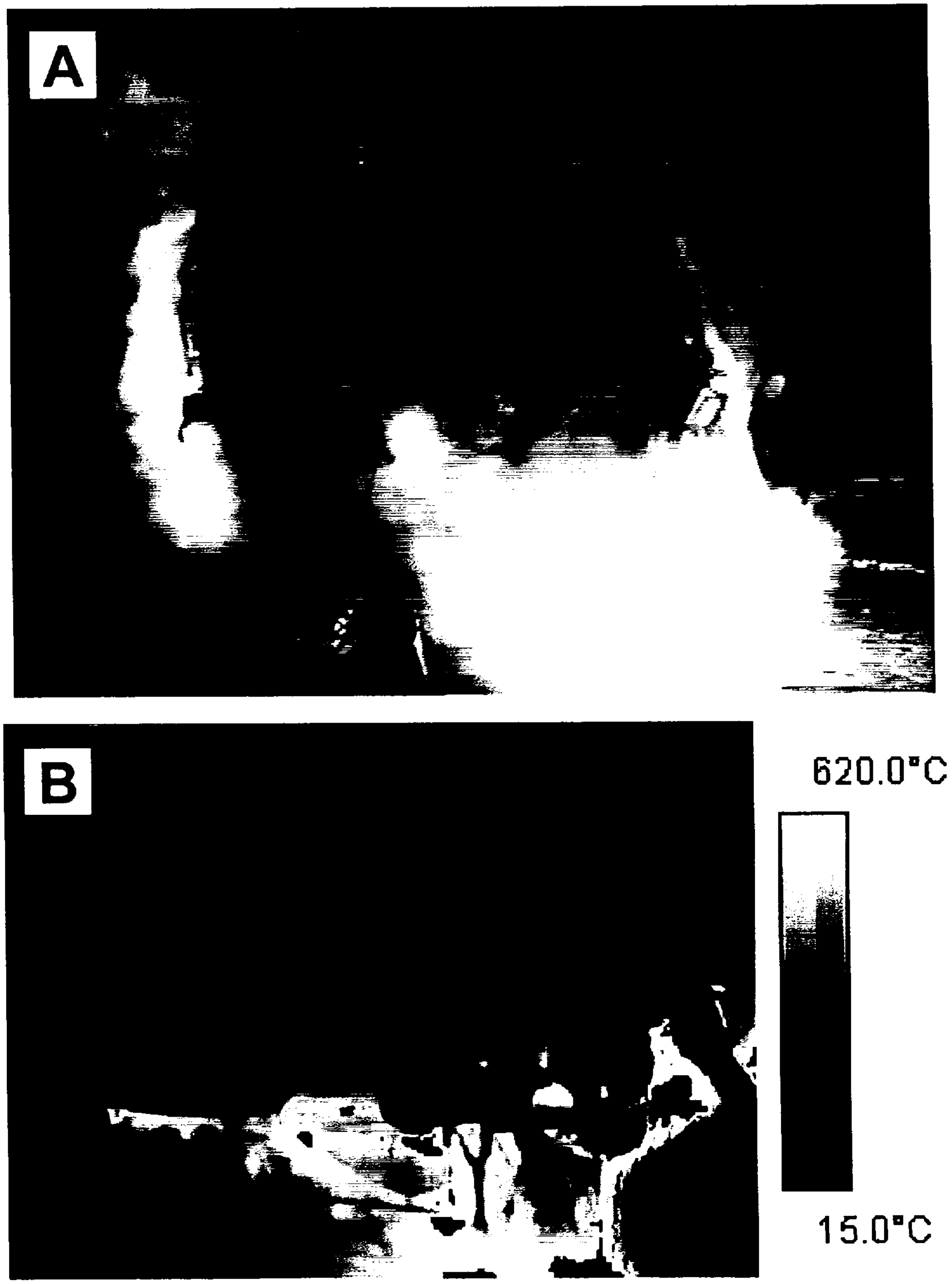

Figure 28. Fire Test F980609 Video still from Video Camera 1 (A), Infrared thermogram from IR3 (B), video still from Camera 4 (C), and Infrared thermogram from IR4 (D) at 120 seconds post-ignition.

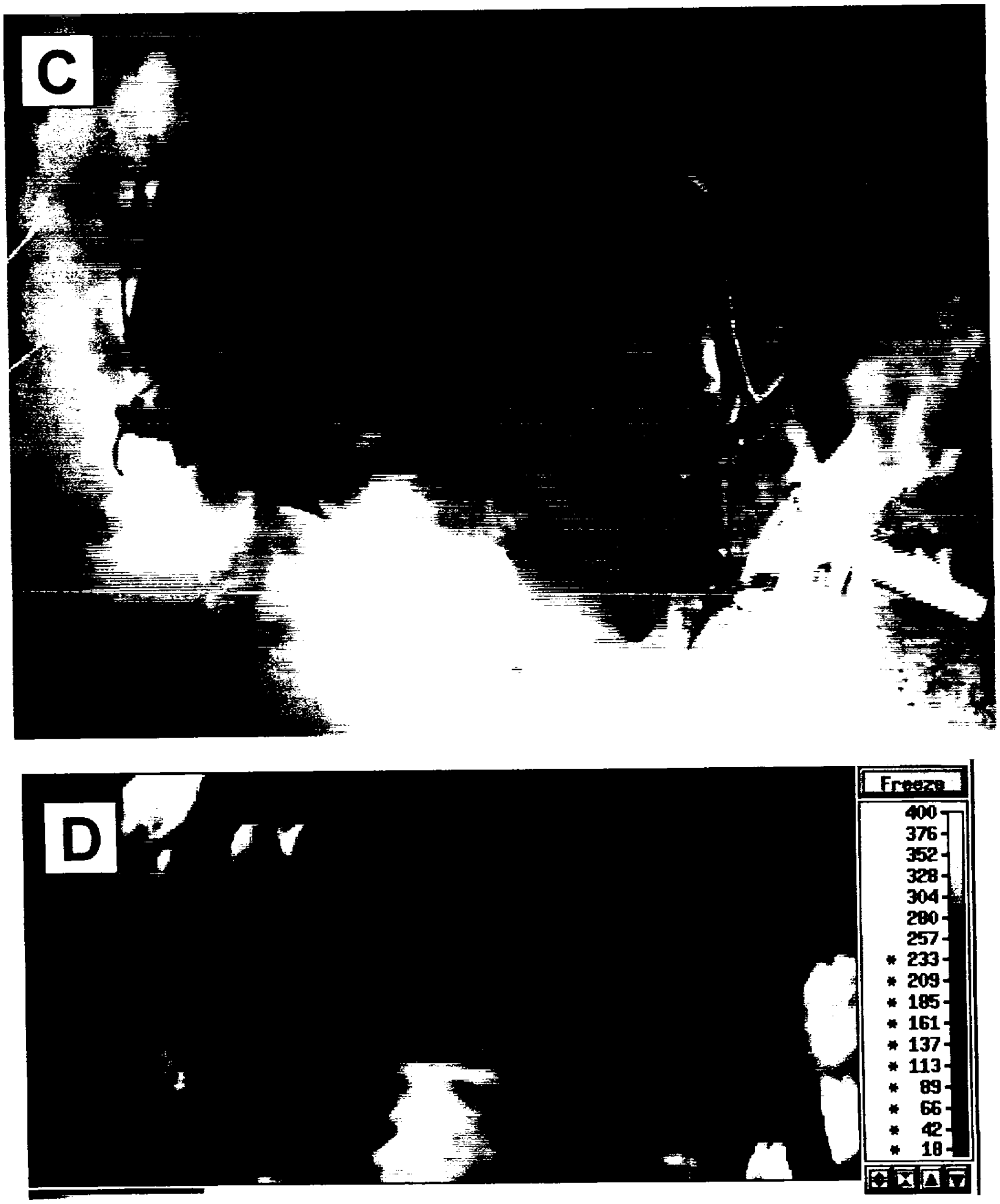

Figure 28, continued. Fire Test F980609 Video still from Video Camera 1 (A), Infrared thermogram from IR3 (B), video still from Camera 4 (C), and Infrared thermogram from IR4 (D) at 120 seconds post-ignition.

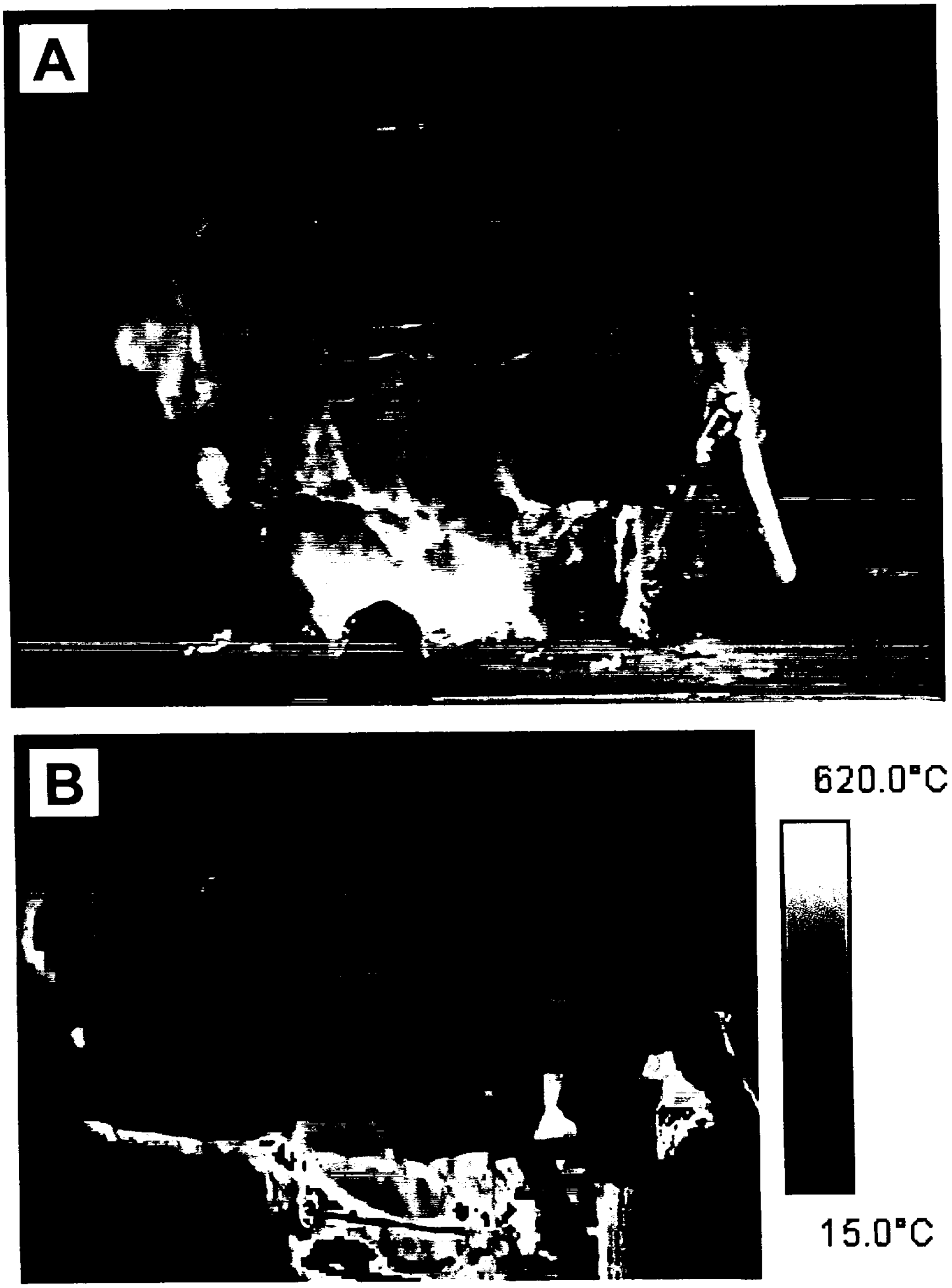

Figure 29. Fire Test F980609. Video still from Video Camera 1 (A), Infrared thermogram from IR3 (B), video still from Camera 4 (C), and Infrared thermogram from IR4 (D) at 125 seconds post-ignition.

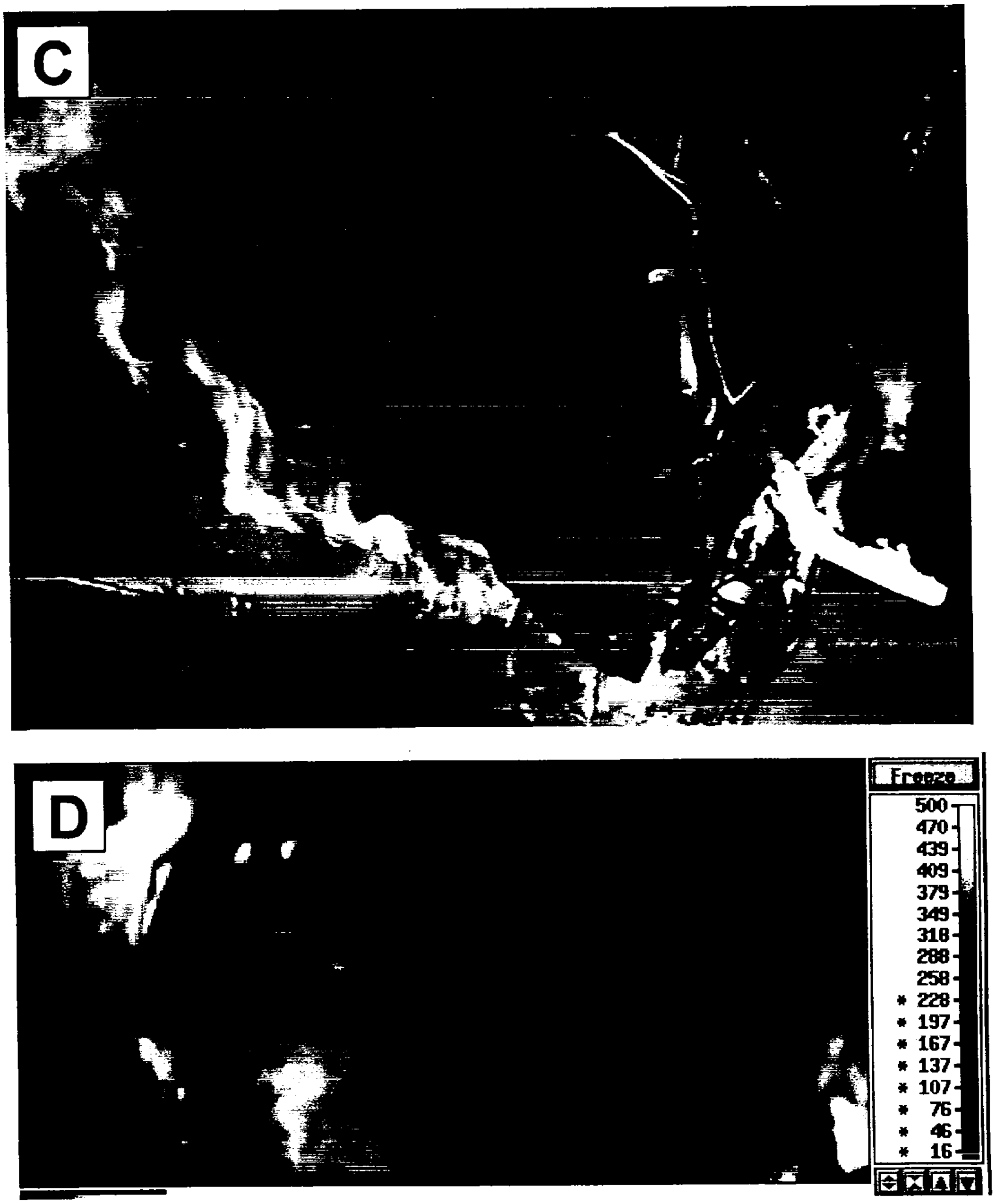

Figure 29, continued. Fire Test F980609. Video still from Video Camera 1 (A), Infrared thermogram from IR3 (B), video still from Camera 4 (C), and Infrared thermogram from IR4 (D) at 125 seconds post-ignition.

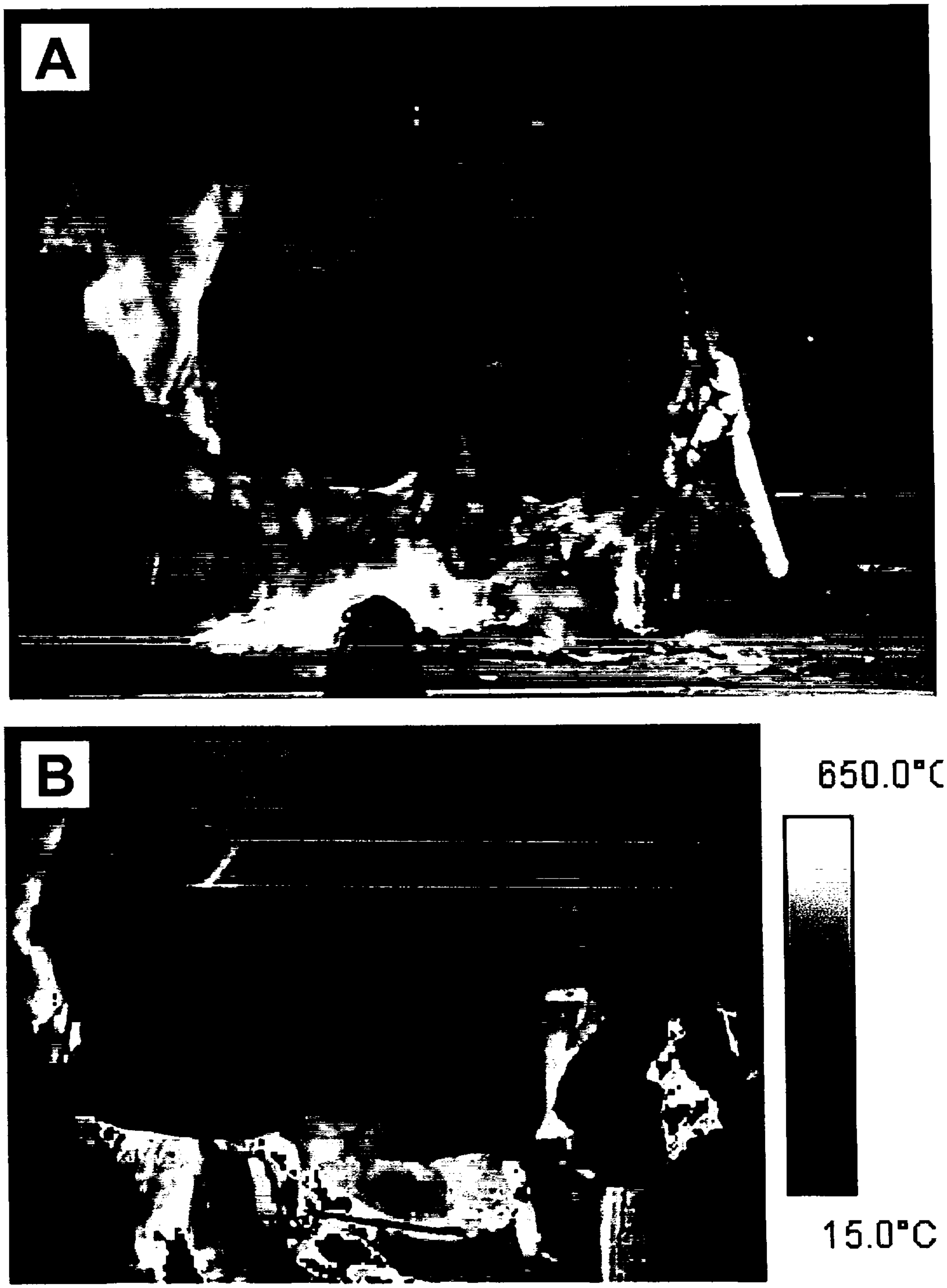

Figure 30. Fire Test F980609. Video still from Video Camera 1 (A), Infrared thermogram from IR3 (B), video still from Camera 4 (C), and Infrared thermogram from IR4 (D) at 150 seconds post-ignition.

Figure 30, continued. Fire Test F980609. Video still from Video Camera 1 (A), Infrared thermogram from IR3 (B), video still from Camera 4 (C), and Infrared thermogram from IR4 (D) at 150 seconds post-ignition.

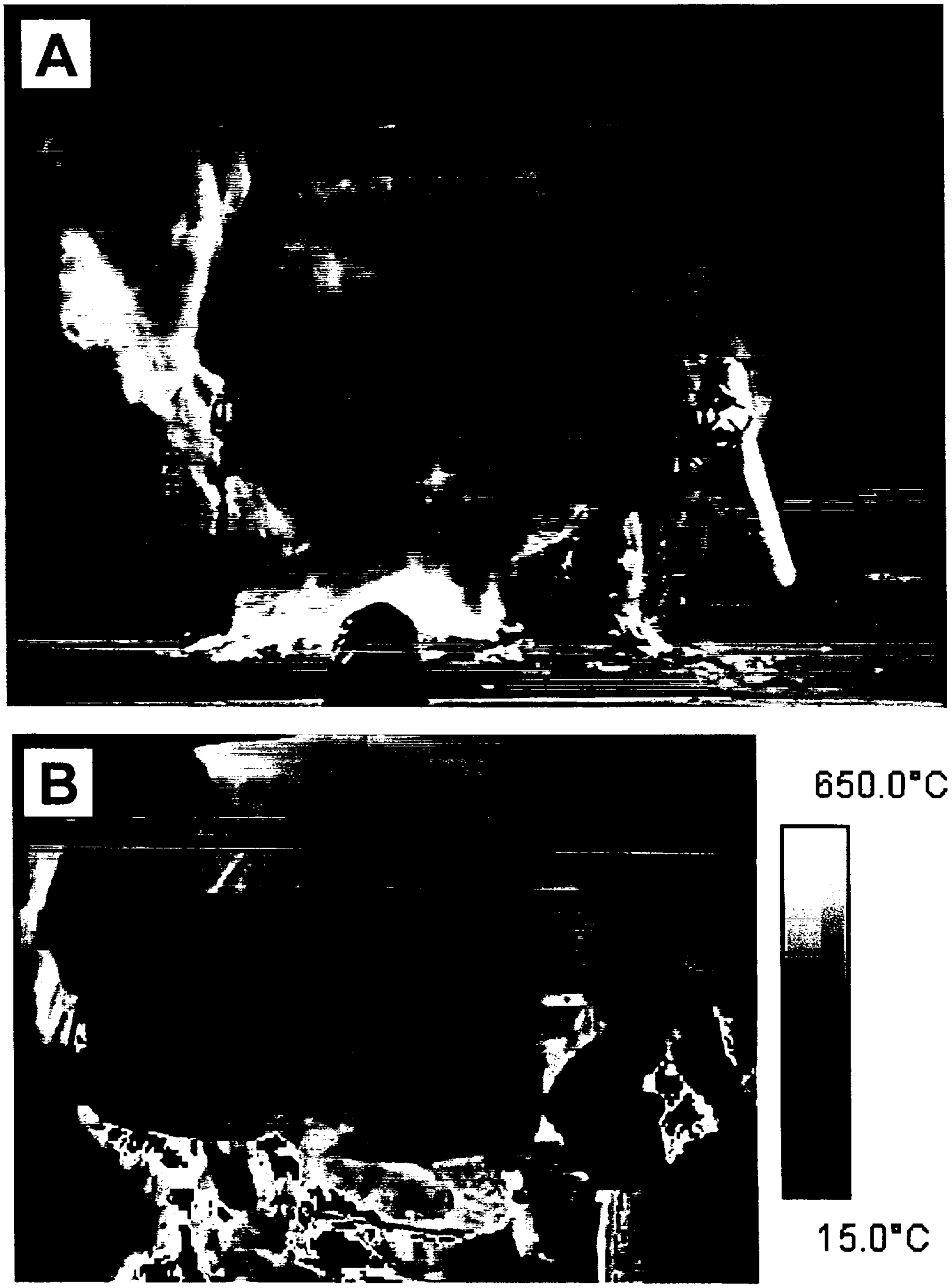

Figure 31. Fire Test F980609. Video still from Video Camera 1 (A), Infrared thermogram from IR3 (B), video still from Camera 4 (C), and Infrared thermogram from IR4 (D) at 157 seconds post-ignition.

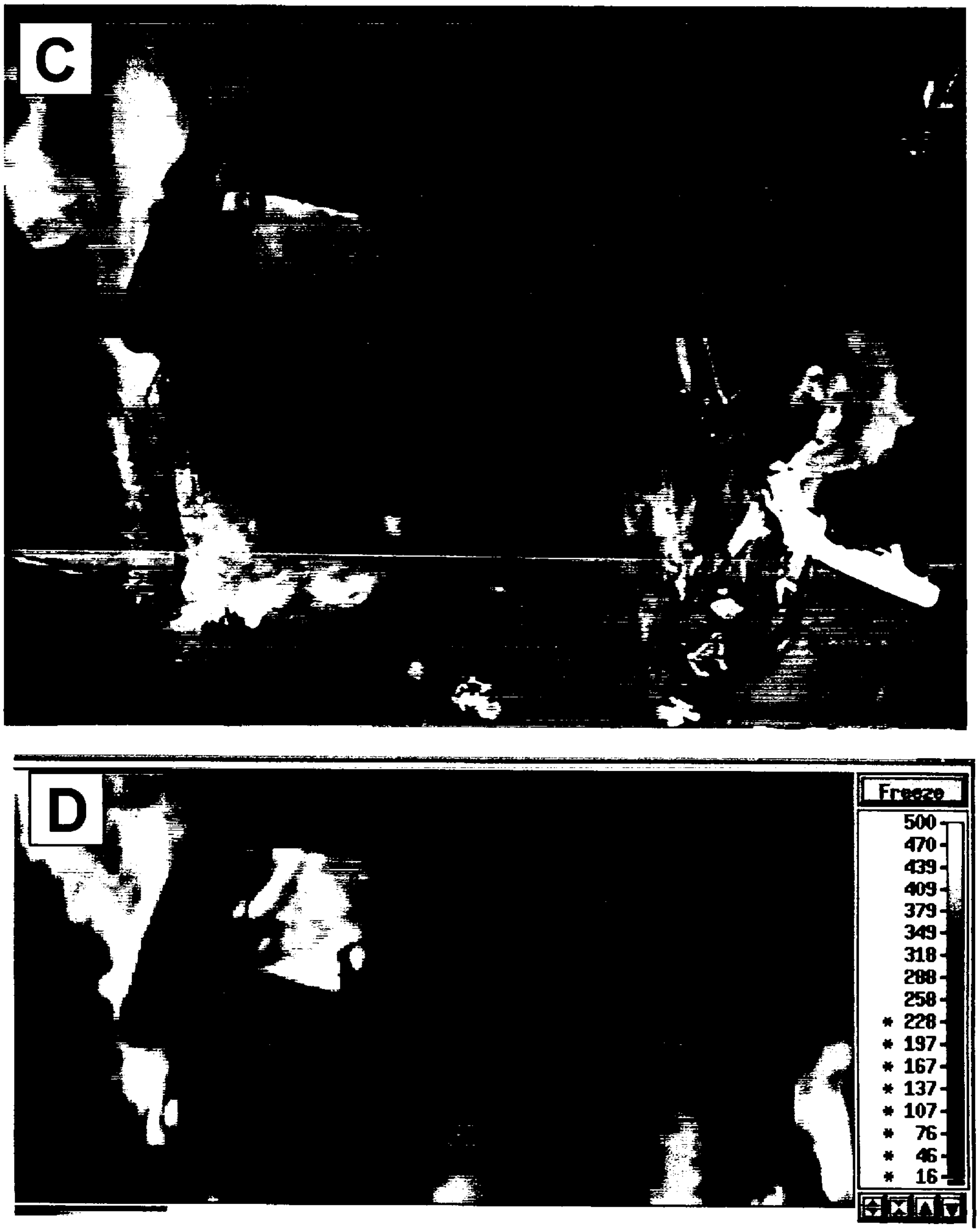

Figure 31, continued. Fire Test F980609 Video still from Video Camera 1 (A), Infrared thermogram from IR3 (B), video still from Camera 4 (C), and Infrared thermogram from IR4 (D) at 157 seconds post-ignition.

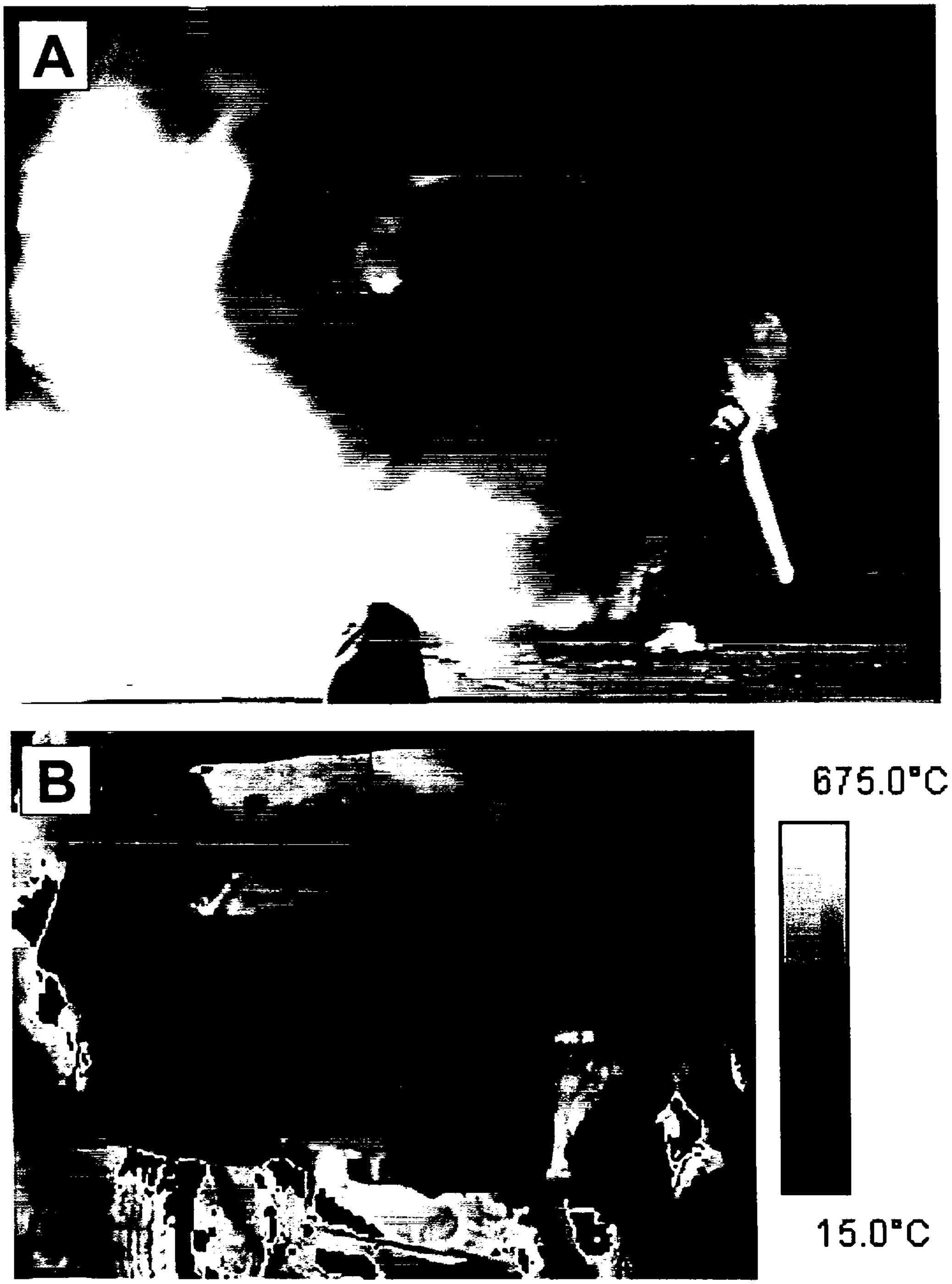

Figure 32. Fire Test F980609. Video still from Video Camera 1 (A), Infrared thermogram from IR3 (B), video still from Camera 4 (C), and Infrared thermogram from IR4 (D) at 158 seconds post-ignition.

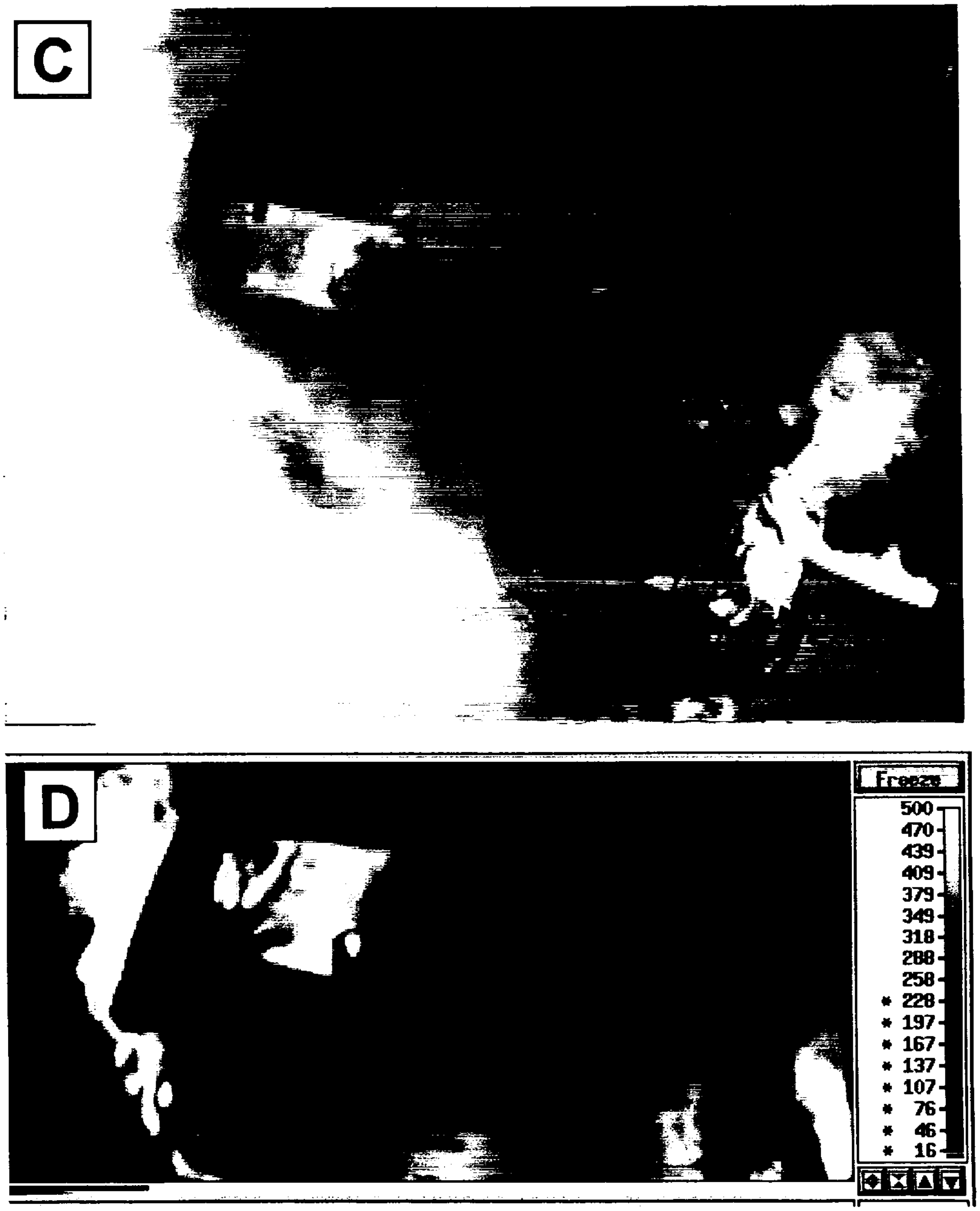

Figure 32, continued. Fire Test F980609. Video still from Video Camera 1 (A), Infrared thermogram from IR3 (B), video still from Camera 4 (C), and Infrared thermogram from IR4 (D) at 158 seconds post-ignition.

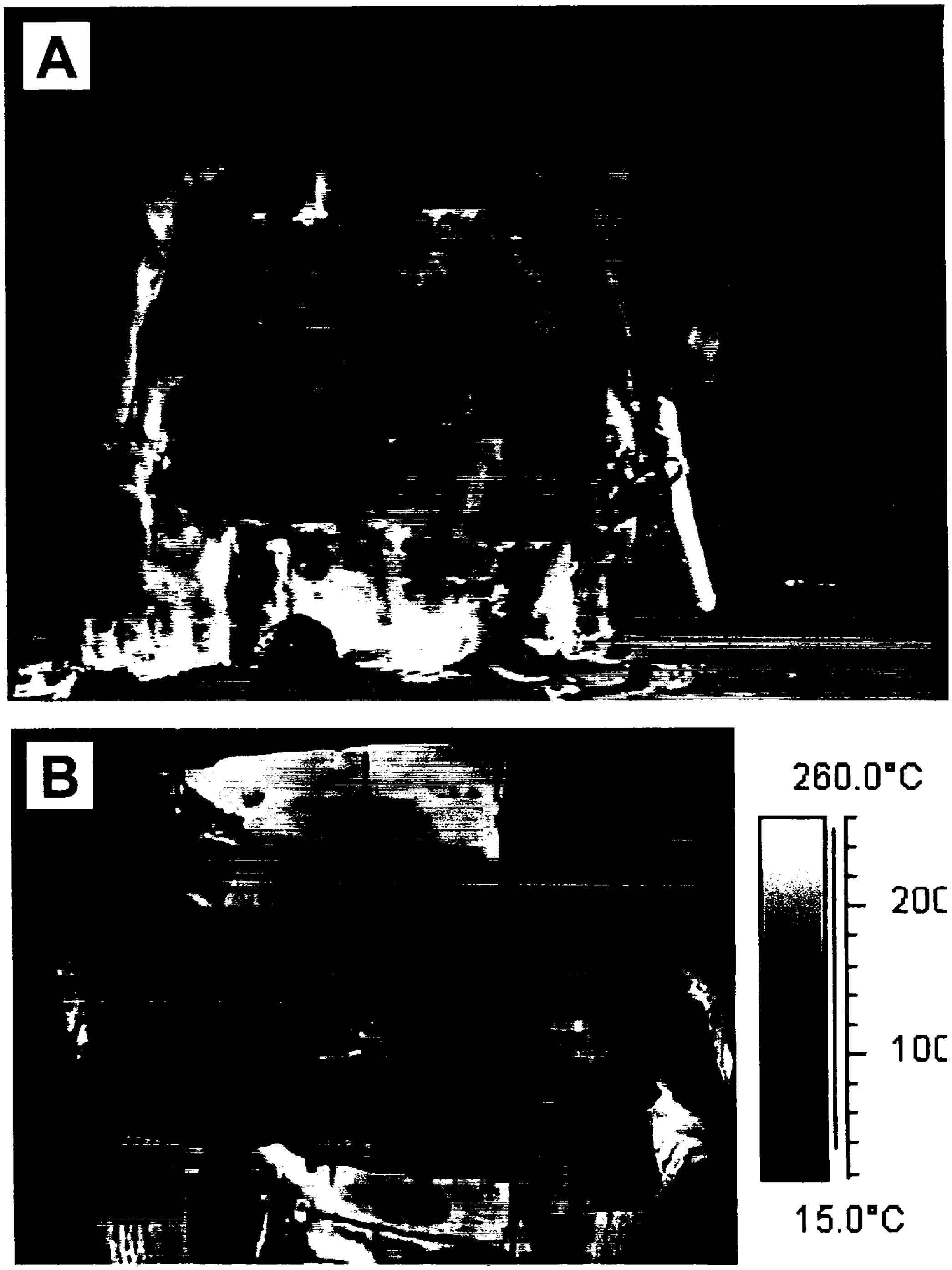

Figure 33. Fire Test F980609 Video still from Video Camera 1 (A), Infrared thermogram from IR3 (B), video still from Camera 4 (C), and Infrared thermogram from IR4 (D) at 158 seconds post-ignition at 170 seconds post-ignition.

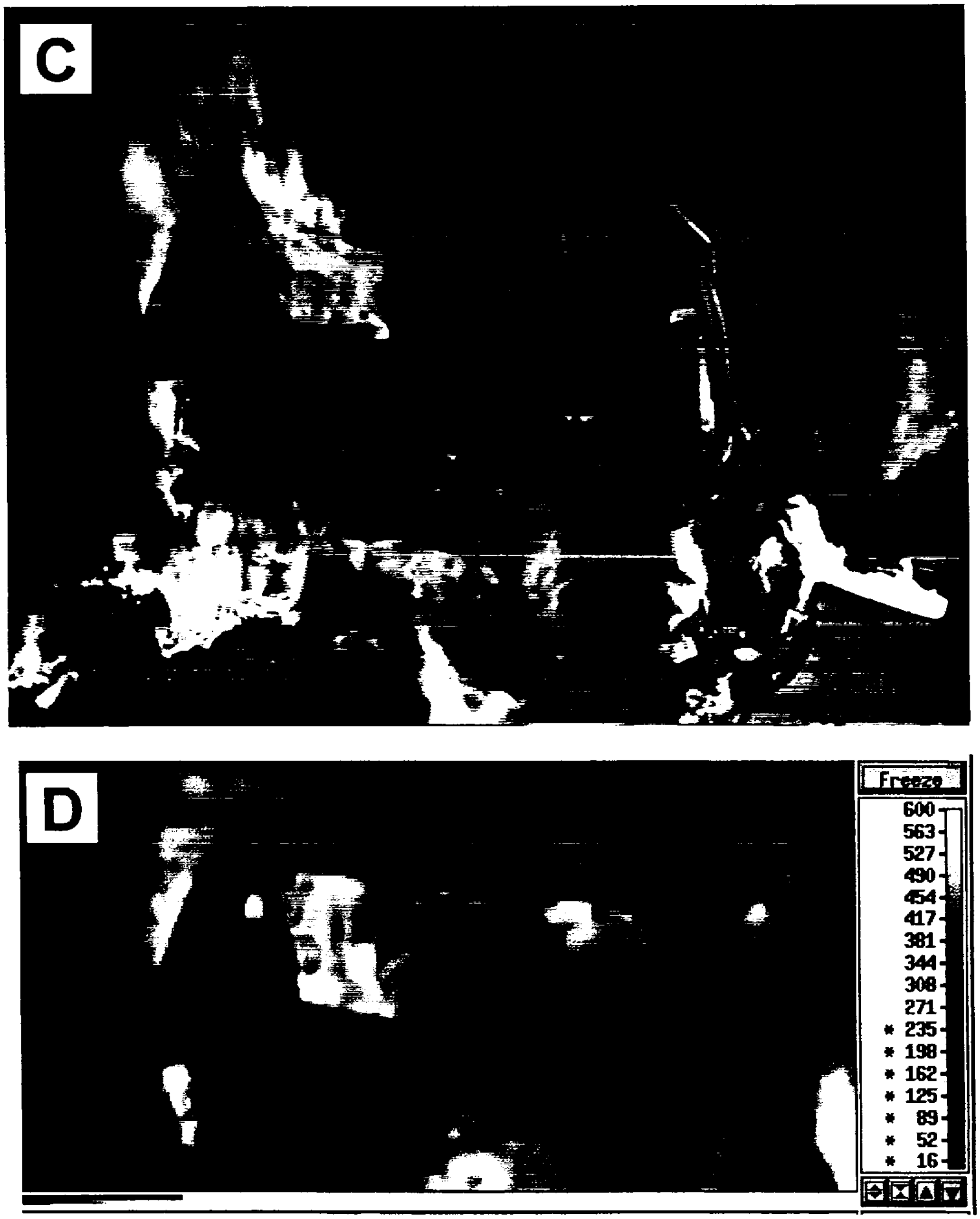

Figure 33, continued. Fire Test F980609 Video still from Video Camera 1 (A), Infrared thermogram from IR3 (B), video still from Camera 4 (C), and Infrared thermogram from IR4 (D) at 170 seconds post-ignition at 170 seconds post-ignition.

Figure 34. Fire Test F980609. Photograph of the left side of the rear compartment of the test vehicle after the crash test and before this fire test.

Thermocouples WW3, WW4, and WW5 were located in this seam opening. Heat Flux Transducer HFT02 was located in the roof of the test vehicle above this seam opening. Figure 35 shows plots of the temperature data recorded from Thermocouples WW3, WW4, and WW5, and T18, and heat flux data recorded from HFT02 from –50 to +300 seconds post-ignition.

Trends in the temperature data recorded from Thermocouples WW3, WW4, and WW5 indicate that heated gases started to enter the seam opening within a few seconds after ignition. For example, temperatures recorded from these thermocouples increased from the ambient temperature before ignition to approximately 600, 150, and 400°C, respectively, by 20 seconds post-ignition (Fig. 35). Temperatures recorded from WW3 were variable between 20 to 120 seconds post-ignition, decreasing to approximately 380°C at about 50 seconds post-ignition, then increasing to approximately 500°C between 60 and 80 seconds post-ignition, then decreasing to approximately 500°C between 95 and 115 seconds post-ignition (Fig. 35). Temperatures recorded from WW4 and WW5 were approximately constant at 150 and 400°C, respectively, between about 20 and 120 seconds post-ignition (Fig. 35).

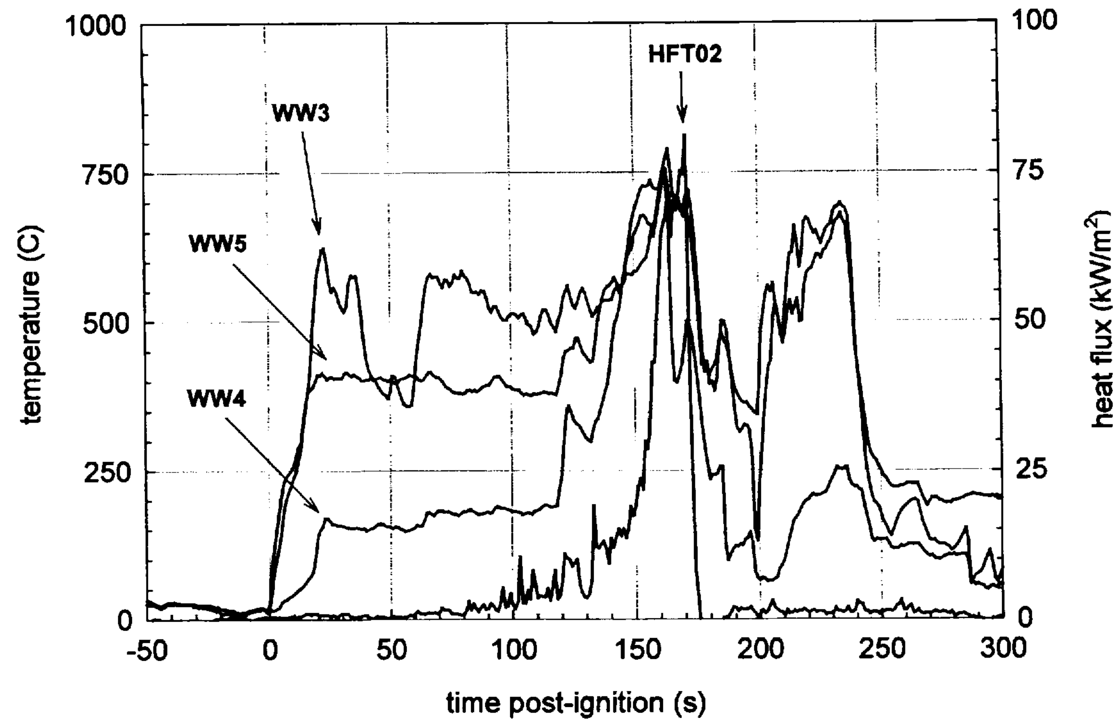

Figure 35. Fire Test F980609. Plots of data recorded from Thermocouples WW3, WW4, and WW5, and from Heat Flux Transducer HFT02.

Temperatures recorded from WW3, WW4, and WW5 started to increase between 120 and 125 seconds post-ignition, reaching maximum temperatures of approximately 790, 650, and 715°C, respectively, between 160 and 165 seconds post-ignition (Fig. 35). The timing of the start of these temperature increases observed in the recorded thermocouple data coincided with the timing of the first appearance of flames in the area above the left rear wheelhouse observed in the video stills from Cameras 1 and 4 (Fig.'s 27 through 33).

The heat flux to the lower surface of the roof trim panel above the left rear wheelhouse increased from < 20 kW/m^2 before 150 seconds post-ignition to approximately 70 kW/m^2 by 160 seconds post-ignition (Fig. 34). The timing of this increase in the heat flux to the area of the roof panel above the left rear wheelhouse coincided with the timing of the fire plume reaching the roof of the test vehicle observation in the video stills from Cameras 1 and 4 (Fig.'s 27 through 33).

Data recorded from thermocouples on the left quarter trim panel around the quarter glass opening indicated that sections of the trim panel had ignited before flames had entered the rear compartment through the seam opening in the left rear wheelhouse. The left quarter glass shattered during the crash test. The left quarter trim panel was broken, deformed, and dislodged during the crash test. Figure 36 shows the approximate locations of thermocouples on the left quarter trim panel around the quarter glass opening.

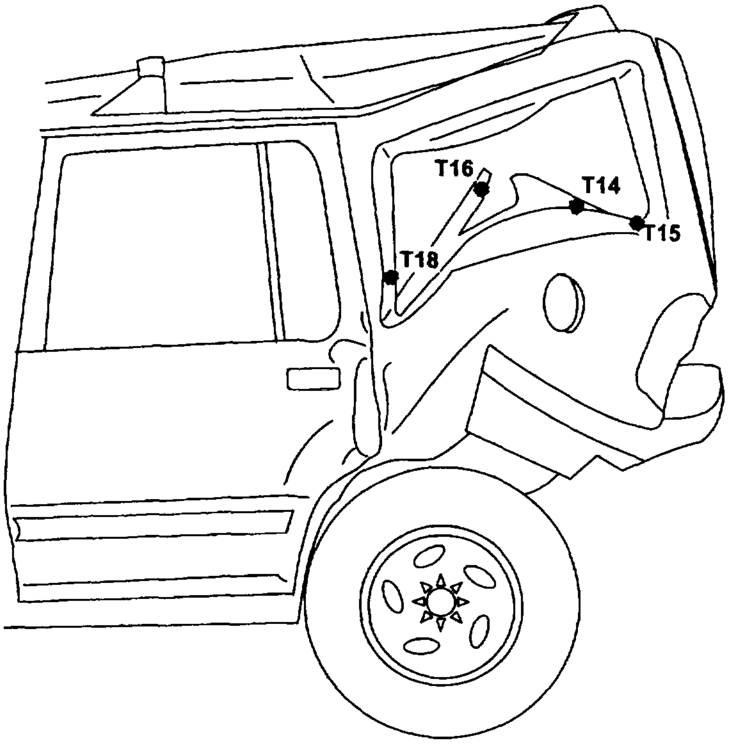

Figure 36. Fire Test F980609. Approximate locations of Thermocouples T14, T15, T16, and T18 on the left quarter trim panel.

Thermocouples T14 and T15 were located along the edge of the left quarter trim panel adjacent to the lower edge of the quarter glass opening (Fig. 36). Thermocouple T16 was located on a section of the quarter trim panel that broke during the crash test and extended outward into the quarter glass opening. Thermocouple T18 was located on a section of the quarter trim panel covering the C-pillar. Thermocouples T20, T21, and T22 were located on the section of the left quarter trim panel along the header to the left quarter glass opening (Fig. 36).

Plots of data recorded from thermocouples located on the left quarter trim panel around the quarter glass opening are shown in Figures 37 and 38. Temperatures recorded from Thermocouple T16 increased from < 200°C at 110 seconds post-ignition to > 650°C at 130 seconds post-ignition (Fig. 37).

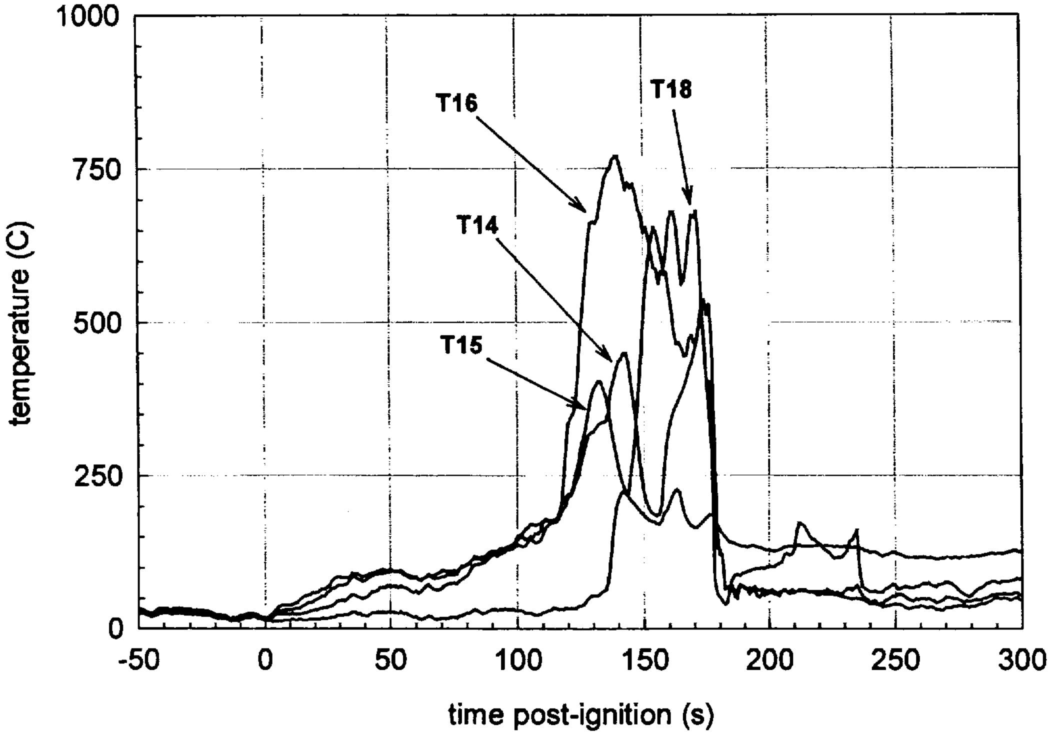

Figure 37. Fire Test F980609. Plots of data recorded from Thermocouples T14, T15, T16, and T18.

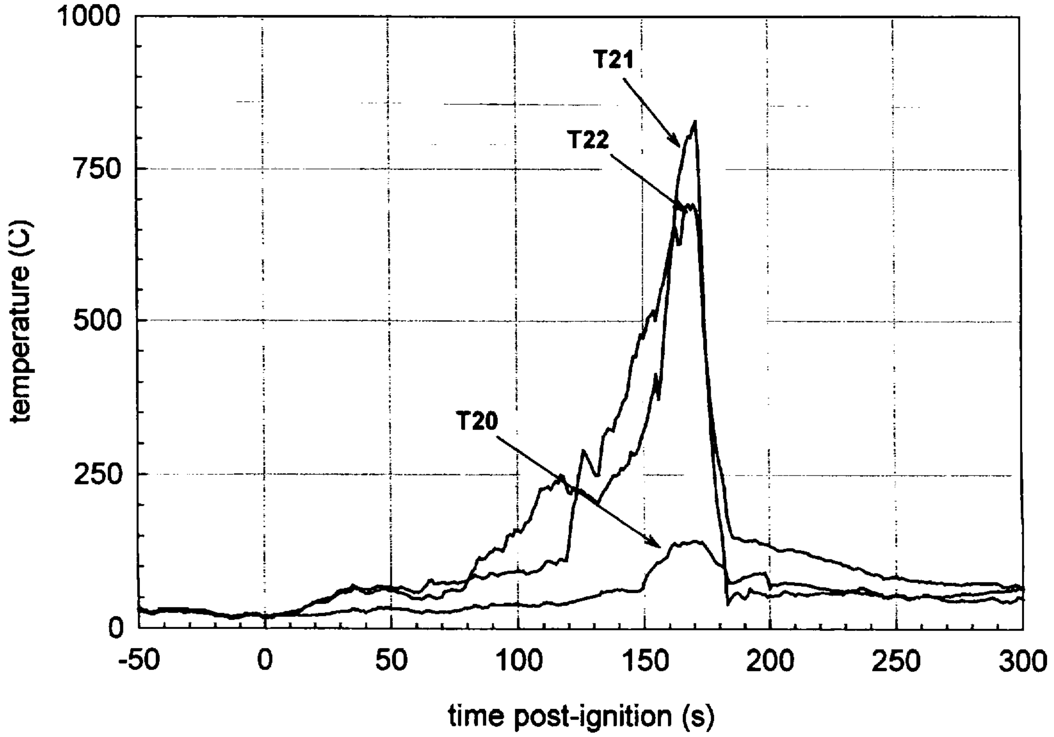

Figure 38. Fire Test F980609. Plots of data recorded from Thermocouples T20, T21, and T22.

Temperatures recorded from Thermocouple T18 increased from approximately 50°C at 130 seconds post-ignition to approximately 650°C at 155 seconds post-ignition (Fig. 37). Temperatures recorded from Thermocouples T14 and T15 were <450°C throughout this test (Fig. 37). Temperatures recorded from Thermocouples T21 and T22 increased monotonically from the time of ignition and exceeded 600°C between 160 and 170 seconds post-ignition (Fig. 38). Temperatures recorded from Thermocouple T20 were < 150°C throughout this test (Fig. 38).

These data indicate that the section of the broken left quarter trim panel that extended outward through the quarter glass opening ignited between 100 and 130 seconds post-ignition. A section of the left quarter trim panel along the C-pillar at the lower edge of the quarter glass opening ignited between 130 and 155 seconds post-ignition. The timing of ignition of the left quarter trim panel in these areas preceded the first evidence of flames entering the rear compartment through a seam opening in the wheelhouse (Fig. 35). These areas of the left quarter trim panel appeared to have been exposed through the left quarter glass opening to a fire plume emerging from the left rear wheelhouse starting at about 100 seconds post-ignition. Video Stills from Cameras 1 and 2 at 100 seconds post ignition show a fire plume emerging from the left rear wheelhouse and extending upward along the outer quarter panel and outboard of the left quarter glass opening (Fig 39). Review of these videos showed flames entering the left quarter glass opening and contacting left quarter trim panel. The thermocouple data indicates that a section of the left quarter trim panel along the header at the rear of the quarter glass opening ignited between 160 and 170 seconds post-ignition, which is coincident with the timing of flame-spread through the seam opening in the wheelhouse (Fig. 35). Sections of the left quarter trim panel along the rear portion of the lower edge of the quarter glass opening and the header at the front of the quarter glass opening did not ignite during this test.

This assessment of areas of the left quarter trim panel that ignited during this test is consistent with the pattern of heat and fire damage observed in the test vehicle after this test. Figure 40 is a photograph of the interior left corner of the test vehicle after this test. Sections of the quarter trim panel adjacent to the lower horizontal and front vertical edges of the quarter glass opening were consumed by fire. Thermocouple T16 is visible in the left quarter glass opening. A section of the quarter trim panel that covered the D-pillar was melted and charred, and had sagged downward. The section of the left quarter trim panel along the header of the quarter glass opening where Thermocouples T21 and T22 were located was consumed by fire. The section of the left quarter trim panel along the header of the quarter glass opening where Thermocouple T20 was located was not burned or charred. The plastic resin on the inner surface (back-side) of a larger section of the broken trim panel that was inboard of this seam opening had melted and started to drip. This section of the quarter trim panel did not appear to have ignited during this test.

Figure 39. Fire Test F980609. Video stills from Cameras 1 and 2 at 100 seconds post-ignition.

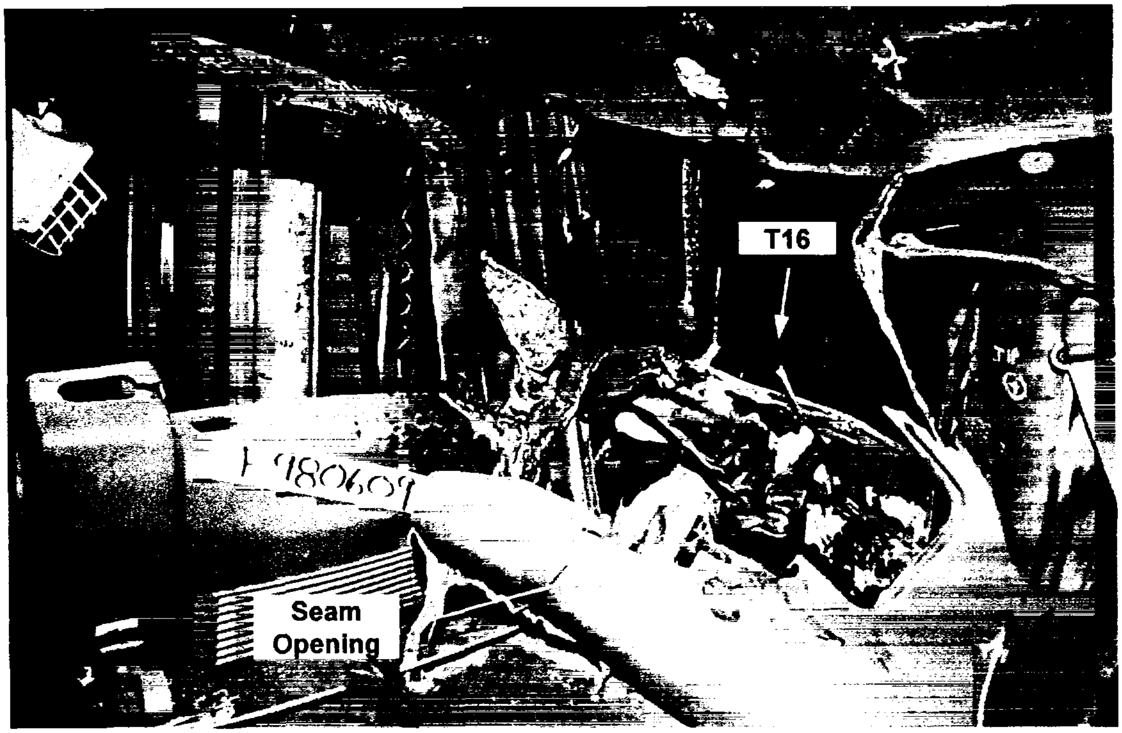

Figure 40. Fire Test F980609. Photograph of the interior left rear corner of the test vehicle after this test. Thermocouple T16 and a seam opening in the left rear wheelhouse are labeled.

5.2 Flame-Spread through a Seam Opening in the Right Rear Wheelhouse

Video stills from Cameras 1 and 4 show that a fire plume appeared in the lower right corner of the liftgate glass opening between 160 and 170 seconds post-ignition (Fig.'s 32 and 33). The presence of flames in this area of the test vehicle could not be attributed to flame-spread laterally across the rear compartment. The fire plume visible in the lower right corner of the liftgate glass opening appeared to emanate from the lower right rear corner of the rear compartment, the approximate area of a crash-induced seam opening between the rear compartment floor panel and the right inner quarter panel. Two thermocouples were located in this seam opening. Figure 41 shows a plot of temperature data recorded from Thermocouple WW9. No valid data was recorded from Thermocouple WW8[7], the other thermocouple located in this seam opening.

---

[7] Each thermocouple was checked after installation in the test vehicle to ensure that the thermocouple junction was not damaged or the thermocouple leads were not shorted to the grounded shield during the installation process. While preparing for this test, it was determined that the thermocouple junction of WW8 was open. This damage occurred either during shipment of the test vehicle to the test facility or while preparing the test vehicle for this test.

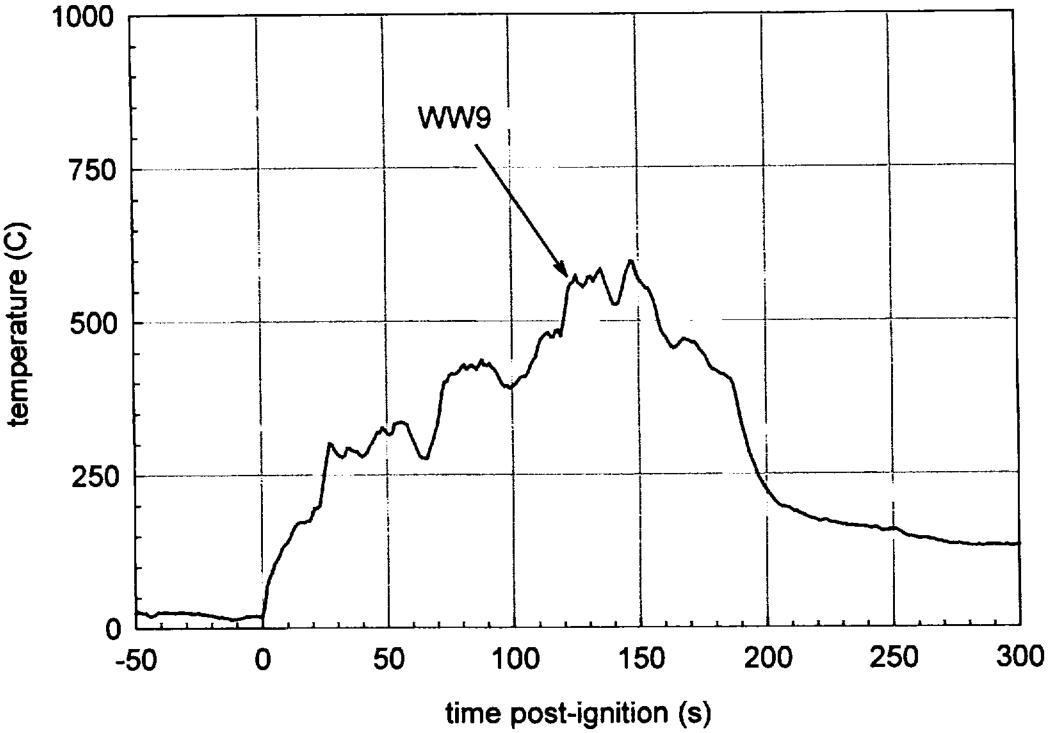

Figure 41. Fire Test F980609. Plot of data recorded from Thermocouple WW9.

Temperatures recorded from Thermocouple WW9 increased from an ambient temperature of approximately 20°C at the time of ignition to a maximum of 597°C at 147 seconds post-ignition, and decreased to 225°C at 200 seconds post-ignition (Fig. 38). This temperature data indicates that heated gases started to flow into this seam opening during the first few seconds after ignition, and continued to flow into this seam opening until this test was ended and the fire was extinguished.

Figure 42 shows a series of diagrams of the right inner quarter panel with estimated isothermal contour plots of temperature profiles on the inner surface of the right quarter trim panel. [8] Temperatures recorded from these thermocouples started to increase from an ambient temperature of approximately 20°C within 5 seconds post-ignition (see Plots C76 through C83 in **APPENDIX C**), indicating that heated gases from started to flow into the crash-induced seam

---

[8] Isothermal contours of the temperature at the inner surface of the right quarter panel were estimated from the temperature data recorded from Thermocouples T1 through T8 using a three-dimensional interpolation algorithm available in SigmaPlot for Windows Version 4.00 [6]. This algorithm uses an inverse distance method to generated temperature values for points on a uniformly spaced Cartesian grid from the [x,y,t] triple data from these thermocouples. Refer to **APPENDIX C** for the approximate locations of the F-thermocouples on the floor panel and the data recorded from the F-thermocouples.

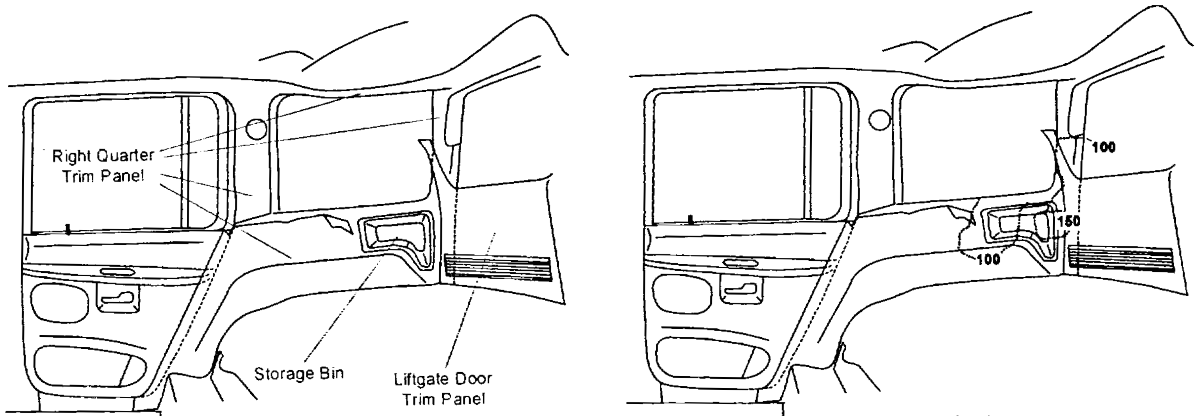

100 seconds post-ignition

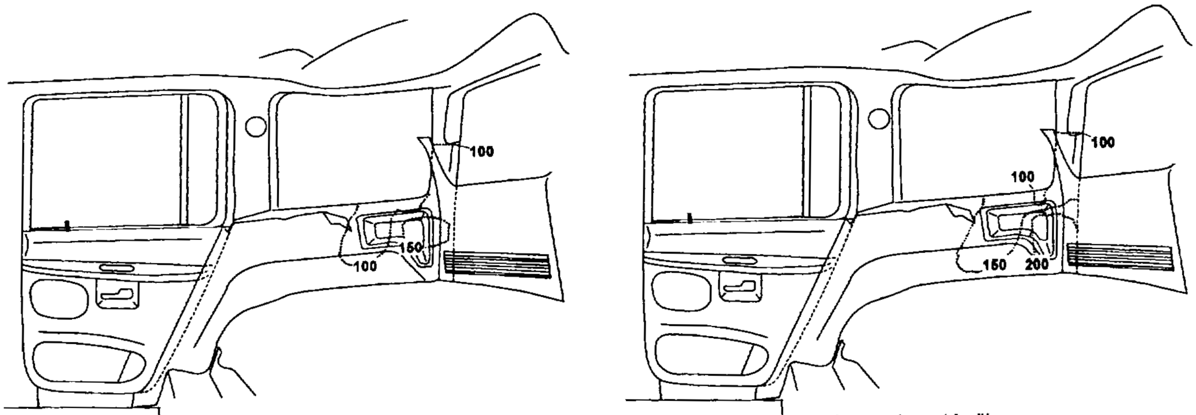

110 seconds post-ignition

120 seconds post-ignition

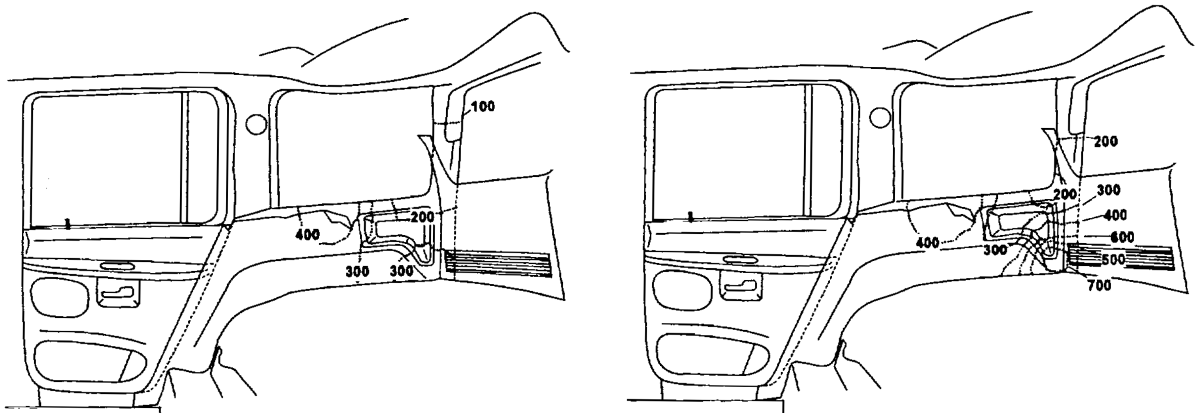

130 seconds post-ignition

140 seconds post-ignition

Figure 42. Fire Test F980609. Isothermal contour plots showing estimated temperatures on the inner surface of the right quarter trim panel 100, 110, 120, 130, 140, 150, 160, 170, and 180 seconds post-ignition.

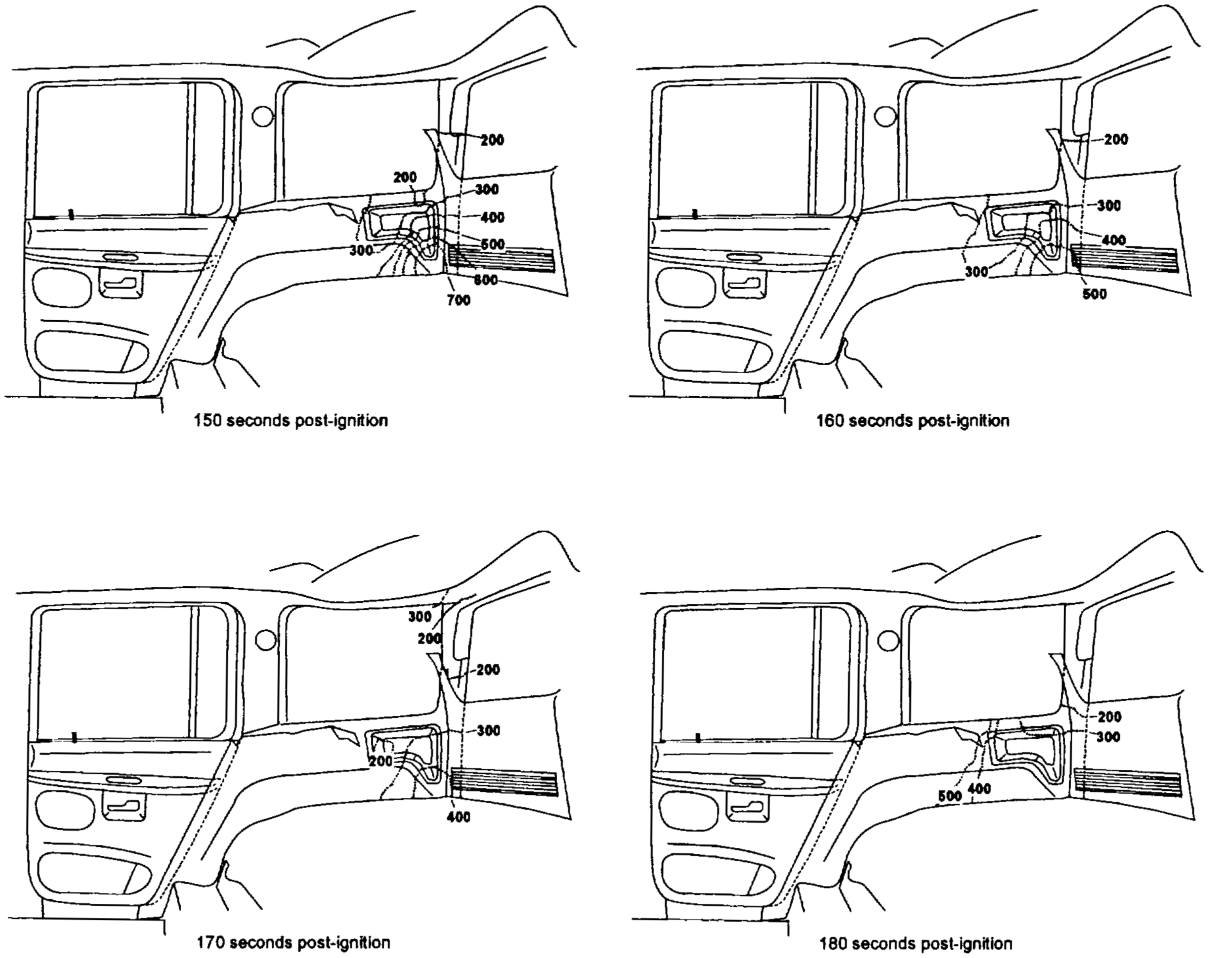

150 seconds post-ignition

160 seconds post-ignition

170 seconds post-ignition

180 seconds post-ignition

Figure 42, continued. Fire Test F980609. Isothermal contour plots showing estimated temperatures on the inner surface of the right quarter trim panel 100, 110, 120, 130, 140, 150, 160, 170, and 180 seconds post-ignition.

opening between the rear compartment floor panel and the right inner quarter panel a few seconds after ignition of the gasoline vapor under the rear compartment of the test vehicle. By 110 seconds post-ignition, estimated temperatures on the inner surface of the right quarter trim panel were < 200°C (Fig. 42). Estimated temperatures on the lower inner surface of the storage bin were between 100 and 150°C at 110 seconds post-ignition, increased to > 700°C by 140 seconds post-ignition, decreased to < 600°C by 160 seconds post-ignition, and decreased to < 400°C by 180 seconds post-ignition (Fig. 42). This trend in the estimated temperatures indicates that flames were present in the enclosed space between the trim panel and the right quarter panel for a 20 to 30 second period between 120 and 150 seconds post-ignition. Estimated temperatures behind the forward lower section of the trim panel increased from < 300°C at 170 seconds post-ignition to > 500°C at 180 seconds post-ignition. The cause of this increase in temperature was not determined, but may be related to the change in attitude of the test vehicle after the left rear tire blew-out at 158 seconds post-ignition and the apparent increase in the amount of flames in the right rear wheelhouse (see Fig.'s 29 through 32).

This assessment of flame-spread into the space between the right quarter trim panel and the right quarter panel is generally consistent with the pattern of heat and fire damage observed on the right quarter trim panel after this test. Figure 43 contains photographs of the right quarter trim panel and storage bin from the test vehicle after this test. A felt material was adhered to the inner surfaces of sections of the trim panel and storage bin (Fig. 43). Soot was deposited on the inner surfaces of the trim panel where it was against the C- and D-pillars (Fig. 43). The fiber mat was burned and charred where the estimated temperatures shown in Figure 41 were greater than approximately 400°C at some time during this test, and was not burned or charred where the estimated temperatures were < about 300°C (Fig. 43). The bottom edge of the trim panel that was in contact with the rear compartment floor panel was melted (Fig. 43). The outer surface of

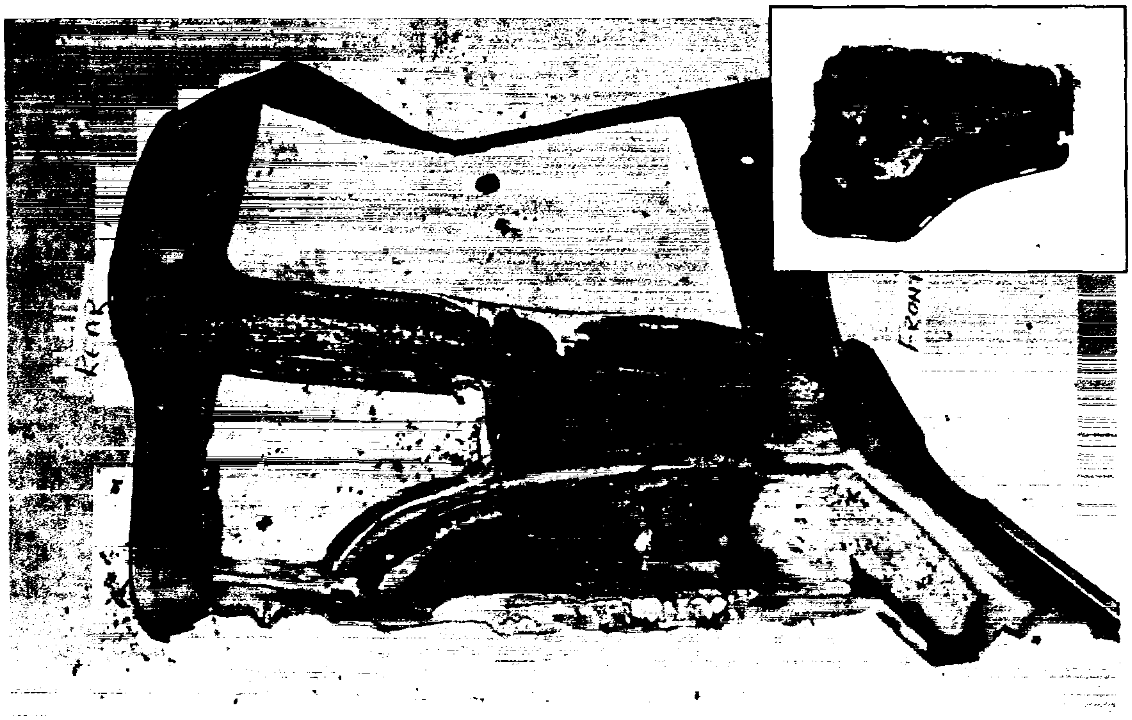

Figure 43. Fire Test F980609. Photograph of the back-side of the right quarter trim panel from the test vehicle after this test. The insert is a photograph of the storage bin in the right quarter trim panel.

the right quarter trim panel contained deposits of soot on the sections covering of the C- and D-pillars and the header and sill of the glass opening (Fig. 44). There was no evidence of burning or charring on the outer surfaces of the trim panel, indicating that flames did burn through the right quarter trim panel during this test. Although the video and thermocouple data acquired during this test indicate that flames spread into the space behind the right quarter trim panel through a seam opening between the rear compartment floor panel and right quarter panel, this does not appear to account for the fire plume visible in the lower right glass opening in the liftgate at the end of this test.

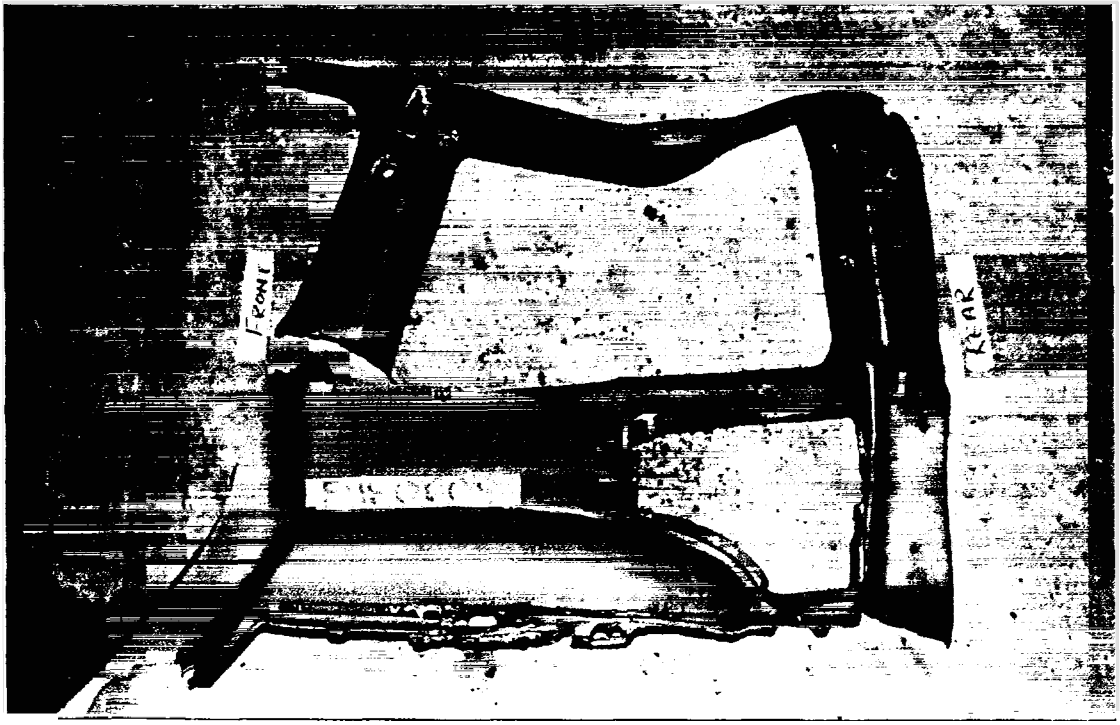

Figure 44. Fire Test F980609. Photograph of the front-side of the right quarter trim panel from the test vehicle after this test.

5.3 Flame-Spread Under the Liftgate

A fire path under the liftgate was discovered during inspection of the test vehicle after this test. Figure 45 is a photograph of the liftgate from the test vehicle after this test. Soot was observed on the lower interior surface of the liftgate trim panel, the lower surfaces of the inner and outer liftgate panels, and the seal along the bottom of the liftgate (Fig. 45). The liftgate trim panel was not burned or charred (Fig. 45).

Figure 45. Fire Test F980609. Photograph of the right-side of the liftgate trim panel from the test vehicle after this test.

Figure 46 contains photographs of the right side of the liftgate sill. The upper photograph in Figure 46 shows the right side of the liftgate sill, with the scuff plate in place as it was during this test. A section of the liftgate scuff plate had softened and deformed (Arrow). The forward edge of this section of the scuff plate was melted and appeared to have ignited. A section of the floor carpet in the rear compartment forward of this area of the sill scuff and below the area of the liftgate trim panel that contained soot deposits was consumed by fire. The edge of the carpet was charred. The lower photograph in Figure 46 shows the right side of the liftgate sill with the scuff plate removed and rotated to show it s lower surface. Soot was observed on the lower surface of the section of the scuff plate that had softened and deformed (Arrow). The rear compartment floor carpet under the right side of the scuff plate was consumed by fire. Soot was observed on the exposed liftgate sill.

The video stills from Cameras 1 and 4 at 170 seconds post-ignition show a fire plume on the exterior surface of the right side of the liftgate in the area where the scuff plate and rear compartment floor carpet were burned (Fig. 33). Video stills from Cameras 1 and 4 prior to this time show flames sporadically along the lower right edge of the liftgate sporadically throughout this test (Fig.'s 27 through 32). The timing of flame-spread under the liftgate could not be determined precisely because no thermocouples were located in this area.

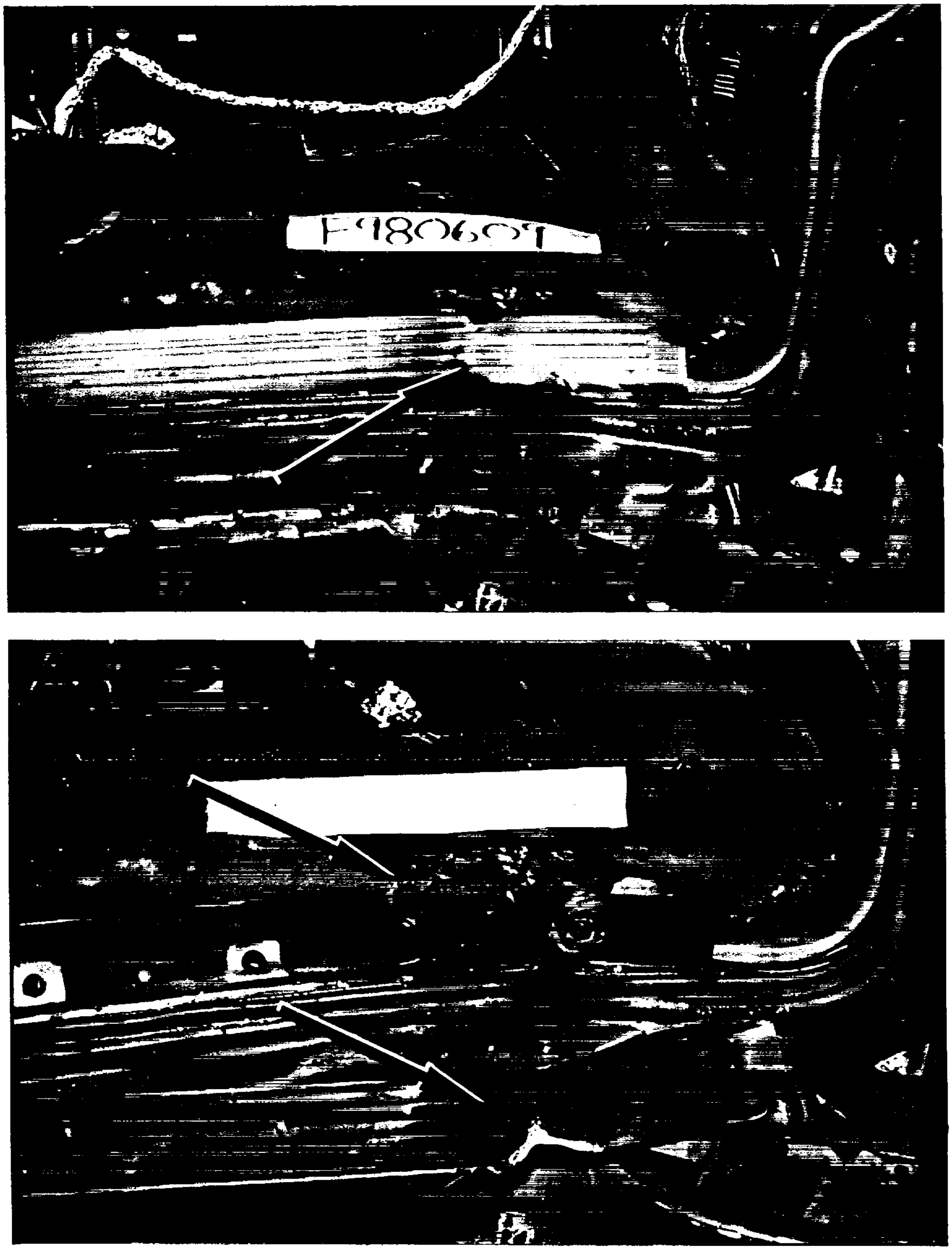

Figure 46. Fire Test F980609. Photographs of the right side of the rear liftgate sill in the test vehicle after this test. The upper photograph shows the scuff plate in-place. The lower photograph shows the scuff plate has been detached and rotated to its lower surface. The arrows indicate sections of the scuff plate and rear compartment floor carpet where heat and fire damage was observed.

5.4 Conduction through the Rear Compartment Floor Panel and Flame-Spread through the Rear Compartment Floor Panel Drain Hole Plugs

The floor panel in the rear compartment of the test vehicle contained two drain holes located along the longitudinal center-line of the test vehicle (see Fig. 27), and a clearance hole drilled in floor panel for a heat flux transducer.[9] Rubber plugs[10] were in place in both drain holes at the start of this test. Sections of the floor carpet and pad under the floor carpet in the rear compartment were burned and charred. The recorder test data and physical evidence from inspection of the test vehicle after this test indicated that the maximum temperature of the floor panel in the rear compartment during this test was > 500°C and that flames burned-through both of these drain hole plugs in the rear compartment floor panel. It was not possible to determine unambiguously to what extent thermal damage to the carpet pad was caused by flame-spread through these openings.

Figure 47 shows a series of diagrams of the test vehicle with the isothermal contours of the estimated floor panel temperature at 0, 5, 25, 50, 75, 100, 120, 125, 150, 170, and 175 seconds post-ignition.[11] This analysis indicated that the temperature of the floor panel started to increase by 5 seconds post-ignition (Fig. 47). The temperature of the rear compartment floor panel was not uniform either before ignition or during this test. Estimated temperatures were highest in an area extending from the "kick-up" at the front of the rear compartment to a line intersecting the center of the spare tire toward the rear of the rear compartment, and from the rear left wheelhouse to a line parallel to and right of the longitudinal center-line of the test vehicle (Fig. 46). This area corresponded approximately to the area where estimated temperatures were greatest below the rear compartment floor panel (Fig.25). The maximum estimated floor panel temperature was >500 °C at 175 seconds post-ignition (Fig. 47).

Physical inspection of the test vehicle after this test indicated that the pattern of thermal damage to the floor carpet and pad under the floor carpet in the rear compartment was consistent with the temperature estimates shown in Figure 47. The floor carpet was removed from the rear compartment, exposing the underlying carpet pad which was discolored and charred (Fig. 48).

---

[9] A 1 in. diameter hole was drilled in the floor panel for Heat Flux Transducer 01 (**APPENDIX E**). Flame-resistant caulking was applied to the floor panel around the base of the heat flux transducer. This caulk acted as a fire resistant barrier to flame-spread through the gap around the body of the heat flux transducer body.

[10] The drain hole plugs in the test vehicle were made of ethylene/propylene/butadiene copolymer.

[11] Isothermal contours of temperatures on the upper surface of the floor panel in the rear compartment floor panel were estimated from temperature data recorded from Thermocouples F6, F8, F10, F13, F15, F17, F19, F21, F23, F25, WW2, and WW7 using a three-dimensional interpolation algorithm available in SigmaPlot for Windows Version 4.00 [6]. This algorithm used an inverse distance method to interpolate temperature values for points on a uniformly spaced Cartesian grid from the [x,y,t] triple data from these thermocouples. Refer to **APPENDIX C** for the approximate locations of these thermocouples.

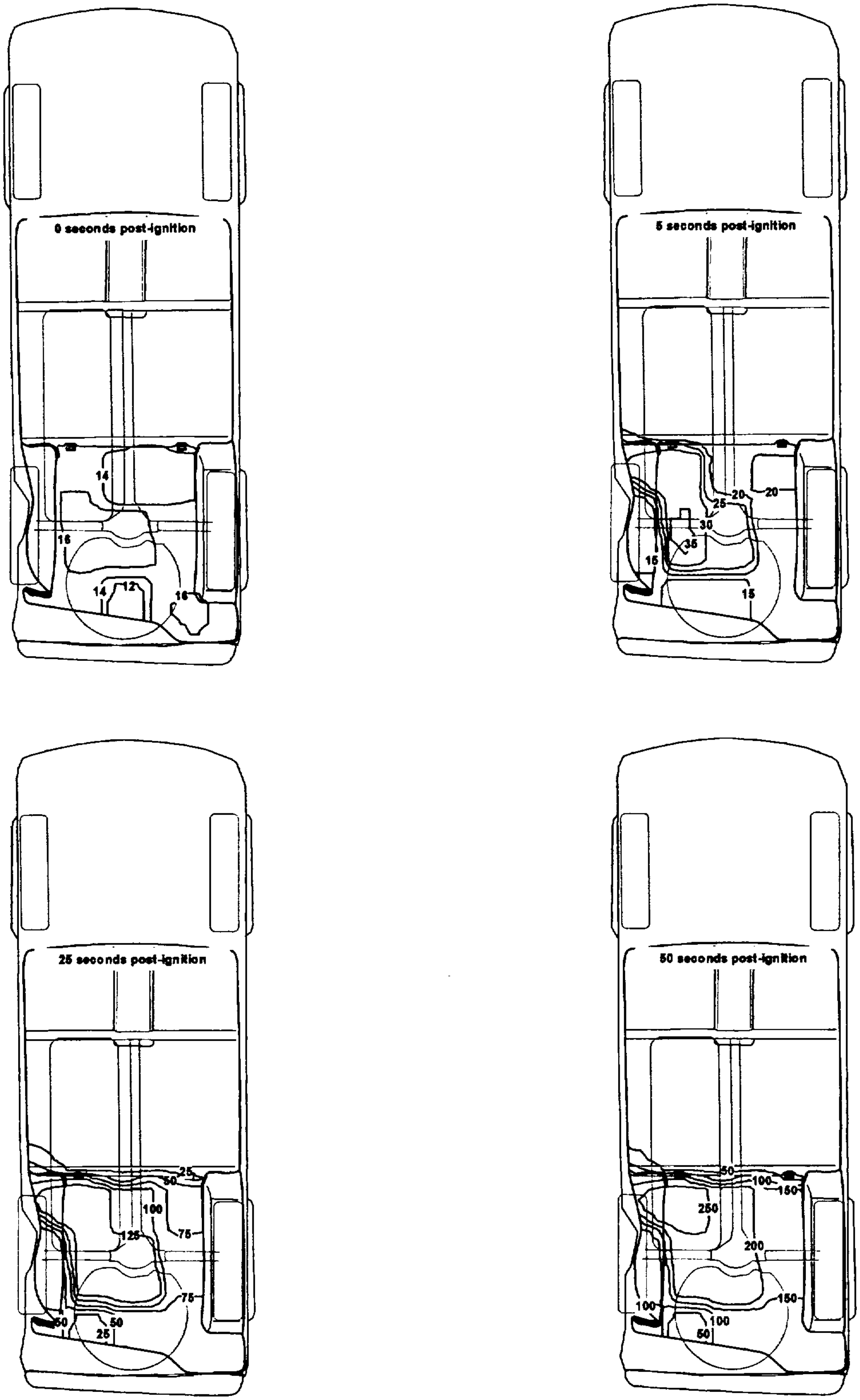

Figure 47. Fire Test F980609. Diagrams showing isothermal contour plots of estimated temperature of the rear compartment floor panel at 0, 5, 25, 50, 75, 100, 125, 150, 170 and 175 seconds post-ignition.

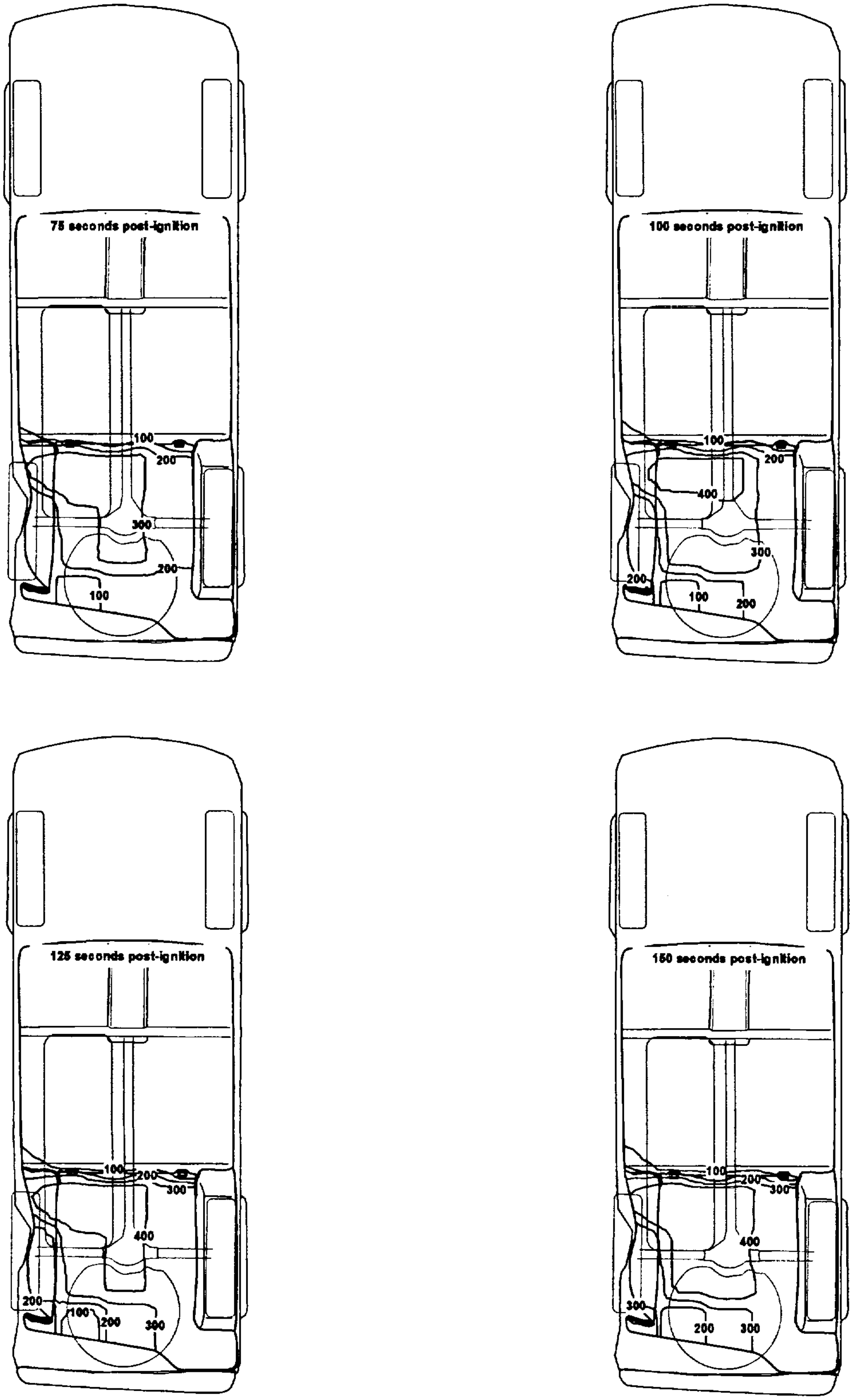

Figure 47, continued. Fire Test F980609. Diagrams showing isothermal contour plots of estimated temperature of the rear compartment floor panel at 0, 5, 25, 50, 75, 100, 125, 150, 170 and 175 seconds post-ignition.

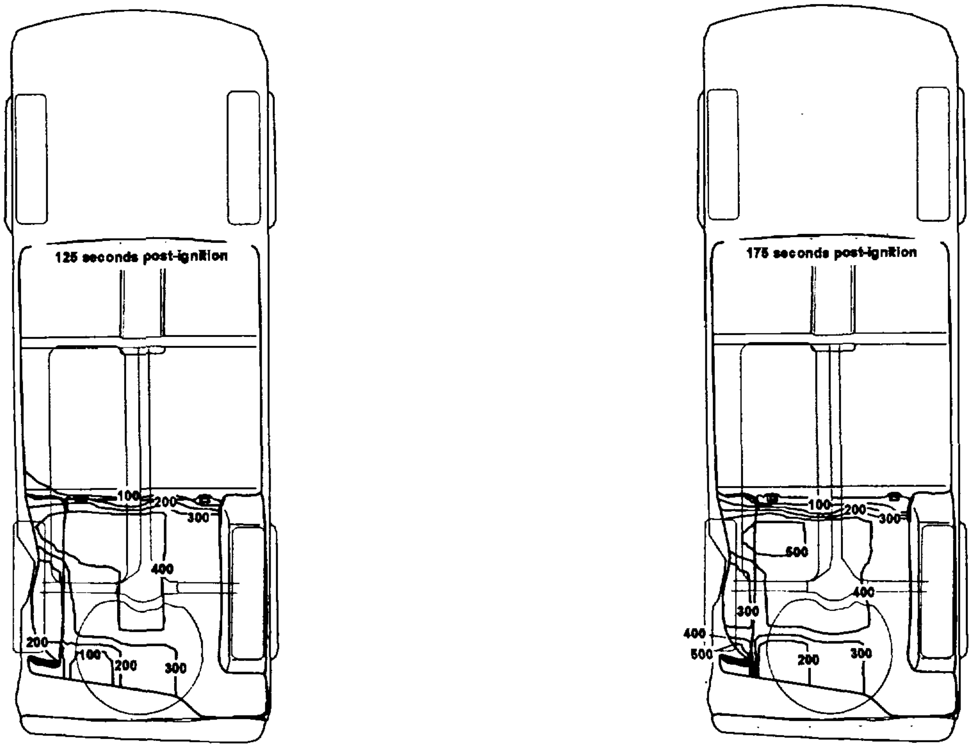

Figure 47, continued. Fire Test F980609. Diagrams showing isothermal contour plots of estimated temperature of the rear compartment floor panel at 0, 5, 25, 50, 75, 100, 125, 150, 170, and 175 seconds post-ignition.

The charred area of the carpet pad was over the section of the floor panel with estimated temperatures >400°C (Fig. 47).

The recorder test data and physical evidence from inspection of the test vehicle after this test indicated that flames burned through both of these drain hole plugs closing the two drain holes located along the longitudinal center-line in the rear compartment floor panel of the test vehicle (see Fig. 27). It was not possible to determine unambiguously to what extent thermal damage to the carpet pad was caused by flame-spread through these openings. For example, Figure 49 is a plot of data recorded from a thermocouple in the center of the upper surface of the rear plug (Arrow A, Fig. 48). The maximum temperature recorded from this thermocouple during this test was <325°C (Fig. 49), which was less than the 600°C threshold used in this report to indicate flames. A section was missing from one end of this plug, and the edges around the missing sections were charred and brittle (insert, Fig. 49). The upper surface of the carpet pad over this drain hole was discolored, but not burned or charred (Arrow A, Fig. 48).

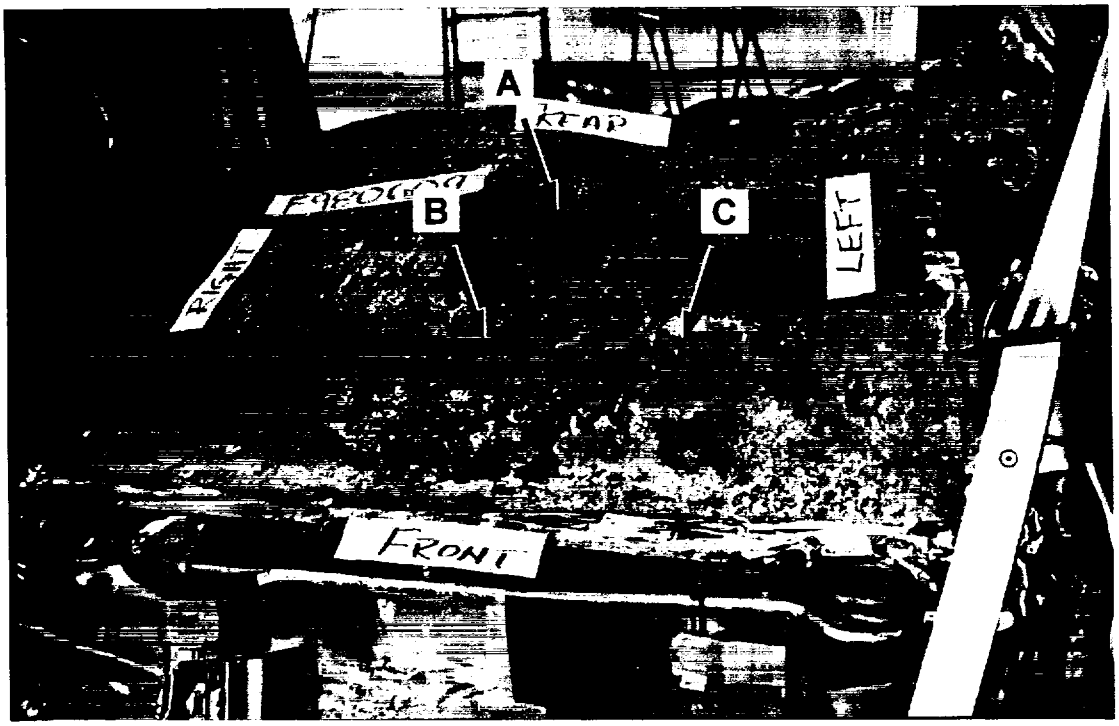

Figure 48. Fire Test F980609. Photograph of the rear compartment floor panel with the carpet removed from the test vehicle after this test. The rear compartment floor panel contained two drain holes (Arrows A and B) and a clearance hole drilled in the rear compartment floor panel for HFT01 (Arrow C).

The carpet pad around the drain hole in the forward section of the rear compartment was charred and burned (Arrow A, Fig. 48). The plug in this drain hole was consumed by fire during this test. No thermocouples were installed on this plug for this test, so it was not possible to determine if flames entered this drain hole during this test.

Figure 50 is a photograph of the under side of the carpet from the rear compartment of the test vehicle after this test. The edge of the floor carpet on the left side of the rear compartment was burned and melted where it was adjacent to the left rear wheelhouse (Fig. 48). Pieces of the carpet pad were stuck to the under side of the floor carpet where the backing had melted and re-solidified after the test (Fig. 50). A section of the carpet that was under the right side of the scuff plate, where flames spread under the liftgate, was burned and melted (Fig. 50). The backing of the floor carpet overlaying the forward section of the rear compartment was discolored and contained soot deposits (Fig. 50).

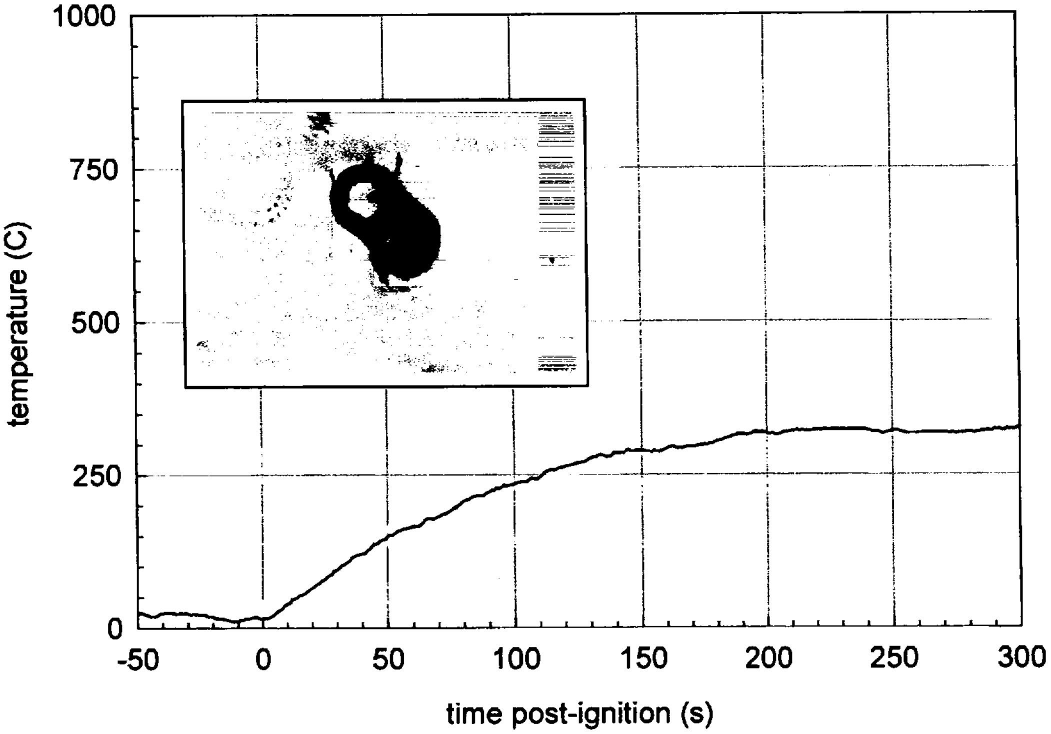

Figure 49. Fire Test F989698. Plot of data recorded from Thermocouple FP1. The insert is a photograph of the drain hole plug from the rear section of the rear compartment floor panel. Thermocouple FP1 was located on a section of the drain hole plug that did not burn through during this test.

It was not possible to determine if the two holes in this area and soot deposits on the carpet backing along the front of the rear compartment were caused by heated gases and flames flowing through the drain hole in the front section of the rear compartment floor panel and the clearance hole drilled in the floor panel for the heat flux transducer or by contact with the heated floor panel. The thermocouple on the drain plug in the rear section of the rear compartment floor panel was on a section of the plug that did not burn through during this test. Thus, the temperature data plotted in Figure 49 are a measure of the temperature of the upper surface of this plug, and cannot be used to determine if heated gases and flames flowed through the drain hole in the rear section of the floor panel during this test. The areas where the carpet pad (Fig. 48) in the rear compartment were burned and charred, and where the floor carpet was burned and contained deposits of soot (Fig. 50) coincided with the area where the estimated temperature of the floor panel was greater that 400°C (Fig. 47). The plug in the drain hole in the front section of the floor panel had burned through during this test. Without thermocouple data, it was not possible to determine if heated gases or flames flowed through this drain hole during test.

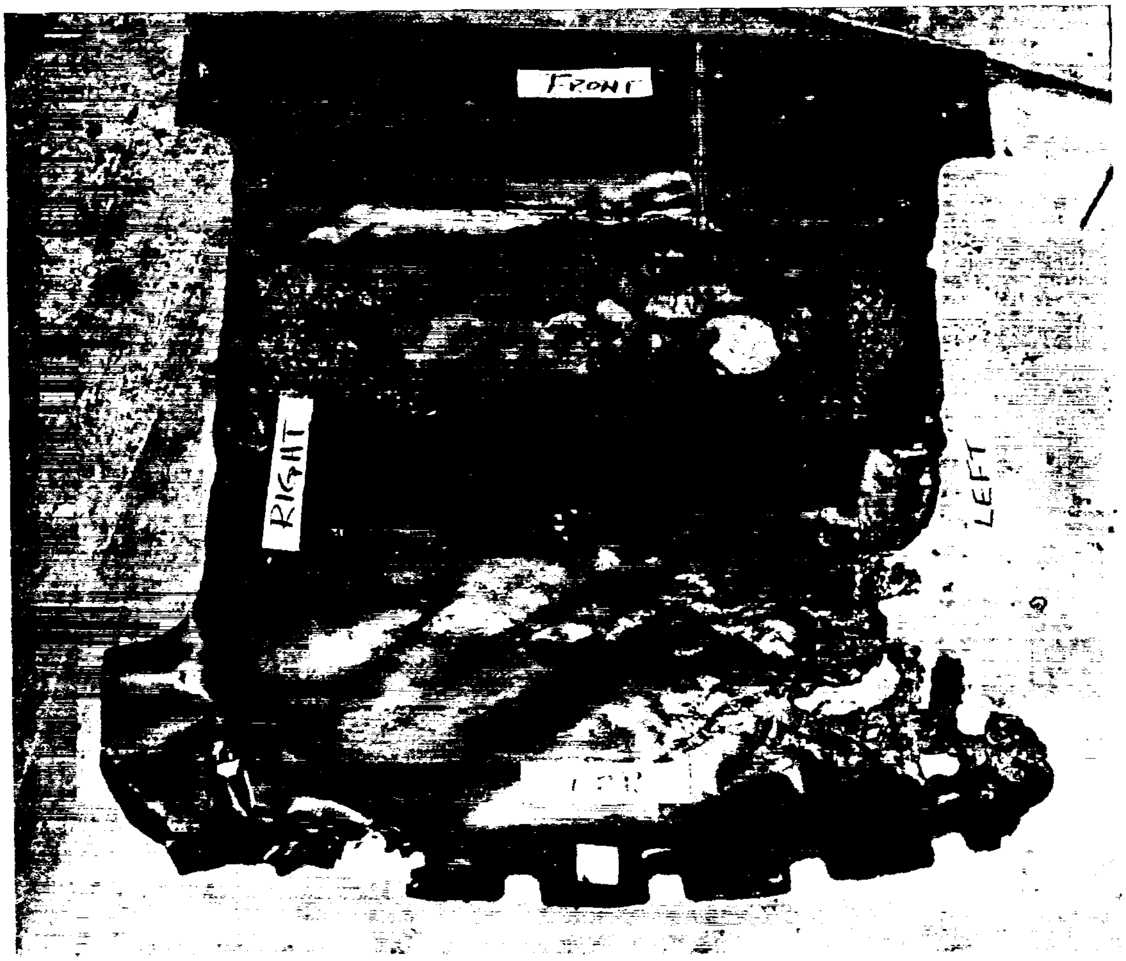

Figure 50. Fire Test F980609. Photograph of the lower surface of the rear compartment floor carpet from the test vehicle after this test.

5.5 Flame-Spread on the Roof Trim Panel

The recorded thermocouple data indicated that temperatures along the lower surface of the roof trim panel in the test vehicle temperatures started to increase within 5 seconds post-ignition ignition (APPENDIX C). Figure 51 shows a series of diagrams of the test vehicle with the isothermal contours of the estimated temperatures below the roof trim panel at 0, 5, 25, 50, 75, 100, 120, 125, 150, 170, and 175 seconds post-ignition.[12]

---

[12] Isothermal contours of temperatures along the lower surface of the roof trim panel were estimated from temperature data recorded from Thermocouples R1, R2, R3, R4, R5, R6, R7, R8, R9, R10, R11, R12, R13, and T22 using a three-dimensional interpolation algorithm available in SigmaPlot for Windows Version 4.00

The timing of flame-spread along the lower surface of the roof trim panel inferred from the estimated isothermal contours in Figure 51 is consistent with the observation of flames in the rear compartment in Figures 27 through 33. The estimated isothermal contour plots indicate that heated gases started to accumulate along the roof trim panel in the rear compartment by 25 seconds post-ignition (Fig. 51). Except for a small area along the left side of the rear compartment, estimated temperatures along the lower surface of the roof trim panel were <150°C until about 125 seconds post-ignition (Fig. 51). Estimated temperatures along a section of the roof trim panel above the broken left quarter trim panel were >150°C by 100 seconds post-ignition and > 200°C by 120 seconds post-ignition (Fig. 51). This is consistent with heated gases and flames entering the rear compartment through the left quarter glass opening and igniting sections of the broken left quarter trim panel at about this time (see **SECTION 5.1**).

Flames were first observed in the space above the left rear wheel house starting at about 125 seconds post-ignition (Fig. 29) – about the time the spare time blew out. Estimated temperatures along the roof trim panel above this area were >250°C by 125 seconds post-ignition (Fig. 51). The estimated isothermal contour plots indicate that flames first contacted the roof trim panel in the rear left corner of the rear compartment between 150 and 157 seconds post-ignition (Fig. 51). This is consistent with the apparent height of the fire plume visible in the video stills and the apparent temperatures in the infrared thermograms in Figures 30 and 31. The estimated isothermal contour plots indicate that flames spread along the roof trim panel to the right side of the rear compartment and forward to above the rear seats between 157 and 170 seconds post-ignition (Fig. 51).

The pattern of thermal damage observed on the roof trim panel after this test was consistent with extent of flame-spread inferred from the estimated isothermal contour plots. The fabric covering on the lower surface of the roof trim panel was burned and charred (Fig. 52) in areas where the maximum estimated temperature was greater than about 500°C (Fig. 51). The extent of charring appeared to correlate with the estimated temperature. For example, areas where the $t_{estimated} >$ 700°C were more extensively charred than areas where 500°C $< t_{estimated} <$ 600°C.

---

[6]. This algorithm used an inverse distance method to interpolate temperature values for points on a uniformly spaced Cartesian grid from the [x,y,t] triple data from these thermocouples. Refer to **APPENDIX C** for the approximate locations of these thermocouples.

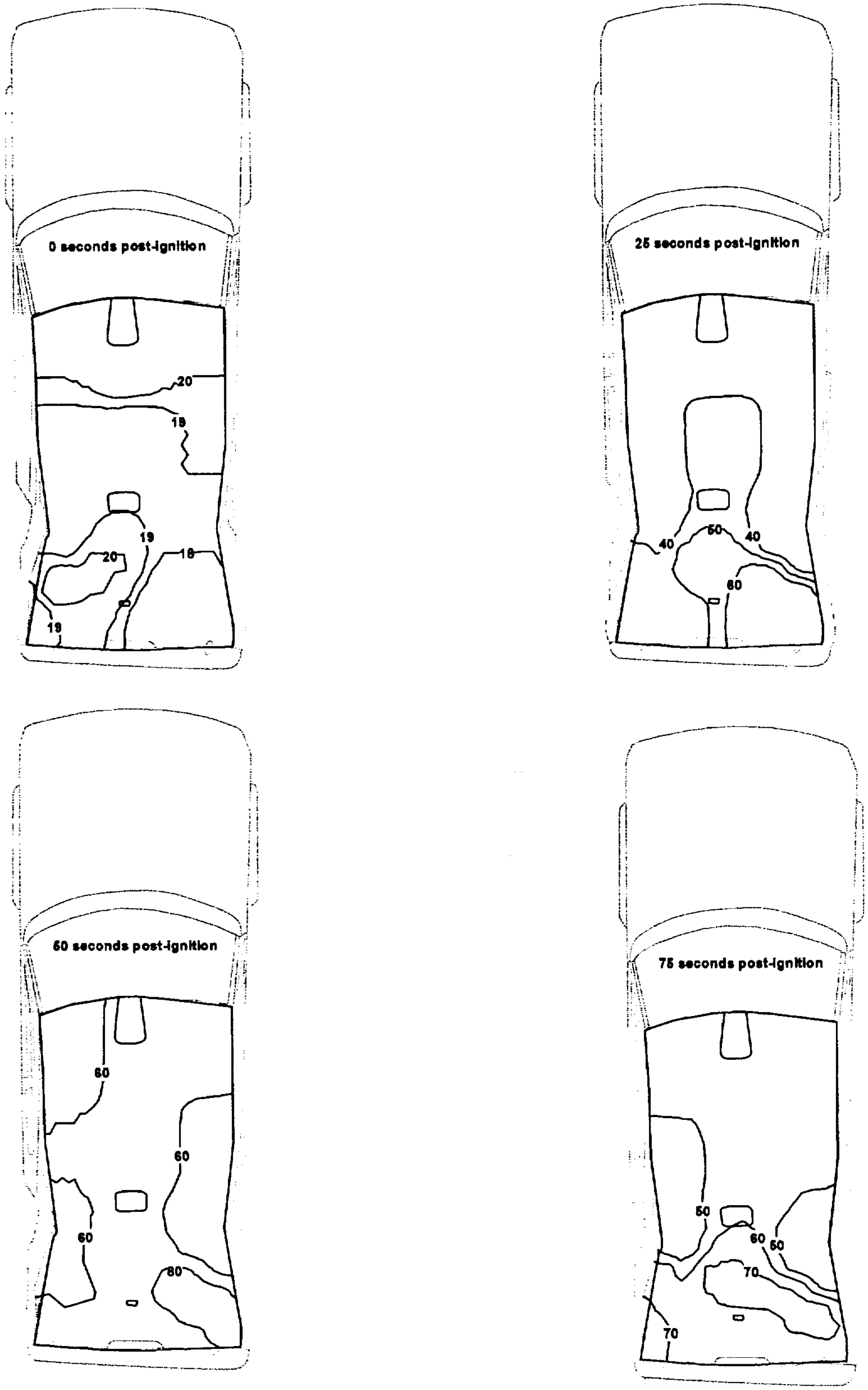

Figure 51. Fire Test F980609. Diagrams showing isothermal contour plots of estimated temperature of the rear compartment floor panel at 0, 5, 25, 50, 75, 100, 125, 150, 170, and 175 seconds post-ignition.

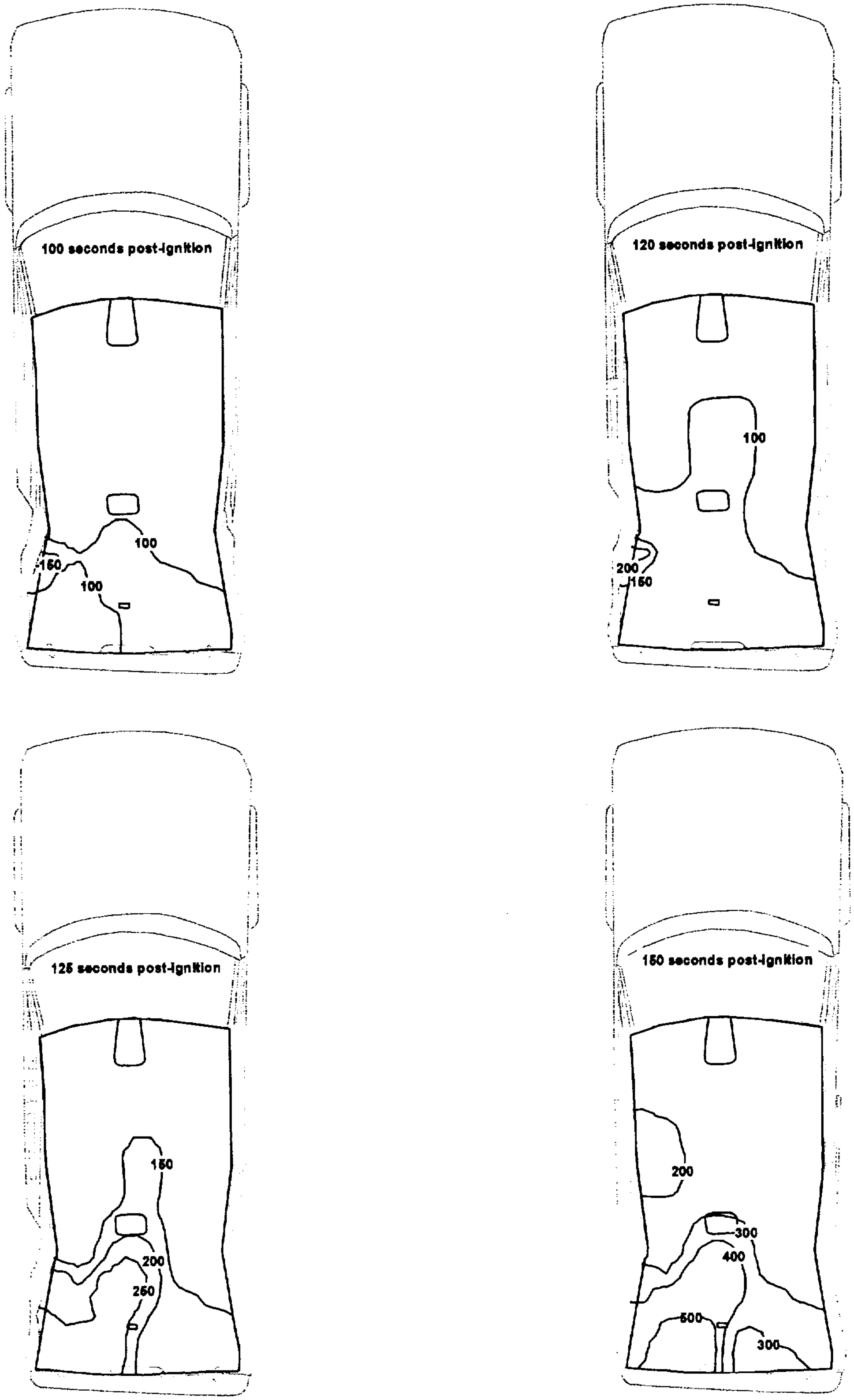

Figure 51, continued. Fire Test F980609. Diagrams showing isothermal contour plots of estimated temperature of the rear compartment floor panel at 0, 5, 25, 50, 75, 100, 125, 150, 170, and 175 seconds post-ignition.

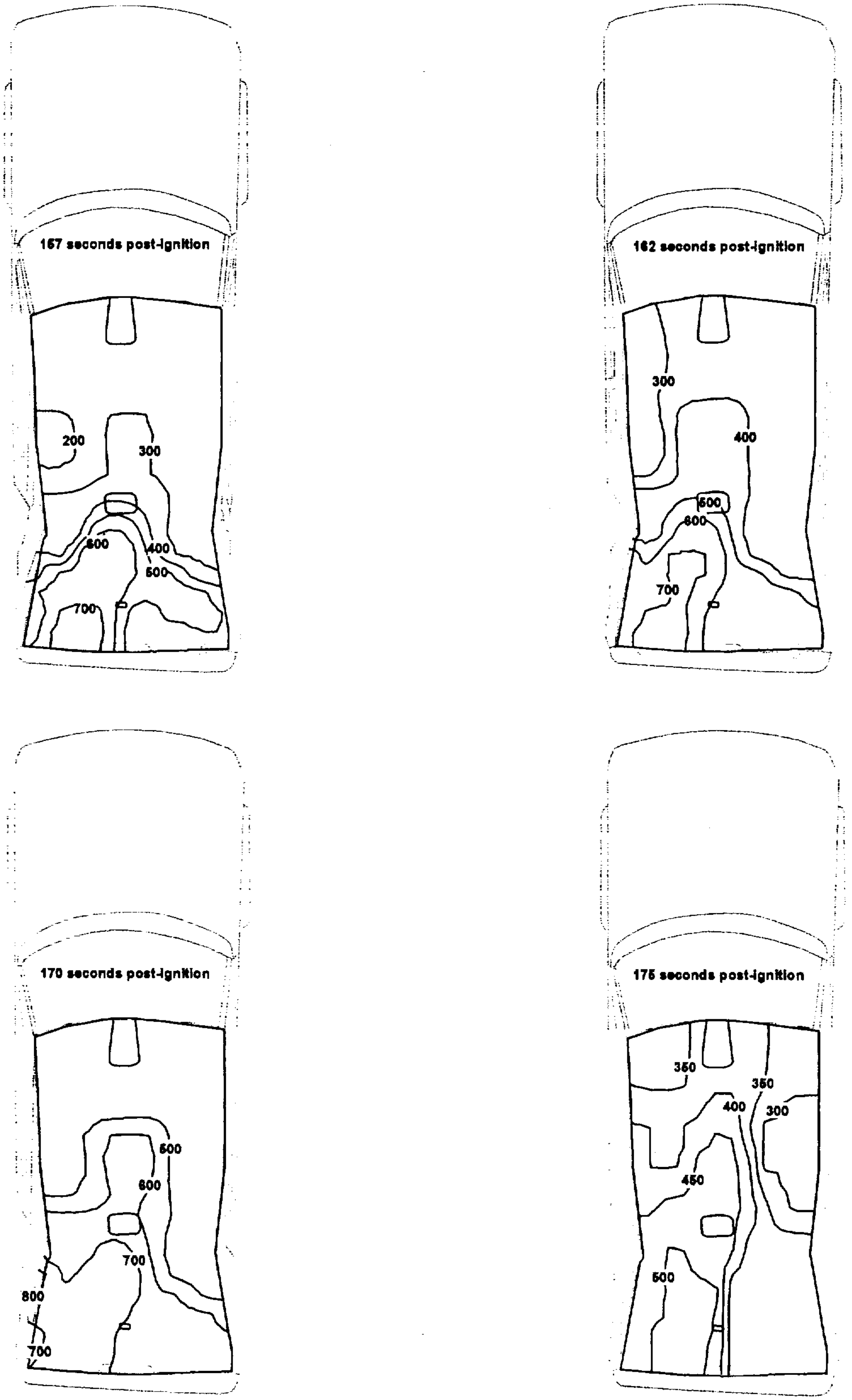

Figure 51, continued. Fire Test F980609. Diagrams showing isothermal contour plots of estimated temperature of the rear compartment floor panel at 0, 5, 25, 50, 75, 100, 125, 150, 170, and 175 seconds post-ignition.

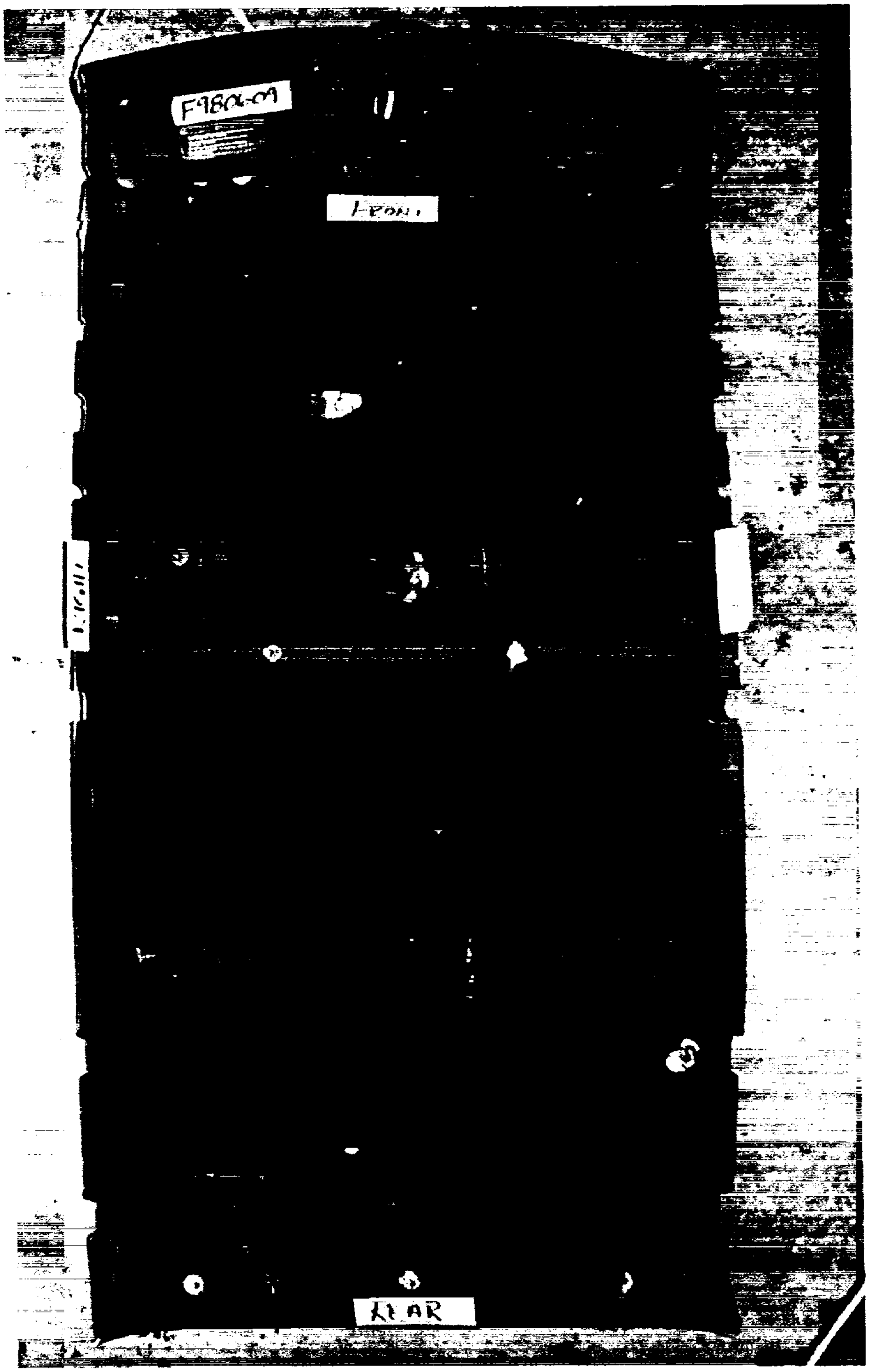

Figure 52. Fire Test F980609. Photograph of the roof trim panel from the test vehicle after this test.

6 Combustion Conditions

The output of combustion products from a fire depends on the material burning and on the supply of air to the flame. A well-ventilated fire is one in which the air supplied to the flames is sufficient for complete combustion. In partially enclosed spaces, such as an engine compartment or passenger compartment, airflow to the flames may be inadequate for complete combustion. In this case, called a ventilation-controlled or under-ventilated fire, the supply of air limits both the heat released by the fire and oxidation (combustion) of the gaseous fuel in the fire zone. As ventilation decreases, the output of carbon monoxide, hydrocarbons, smoke, and other products of incomplete combustion increase. The chemical composition of these gases depends on the chemical compositions of the materials burning and on the burning conditions, primarily ventilation. Accumulation of partially oxidized gases and unoxidized thermal decomposition products in an enclosed space can create a hazardous condition. In most cases, these gases are heated relative to the surrounding air and, because of their buoyancy, typically accumulate below the ceiling or roof of the enclosed space, forming what is called the upper layer. The upper layer can be ignited by flames from burning objects (piloted ignition) or can ignite spontaneously (autoignition) when the temperature of the gases exceeds a minimum threshold temperature (autoignition temperature), which depends on the chemical composition and the fuel/oxygen ratio of the upper layer. Once ignited, radiation from the burning upper layer transfers heat downward, and may ignite combustible materials below the burning upper layer. Some of the partially oxidized gases and unburned thermal decomposition products may be toxic (see **SECTION 7**).

The equivalence ratio is a quantitative measure of ventilation:

$$\Phi = \frac{\left[{}^{fuel}\!/_{O_2}\right]_{fire}}{\left[{}^{fuel}\!/_{O_2}\right]_{stoichiometric}}$$

where Φ is the equivalence ratio, $[\text{fuel}/O_2]_{fire}$ is the fuel-to-oxygen ratio in the fire, and $[\text{fuel}/O_2]_{stoichiometric}$ is the fuel-to-oxygen ratio required for complete combustion. In most instances, the equivalence ratio cannot be measured directly in a large-scale test such as the one described here. Ventilation, and thus the equivalency ratio is not uniform in situations where objects are burning in different physical environments, such as a burning motor vehicle where different materials burn at different times and in different environments. Estimates of the average ventilation were obtained from the data acquired during this test. It was impossible to isolate and measure the fire products produced by each of the materials burning, and to measure airflow into each of the unique environments that existed during this test.

Heat and combustion gases produced by burning objects in the test vehicle rose into the Fire Products Collector at the test facility. Thus, data from the Fire Products Collector can be used to estimate the average ventilation for the burning vehicle. A similar approach can be used to estimate the average ventilation for the passenger compartment using the gas concentration data from the FTIR gas analyzer and the air temperature data from the aspirated thermocouples. Estimation of ventilation from these data was done by comparison to the results obtained from testing individual materials in small-scale flammability tests,[11] where the equivalence ratio was measured precisely [7].

Five derived parameters were used in this comparison. Values of these parameters for polymeric materials similar to those used in the test vehicle are shown in Table 1.

Table 2

Fire Products for Well-ventilated Fires[1,2]

material	$Y(CO)/Y(CO_2)$ (g/g)	$Y(HC)/Y(CO_2)$ (g/g)	$Y(CO_2)/\Delta H_{CON}$ (g/kJ)	$Y(CO)/\Delta H_{CON}$ (g/kJ)	$Y(HC)/\Delta H_{CON}$ (g/kJ)
gasoline[3]	0.011 – 0.014	0.0032 – 0.0039	0.14 – 0.16	0.0021 – 0.0026	0.00058 – 0.00073
poly(ethylene)	0.0087	0.0025	0.13	0.0011	0.00032
poly(propylene)	0.0086	0.0022	0.12	0.0011	0.00027
poly(styrene)	0.026	0.0060	0.21	0.0054	0.00127
polyester	0.05	0.019	0.15	0.0065	0.00185
Nylon	0.018	0.0078	0.13	0.0035	0.00098
Flexible urethane foams	0.006 - 0.027	0.0013 - 0.0033	0.15 - 0.21	0.0012 - 0.0055	0.00023 - 0.00069
Rigid urethane foams	0.015 - 0.046	0.006 - 0.036	0.17 - 0.23	0.0028 - 0.0081	0.00011 - 0.00070

[1] Values reported in Table 2 were calculated from data reported in Table 3-4.11 in reference 9.

[2] Y(CO) is the mass-yield of carbon monoxide (g). $Y(CO_2)$ is the mass-yield of carbon dioxide (g). Y(HC) is the mass-yield of gaseous hydrocarbons (g). $Y(CO_2)/\Delta H_{con} = (C_{CO_2}/c_p\Delta T)(\rho_{CO_2}/\rho_{air})$, $Y(CO)/\Delta H_{con} = (C_{CO}/c_p\Delta T)(\rho_{CO}/\rho_{air})$, and $Y(HC)/\Delta H_{con} = (C_{HC}/c_p\Delta T)(\rho_{HC}/\rho_{air})$. ΔH_{CON} is the convective heat of combustion per unit fuel vaporized (kJ/g). The C_j are the gas-phase concentrations (volume fraction) of carbon dioxide, carbon monoxide, and total hydrocarbons. The ρ_j are the gas-phase densities (g/m^3) of carbon dioxide, carbon monoxide, total hydrocarbons, and air. c_p is the heat capacity of air (kJ/g-K). ΔT is the difference between the gas temperature and the temperature of the ambient air (K).

[3] Values for gasoline were estimated from the data in Table 3-4.11 in reference 9 assuming an aliphatic hydrocarbon content of 60 to 70 % and an aromatic hydrocarbon content of 30 to 40%.

---

[11] Small-scale flammability tests to determine combustion properties of materials were conducted in the Factory Mutual Research Corporation Flammability Apparatus is a small-scale test apparatus (see reference 7).

These parameters include Y(CO)/Y(CO_2), Y(HC)/Y(CO_2), Y(CO_2)/ΔH_{CON}, Y(CO)/ΔH_{CON}, Y(HC)/ΔH_{CON}. The values of these parameters in Table 1 were determined for the well-ventilated combustion of a poly(ethylene), a poly(propylene), a poly(styrene), a polyester, a Nylon, a group of flexible urethane foams, and a group of rigid urethane foams.[12]

Analysis of the data from the Fire Products Collector suggested that production of carbon monoxide relative to carbon dioxide was greater than expected for well-ventilated combustion of gasoline and of materials similar to those used in the test vehicle. Figure 53 shows a plot of [G_{CO}]/[G_{CO2}] versus time post-ignition, where G_{CO} and G_{CO2} are the carbon monoxide- and carbon dioxide-release rates measured using the Fire Products Collector (**APPENDIX G**).

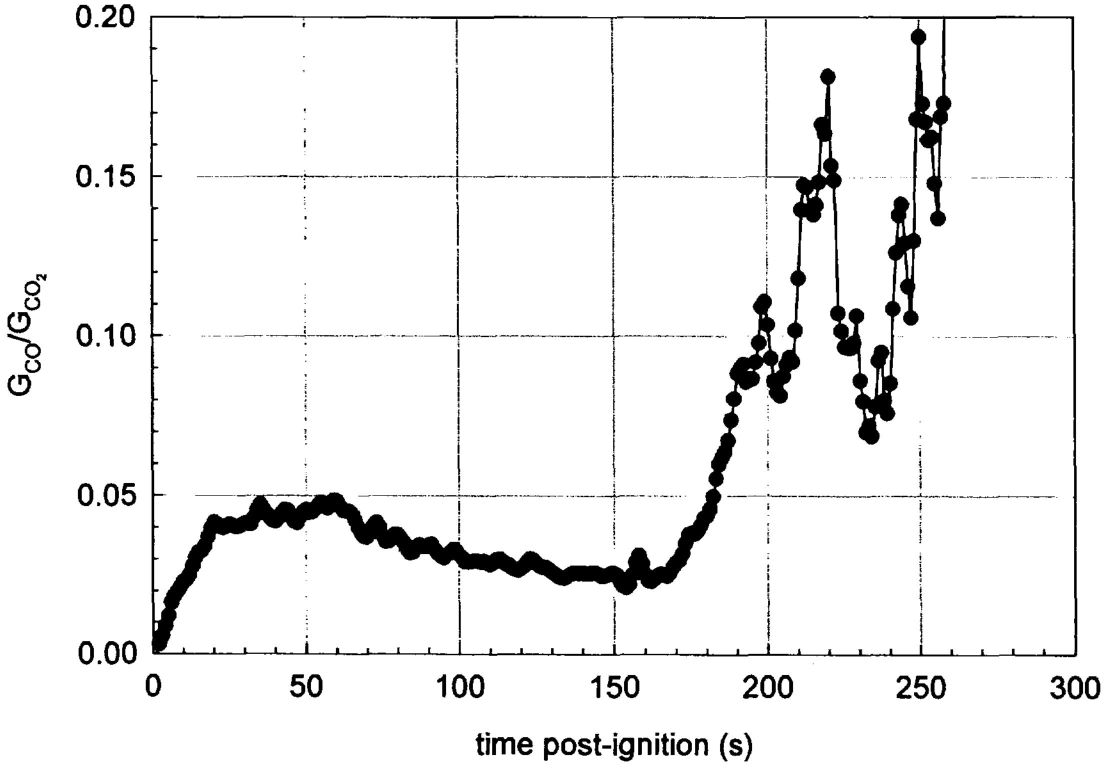

Figure 53. Fire Test F980609. Plot of [G_{CO}]/[G_{CO2}] versus time post-ignition determined from the carbon monoxide- and carbon dioxide-release rate data from the Fire Products Collector.

---

[12] The compositions and physical properties such as density, thermal conductivity, and heat capacity of these materials were not specified. As these properties can effect the combustion characteristics of these materials, testing of materials in the current US motor vehicle fleet may yield somewhat different values than those shown in Table 1.

The ratio $[G_{CO}]/[G_{CO2}]$ calculated for this test is equivalent to the ratio $[Y(CO)]/[Y(CO_2)]$ determined for individual materials listed in Table 1. Values of $[G_{CO}]/[G_{CO2}]$ greater than the ranges in Table 1 indicate the fire was under-ventilated. That is, the supply of oxygen to the flames was not sufficient for stoichiometric combustion. Before ignition, $[G_{CO}]/[G_{CO2}]$ was undefined because $G_{CO} = G_{CO2} = 0$.

The value of $[G_{CO}]/[G_{CO2}]$ started to increase at the time of ignition, asymptotically approached 0.05 at 60 seconds post-ignition (Fig. 53). One possible explanation for the behavior of $[G_{CO}]/[G_{CO2}]$ observed during the first 60 seconds of this test is that airflow into the restricted space below the test vehicle was insufficient for stoichiometric combustion as the vaporization rate of gasoline from the liquid pool increased. Gasoline was the only fuel burning at ignition, and the predominant fuel for the fire during at this time. Values of $[G_{CO}]/[G_{CO2}] \leq 0.014$, observed for the first few seconds after ignition (Fig. 53), indicate that the fire was well-ventilated. As radiation from the burning gasoline vapor heated the surface of the gasoline pool, the vaporization rate of hydrocarbons from the liquid gasoline increased, which resulted in an increasing heat release rate (**APPENDIX G**, Plot G1). Oxygen in the air flowing into the space under the vehicle would have been consumed at an increasing rate. If the airflow into the space under the test vehicle was not sufficient to accommodate this increasing oxygen consumption by the fire, then the efficiency of combustion would have decreased as observed in Figure 53.

At about 60 seconds post-ignition, the value of $[G_{CO}]/[G_{CO2}]$ started to decrease, approaching a value of 0.02 between 165 and 170 seconds post-ignition – the time the test was ended and fire suppression began (Fig. 53). The heat release rate measured with the Fire Products Collector at the test facility increased from 0 to 450 – 500 kW from the time of ignition through about 30 seconds post-ignition, and remained approximately constant between 30 and 60 seconds post-ignition (APPENDIX G, Plot G1). The flow rate of gasoline from the outlet of the gasoline delivery system remained constant throughout this test and heat release rate from the burning gasoline appeared to have reached a steady-state at this time. The increase in heat release rate measured by the Fire Products Collector starting at about 60 seconds indicated that other combustible materials such as the tires started to ignite at this time. One consequence of flame-spread to these other materials was that a significant portion of the growing fire plume extended out from the restricted space below the test vehicle. This may have allowed higher buoyant flow and greater air entrainment into the flames extending away from the vehicle, resulting in an increase in the overall combustion efficiency after 60 seconds post-ignition. A correlation between heat output and ventilation has been demonstrated in laboratory experiments during combustion for a number of solid materials similar to the materials used in the test vehicle [7].

The value of $[G_{CO}]/[G_{CO2}]$ started to increase when fire suppression began between 170 and 175 seconds post-ignition, indicating that the overall combustion efficiency decreased as the flames were extinguished. Although flames were visibly suppressed relatively quickly, many materials in the test vehicle continued to produce smoke. Continued thermal decomposition of these materials after the flames were visibly extinguished would have increased the production of partially oxidized and unoxidized gases relative to carbon dioxide, resulting in increasing values of $[G_{CO}]/[G_{CO2}]$.

A similar analysis was performed using gas concentration data from the passenger compartment (**APPENDIX H**). This data was used to calculate values for $[C_{CO} \times d_{CO}]/[C_{CO2} \times d_{CO2}]$ and $[C_{HC} \times d_{HC}]/[C_{CO2} \times d_{CO2}]$ (Fig.'s 54 and 55).

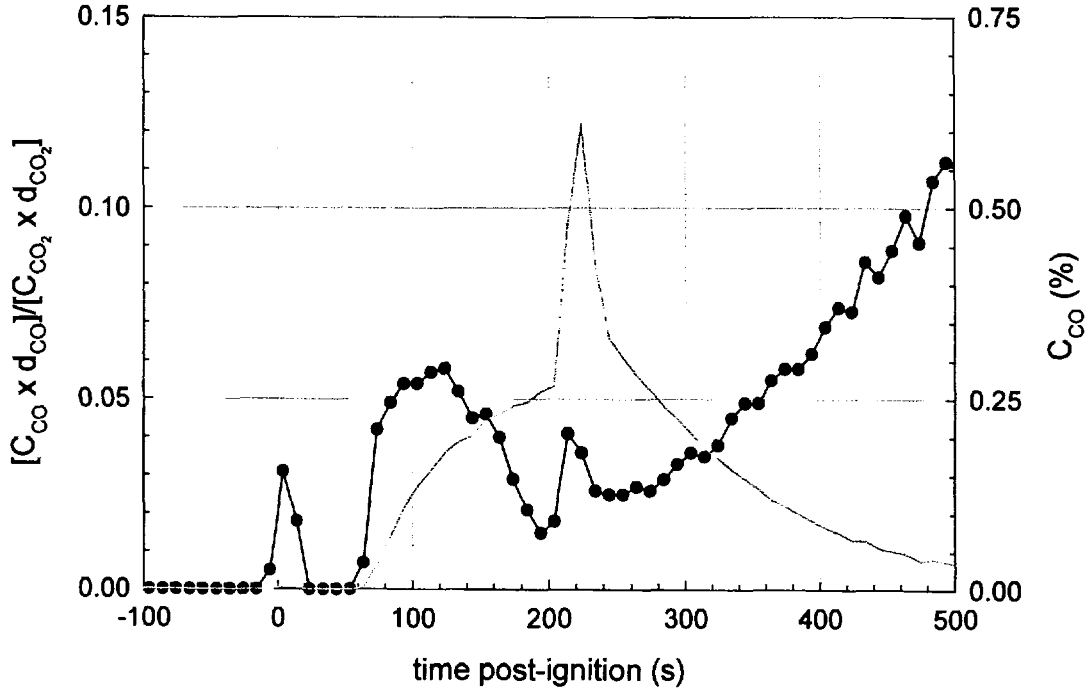

Figure 54. Fire Test F980609. Plots of $[C_{CO} \times d_{CO}]/[C_{CO2} \times d_{CO2}]$ (–●–, left axis) and the concentration of carbon monoxide (—, right axis) in the passenger compartment.

Values for $[C_{CO2} \times d_{CO2}]/[t_{air} \times Cp_{air}]$, $[C_{CO} \times d_{CO}]/[t_{air} \times Cp_{air}]$, and $[C_{CO2} \times d_{CO2}]/[t_{air} \times Cp]$ could not be determined for this test because air temperature data in the passenger compartment was not available. The terms in these ratios are defined as follows: C_j is the gas-phase concentration of species j; d_j is the vapor density of species j; t_{air} is the air temperature; and Cp_{air} is the heat capacity of air. The product [$C_j \times d_j$] equals the mass-concentration of species j in the passenger compartment; therefore the [$C_{CO} \times d_{CO}$]/[$C_{CO2} \times d_{CO2}$] and [$C_{HC} \times d_{HC}$]/[$C_{CO2} \times d_{CO2}$] are equivalent to the ratios [Y(CO)]/[Y(CO_2)] and [Y(HC)]/[Y(CO_2)] determined for individual materials listed in Table 1.

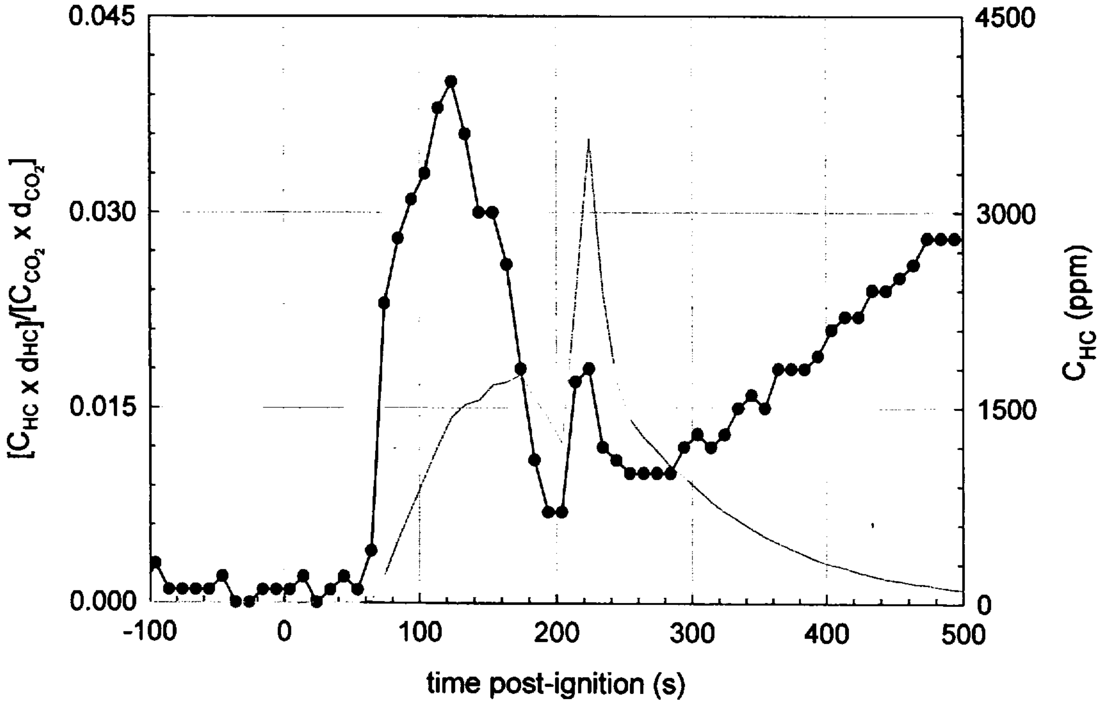

Figure 55. Fire Test F980609. Plots of [$C_{HC} \times d_{HC}$]/[$C_{CO2} \times d_{CO2}$] (—●—, left axis) and the concentration of total hydrocarbons (—, right axis) in the passenger compartment.

The concentrations of carbon dioxide, carbon monoxide, methane, ethylene, and acetylene measured in the passenger compartment remained at pre-ignition levels until about 60 seconds post-ignition (Plots H1 through H5, **APPENDIX H**). The back ground concentrations of carbon monoxide, methane, ethylene, and acetylene in the test vehicle were low, values of [$C_{CO} \times d_{CO}$]/[$C_{CO2} \times d_{CO2}$] and [$C_{HC} \times d_{HC}$]/[$C_{CO2} \times d_{CO2}$] were approximately 0 from the time of ignition until approximately 60 seconds post-ignition (Fig.'s 54 and 55). Values of [$C_{CO} \times d_{CO}$]/[$C_{CO2} \times d_{CO2}$] and [$C_{HC} \times d_{HC}$]/[$C_{CO2} \times d_{CO2}$] started to increase at about 80 seconds post-ignition, peaked between 120 and 130 seconds post-ignition, and decreased until the end of the test and fire suppression began (Fig.'s 54 and 55). These trends reflect changes in the source of the combustion gases in the passenger compartment, as well as flame-spread to materials in the passenger compartment.

The concentrations of carbon dioxide, carbon monoxide, methane, ethylene, and acetylene started to increase (Plots H1 through H5, **APPENDIX H**) as combustion products from the burning gasoline started to enter the rear compartment through seam openings around the rear wheelhouses between 60 and 70 seconds post-ignition (**Section 5**). Data from the Fire Products Collector indicated that the burning gasoline was under-ventilated at this time (Fig. 53). The relative concentrations of carbon dioxide, carbon monoxide, partially oxidized, and unoxidized hydrocarbons in the gas mixture entering the passenger compartment from below the test vehicle would have reflected this condition. The temperature of metal surfaces on the wheelhouse panels and rear compartment floor panel was sufficient to have resulted in thermal decomposition of materials in contact with these surfaces at this time. The mixture of gases produced by these thermal decomposition reactions would have contained relatively higher concentrations of carbon monoxide, partially oxidized, and unoxidized hydrocarbons than carbon dioxide. Both conditions are consistent with the observation that values of $[C_{CO} \times d_{CO}]/[C_{CO2} \times d_{CO2}]$ and $[C_{HC} \times d_{HC}]/[C_{CO2} \times d_{CO2}]$ were greater than their respective reference values in Table 2 between about 90 and 160 seconds post-ignition (Fig.'s 53 and 54).

Decreasing values of $[C_{CO} \times d_{CO}]/[C_{CO2} \times d_{CO2}]$ and $[C_{HC} \times d_{HC}]/[C_{CO2} \times d_{CO2}]$ between 130 and 200 seconds post-ignition (Fig.'s 54 and 55) are consistent with flame-spread to objects in the rear compartment during this time, and an increasing combustion efficiency of the fire outside the rear compartment. This timing is consistent with the timing of flame-spread into the passenger compartment determined in **SECTION 5**, where the first direct evidence of flames inside the passenger compartment was between 100 and 130 seconds post-ignition. The values of $[C_{CO} \times d_{CO}]/[C_{CO2} \times d_{CO2}]$ and $[C_{HC} \times d_{HC}]/[C_{CO2} \times d_{CO2}]$ started to decrease at 130 seconds post-ignition, approaching the ranges expected for well-ventilated combustion at 200 seconds post-ignition. The values of $[C_{CO} \times d_{CO}]/[C_{CO2} \times d_{CO2}]$ and $[C_{HC} \times d_{HC}]/[C_{CO2} \times d_{CO2}]$ increased when fire suppression began between 170 and 175 seconds post-ignition, indicating that the overall combustion efficiency decreased as the flames were extinguished.

7 Estimation of Skin Temperature Profiles from Measured Heat Flux Data, Fractional Equivalent Dose Parameters from Measured Gas Concentration Data, and Thermal Damage to the Respiratory Tract from Measured Air Temperature Data

The mathematical model "BURNSIM: A Burn Hazard Assessment Model" [8] was used to estimate the time and depth of burns to exposed skin. The inputs to this model were heat fluxes derived from the directional flame thermometer measurements and air temperatures measured using the aspirated thermocouple probe.

Two models were used to estimate the potential for toxicity from exposure to the combustion gases measured in the passenger compartment. The Federal Aviation Administration (FAA) Combined Hazard Survival Model [9] was used to estimate the time to incapacitation and the time to lethality. A model described by Purser [10] also was used to estimate the time to incapacitation. Both models estimate the risk from exposure to hot air, reduced oxygen, carbon monoxide, carbon dioxide, hydrogen cyanide, hydrogen chloride, hydrogen fluoride, hydrogen bromide, acrolein, and nitrogen dioxide. Both models also account for the physiological effect of carbon dioxide-induced hyperventilation, which increases the respiratory uptake.

7.1 The BURNSIM Model

The computer model BURNSIM was the analytical tool chosen to estimate skin temperature depth profiles from the heat flux data in **APPENDIX G**. The BURNSIM model divides the skin into a series of ten layers, with a uniform thickness of 0.2 mm per layer. The top layer was divided into 8 layers each with a uniform thickness of 0.025 mm to better account for the non-instantaneous heat transfer from the epidermal surface into the first layer.

Skin Model of BURNSIM

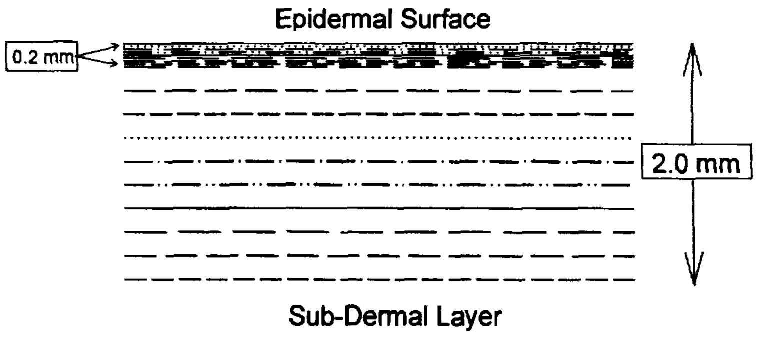

The BURNSIM analysis used here incorporated the following assumptions to estimate skin temperature profiles. The absorbtivity of exposed skin was assumed to be 0.60 (i.e., the skin absorbs 60% of the radiation incident upon the epidermal surface). The absorbtivity of surface hair was assumed to be 0.05 (i.e., surface hair absorbs 5% of the incident radiation before it reached the skin). Exposed skin was assumed to absorb 100% of the measured convective heat flux to its surface. The temperature of each layer was estimated as a function of the time of exposure to an external heat flux. A portion of the absorbed heat is removed from the skin by the circulatory system. Thermal damage to a layer of skin exceeds the capacity of the physiological repair processes when the temperature of that layer exceeds 45°C.

In estimating skin temperature, the analysis presented in this paper using BURNSIM did not account for the presence of facial or head hair, or clothing covering the skin, all of which may block direct heat transfer to the skin. This analysis also did not account for variations in skin thickness among individuals, or variations in skin thickness at different parts of the body on the same individual. For example, skin thickness can vary from 1 to 5 mm with body location. This analysis also did not account for effect of skin pigmentation on absorbtivity. In using the radiative and convective heat flux estimates shown in **APPENDIX G** to estimate skin temperature profiles, this analysis assumed that the location and orientation of the skin was identical to that of the HFT/RAD transducer assemblies used to measure heat flux. Small changes in position or angle of the surface can result in large differences between in the incident heat flux to the surface (see below). Based on the currently available information and data, the accuracy of the estimated skin temperature depth profiles in humans exposed to heat flux levels from fire such as measured in this test obtained using BURNSIM has not been determined.

7.1.1 Estimation of Skin Temperature Profiles using BURNSIM

The absorbed heat flux at each of the HFT/RAD assembly locations was estimated from the data recorded from HFT/RAD 10 through HFT/RAD 15. Estimates of absorbed heat flux obtained by analysis of the data recorded from these transducers were input into the BURNSIM model to estimate skin temperature profiles for exposed skin at these locations. The BURNSIM calculations were performed using data recorded between 0 and 241 seconds post-ignition. The resulting estimated temperature profiles are shown in Figures 56 through 61.

Each of the estimated skin temperature profiles in Figures 56 through 61 contain a single peak at approximately 170 seconds post-ignition. The total and radiative heat fluxes recorded from HFT/RAD 10 through HFT/RAD 15 increased as a section of the left quarter trim panel had ignited, and flames and heated gases spread forward along the lower surface of the head lining panel, and decreased as flames in the rear compartment and along the head lining panel were extinguished. HFT/RAD 10 through HFT/RAD 15 were located above the driver's and front passenger's seats in areas that were not exposed to flames during this test. These transducers

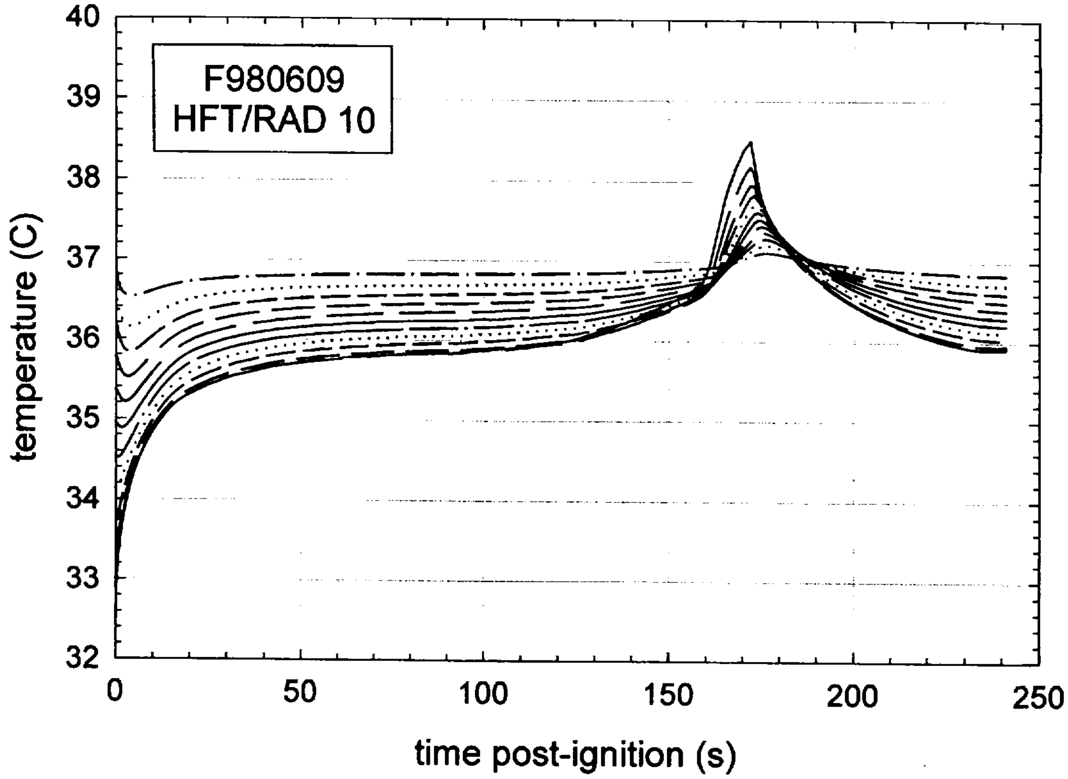

Figure 56. Fire Test F980609. Skin temperature profiles estimated from heat flux data recorded from HFT/RAD Assembly 10 (**APPENDIX E**, Plots E3 and E4).

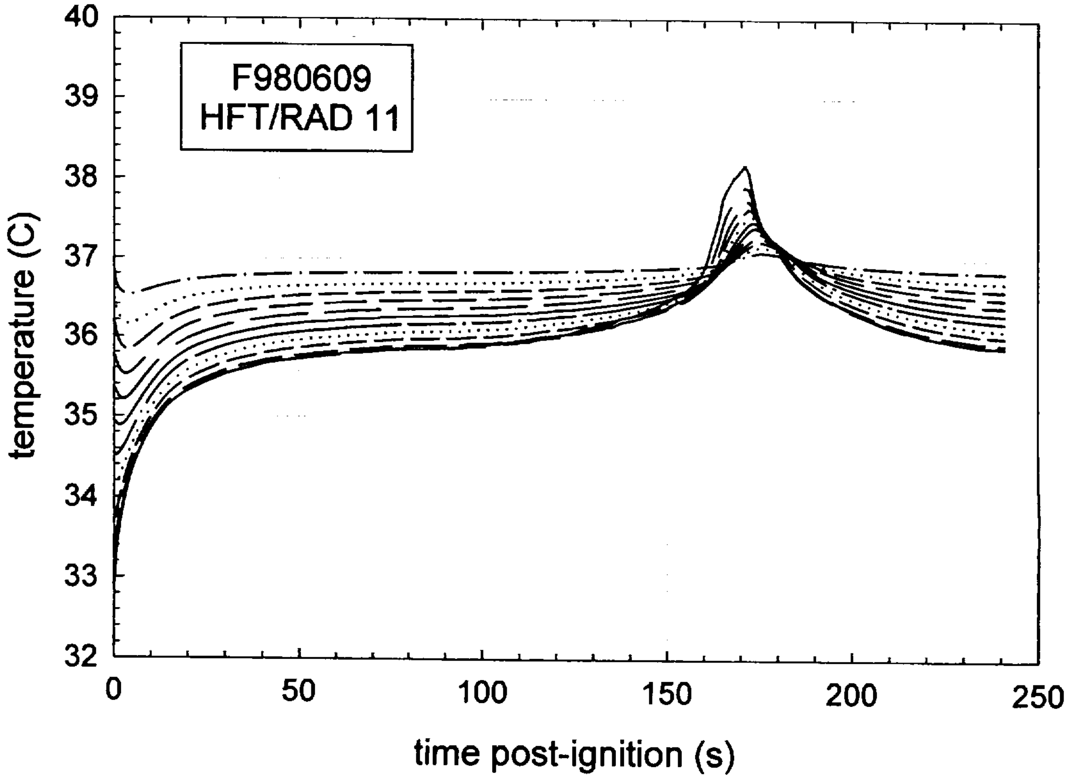

Figure 57. Fire Test F980609. Skin temperature profiles estimated from data recorded from HFT/RAD Assembly 11 (**APPENDIX E**, Plots E5 and E6).

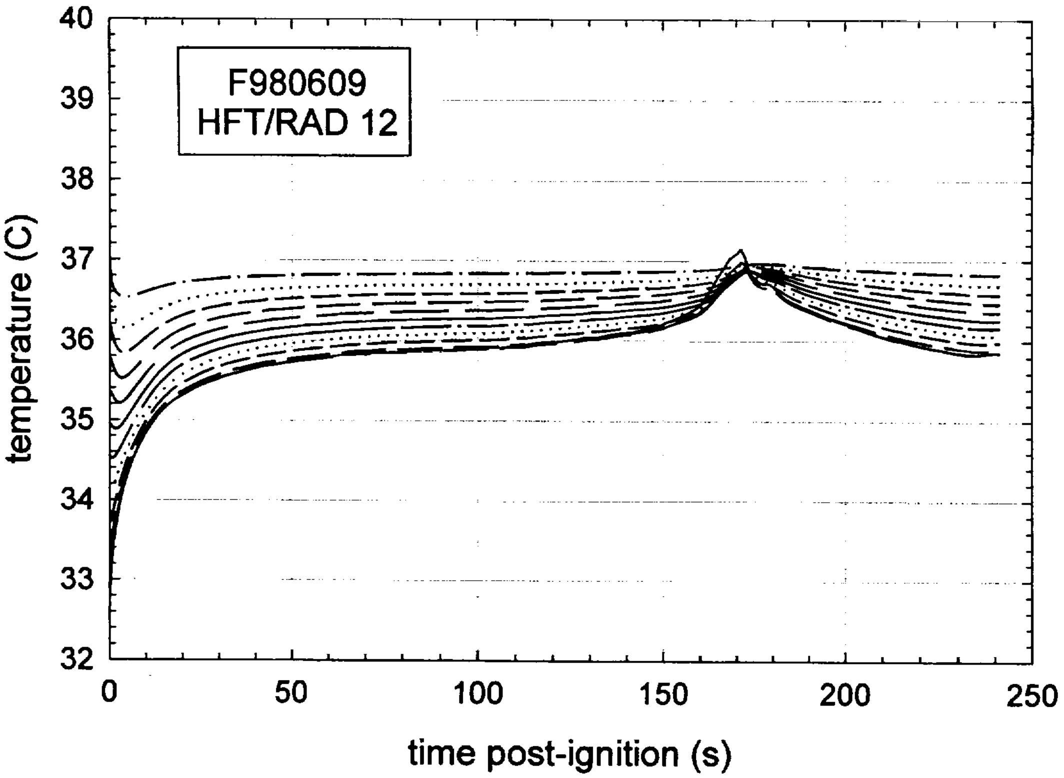

Figure 58. Fire Test F980609. Skin temperature profiles estimated from data recorded from HFT/RAD Assembly 12 (**APPENDIX E**, Plots E7 and E8).

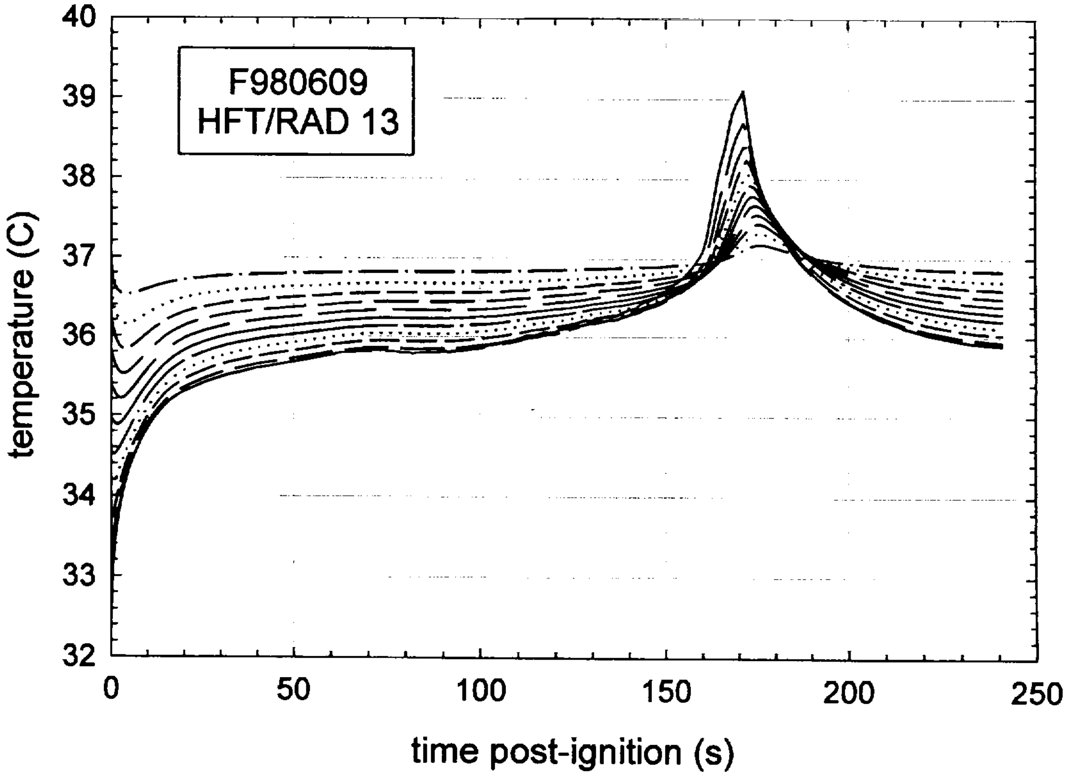

Figure 59. Fire Test F980609. Skin temperature profiles estimated from data recorded from HFT/RAD Assembly 13 (**APPENDIX E**, Plots E9 and E10).

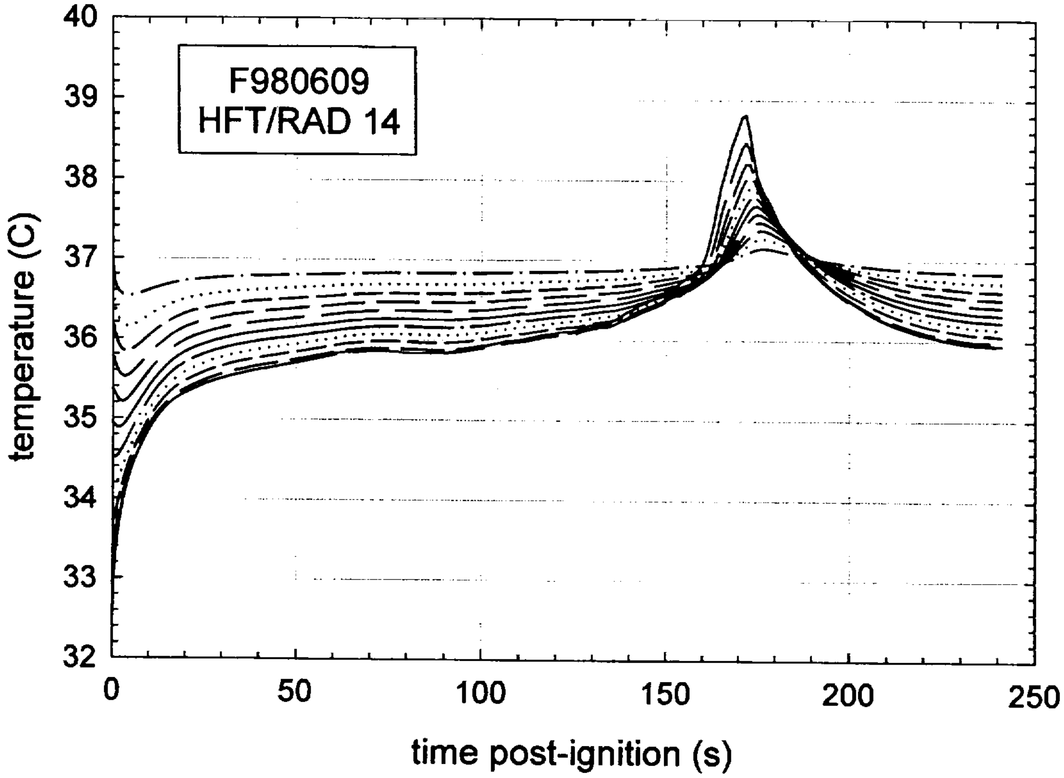

Figure 60. Fire Test F980609. Skin temperature profiles estimated from data recorded from HFT/RAD Assembly 14 (**APPENDIX E**, Plots E11 and E12).

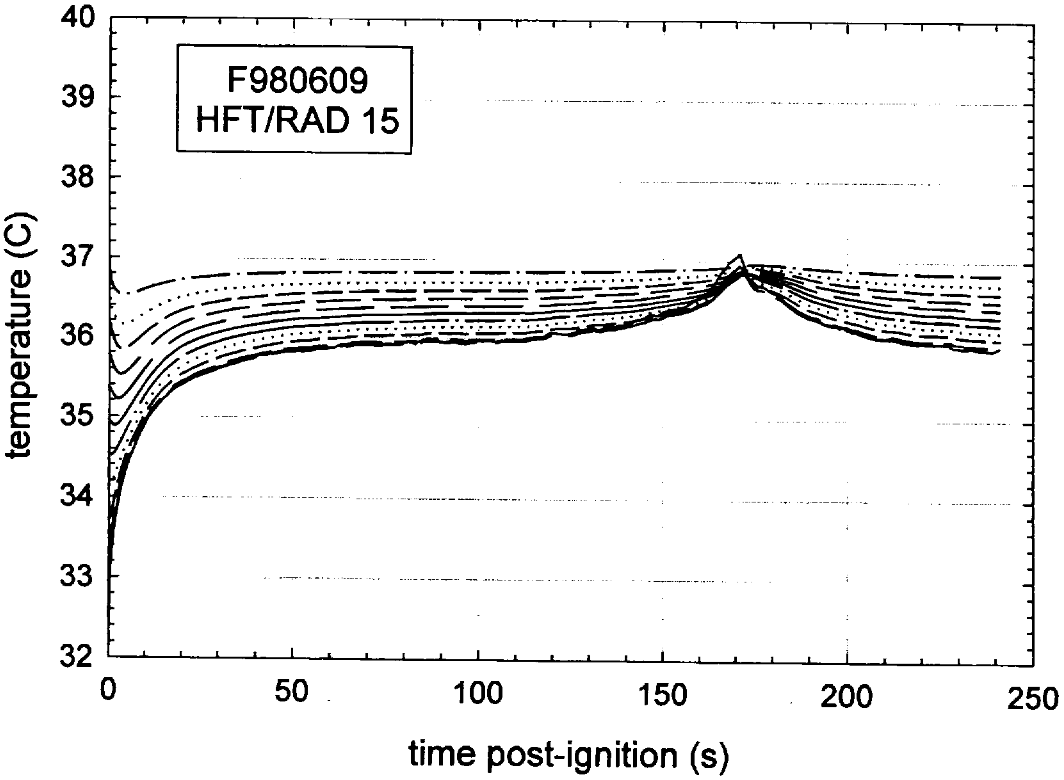

Figure 61. Fire Test F980609. Skin temperature profiles estimated from data recorded from HFT/RAD Assembly 15 (**APPENDIX E**, Plots E13 and E14).

appear to have responded to radiation from flames in the rear compartment and along the headlining panel, and to heated gases accumulating in the front of the passenger compartment. For example, the total and radiative heat fluxes recorded from HFT/RAD 10, which was located above the front passenger's seat facing upwards started to increase from background levels at approximately 50 seconds post-ignition. Flames had not spread into the passenger compartment at this time (Section 5) and the estimated temperature along the headlining panel above the front passenger's seat was < 60°C (Fig. 51).

The heat flux to HFT/RAD 10 increased as heated gases and flames spread forward along the head lining panel. A total heat flux of approximately 1.5 kW/m^2 and a radiative heat flux of approximately 1 kW/m^2 were recorded from HFT/RAD 10 between 165 and 170 seconds post-ignition (**Appendix E**, Plots E3 and E4). The estimated temperature along the headlining panel above the front passenger's seat at this time was between 400 and 500°C (Fig. 51). This heat flux data indicated that radiation from the heated gases along the headlining panel accounted for approximately 2/3 of the heat transferred to the transducer at this time. Convection from the heated gases surrounding this transducer accounted for the remaining 1/3 of the heat transferred to the transducer. The skin temperatures at the epidermal surface and sub-dermal interface estimated from this heat flux data were approximately 38.4 and 37.0°C, respectively, at 170 seconds post-ignition (Fig. 56).

7.2 The FAA Combined Hazard Survival Model and Purser's Model of Combustion Gas Toxicity

The FAA Combined Hazard Survival Model and Purser's model utilize the concept of a Fractional Effective Dose [FED] to estimate the cumulative effects of exposure to a mixture of gases produced by burning materials. For exposure to a single gas with an unchanging concentration in air, the Fractional Effective Dose for Incapacitation [FED(I)] is defined as the product of the gas-phase concentration and the time of exposure ($C \times t$) normalized to the concentration-time product that results in incapacitation of 50% of an exposed population [8, 9]. Similarly, the Fractional Effective Dose for lethality [FED(L)] is defined as the product of the gas-phase concentration and the time of exposure normalized to the concentration-time product that results in the death of 50% of an exposed population [see references in 8 and 9]. The estimates of FED(I) and FED(L) obtained using the FAA Combined Hazard Survival Model or Purser's model of combustion gas toxicity and presented in this report cannot be used to predict precisely when the gas concentrations measured in this test would have resulted in incapacitating narcosis or death for a vehicle occupant. Whether exposure to these gases results in toxicity depends on a number of complex physical and physiological variables.

Some of the physical variables include the exact chemical composition of the gaseous mixture, the concentration of each component of the gaseous mixture, and the time of exposure. Exposure to these gases in a burning vehicle can be highly variable, and depend on factors such as elevation in the passenger compartment and airflow through the passenger compartment. As mentioned in the previous section, combustion gases are hotter than the ambient air and form an upper-layer. As both heat and mass are conserved in a fire, the existence of a steep vertical air-temperature gradient implies the existence of similarly steep vertical concentration gradients for gaseous combustion products accumulating in the passenger compartment. The location of the head and nose in the passenger compartment will affect the exposure concentration. An occupant whose head was located below the level where gases were measured, such as an occupant bent over in the seat, would have been exposed to lower concentrations of combustion gases than those shown in **APPENDIX H**. Airflow through the passenger compartment will dilute or remove these gases.

Uncertainties in the responses of humans exposed to these gases also complicate the determination of when and whether toxicity occurs. The mathematical equations for the calculation of FED(I) and FED(L) were derived by analysis of data from controlled experiments in which different species of laboratory animals were exposed to a range of concentrations of each gas. In using data from these laboratory animal experiments to define FED(I) and FED(L), both models implicitly assume that humans respond the same as laboratory animals to exposure to these gases – an assumption that is largely untested and may not be accurate. For example, except for incapacitation from exposure to carbon dioxide, none of the model predictions using either the FAA Combined Hazard Survival Model or Purser's model have been validated for humans. That is, the accuracy of FED(I) and FED(L) in predicting human responses to exposure to the combustion gases measured in this test has not been determined. Consequently, there is a high degree of uncertainty as to the effect exposure to these levels of combustion gases would actually have on a human vehicle occupant. In addition, neither of these models accounts for variation in individual responses to these gases nor the effect of trauma suffered during the crash on an occupant's response to these gases.

The equations presented in both the FAA Combined Hazard Survival Model and in Purser's model divide the exposure into one-minute intervals when the concentration of the gaseous species changes with time. In this test, Fourier Transform Infrared spectra were obtained at seven-second intervals to characterize the changing gas concentrations observed in the passenger compartment. The equations presented in the FAA Combined Hazard Survival Model and in Purser's model were modified to account for the faster sampling times used in this test.

These modified equations are shown below and were used to derive the estimated of FED(I) and FED(L) shown in **SECTION 7.2.1.**

Carbon dioxide-induced hyperventilation can increase the respiratory uptake of airborn combustion products. The FAA Combined Hazard Survival Model uses a multiplication factor to account for the increased respiratory uptake of gaseous combustion products because of exposure to elevated levels of carbon dioxide [V_{CO2}]:

$$V_{CO_2} = \frac{\exp\left(1.9086 + 0.2496 \times C_{CO_2}\right)}{6.8} \tag{1}$$

where the units of C_{CO2} are %. This equation was not modified for the analysis presented in **SECTION 7.2.1**.

The Fractional Effective Doses for Incapacitation from exposure to carbon dioxide, carbon monoxide, hydrogen chloride, hydrogen cyanide and decreased oxygen were calculated using the following equations modified to account for sampling intervals of less than 1 minute:

$$FED(I)_{CO_2} = \left(\frac{t}{60}\right) \times \sum \left\{ \frac{1}{2193.8 - \left(311.6 \times C_{CO_2}\right)} \right\} \tag{2}$$

when $5.5 \leq C_{CO2} \leq 7.0\%$,

$$FED(I)_{CO_2} = \left(\frac{t}{60}\right) \times \sum \left\{ \frac{1}{\exp\left(6.1623 - \left(0.5189 \times C_{CO_2}\right)\right)} \right\} \tag{3}$$

when $C_{CO2} > 7.0\%$,

$$FED(I)_{CO} = \left(\frac{t}{60}\right) \times \left(\frac{1}{3.4250}\right) \times \sum \left\{ V_{CO_2} \times C_{CO} \right\} \tag{4}$$

when $V_{CO2} \times C_{CO} > 0.01\%$,

$$FED(I)_{HCl} = \left(\frac{t}{60}\right) \times \sum \left\{ \frac{1}{3 + \dfrac{336{,}000}{\left(V_{CO_2} \times C_{HCl}\right) - 300}} \right\} \tag{5}$$

when $V_{CO2} \times C_{HCl} > 300$ ppm;

$$FED(I)_{HCN} = \left(\frac{t}{60}\right) \times \left(\frac{1}{564}\right) \times \sum \left\{\left(V_{CO_2} \times C_{HCN}\right) - 63\right\} \qquad (6)$$

when $V_{CO2} \times C_{HCN} > 63$ ppm; and

$$FED(I)_{O_2} = \left(\frac{t}{60}\right) \times \sum \left\{\frac{1}{\exp\left(8.55 - \left(0.511 \times \left(20.9 - C_{O_2}\right)\right)\right)}\right\} \qquad (7)$$

when $C_{O2} < 11\%$. The value of t in these equations was the time in seconds between acquisition of FTIR spectra. The overall Fractional Effective Dose for Incapacitation was calculated by summing the terms in equations 2 through 7:

$$FED(I)_{TOTAL} = FED(I)_{CO_2} + FED(I)_{CO} + FED(I)_{HCl} + FED(I)_{HCN} + FED(I)_{O_2} \qquad (8)$$

The Fractional Effective Doses for Lethality from exposure to carbon monoxide and hydrogen cyanide were calculated using the following equations modified to account for sampling intervals of less than 1 minute:

$$FED(L)_{CO} = \left(\frac{t}{60}\right) \times \sum \left\{\frac{1}{\exp\left(5.85 - \left(0.00037 \times V_{CO_2} \times C_{CO}\right)\right)}\right\} \qquad (9)$$

when $2000 \le V_{CO2} \times C_{CO} \le 9000$ ppm,

$$FED(L)_{CO} = \left(\frac{t}{60}\right) \times \sum \left\{\frac{1}{0.4 + \left(\frac{58{,}000}{V_{CO_2} \times C_{CO}}\right)}\right\} \qquad (10)$$

when $V_{CO2} \times C_{CO} > 9000$ ppm, and

$$FED(L)_{HCN} = \left(\frac{t}{60}\right) \times \left(\frac{1}{2586}\right) \times \sum \left\{\left(V_{CO_2} \times C_{HCN}\right) - 43.2\right\} \qquad (11)$$

when $V_{CO2} \times C_{HCN} > 43.2$ ppm;

The overall Fractional Effective Dose for Lethality was calculated by summing the terms in equations 8 through 10:

$$FED(L)_{TOTAL} = FED(L)_{CO} + FED(L)_{HCN} \tag{12}$$

The model described by Purser also uses a multiplication factor to account for the enhanced respiratory uptake of toxic gases because of exposure to elevated levels of carbon dioxide:

$$V_{CO_2} = \frac{\exp(1.9086 + (0.2496 \times C_{CO_2}))}{6.8} \tag{13}$$

The Fractional Effective Doses for Incapacitation from exposure to carbon monoxide and hydrogen cyanide were calculated using the following equations modified to account for sampling intervals of less than 1 minute:

$$FED(I)_{CO_2} = \left(\frac{t}{60}\right) \times \sum \left\{ \frac{1}{\exp(6.1623 - (0.5189 \times C_{CO_2}))} \right\} \tag{14}$$

when $C_{CO2} > 5\%$,

$$FED(I)_{CO} = \left(\frac{t}{60}\right) \times V_{CO_2} \times \sum \left\{ \frac{0.00082925 \times C_{CO}}{30} \right\} \tag{15}$$

where the units of C_{CO} are ppm,

$$FED(I)_{HCN} = \left(\frac{t}{60}\right) \times V_{CO_2} \times \sum \left\{ \frac{4.4}{185 - C_{HCN}} \right\} \tag{16}$$

when $80 \leq C_{HCN} \leq 180$ ppm,

$$FED(I)_{HCN} = \left(\frac{t}{60}\right) \times V_{CO_2} \times \sum \left\{ \frac{1}{\exp(5.396 - (0.023 \times C_{HCN}))} \right\} \tag{17}$$

when $C_{HCN} > 180$ ppm; and

$$FED(I)_{O_2} = \left(\frac{t}{60}\right) \times \sum \left\{ \frac{1}{\exp(8.13 - (0.54 \times (20.9 - C_{O_2})))} \right\} \tag{18}$$

when $C_{O2} < 11.3\%$.

As in the FAA model, the value of t in these equations was the time in seconds between acquisition of FTIR spectra. The overall Fractional Effective Dose for Incapacitation was calculated by summing the terms in equations 14 through 18:

$$FED(I)_{TOTAL} = FED(I)_{CO_2} + FED(I)_{CO} + FED(I)_{HCN} + FED(I)_{O_2} \qquad (19)$$

Both the FAA Combined Hazard Survival model and Purser's model predict that 50% of an exposed population would experience incapacitating narcosis (*i.e.*, an occupant loses consciousness and would be unable to exit a vehicle without assistance) when $FED(I)_{TOTAL} = 1.0$. Similarly, both of these models predict that 50% of an exposed population would die when $FED(L)_{TOTAL} \geq 1.0$.

7.2.1 Estimation of Fractional Equivalent Dose Parameters

The analysis presented in this report included estimates of FED(I) and FED(L) for carbon dioxide, carbon monoxide, and hydrogen cyanide using the FAA Combined Hazard Survival Model and Purser's model for assessment of the toxicity of combustion products. The other gaseous species included in the FAA Combined Hazard Model and Purser's model were not measured during this test; therefore, values of FED(I) or FED(L) were not estimated for these gases. Figures 62 through 66 show plots of $FED(I)_{co2}$, $FED(I)_{co}$, $FED(I)_{HCN}$, and $FED(I)_{HCL}$ computed using the FAA Combined Hazard Survival Model and Purser's model for assessment of the toxicity of combustion products.

Plots of the $FED(I)_{co2}$ parameters estimated using the FAA Combined Hazard Model and Purser's model are shown in Figure 62. Both models yielded estimates of $FED(I)_{TOTAL} > 0$ starting at about 170 seconds post-ignition, when the concentration of carbon dioxide was about 5%. Both models yielded estimates of $FED(I)_{co2} < 0.5$ through 500 seconds post-ignition.

Plots of the $FED(I)_{co}$ parameters estimated using both models are shown in Figure 63. The equations presented in the Purser model for computation of $FED(I)_{co}$ include a term for respiratory minute volume. Minute volumes corresponding to respiration during rest (8.5 L/min) and light activity (25 L/min) were used in these calculations [9]. Purser's model also accounts for the effect of exposure to carbon dioxide on respiratory rate.

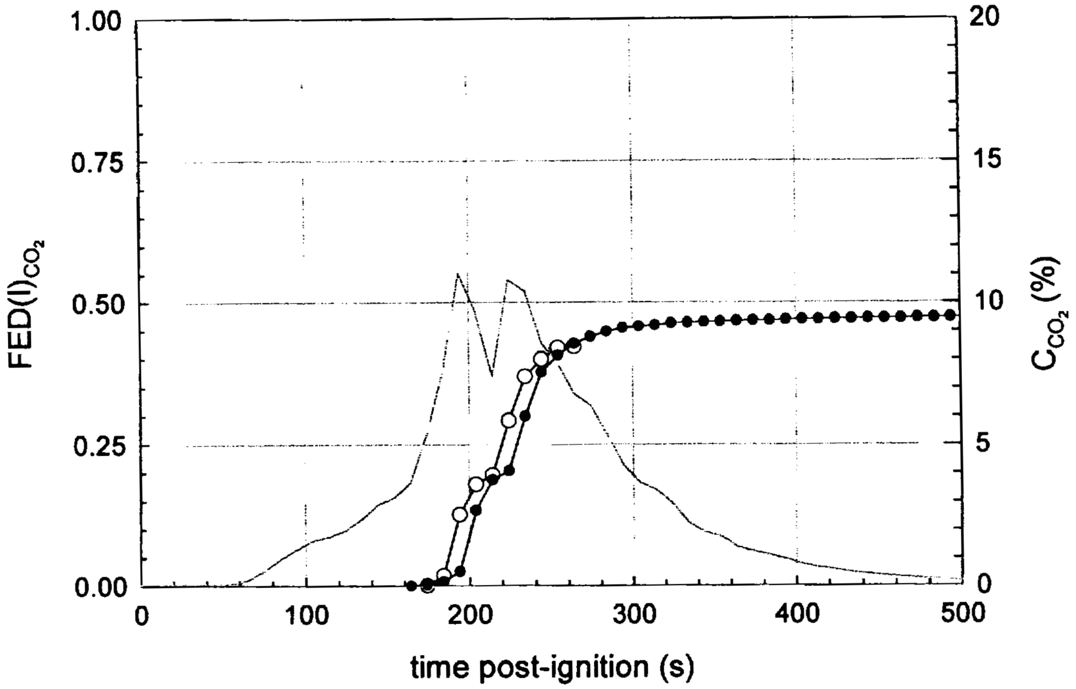

Figure 62. Fire Test F980609. Plots of FED(I)$_{CO2}$ versus time post-ignition: FAA Combined Hazard Survival Model (–○–); and Purser's model (–●–). A plot of C_{CO2} (——) is included for reference.

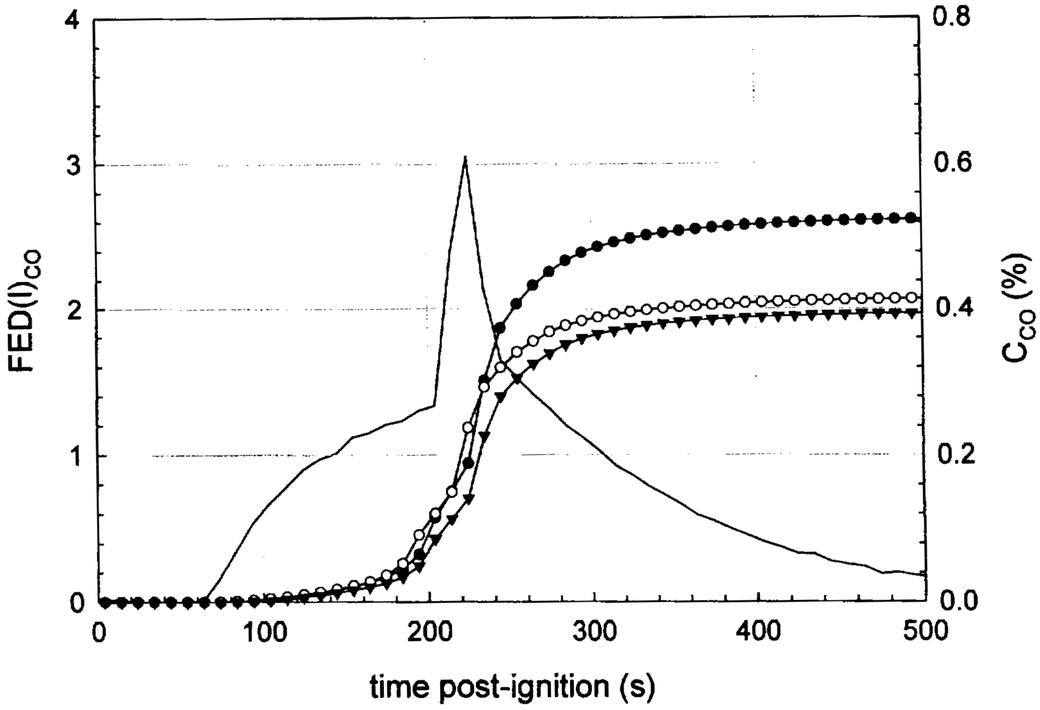

Figure 63. Fire Test F980609. Plots of estimates of FED(I)$_{CO}$ versus time post-ignition computed using the FAA Combined Hazard Survival Model (–○–), the Purser model with a respiratory minute volume of 8.5 L/min (–▼–), and the Purser model with a respiratory minute volume of 25 L/min (–●–). A plot of C_{CO} (——) is included for reference.

The FAA Combined Survival Hazard Model computes only one estimate of $FED(I)_{co}$, which accounts for the effect of exposure to carbon dioxide on respiratory rate [8]. These three estimates of $FED(I)_{co}$ became greater than zero between 70 and 80 seconds post-ignition. The estimates of $FED(I)_{co}$ derived using the FAA model and Purser's model with a respiratory minute volume of 25 L/min became greater than 1 between 220 and 230 seconds post-ignition, and reached values of about 2.1and 2.6, respectively, at 500 seconds post-ignition. The estimate of $FED(I)_{co}$ derived using Purser's model with a respiratory minute volume of 8.5 L/min became greater than 1 between 230 and 240 seconds post-ignition, and reached a value of approximately 2.0 at 500 seconds post-ignition.

Plots of the $FED(I)_{HCN}$ parameters estimated using both models are shown in Figure 64. Both the FAA Combined Survival Hazard Model and Purser's model employ a threshold concentration to determine when to start computing $FED(I)_{HCN}$ (refer to equations 6 and 14, respectively). The estimates of $FED(I)_{HCN}$ using the FAA model started at 174 seconds post-ignition, became greater than 1 between 215 and 220 seconds post-ignition, and reached a maximum value of about 10.3 by 400 seconds post-ignition. The estimates of $FED(I)_{HCN}$ using Purser's model started at 204 seconds post-ignition, and became greater than 1 between 210 and 220 seconds post-ignition.

The concentration of hydrogen chloride in the passenger compartment was less than the threshold for computation of FED(I) and FED(L). Therefore, $FED(I)_{HCL}$ was not computed (Fig. 65).

Plots of the $FED(I)_{TOTAL}$ parameters estimated using both models are shown in Figure 66. The FAA Combined Survival Hazard Model yielded $FED(I)_{TOTAL} > 1$ starting at about 210 seconds post-ignition, where $FED(I)_{CO}$ accounted for 43% of $FED(I)_{TOTAL}$, $FED(I)_{HCN}$ accounted for 46% of $FED(I)_{TOTAL}$, and $FED(I)_{CO2}$ accounted for 11% of $FED(I)_{TOTAL}$. The estimated $FED(I)_{TOTAL}$ reached a value of 12.1 at 300 seconds post-ignition.

Purser's model yielded $FED(I)_{TOTAL} > 1$ starting at about 210 seconds post-ignition using respiratory minute volumes of 8.5 L/min and 25 L/min in the calculations. With a respiratory minute volume of 8.5 L/min, $FED(I)_{CO}$ accounted for 1.5% of $FED(I)_{TOTAL}$, $FED(I)_{HCN}$ accounted for 98% of $FED(I)_{TOTAL}$ and $FED(I)_{CO2}$ accounted for 0.5% of $FED(I)_{TOTAL}$. With a respiratory minute volume of 25 L/min, $FED(I)_{CO}$ accounted for 2% of $FED(I)_{TOTAL}$, $FED(I)_{HCN}$ accounted for 97.5% of $FED(I)_{TOTAL}$ and $FED(I)_{CO2}$ accounted for 0.5% of $FED(I)_{TOTAL}$.

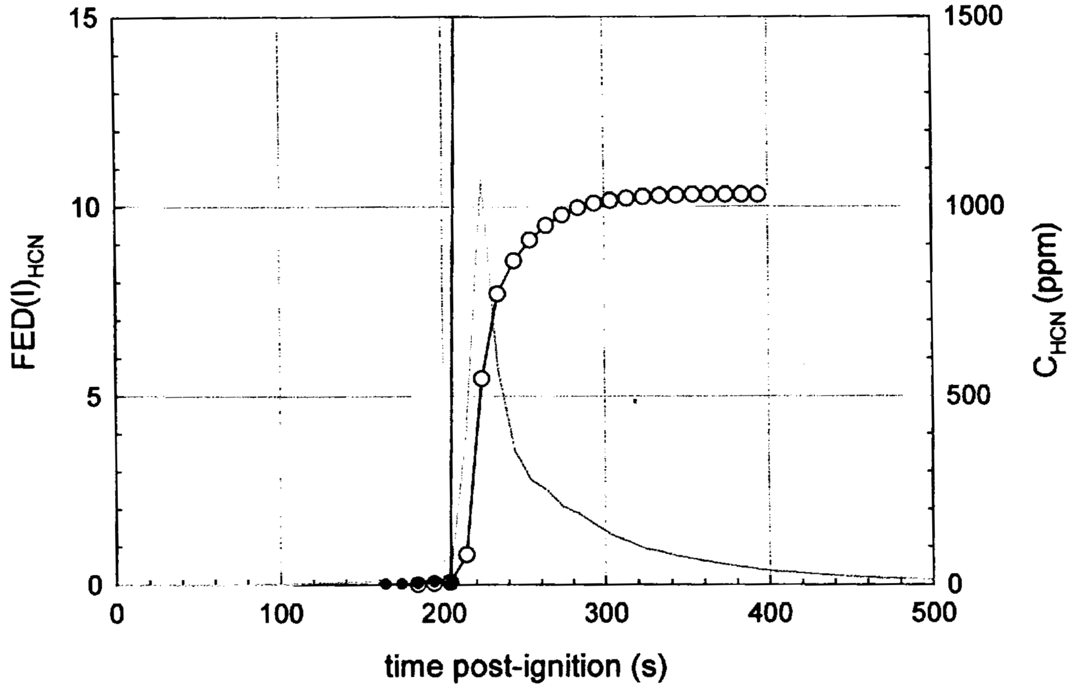

Figure 64. Fire Test F980609. Plots of FED(I)$_{HCN}$ versus time post-ignition: FAA Combined Hazard Survival Model (–O–); and Purser's model (–●–). A plot of C_{HCN} (——) is included for reference.

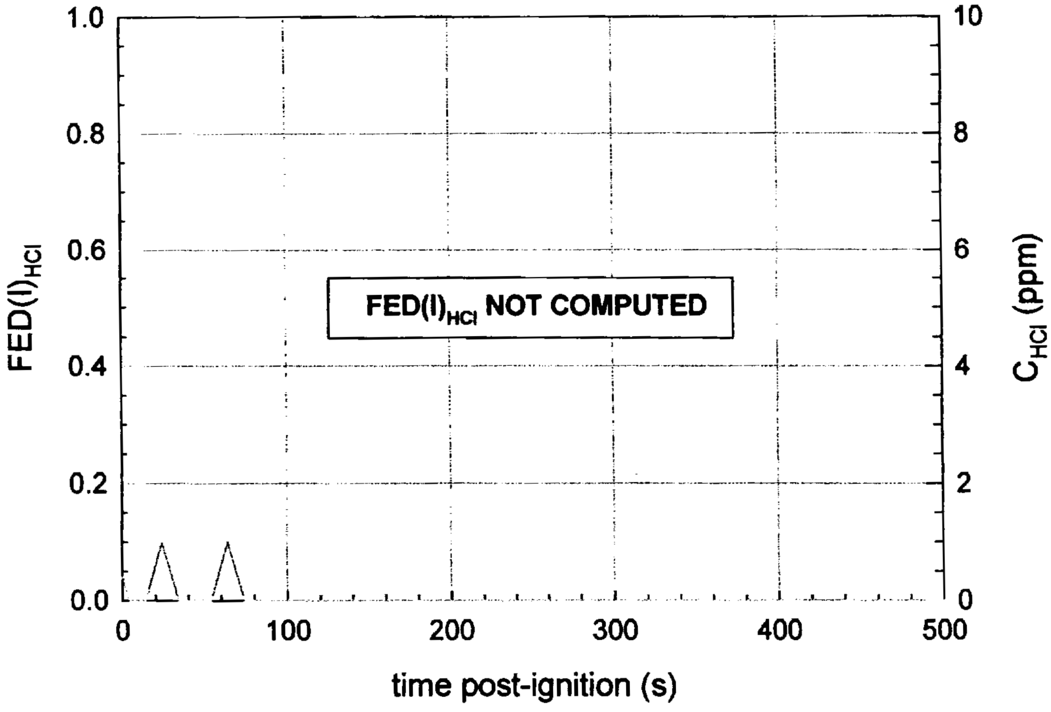

Figure 65. Fire Test F980609. Plots of FED(I)$_{HCL}$ versus time post-ignition: FAA Combined Hazard Survival Model (–O–); and Purser's model (–●–). A plot of C_{HCL} (——) is included for reference.

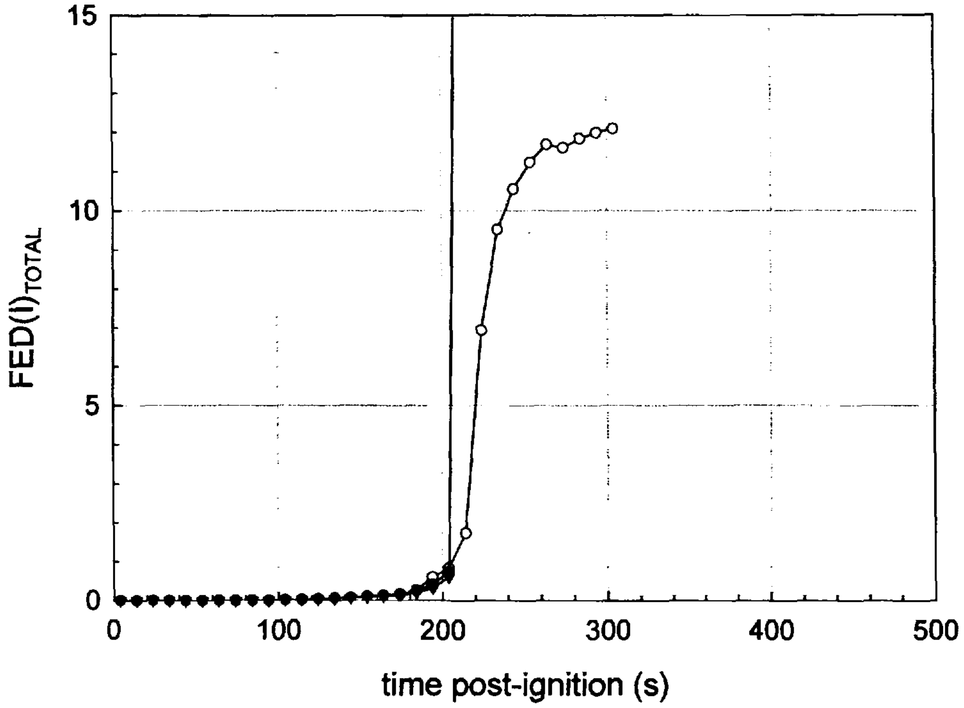

Figure 66. Fire Test F980609. Plots of FED(I)$_{TOTAL}$ versus time post-ignition: FAA Combined Hazard Survival Model (–○–); Purser's model with RMV = 8.5 L/min (–▼–); and Purser's model with RMV = 25 L/min (–●–).

Figure 67 shows plots of FED(L)$_{CO}$, FED(L)$_{HCN}$, and FED(L)$_{TOTAL}$ computed using the FAA Combined Survival Hazard Model. These calculations yielded FED(L)$_{CO}$ < 1 at all times during this test, FED(L)$_{HCN}$ > 1 and FED(L)$_{TOTAL}$ > 1 starting at about 220 seconds post-ignition.

As stated previously, the estimates of FED(I) and FED(L) obtained using the FAA Combined Hazard Survival Model and Purser's model of combustion gas toxicity can not predict precisely when the gas concentrations measured in this test would have resulted in incapacitating narcosis or death. This is especially true for prediction of lethality, where the mathematical relationships in these models were derived from experiments using laboratory animals or accidental, uncontrolled human exposures [8, 9]. Variation in susceptibility to these hazards among the human population also will contribute to the uncertainty in these predictions. In addition, the effect of trauma caused by the crash on an occupant's tolerance to these toxic gases is impossible to quantify.

Another variable that may affect an occupant's susceptibility to the combustion products is the location of the head. The data from the aspirated thermocouples indicated that a steep air-temperature gradient developed in the front of the passenger compartment during this test.

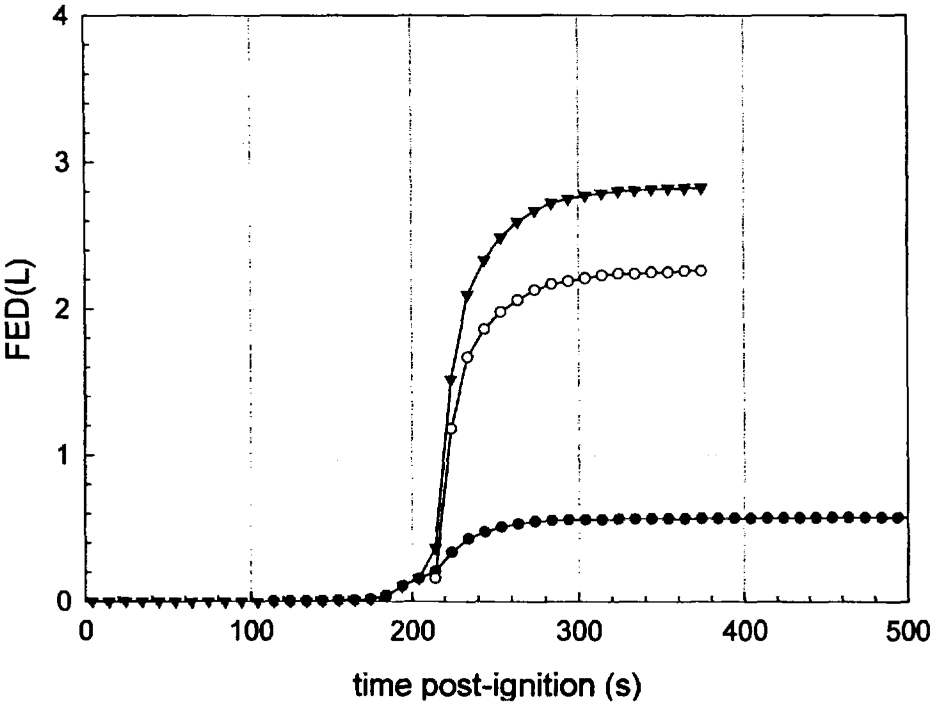

Figure 67. Fire Test F980609. Plots of FED(L)$_{CO}$ (—●—), FED(L)$_{HCN}$ (—○—), and FED(L)$_{TOTAL}$ (—▼—) versus time post-ignition computed using the FAA Combined Hazard Survival Model Fire.

Since both heat and mass are conserved in a fire, the existence of a steep vertical air-temperature gradient implies the existence of a similarly steep vertical concentration gradient for combustion products accumulating in the passenger compartment. The inlet to the gas sampling tube in the passenger compartment was in the breathing zone of that of a six-foot tall adult male sitting upright in either the driver's or front passenger's seat. An occupant whose head was located below the level where gases were sampled would have been exposed to lower concentrations of combustion gases that those shown in **APPENDIX H**. And, the estimated values of FED(I) and FED(L) for this occupant would have been lower than those shown in Figures 61 through 66.

7.3 Estimation of Burn-Injury to the Respiratory Tract

Air temperature data was not obtained during this test (see **APPENDIX D**).

ACKNOWLEDGEMENTS

Dr. Thomas Ohlemiller and Thomas Cleary of the Building and Fire Research Laboratory, National Institute of Standards and Technology were responsible for video taping this fire test, and provided an initial analysis of the test data for fire propagation. Dr. Archibald Tewarson of Factory Mutual Research Corporation provided the data from the Fire Products Collector at the test facility that was collected during this test.

REFERENCES

1. Jack L. Jensen and Jeffrey Santrock. Evaluation of Motor Vehicle Fire Initiation and Propagation. Part 1: Vehicle Crash Test and Fire Propagation Test Program. Submitted to the National Highway Transportation Safety Administration pursuant to the Settlement Agreement between General Motors and the Department of Transportation. Submitted July 31, 1997.

2. Jack L. Jensen and Jeffrey Santrock. Evaluation of Motor Vehicle Fire Initiation and Propagation. Part 8: Crash Tests on a Sport-Utility-Vehicle. Submitted to the National Highway Transportation Safety Administration pursuant to the Settlement Agreement between General Motors and the Department of Transportation. February 15, 2001.

3. Federal Safety Standards. Motor Vehicle Safety Standard No. 214 Side Impact Protection - Passenger Cars, Trucks, Buses & Multipurpose Passenger Vehicles with GVWR of 10,000 Pounds or Less. 60FR57838-39 (November 22, 1995).

4. Federal Safety Standards. Motor Vehicle Safety Standard No. 301 Fuel System Integrity - Passenger Cars; MPV's, Trucks and Busses with GVWR of 10,000 Pounds or Less; and School Buses with GVWR Greater than 10,000 Pounds. 61FR19201-02 (May 1, 1996).

5. NFPA 325 - Guide to Fire Hazard Properties of Flammable Liquids, Gases, and Volatile Solids. National Fire Protection Association, Quincy, MA 02269-9101. 1994 Edition.

6. SigmaPlot® 4.0 for Windows®, SPSS Inc., 444 North Michigan Avenue, Chicago, IL 60611. Copyright © 1997 by SPSS Inc..

7. Archibald Tewarson. "Generation of Heat and Chemical Compounds in Fires" Section 3/Chapter 4, SFPE Handbook of Fire Protection Engineering, 2nd Edition, 1995, pp. 3:53-124.

8. F. S. Knox III, Dena Bonetti, and Chris Perry. User's Manual for BRNSIM/BURNSIM: A Burn Hazard Assessment Model. United States Army Aeromedical Research Laboratory Report No. 93-13. Fort Rucker, Alabama 36362-5292. February 1993.

9. L. C. Speitel. Toxicity Assessment of Combined Gases and Development of a Survival Model. DOT/FAA/AR-95-5. July 1995.

10. David A. Purser. "Toxicity Assessment of Combustion Products" Section 2/Chapter 8, SFPE Handbook of Fire Protection Engineering, 2nd Edition, 1995, pp. 2:85-146

APPENDIX A
VIDEO CAMERA SET-UP

Scientific and technical personnel from the Building and Fire Research Laboratory, National Institute of Standards and Technology were primarily responsible for obtaining a video record of this test. Ten video cameras were used in this test. Figure A1 shows the approximate locations of the video cameras relative to the test vehicle during this test.

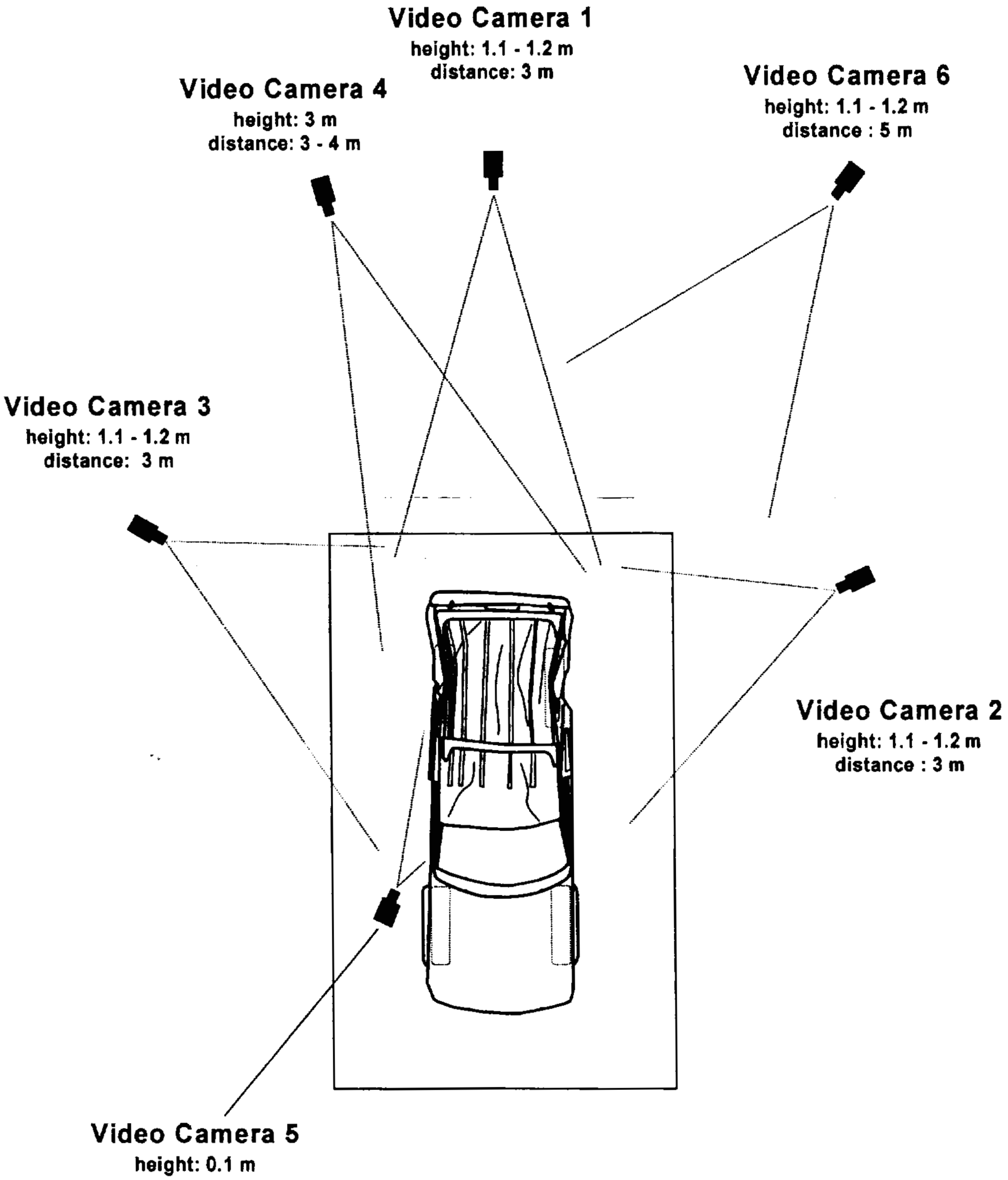

Figure A1. Fire Test F990609. Diagram showing the approximate locations of the video cameras during this test. Distances in this figure are not to scale in this diagram.

Camera 1 was a Hi-8 camcorder mounted on a tripod. It had a field-of-view that included the full height and width of the rear of the test vehicle. Camera 2 was a Hi-8 camcorder mounted on a tripod. It had a field-of-view that included the left side of the test vehicle from about the rear edge of the front fender to beyond the rear bumper. Camera 3 was a Hi-8 camcorder mounted on a tripod. It had a field-of-view that included the right side of the test vehicle from about the rear edge of the front fender to beyond the rear bumper. Camera 4 was a Hi-8 camcorder mounted on a tower fixture approximately 3m above the test vehicle. Its field-of-view included the rear of the test vehicle, with the interior cargo space visible through the broken lift glass in the rear lift gate. Camera 5 was a Hi-8 camcorder mounted on a stand approximately 10cm above the surface of the fluid containment pan. Its field of view included the area between the vehicle underbody and the test surface between the rear wheels. Camera 6 was a Hi-8 camcorder mounted on a tripod. Its field-of-view included the left side and rear of the test vehicle.

Three CCD cameras were installed in the interior of the test vehicle. Electromagnetic interference of unknown origin could not be eliminated from the video signals from these cameras before this test. This interference rendered the video from these cameras unusable, and video was not recorded from any of these cameras during this test.

All video cameras were started before the test. A microphone on each camera recorded the air horn, which signaled removal of the plug from the hole in filler neck, ignition of the gasoline, and the end of the test.

Quartz-halogen floodlights were used to illuminate the exterior of the vehicle. The level of illumination provided by these lamps was insufficient to balance the intensity of light reflecting from the vehicle surfaces with the brightness of the flames. To compensate for this imbalance, the light sensitivity adjustments on the Hi-8 camcorders were set to the manual position so that the apparent brightness of the vehicle surfaces did not change as the fire developed. As a result, the flames were overexposed, causing them to appear more opaque than they actually were.

APPENDIX B
INFRARED THERMOGRAPHY

Infrared thermal imaging radiometers were used to help determine fire propagation, flame, and surface temperatures during this test. These imaging systems measure thermal radiation within a definite waveband, over a variable field of view. The data obtained from these measurements can be analyzed to produce a two-dimensional map of apparent temperature called a thermogram.

Thermal imaging systems produce a spatially resolved map of surface temperatures from the radiant energy emitted in the field of view. The response time of these systems is nanoseconds, giving them the capability to acquire over 1 million discrete measurements per second. The capability of high-speed data acquisition is advantageous in that it can provide a tremendous amount of thermal data during a vehicle fire test, which can be over in only a few minutes. Thermal imaging radiometers can be used concurrently as a vision system and a measurement system. However, the thermal sensitivity, scan speed, and spatial resolution must be optimized for a particular application.

B.1 Infrared Camera Location

Eight thermal imaging systems were used in this test. Figure B1 shows the approximate locations of the infrared cameras relative to the test vehicle during this test. IR Camera 1 was an Inframetrics Model 760 long wavelength system (Inframetrics Inc, Billerica, MA). It was focused through the right side quarter glass opening onto the rear compartment area. IR Camera 2 was an Inframetrics Model 760 long wavelength system. It was focused through the right side quarter glass onto the rear seat backs. IR Camera 3 was an Agima Model long wavelength system. It had a field-of-view that included the area under the rear section of the test vehicle. IR Camera 4 was an Agima Model 900 long wavelength system. It was focused through liftgate glass opening and had a field-of-view that included the interior of the test vehicle. IR Camera 5 was an Inframetrics Model long wavelength system (Inframetrics Inc, Billerica, MA). It was focused through the rear liftgate glass opening onto the headlining panel. IR Camera 6 was an Agima Model 570 long wavelength system. It was mounted on a tripod and had a field-of-view that included the left rear corner of the right side of the test vehicle.

B.2 Data Analysis

Thermal imaging systems measure infrared radiation within a certain spectral band and must be calibrated to convert radiant intensity in that spectral band to temperature. Due to variations in system response, every system has to be calibrated. Calibration curves for the basic thermal imaging radiometers are measured at the factory and stored in read-only memory or in analysis software programs. Additional calibrations are needed for the optical filters. These calibrations are stored in the analysis software programs. Since thermal imaging radiometers are AC coupled devices, they measure differences in thermal radiation. To get absolute temperatures, there must be a reference to provide DC restoration. In these instruments, the reference is an internal blackbody reference source that is viewed periodically by the detector.

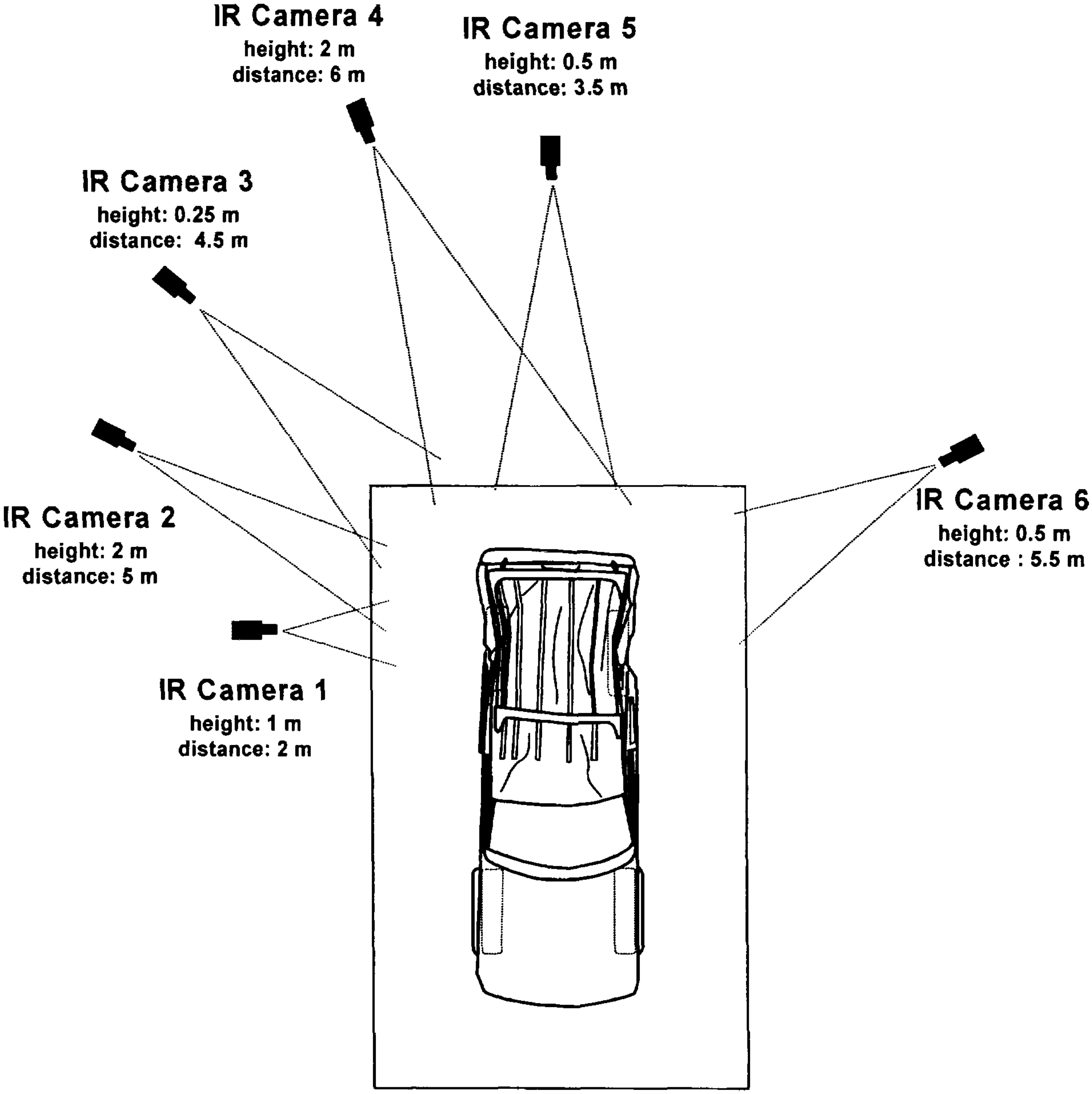

Figure B1. Fire Test F980609. Diagram showing the approximate locations of infrared cameras around the test vehicle during this test. Distances in this diagram are approximate and not drawn to scale in this diagram.

The general radiometric equation was used to convert radiant energy to temperature:

$$I = [E_t \times F(T_t)] + [(1 - E_t) \times F(T_b)] - [E_r \times F(T_r)] - [(1 - E_r) \times F(T_b)] \qquad \text{(B1)}$$

Where I is the difference in radiance between the target and a reference surface; E_t is the emittance of the target surface, generally unknown; E_r is the emittance of the reference surface, T_t is the temperature of the target surface; T_b is the temperature of background surfaces (i.e., ambient temperature), or other emitters such as flames reflected from the target; T_r is the temperature of the reference surface; $F(T_t)$ is the radiance from an ideal emitting surface (i.e., black body) at the temperature of the target surface (T_t); $F(T_r)$ is the radiance from an ideal emitting surface at the temperature of the reference (T_r); and $F(T_b)$ is the radiance from the background relative to the radiance value from the reference surface when $E_r = 1$. Factors other than temperature determine the emittance of an object. These factors include the type of material, the texture of the surface, the wavelength of the detector, and the view-angle. In determining temperatures from the radiant energy from an object, the operator can set the emittance of an unknown target surface to a value of between .01 and 1.0.

Radiant intensity measured by the thermal imaging system is converted to a gray-scale value. An 8 bit system provides gray scale values from 0 to 255 for the radiant energy at each pixel in the instantaneous field of view. A 12 bit system provides gray scale values from 0 to 4095. As the radiometer scans the image, each pixel is assigned a gray scale value, and the gray scale image is stored either in a computer memory or onto videotape. When stored in computer memory, a single frame (1 thermogram) can contain up to 68,000 pixels (discrete measurements) with an assigned 8 bit or 12 bit value. Videotape provides a temporal resolution of 30 frames per second. Depending on the thermal range of the thermal imaging radiometer, a temperature value was assigned to each pixel using either the factory calibration curves accompanying each instrument, or calibration curves stored in IR analysis software.

Separation of the apparent temperatures of various surfaces on and inside a burning vehicle from the captured data is not a trivial task. The data represent a complex combination of emitted infrared energy from those surfaces as well as reflected infrared energy from the flames, and reflected infrared energy from high intensity lights used to illuminate the vehicle for visual data capture. In addition, the flames themselves were emitting infrared radiation due to their sooty content, some part of which was captured by the infrared thermal imaging systems. Also, some of the infrared radiation being emitted by the vehicle surfaces had to pass through flames containing soot from incomplete combustion of synthetic polymers or through clear (clean) flames where more complete combustion was occurring, and/or a combination of both types of flames. In all of these cases, gases in the flame absorbed some of the infrared radiation emitted by objects behind the flame.

The following steps were taken to minimize the impact of unwanted infrared radiation being captured by the thermal imaging systems.

- Anti-reflection tapes, paint, and glazes were applied to highly reflective surfaces on the test vehicle to minimize interference from reflections of the video floor and spot lights on the test vehicle.
- The thermal imaging systems were located in the shadows of the vehicle to block the video lights from shining directly into the radiometer.
- In some cases, flame filters (3.9 μm) were used in an attempt to screen out a portion of the infrared radiation from flames.

Despite these precautions, accurate surface temperatures could not be determined for areas of the vehicle blocked by intense flame. As a result, only surface temperatures determined to be reliable by the IR analysts are reported here. In some cases, specialized data analysis techniques were used to obtain reliable surface temperatures from areas in close proximity to, but not shielded by flame. Where possible, temperature data were reported from areas that lie in the shadow of the flames, which comes from highly emissive surfaces not affected by the flame radiation, and/or is deemed reliable based on the experience of the analysts. Data from nearby thermocouples were compared to IR temperature readings for a more comprehensive analysis.

During the data analysis, the videotapes were reviewed frame-by-frame to observe the burn sequence. The analyst captured images from selected frames on a video board. The image was processed to produce a digitized gray scale value for each element in the pixel matrix utilizing the camera settings automatically documented between video frames on the videotape during data acquisition. Thermograms were produced from the digitized image matrix using a commercial software package (Thermogram Pro V1.3, sold by Inframetrics, Inc., Billerica, MA). This software utilized the NIST traceable calibration tables supplied by the manufacturer with each thermal imaging system.

APPENDIX C
THERMOCOUPLE DATA

The thermocouples used in this test were type-N thermocouples fabricated by Medtherm Corporation (Huntsville, AL). Each thermocouple consisted of an ungrounded thermocouple junction (30 AWG thermocouple wire) enclosed in an Inconel 600 sheath insulated with magnesium oxide (o.d. = 0.040 in. (1 mm), length = 50 ft. (15.2 m)). A transition was made through a stress-relief bushing to a duplex thermocouple extension cable (24 AWG) with fiberglass insulation and a stainless steel over-braid (length = 1 ft. (0.28 m)). Each thermocouple wire terminated in a grounded, compensated Type-N thermocouple plug. The thermocouples were connected to the data acquisition system using Type-N thermocouple extension cables (length = 50 ft. (15.2 m)).

The data acquisition system consisted of a PC (75 MHz Pentium Processor, 16 MB RAM, an 814 MB hard disk, and a 16-bit, Model BG45-AP5CP, ACER Inc., Taiwan R. O. C.) with a 100 kHz I/O board with 16 analog input channels (DaqBoard 200A, IOTech, Inc., Cleveland, OH). Thermocouple multiplex expansion cards (DBK-19, IOTech, Inc., Cleveland, OH) were used for data acquisition from the thermocouples. The expansion cards were mounted in an electronics cabinet and hard-wired to a panel containing compensated Type-N thermocouple jacks.

To reduce electronic noise on the thermocouples, the ground leads from each thermocouple jack was connected to the electronic chassis ground of the thermocouple mutliplex extension cards. The vehicle chassis was connected to the electronic chassis ground by a large-gauge cable. The electronic chassis ground was connected to an isolated earth ground.

The data acquisition software (DASYLab, Daten System Technik GmbH, Mönchengladbach, Germany) was configured to sample each channel at a rate of 10 Hz and store the data in 10-point block averages.

Figures C1 through C7 show the approximate locations of thermocouples in the test vehicle. Plots C1 through C105 show plots of the temperature data recorded from these thermocouples during this test.

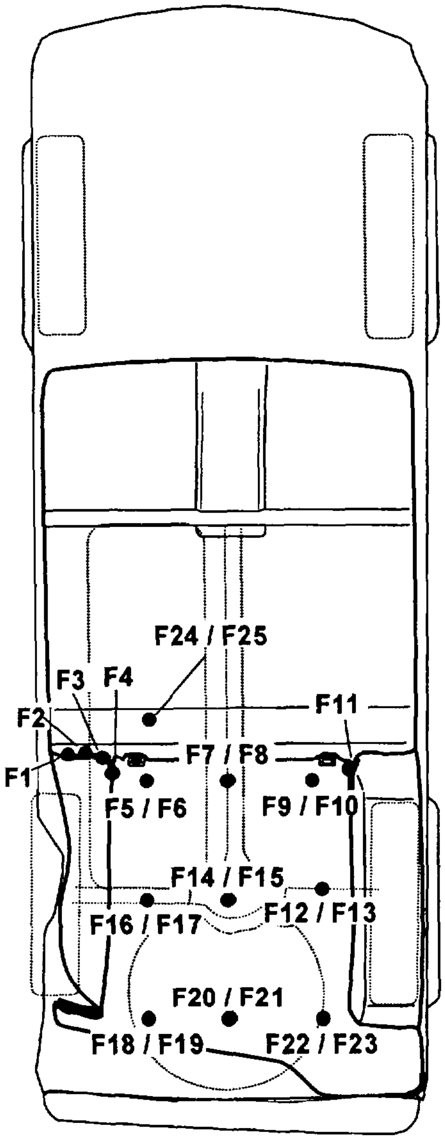

Figure C1. Fire Test F980609. Diagram showing the approximate locations of thermocouples on the floorpan of the test vehicle. Thermocouples F1 through F4 were located in a seam opening at the front of the left rear wheelhouse. Thermocouple F11 was located in a seam opening at the front of the right rear wheelhouse. Thermocouple F5, F7, F9, F12, F14, F16, F18, F20, F22, and F24 were pair was located approximately 1 cm below the lower surface of the floor pan. Thermocouples F6, F8, F10, F13, F15, F17, F19, F21, F23, and F25 were attached to the upper surface of the floor pan with thermally conducting ceramic cement.

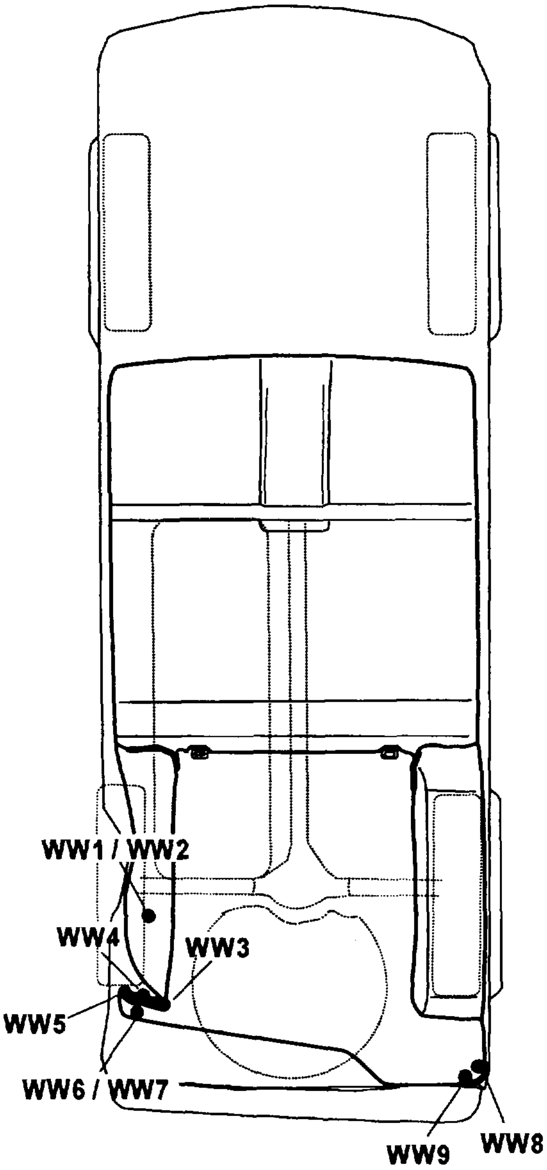

Figure C2. Fire Test F980609. Diagram showing the approximate locations of thermocouples on the left and right rear wheelhouses of the test vehicle. Thermocouples WW1 and WW6 were located approximately 1 cm below the lower surface of the left rear wheelhouse panel. Thermocouples WW2 and WW7 were attached to the upper surface of the left rear wheelhouse panel with thermally conducting ceramic cement. Thermocouples WW3, WW4, and WW5 were located in a seam opening at the rear of the left rear wheelhouse. Thermocouples WW8 and WW9 were located in a seam opening at the rear of the right rear wheelhouse.

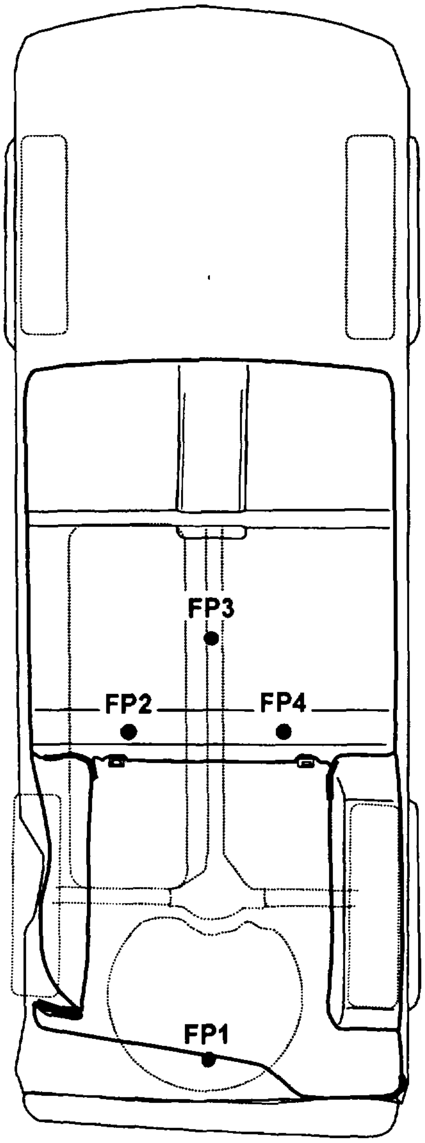

Figure C3. Fire Test F980609. Diagram showing the approximate locations of thermocouples on the floorpan drain hole plugs in the test vehicle. Thermocouples FP1, FP2, FP3, and FP4 were located on the upper surfaces of floor pan drain hole plugs.

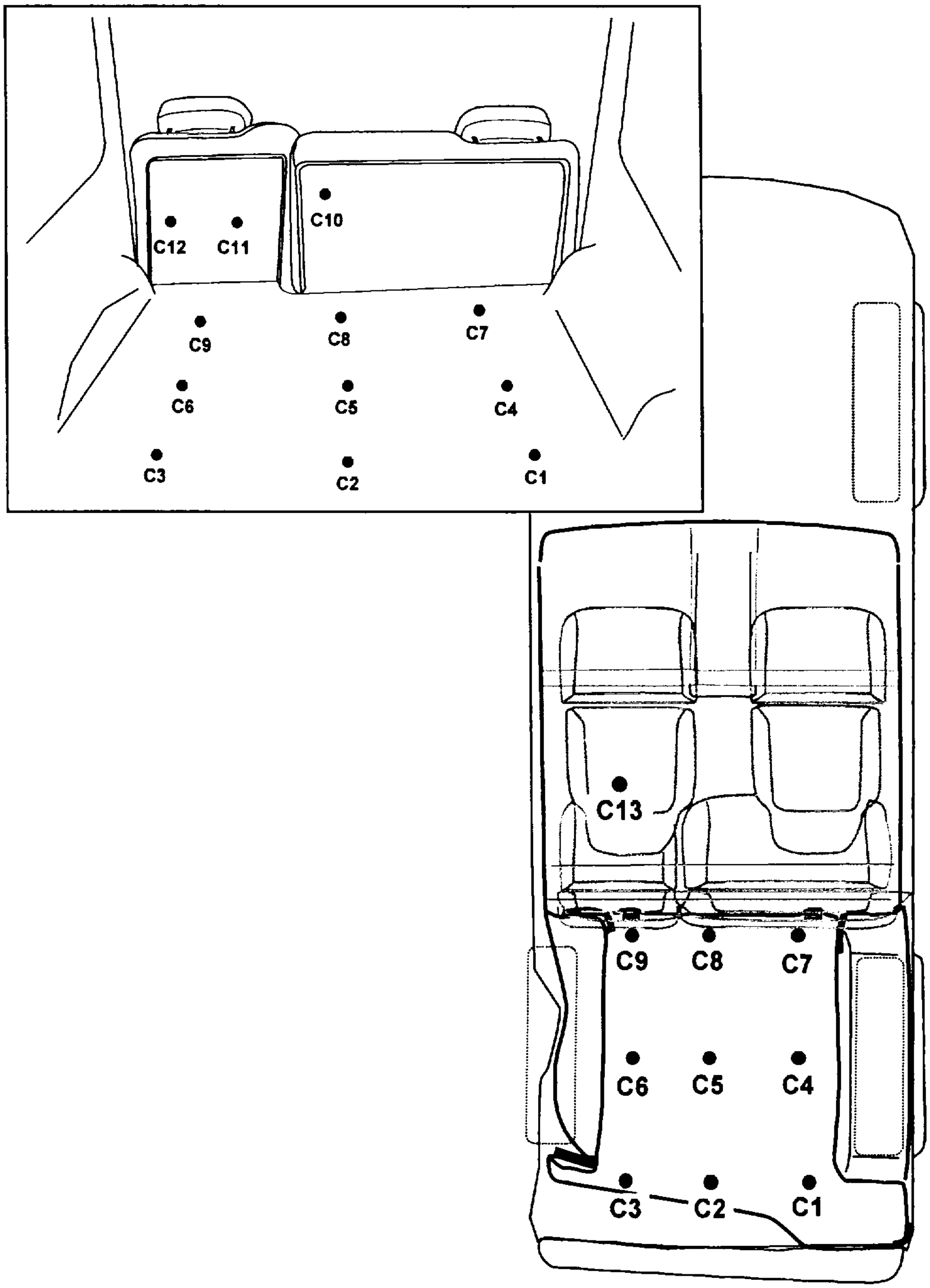

Figure C4. Fire Test F980609. Diagrams showing the approximate locations of thermocouples on the carpet in the test vehicle. Thermocouples, C1, C2, C3, C4, C5, C6, C7, C8, and C9 were located on the upper surface of the carpet in the rear compartment. Thermocouples C10, C11, and C12 were located on the carpet covering the load floor panels. Thermocouple C13 was located on the upper surface of the carpet in front of the left rear seat.

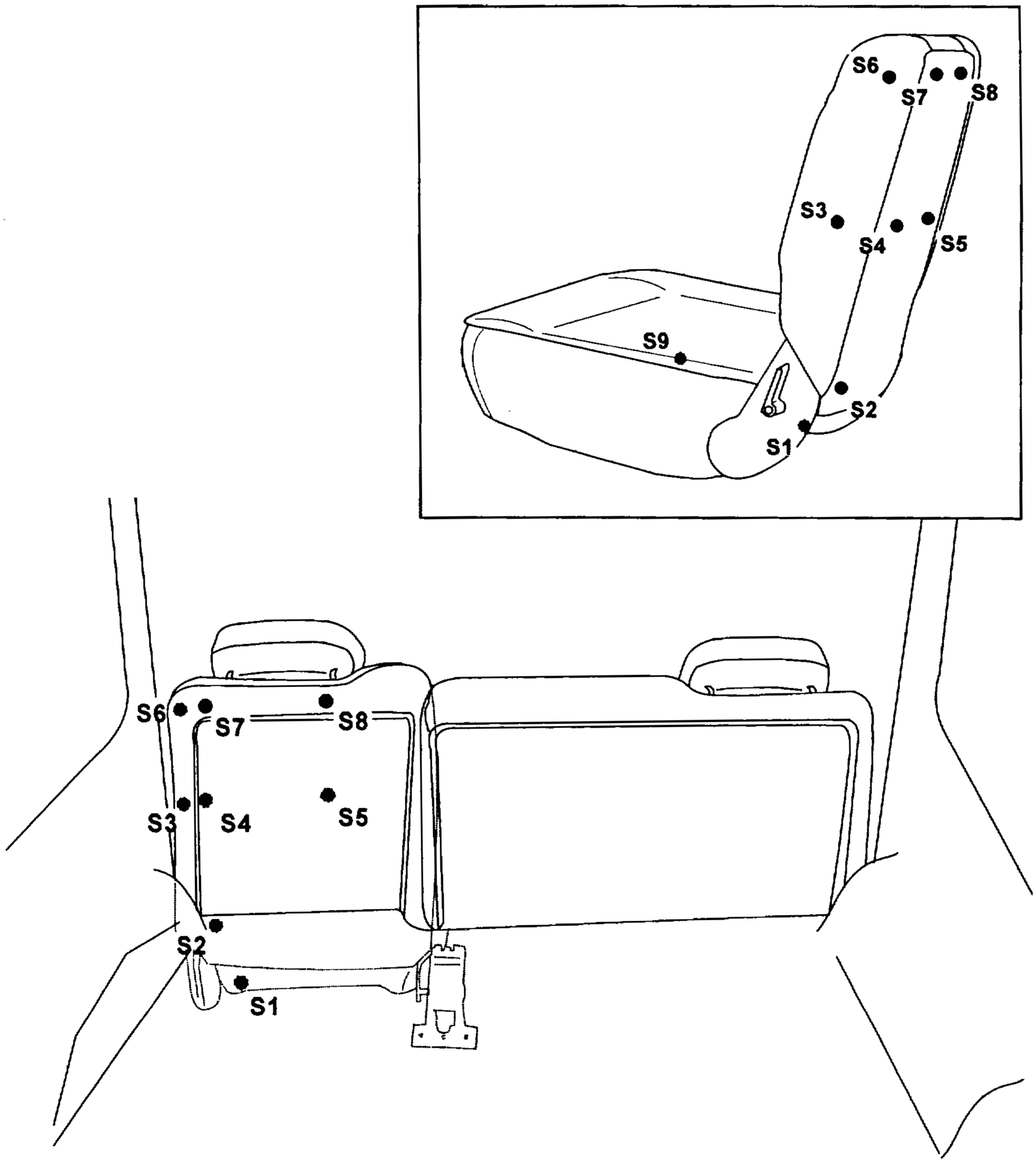

Figure C5. Fire Test F980609. Diagrams showing the approximate locations of thermocouples on the rear left seat in of the test vehicle. Thermocouple S1 was located on the outer surface of the recliner cover. Thermocouples S2 through S8 were located on exterior surface of the cover on the seat back. Thermocouple S9 was located approximately 1cm below the lower surface of the pad in the seat cushion.

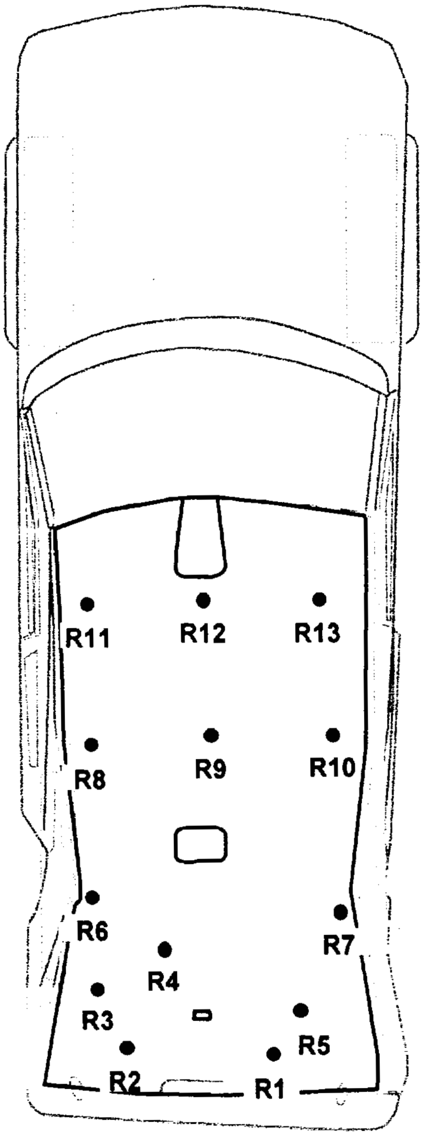

Figure C6. Fire Test F980609. Diagram showing the approximate locations of thermocouples on the roof of the test vehicle. Thermocouples R1, R2, R3, R4, R5, R6, R7, R8, R9, R10, R11, R12, and R13 were located approximately 1 cm below the lower surface of the headlining panel.

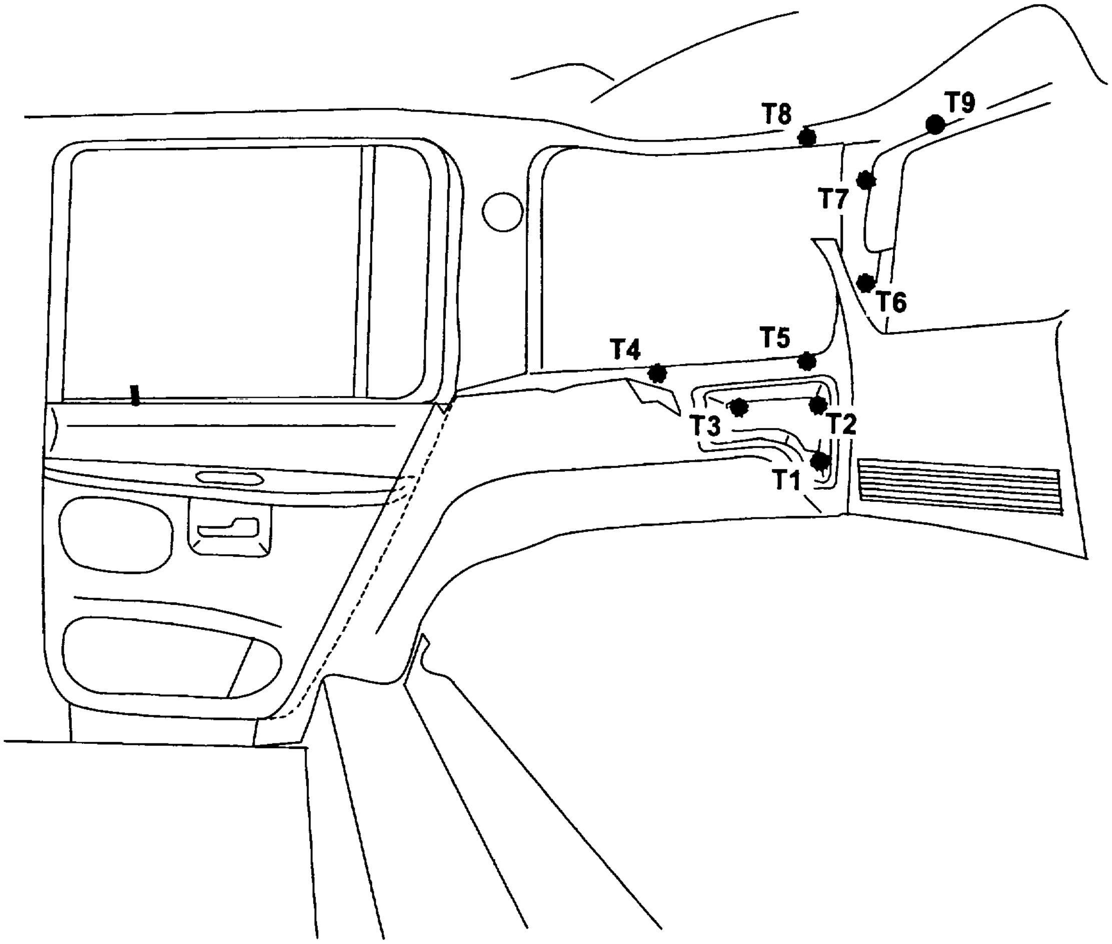

Figure C7. Fire Test F980609. Diagram showing the approximate locations of thermocouples on the right quarter trim panel and rear garnish moldings in the test vehicle. Thermocouples T1, T2, T3, T4, T5, T6, T7, and T8 were located on the unexposed surface of the trim panel. Thermocouple T9 was located on the exposed surface of the rear garnish moldings.

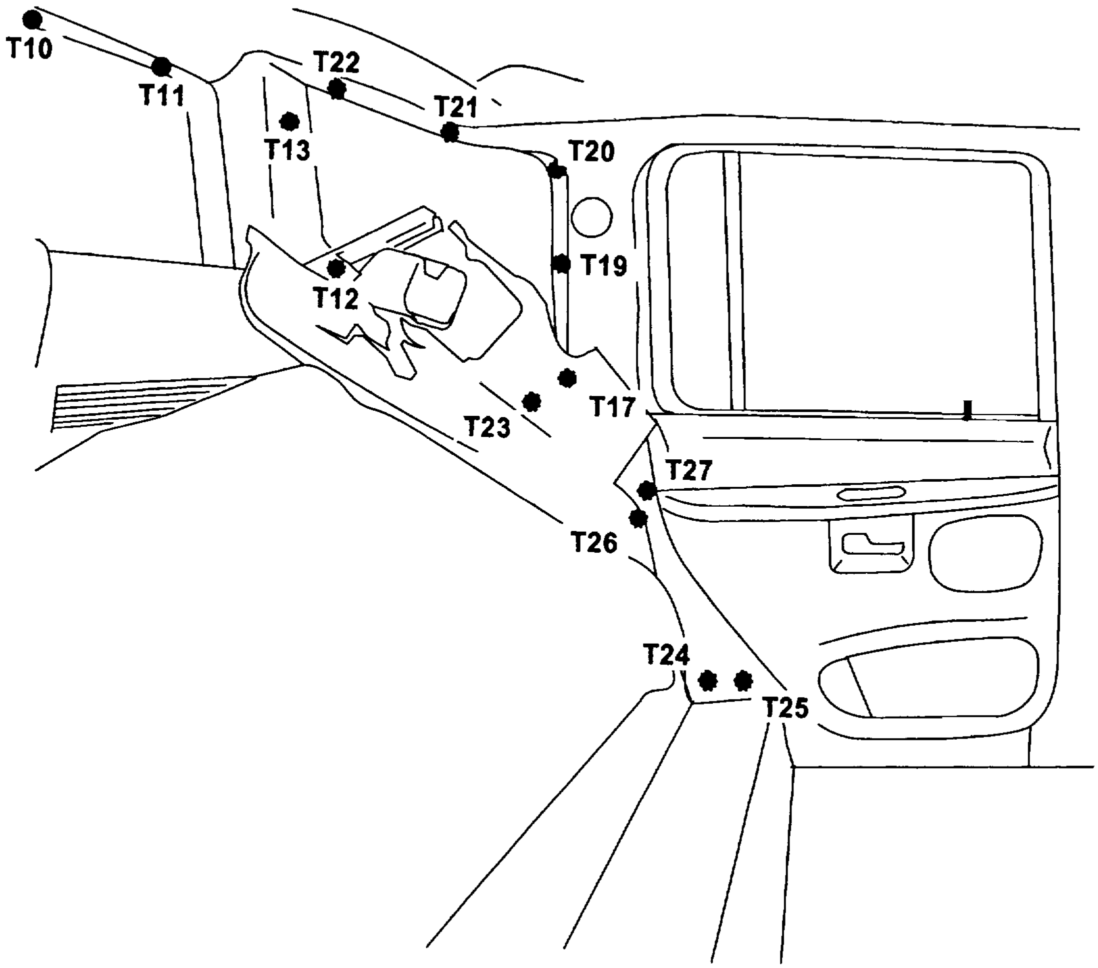

Figure C8. Fire Test F980609. Diagram showing the approximate locations of thermocouples on a section of the left quarter trim and rear garnish moldings panel in the test vehicle. Thermocouples T10 and T11 were located on the exposed surface of the rear garnish moldings. Thermocouples T12, T13, TT17, T19, T20, T21, T22, T23, T24, T25, and T26 were located on the unexposed surface of the left quarter trim panel.

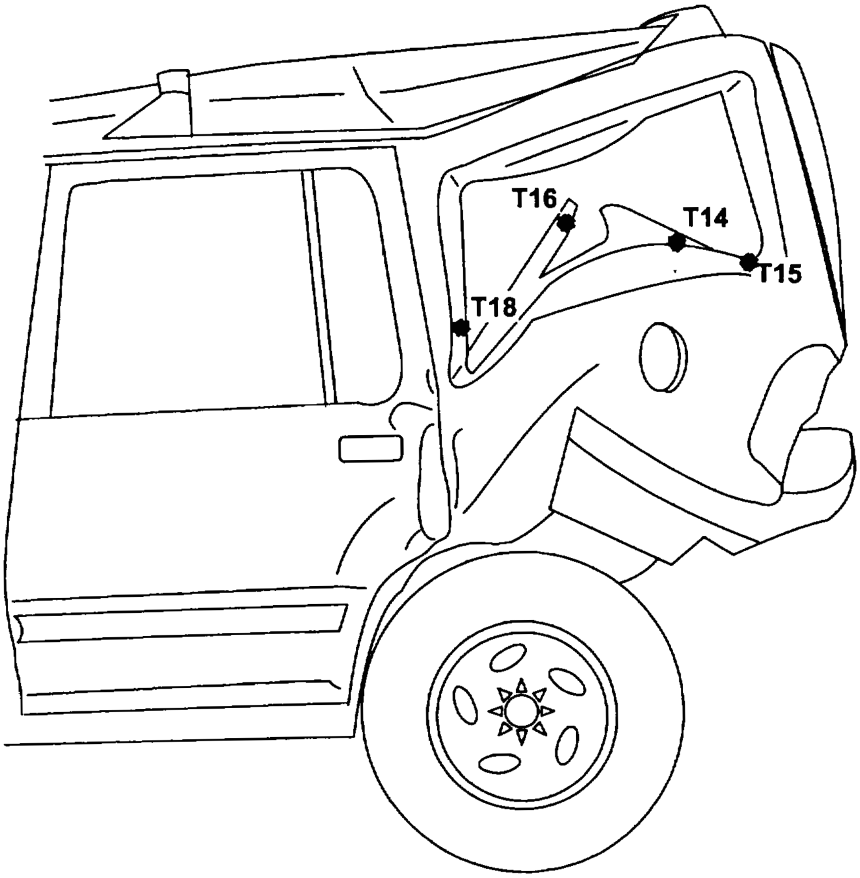

Figure C9. Fire Test F980609. Diagram showing the approximate locations of thermocouples on the left quarter trim panel in the test vehicle. Thermocouples T14, T15, T16, and T18.were located on the unexposed surface of the left quarter trim panel.

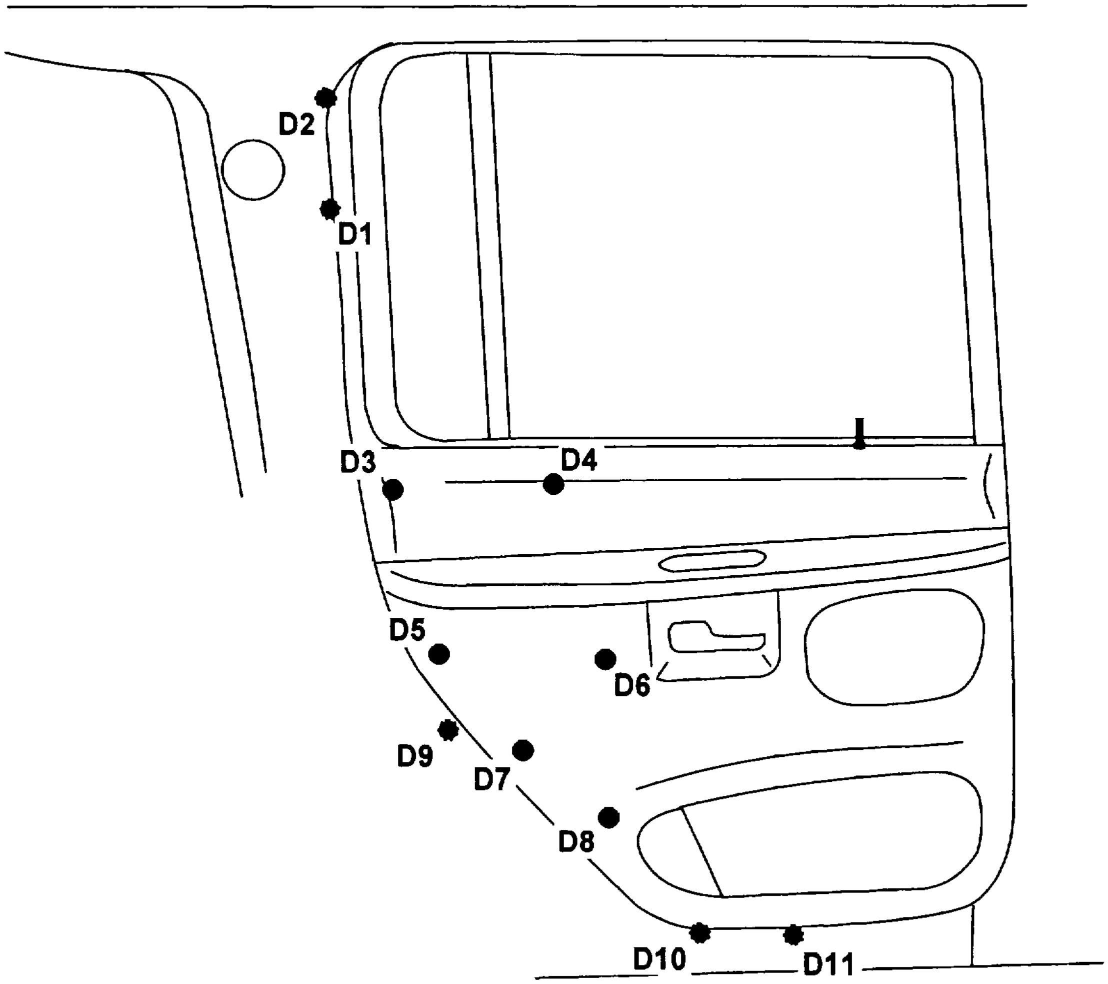

Figure C10. Fire Test F980609. Diagram showing the approximate locations of thermocouples on the left rear door of the test vehicle. Thermocouples D1, D2, D9, D10, and D11 were located in a crash-induced gap along the bottom and rear edged of the left rear door. Thermocouples D3, D4, D5, D6, D7, and D8 were located on the interior surface of the interior trim panel on the left rear door.

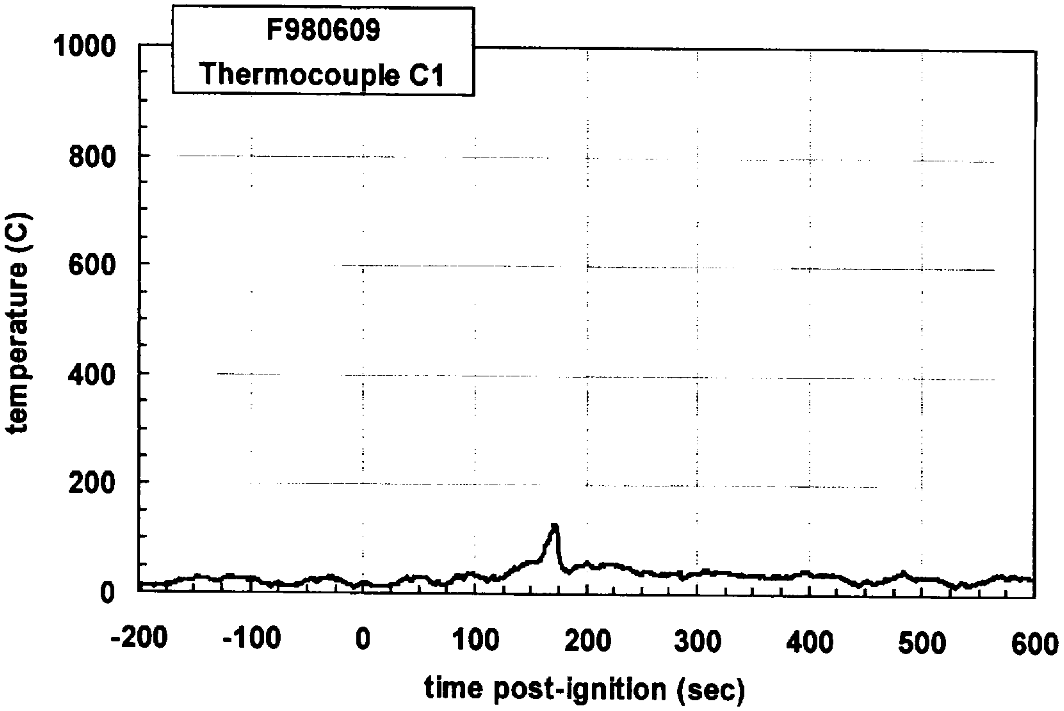

Plot C1. Fire Test F980609. Data plot from thermocouple C1.

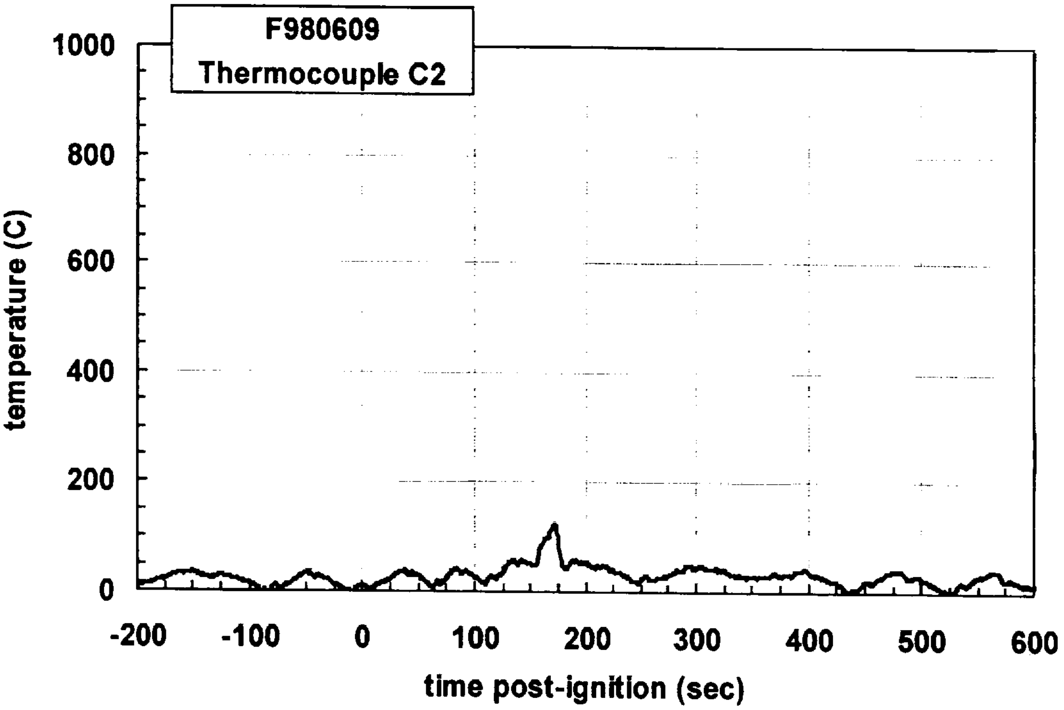

Plot C2. Fire Test F980609. Data plot from thermocouple C2.

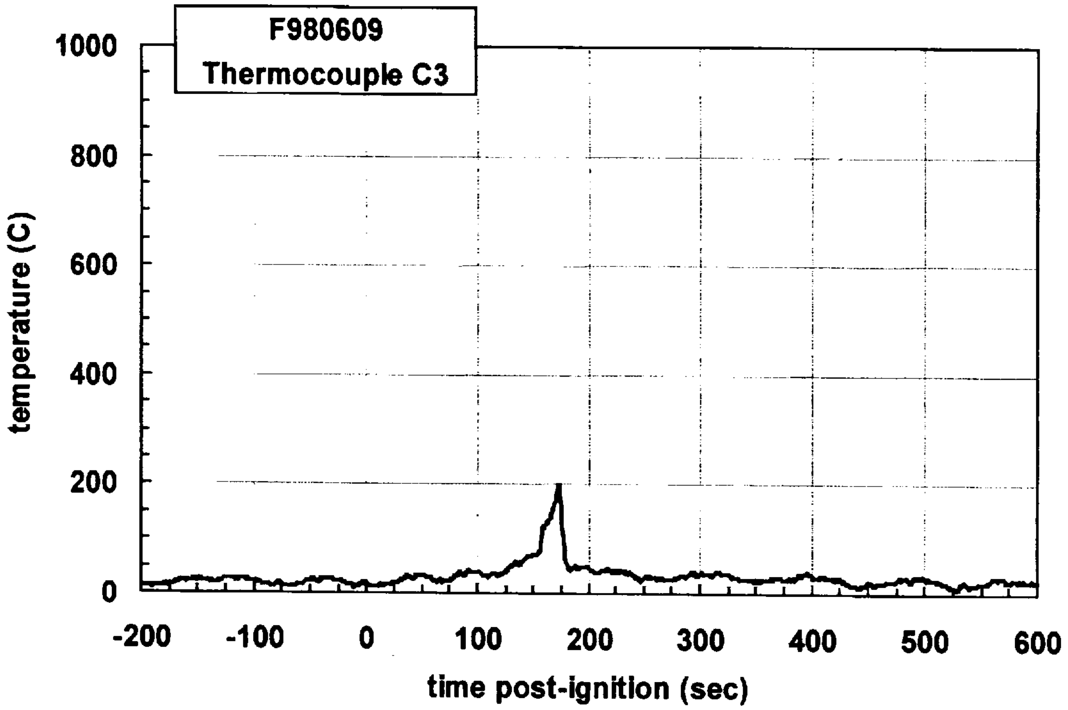

Plot C3. Fire Test F980609. Data plot from thermocouple C3.

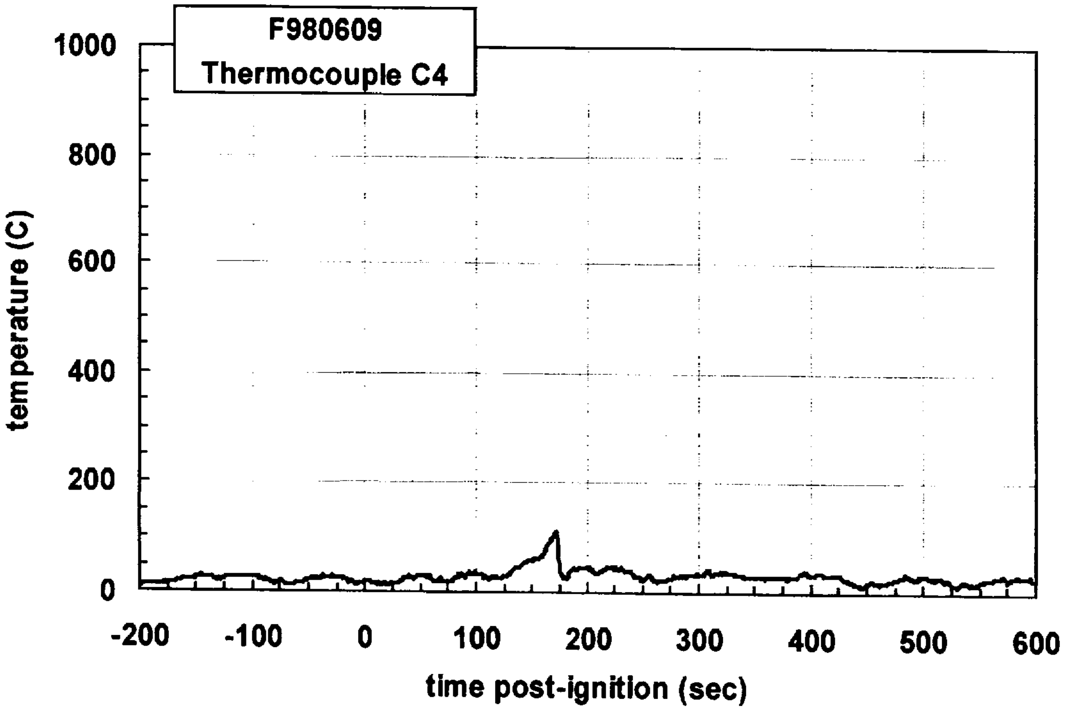

Plot C4. Fire Test F980609. Data plot from thermocouple C4.

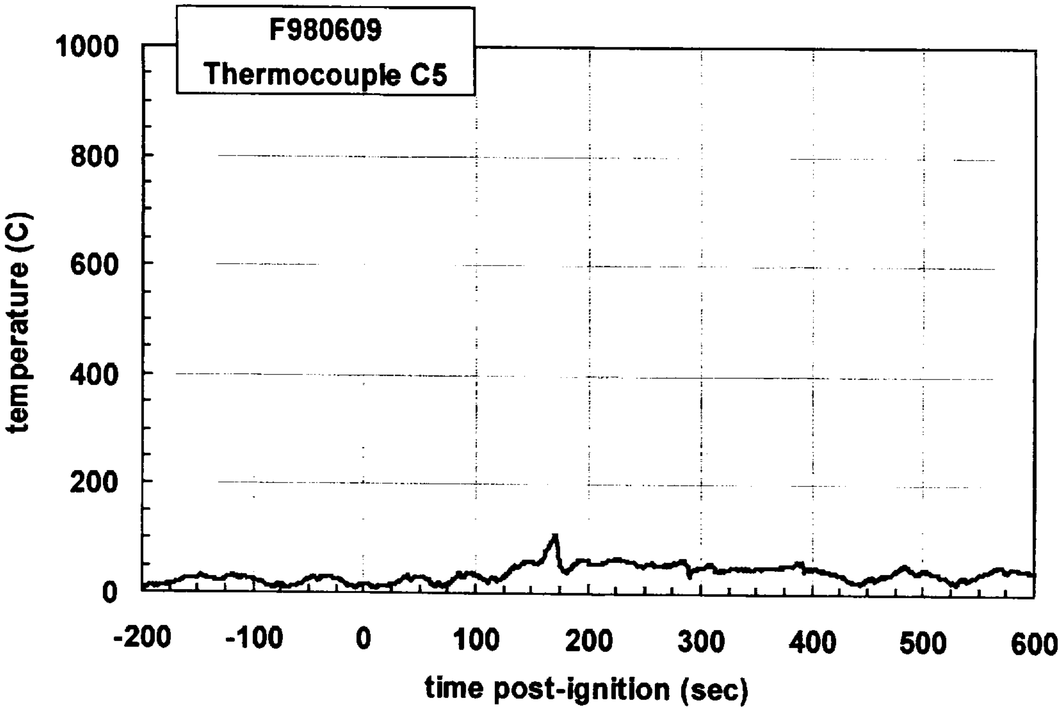

Plot C5. Fire Test F980609. Data plot from thermocouple C5.

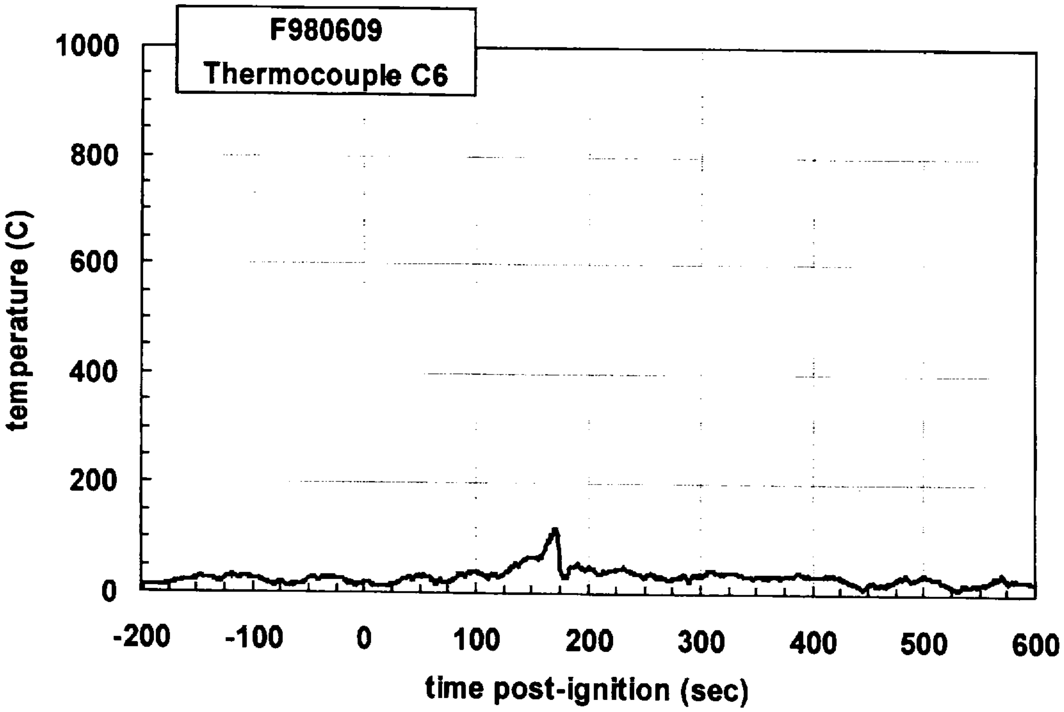

Plot C6. Fire Test F980609. Data plot from thermocouple C6.

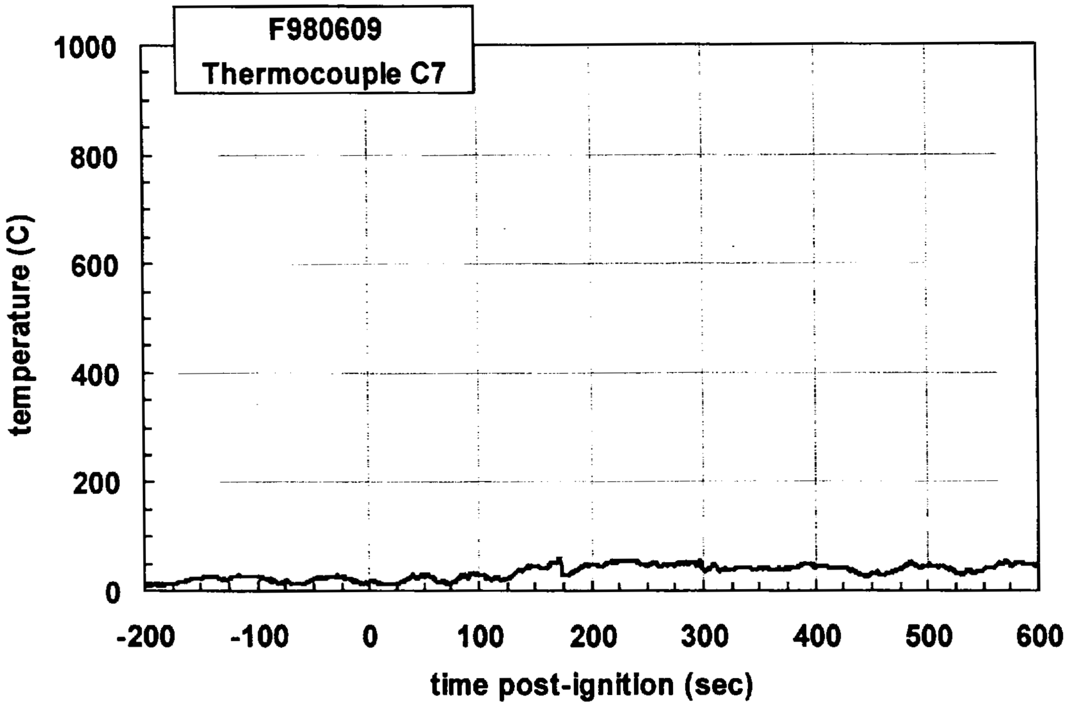

Plot C7. Fire Test F980609. Data plot from thermocouple C7.

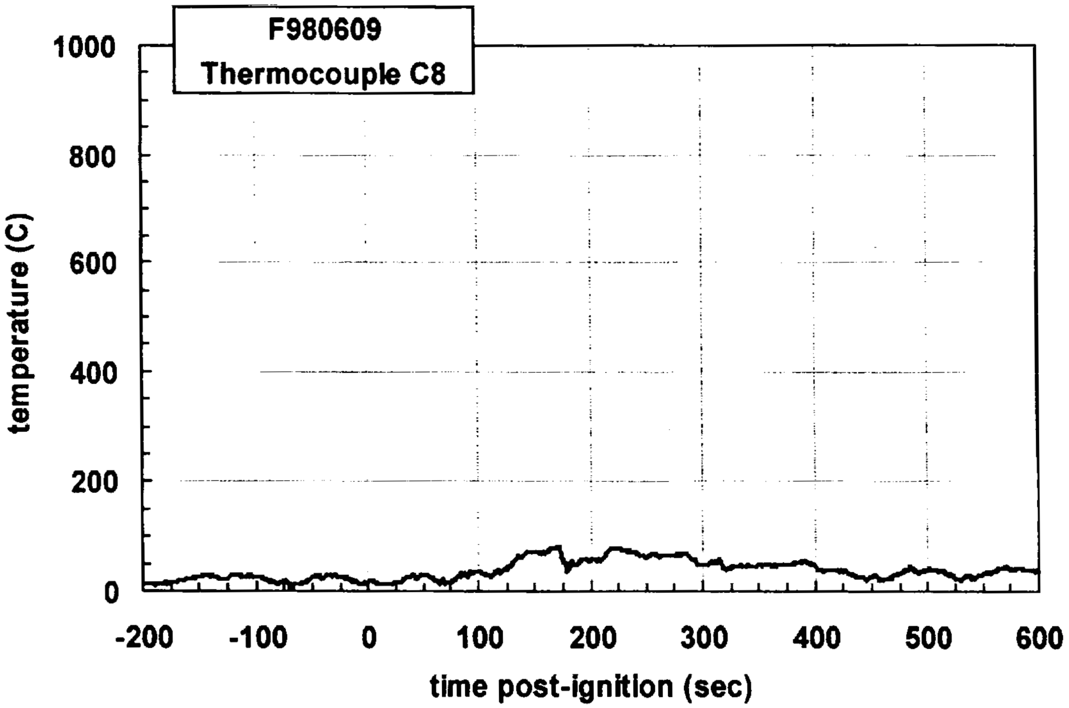

Plot C8. Fire Test F980609. Data plot from thermocouple C8.

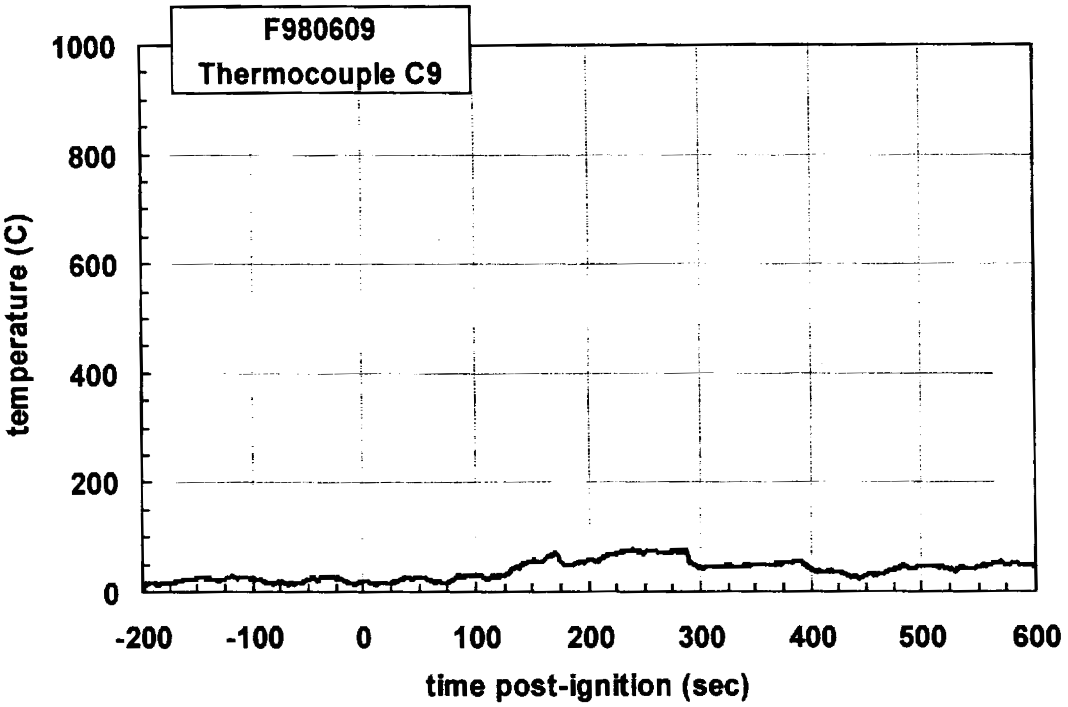

Plot C9. Fire Test F980609. Data plot from thermocouple C9.

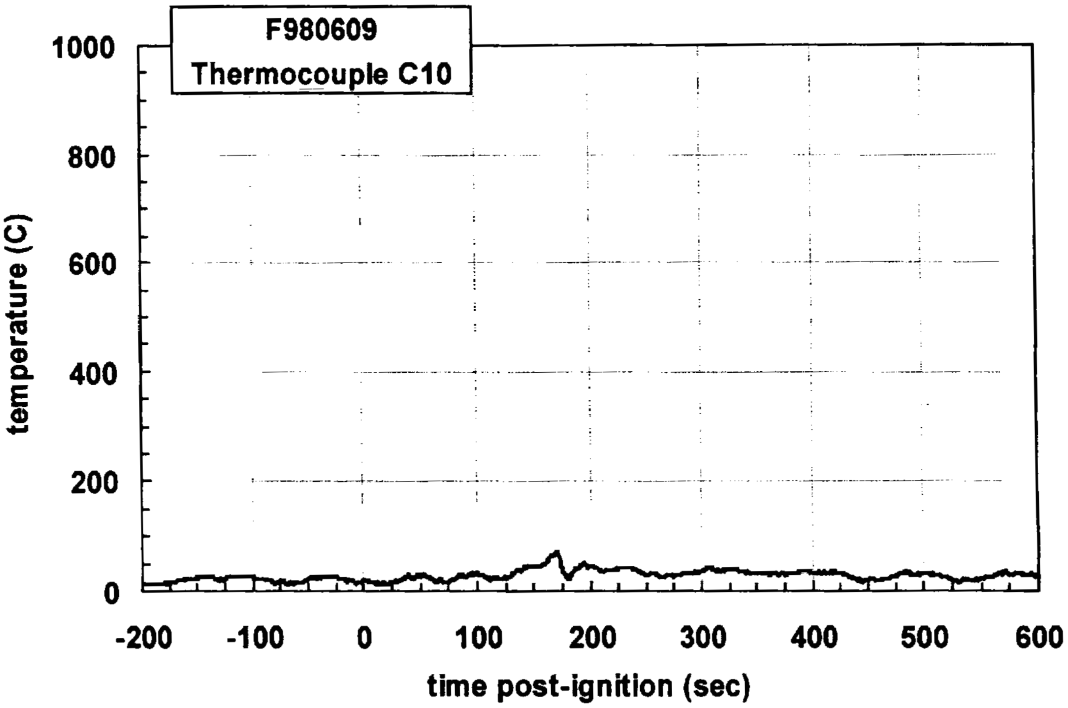

Plot C10. Fire Test F980609. Data plot from thermocouple C10.

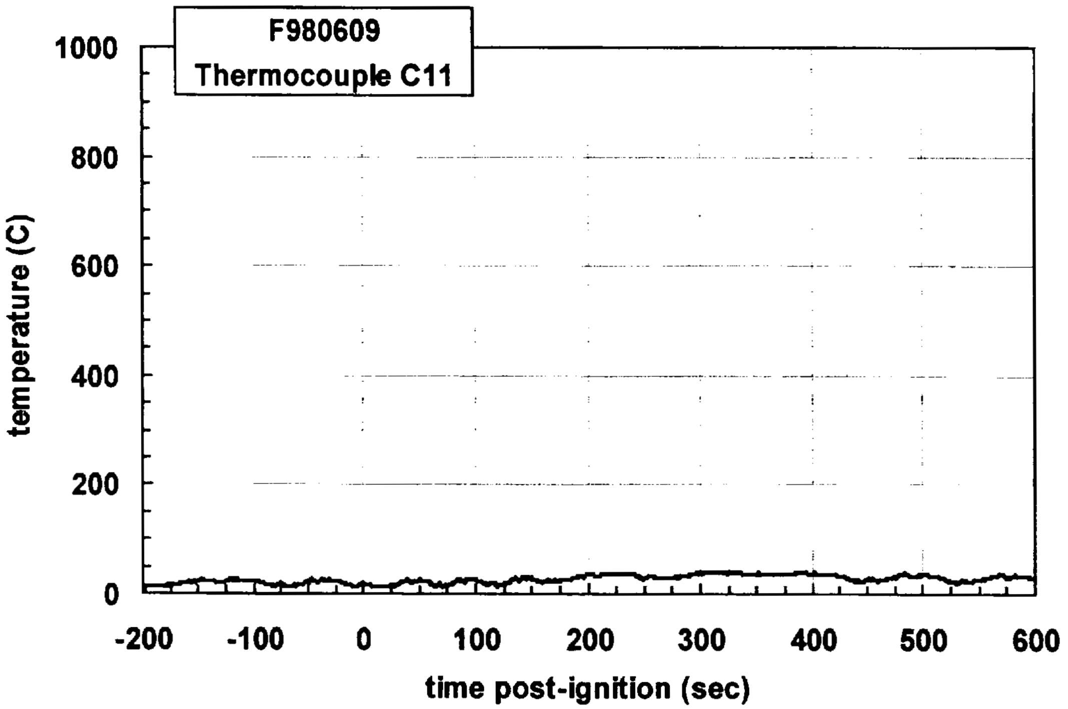

Plot C11. Fire Test F980609. Data plot from thermocouple C11.

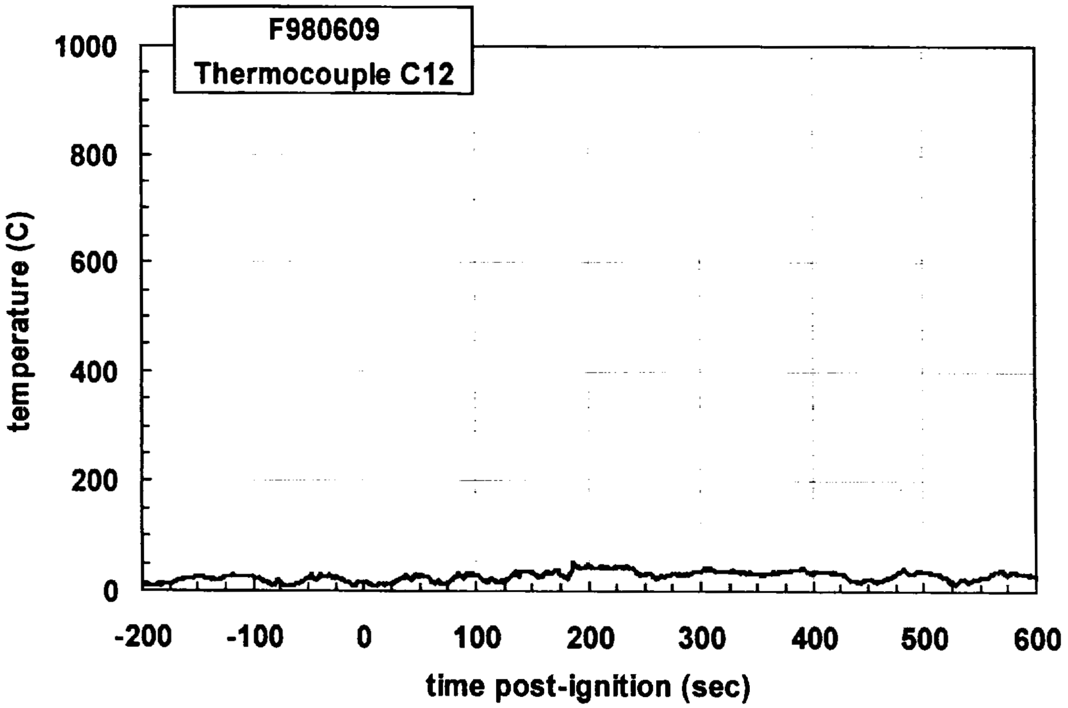

Plot C12. Fire Test F980609. Data plot from thermocouple C12.

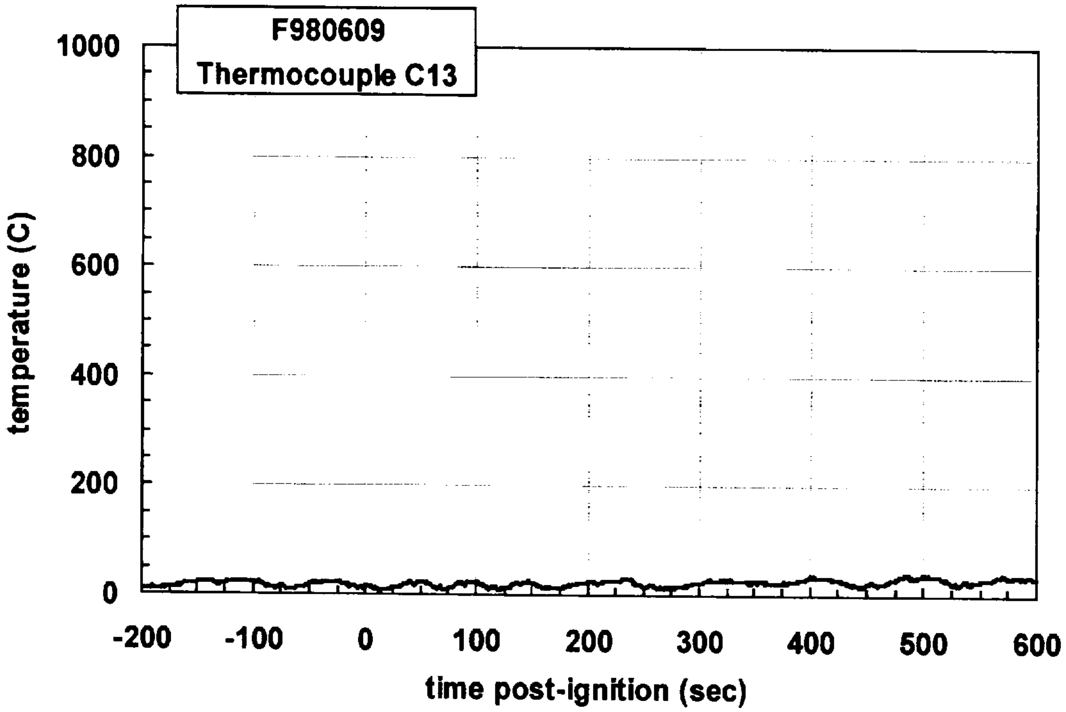

Plot C13. Fire Test F980609. Data plot from thermocouple C13.

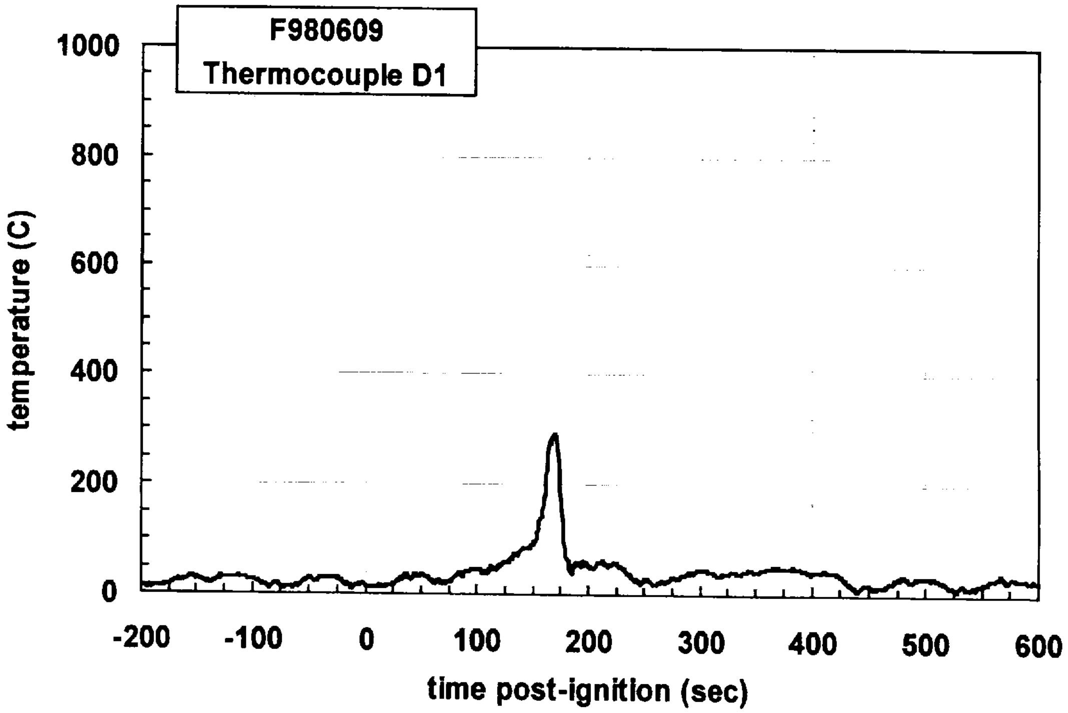

Plot C14. Fire Test F980609. Data plot from thermocouple D1.

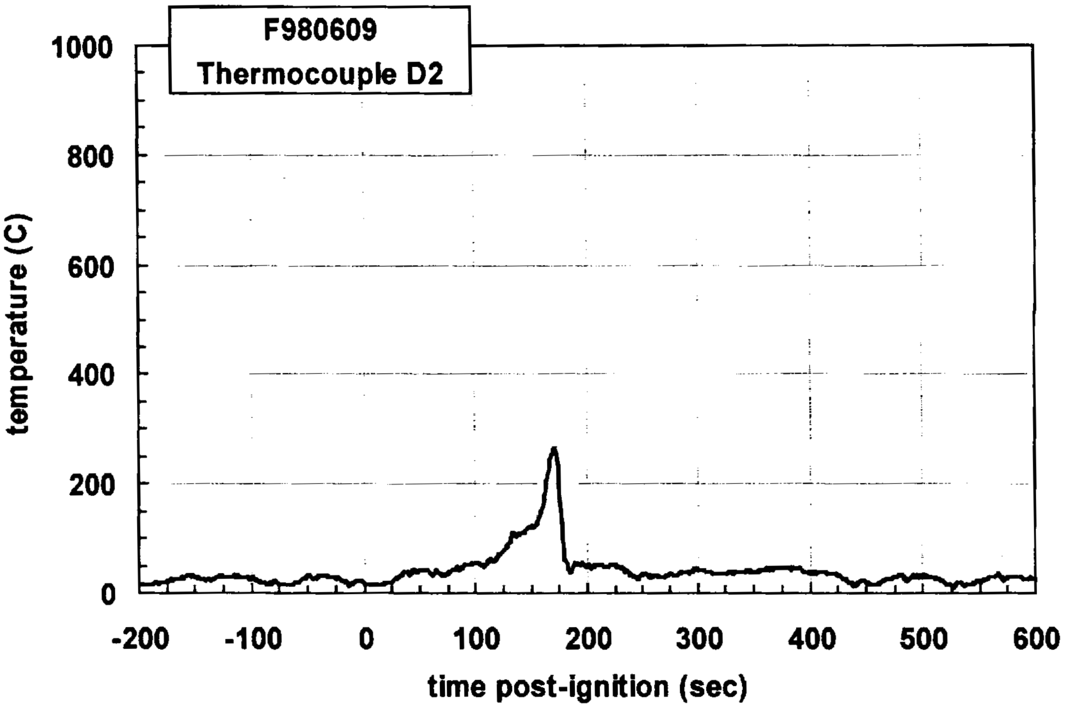

Plot C15. Fire Test F980609. Data plot from thermocouple D2.

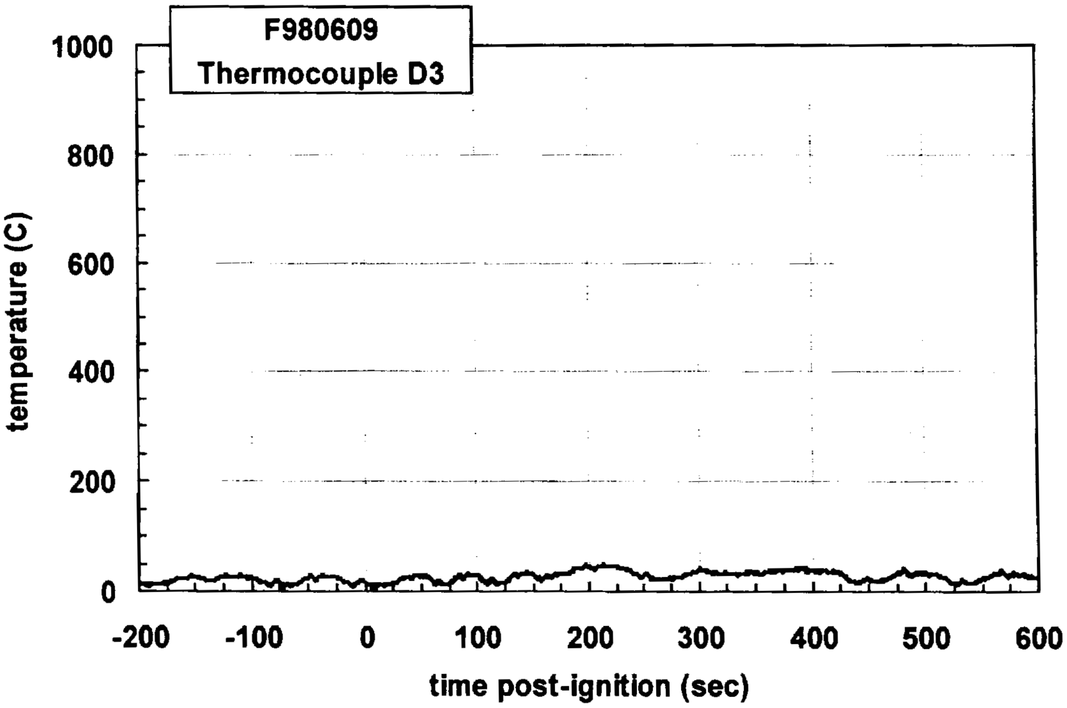

Plot C16. Fire Test F980609. Data plot from thermocouple D3.

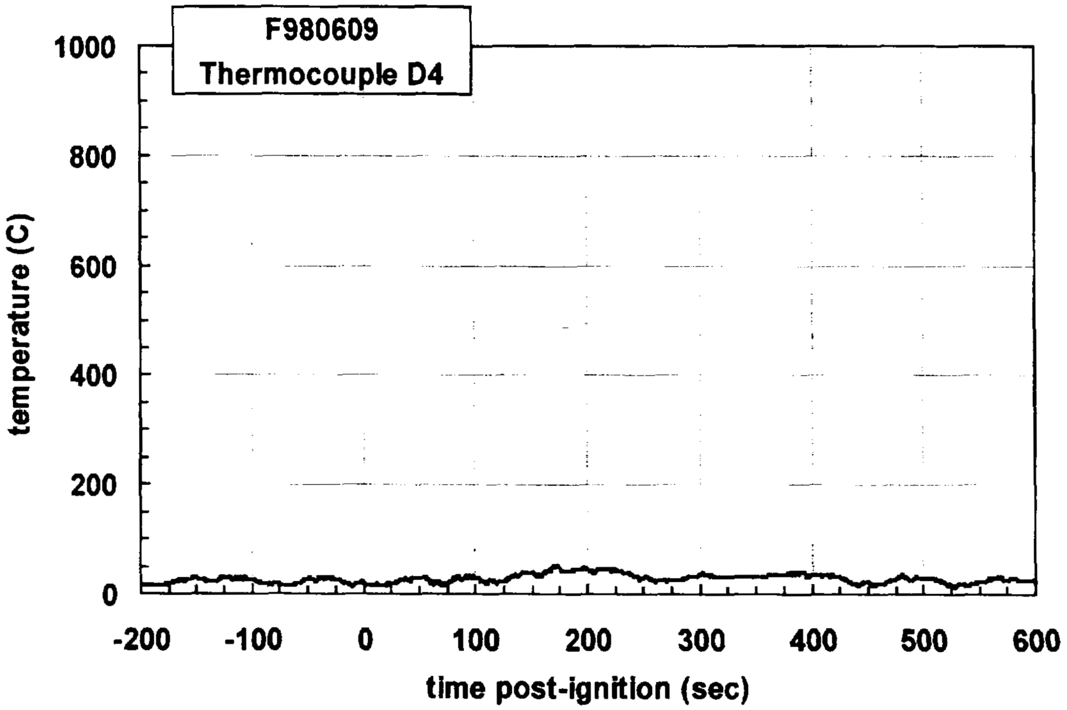

Plot C17. Fire Test F980609. Data plot from thermocouple D4.

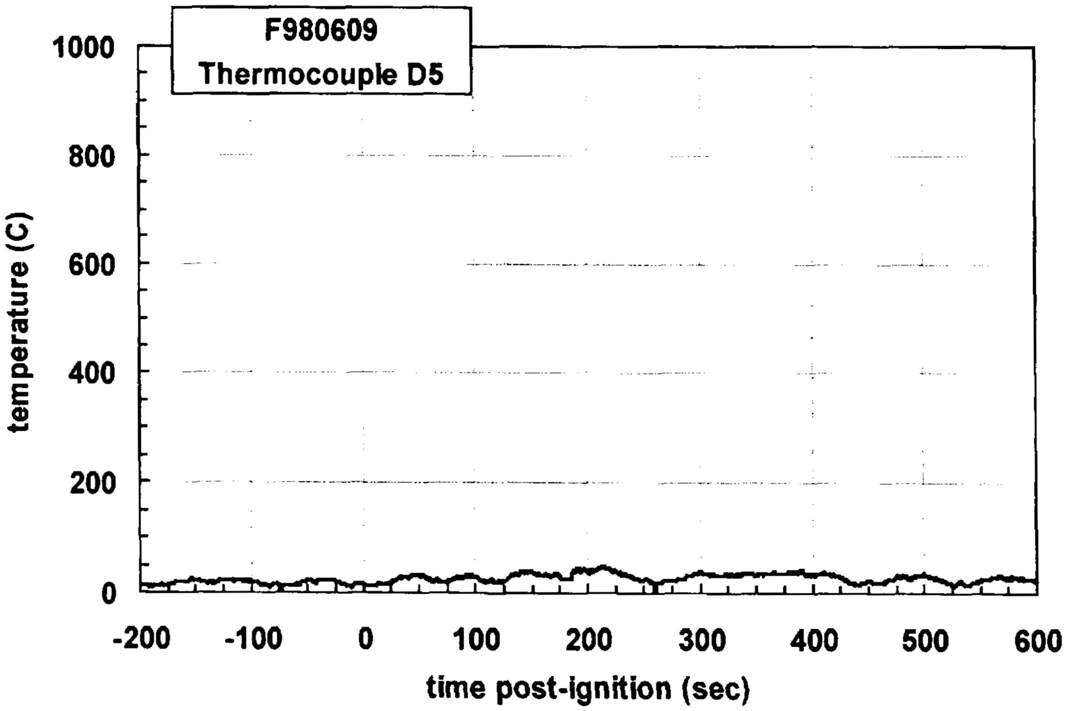

Plot C18. Fire Test F980609. Data plot from thermocouple D5.

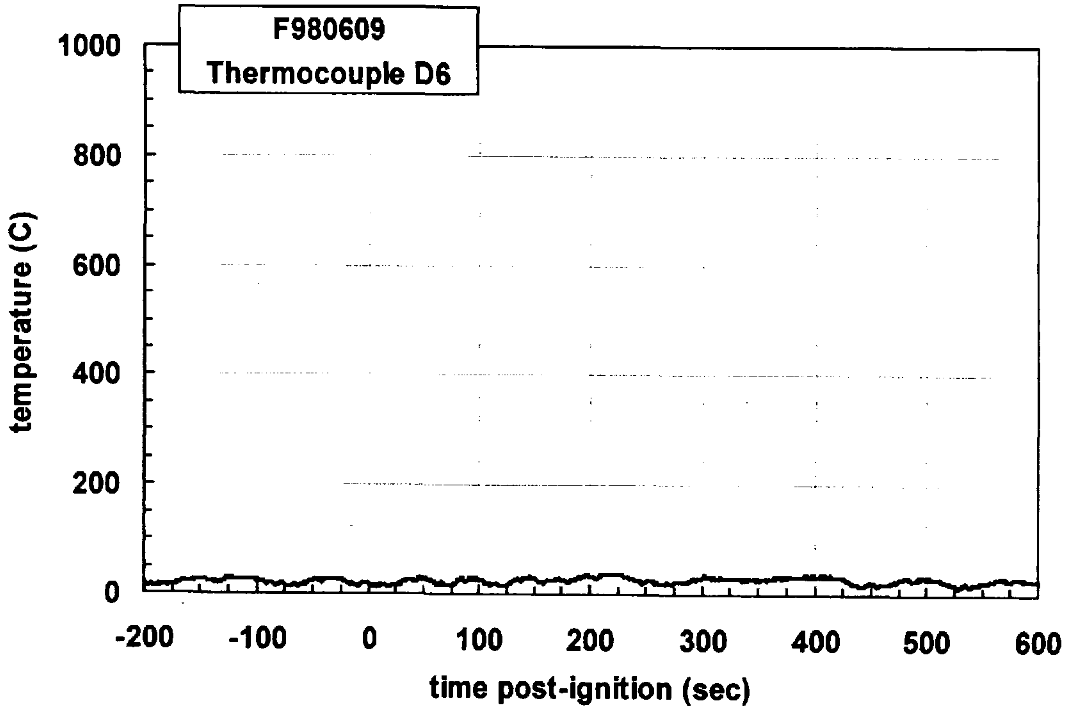

Plot C19. Fire Test F980609. Data plot from thermocouple D6.

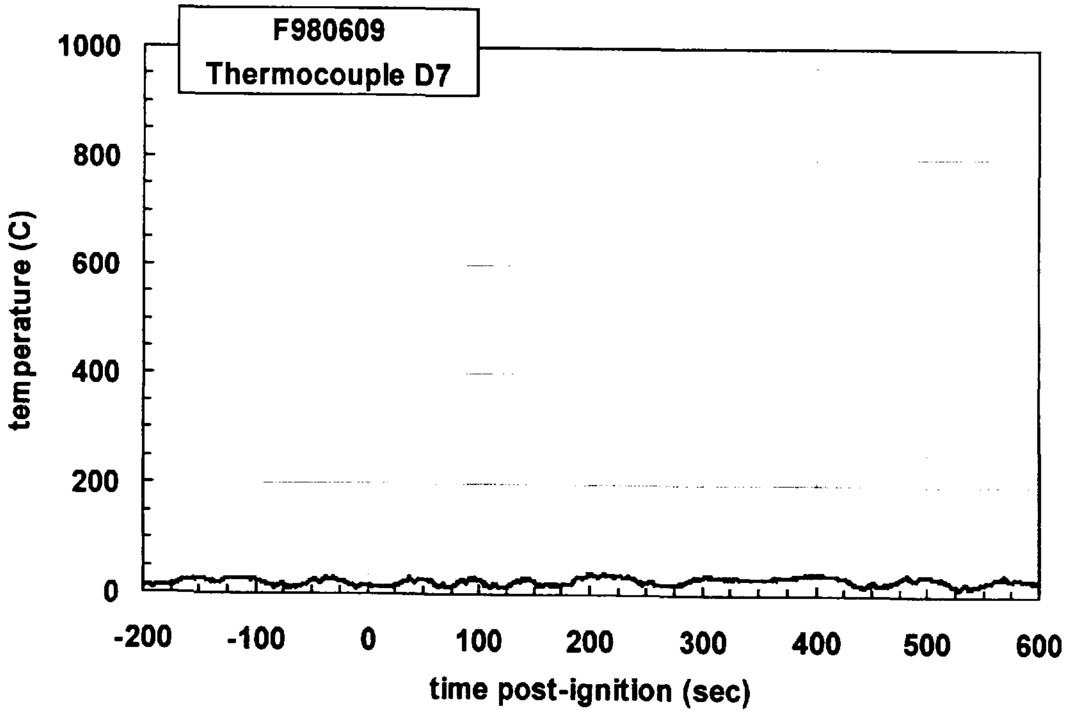

Plot C20. Fire Test F980609. Data plot from thermocouple D7.

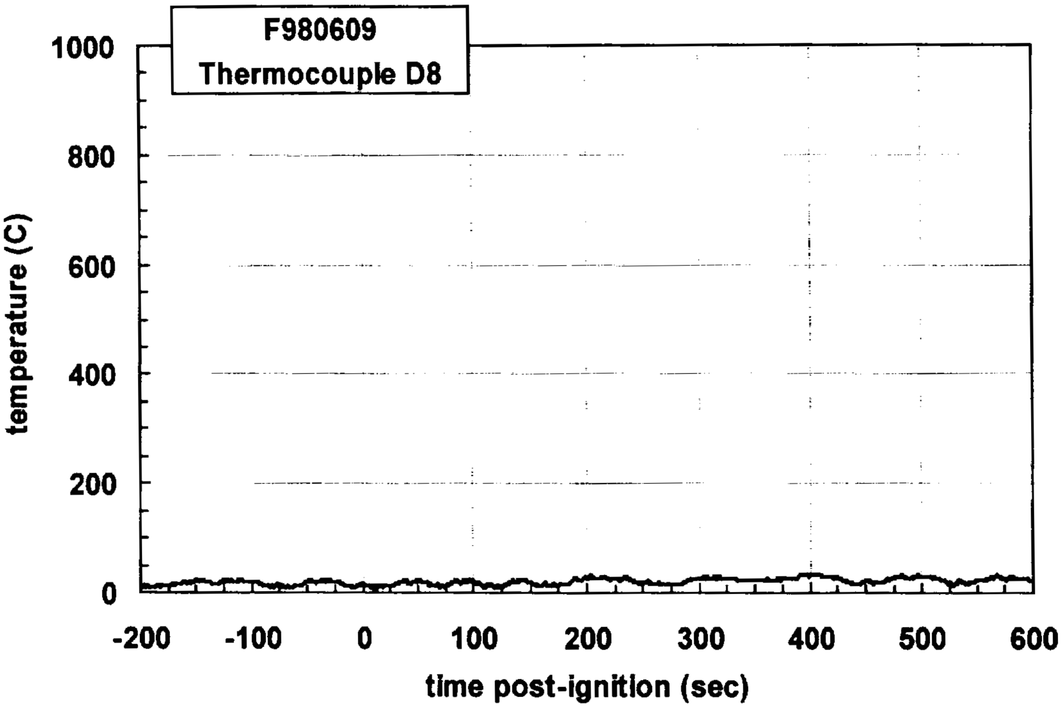

Plot C21. Fire Test F980609. Data plot from thermocouple D8.

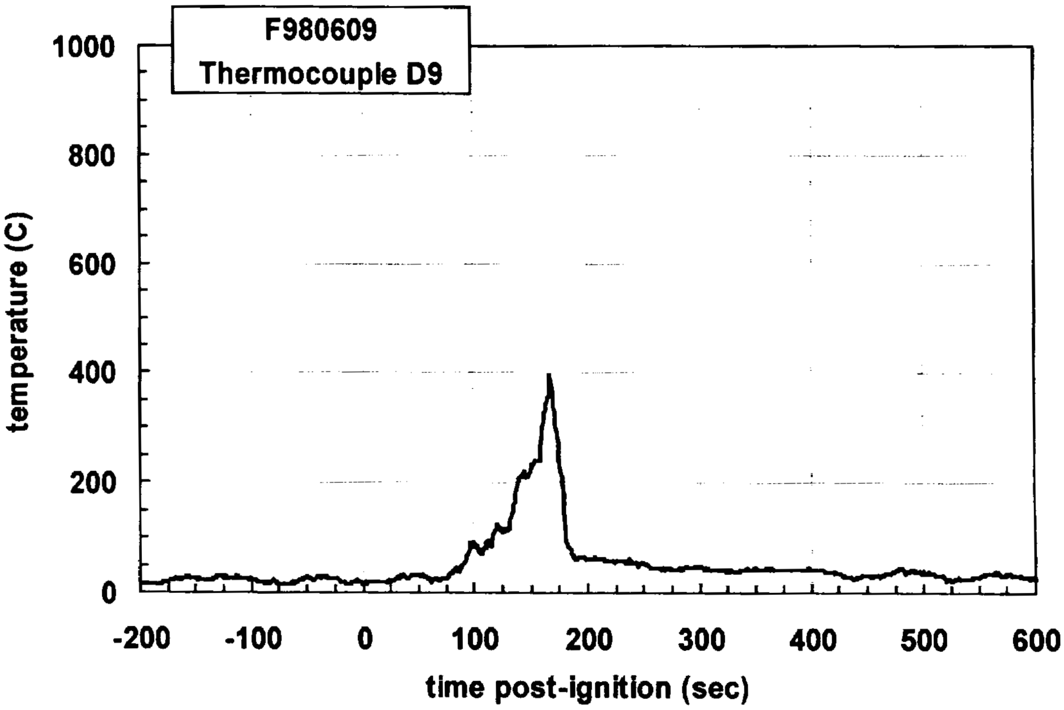

Plot C22. Fire Test F980609. Data plot from thermocouple D9.

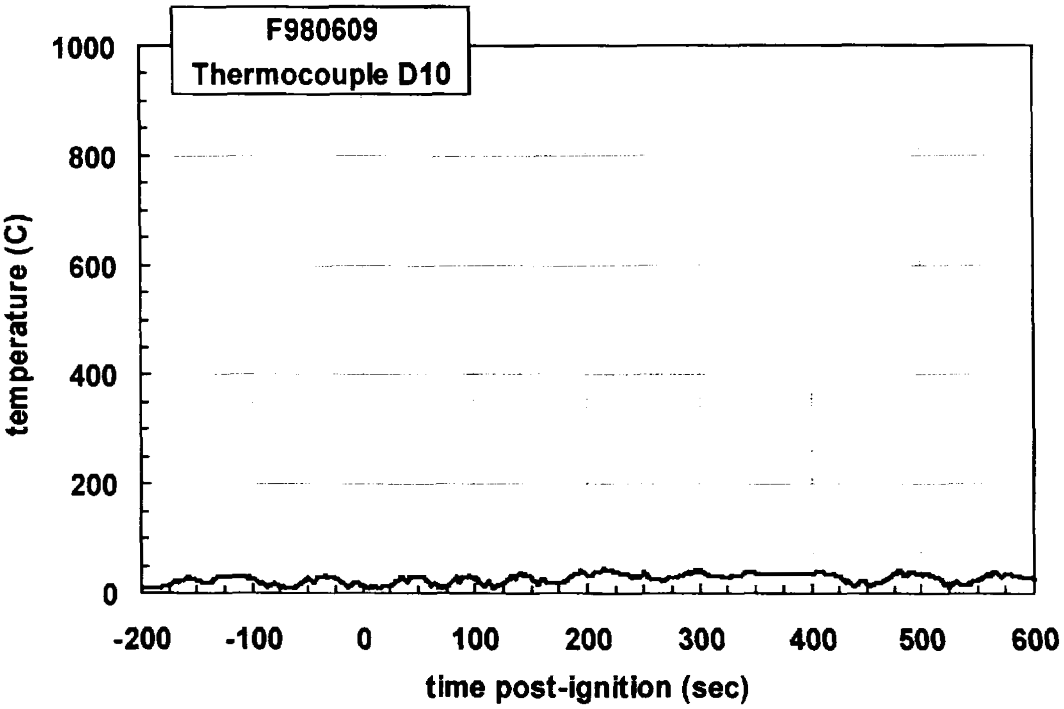

Plot C23. Fire Test F980609. Data plot from thermocouple D10.

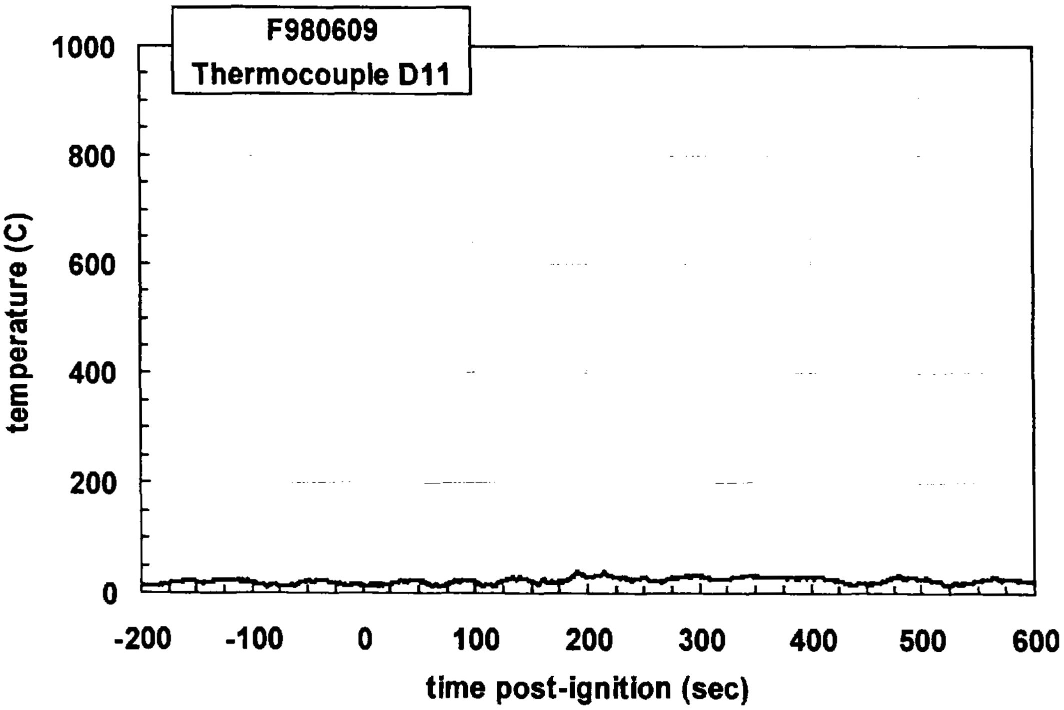

Plot C24. Fire Test F980609. Data plot from thermocouple D11.

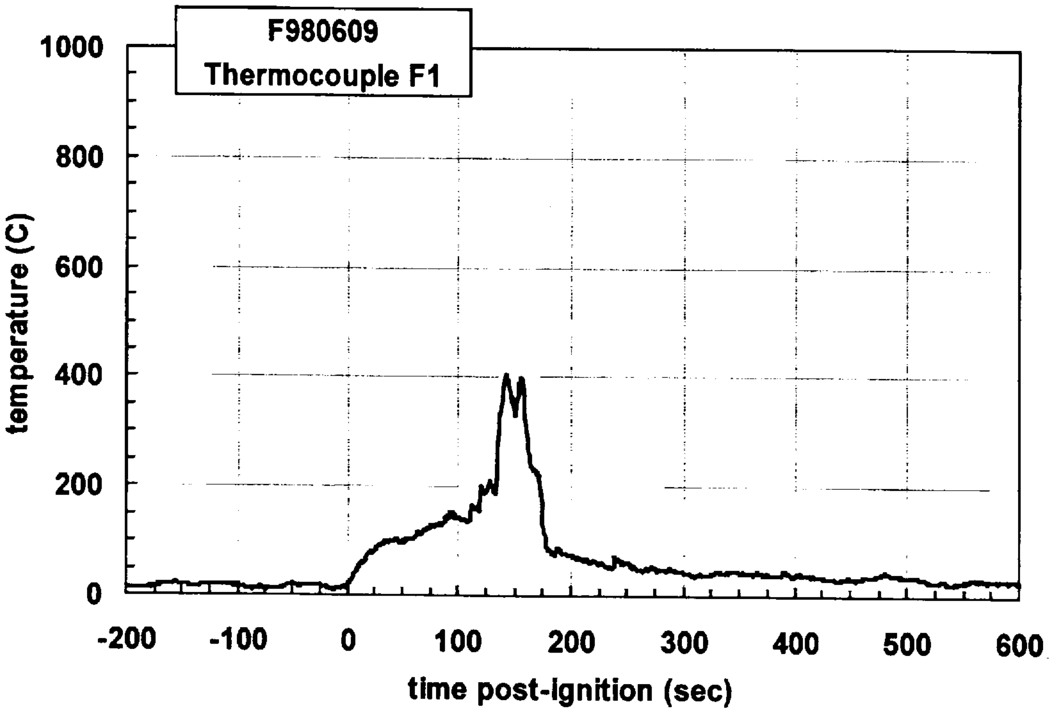

Plot C25. Fire Test F980609. Data plot from thermocouple F1.

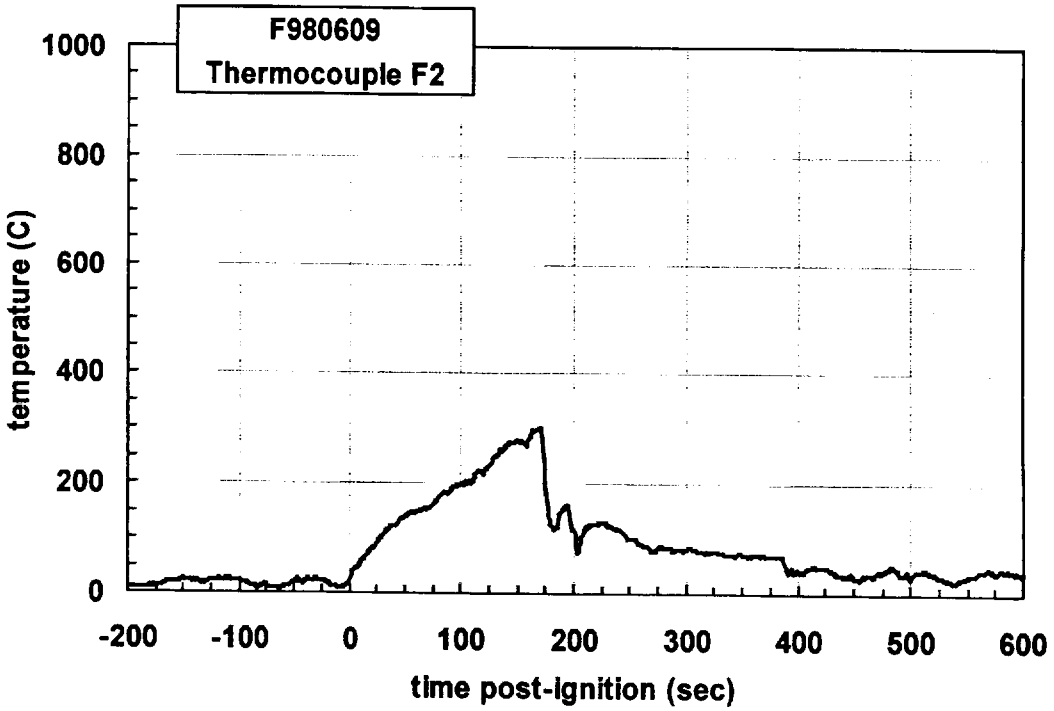

Plot C26. Fire Test F980609. Data plot from thermocouple F2.

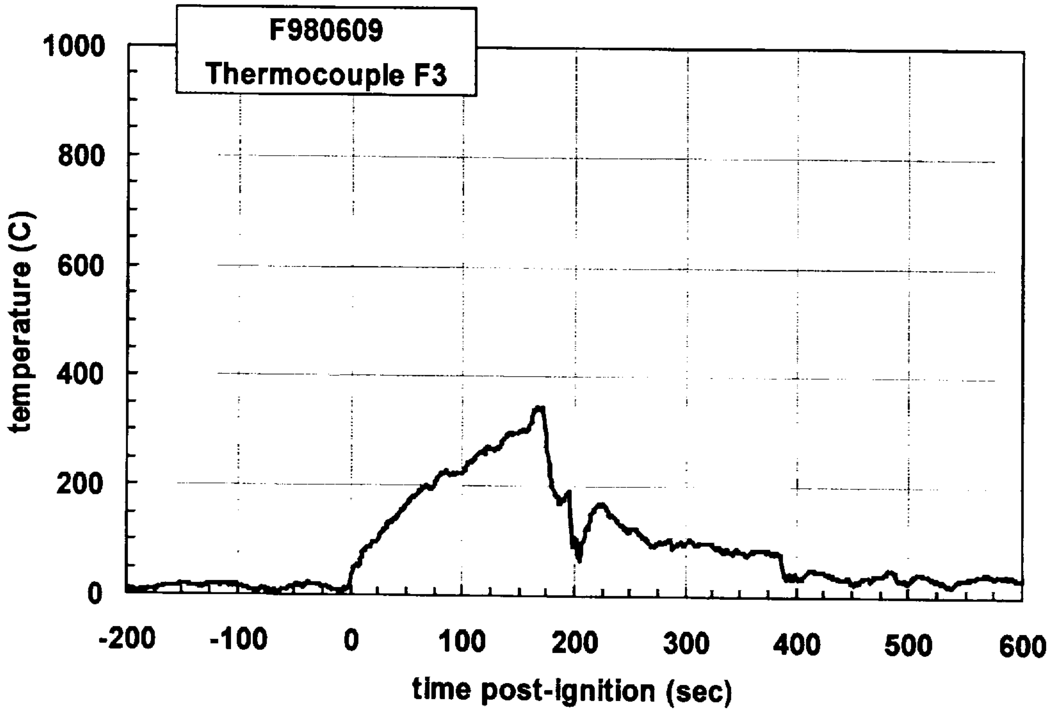

Plot C27. Fire Test F980609. Data plot from thermocouple F3.

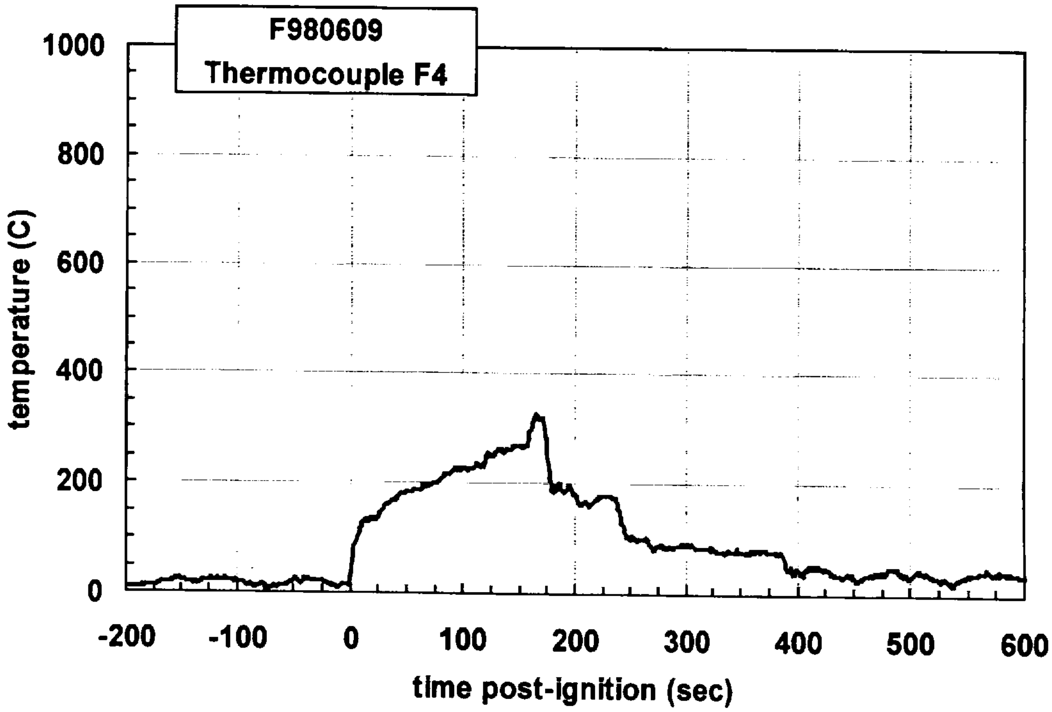

Plot C28. Fire Test F980609. Data plot from thermocouple F4.

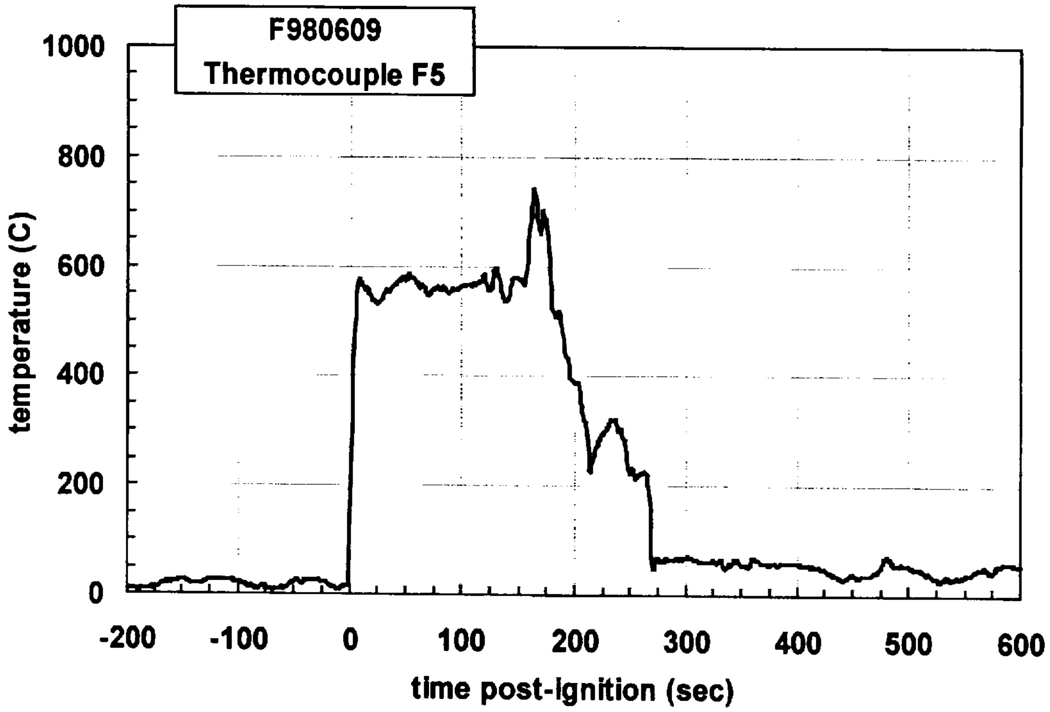

Plot C29. Fire Test F980609. Data plot from thermocouple F5.

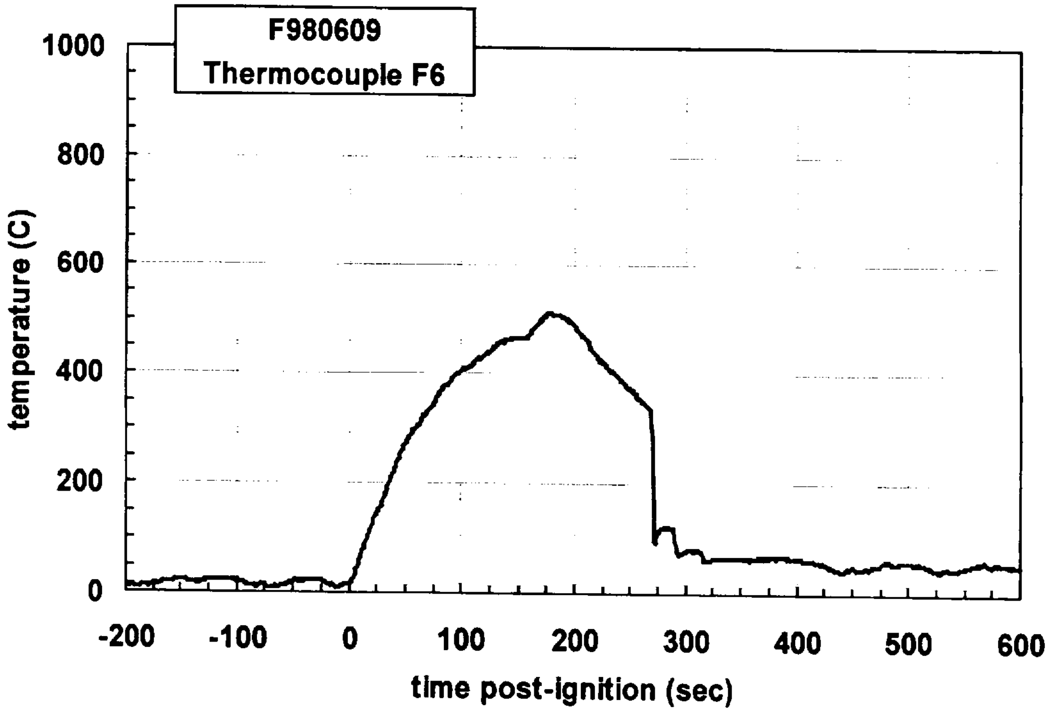

Plot C30. Fire Test F980609. Data plot from thermocouple F6.

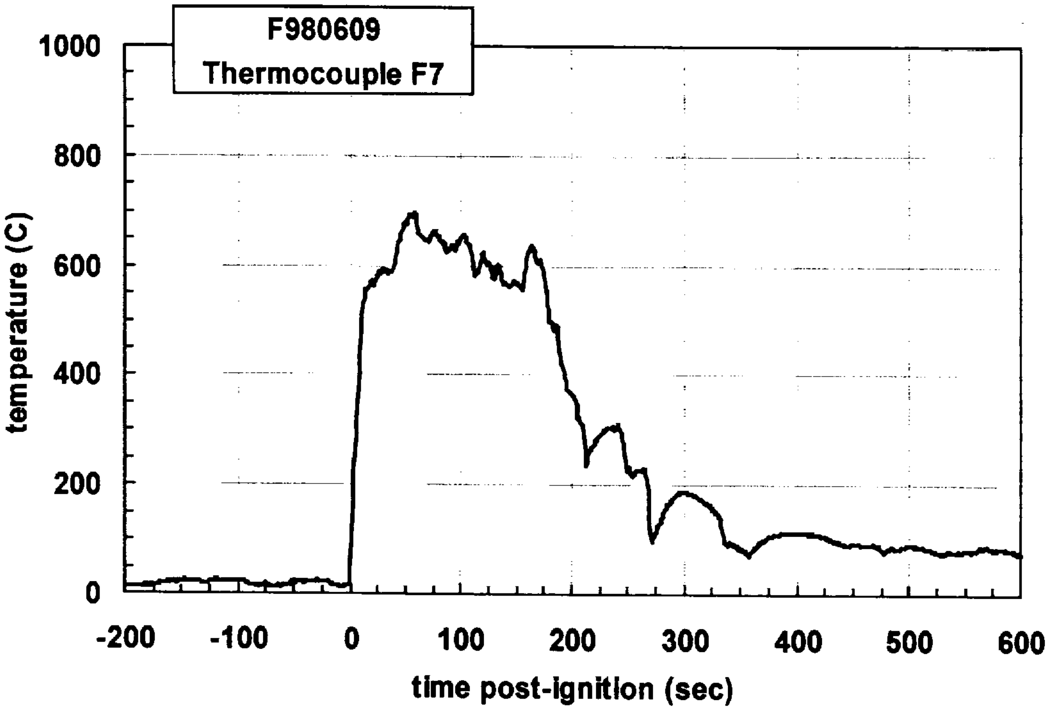

Plot C31. Fire Test F980609. Data plot from thermocouple F7.

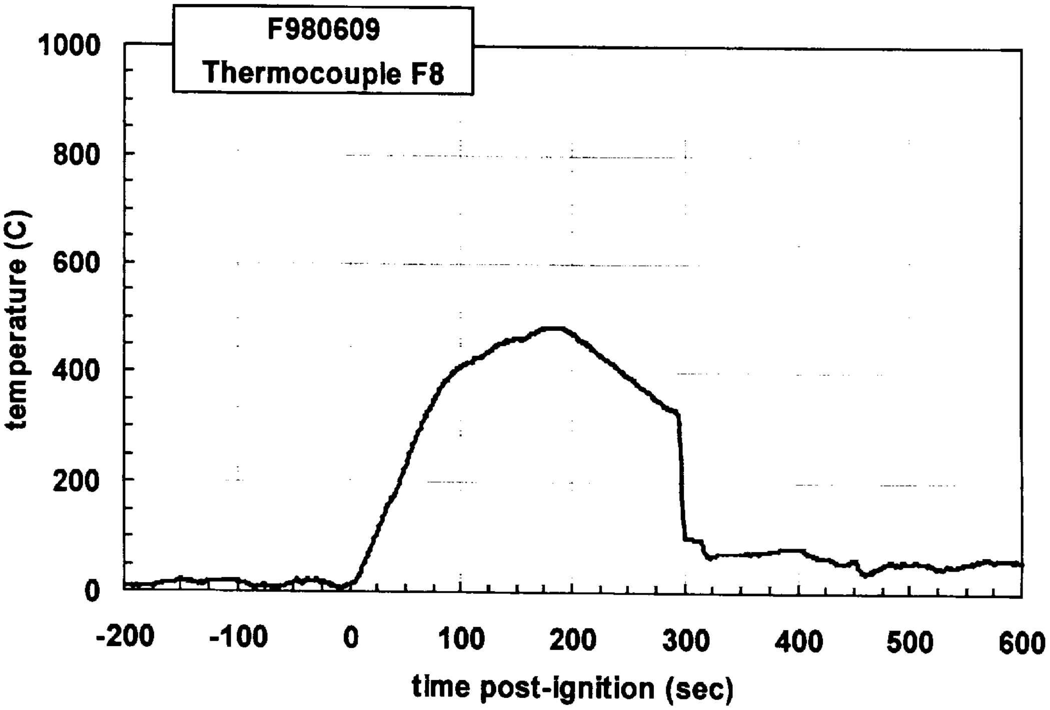

Plot C32. Fire Test F980609. Data plot from thermocouple F8.

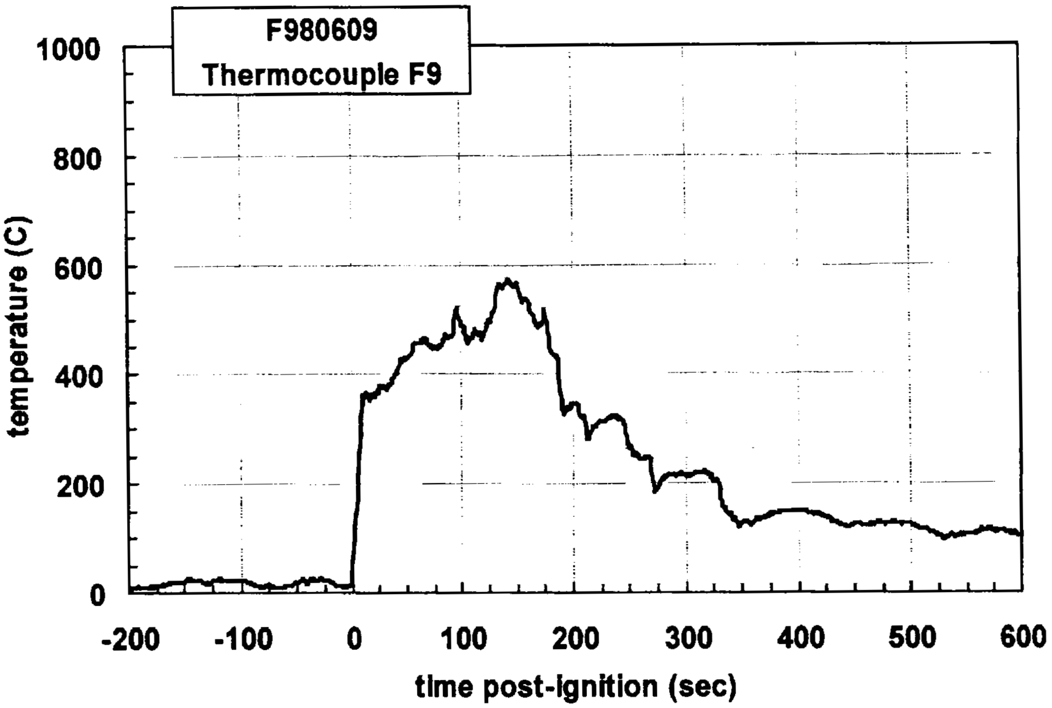

Plot C33. Fire Test F980609. Data plot from thermocouple F9.

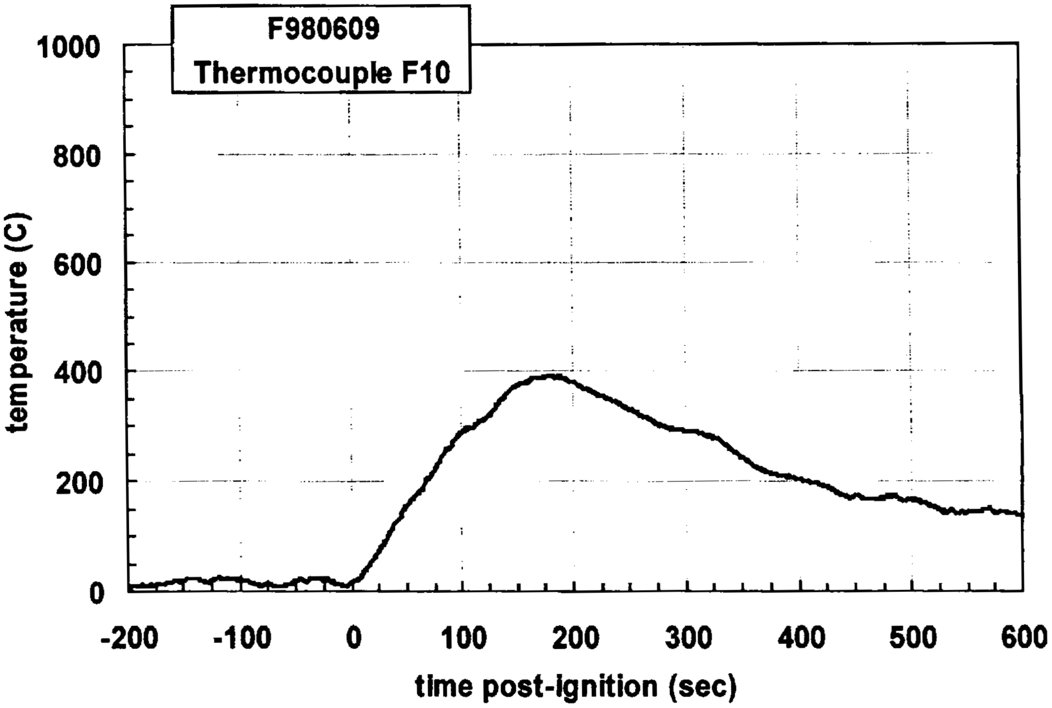

Plot C34. Fire Test F980609. Data plot from thermocouple F10.

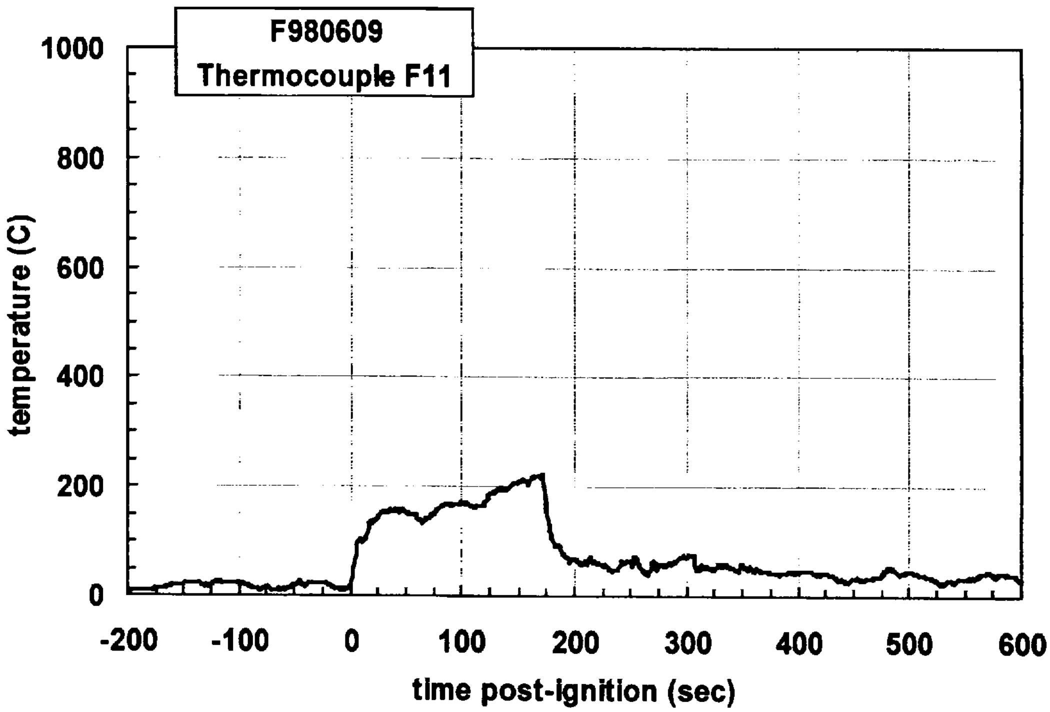

Plot C35. Fire Test F980609. Data plot from thermocouple F11.

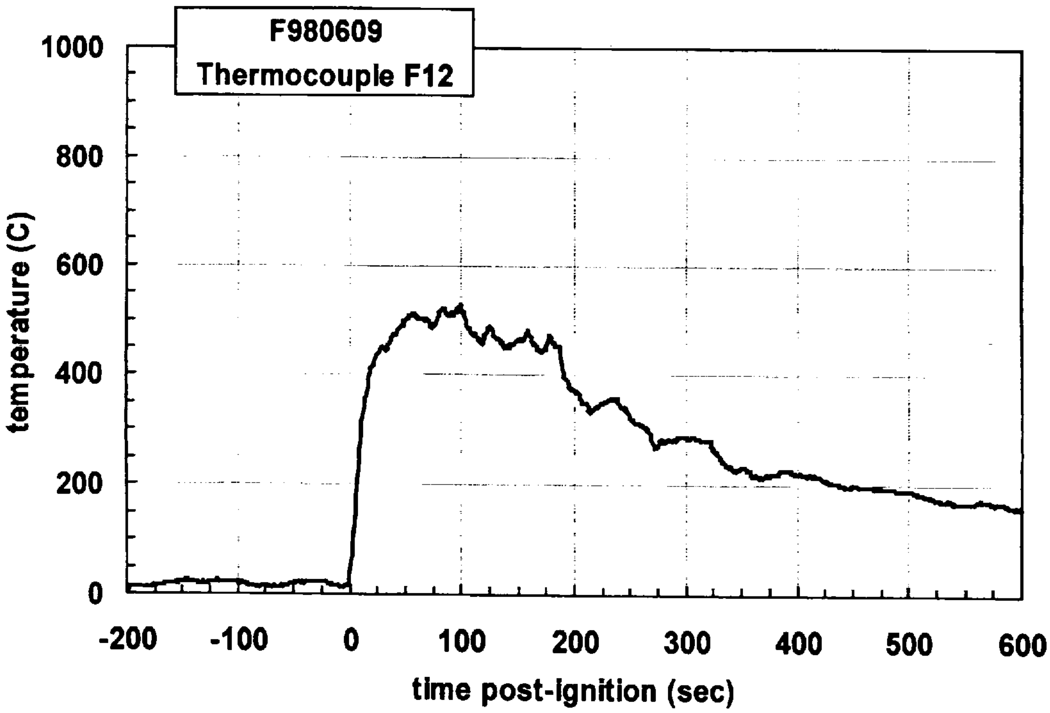

Plot C36. Fire Test F980609. Data plot from thermocouple F12.

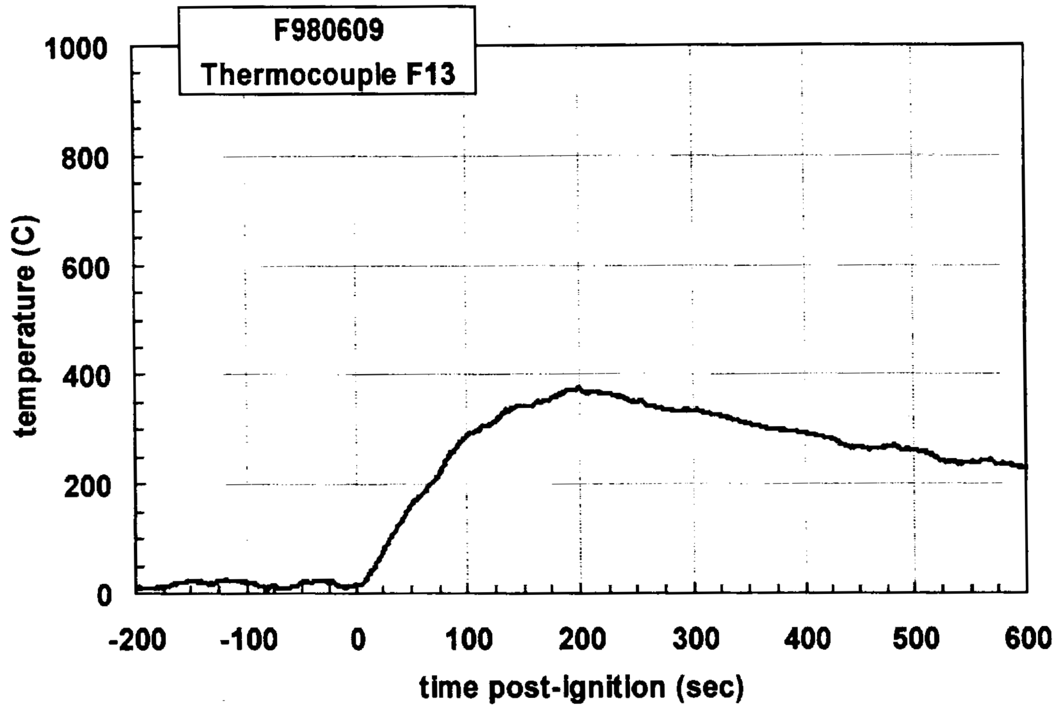

Plot C37. Fire Test F980609. Data plot from thermocouple F13.

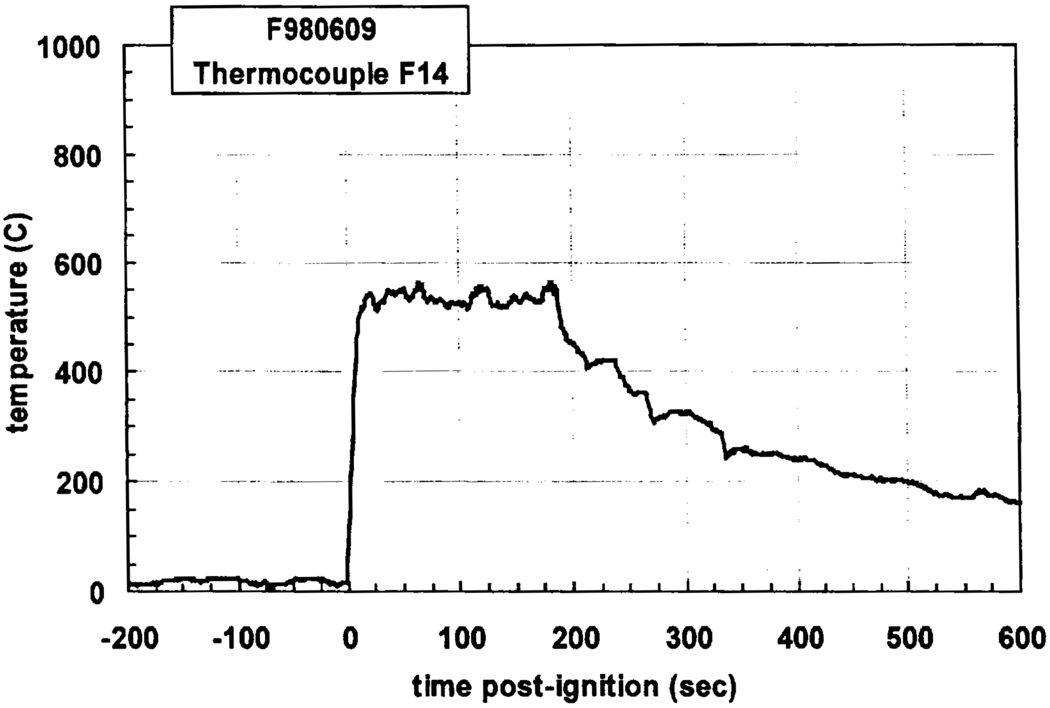

Plot C38. Fire Test F980609. Data plot from thermocouple F14.

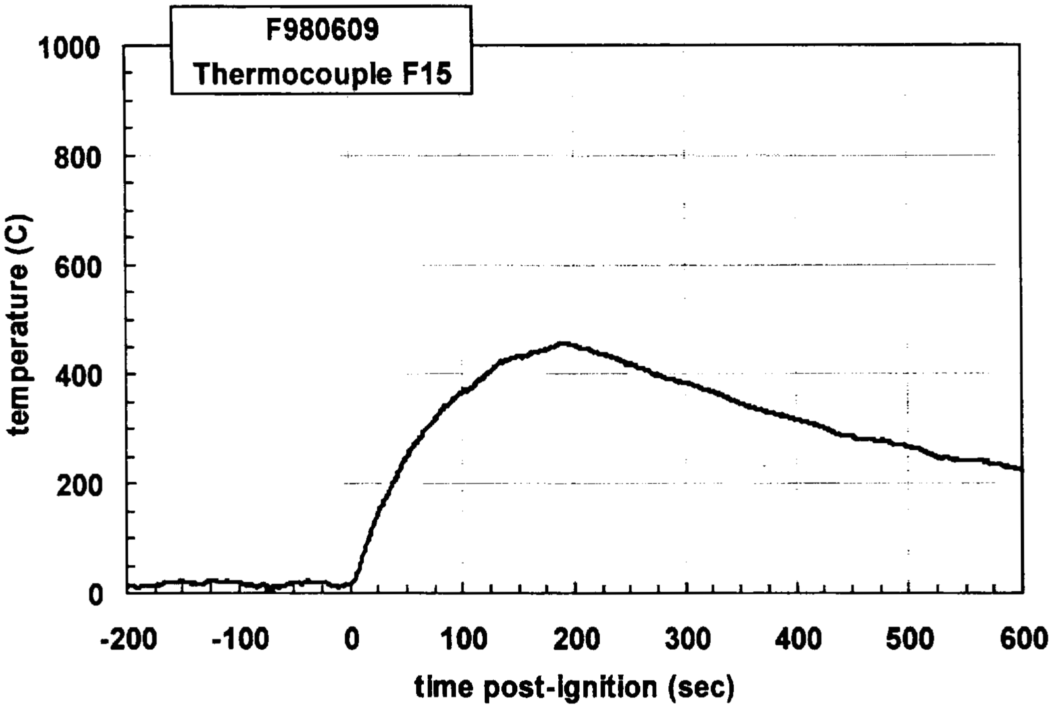

Plot C39. Fire Test F980609. Data plot from thermocoupleF15.

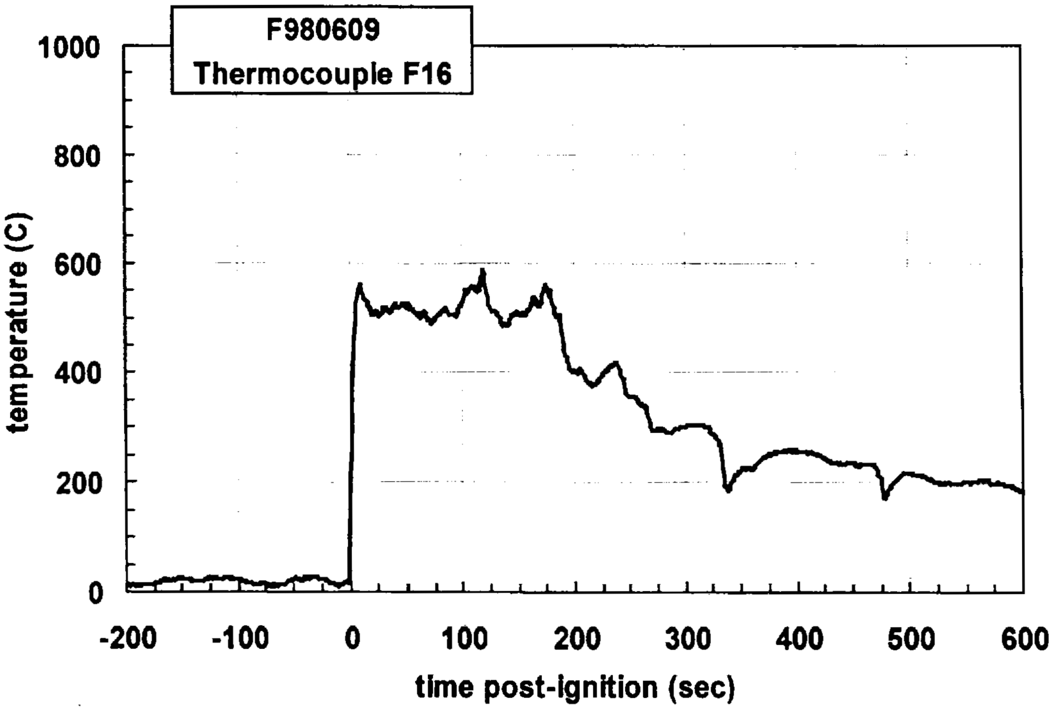

Plot C40. Fire Test F980609. Data plot from thermocouple F16.

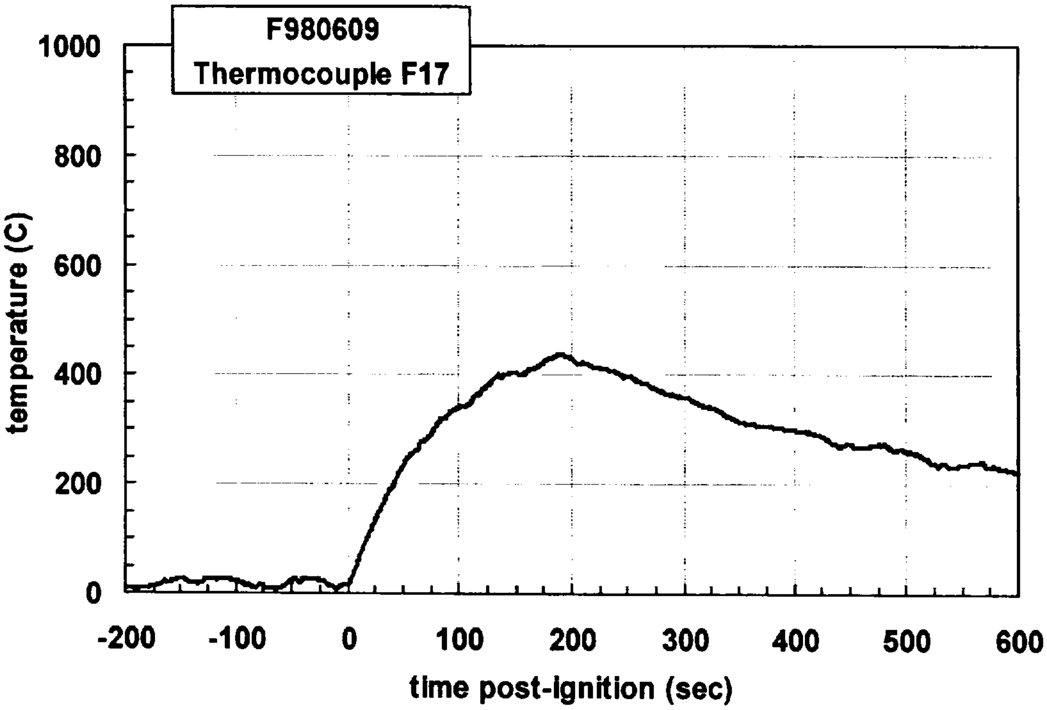

Plot C41. Fire Test F980609. Data plot from thermocouple F17.

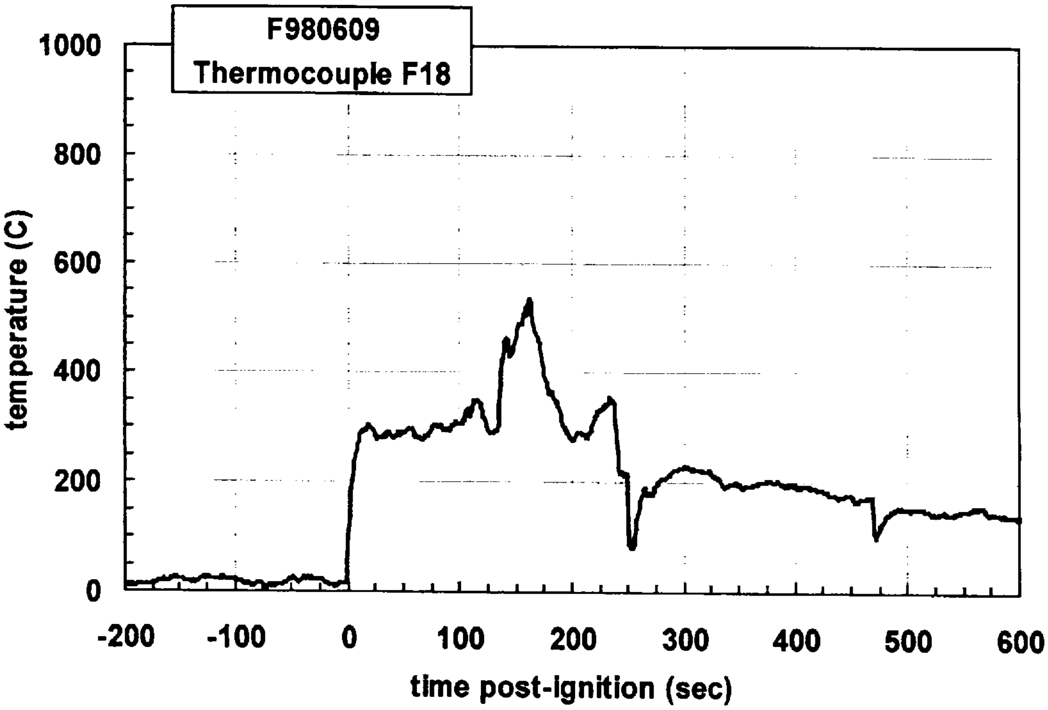

Plot C42. Fire Test F980609. Data plot from thermocouple F18.

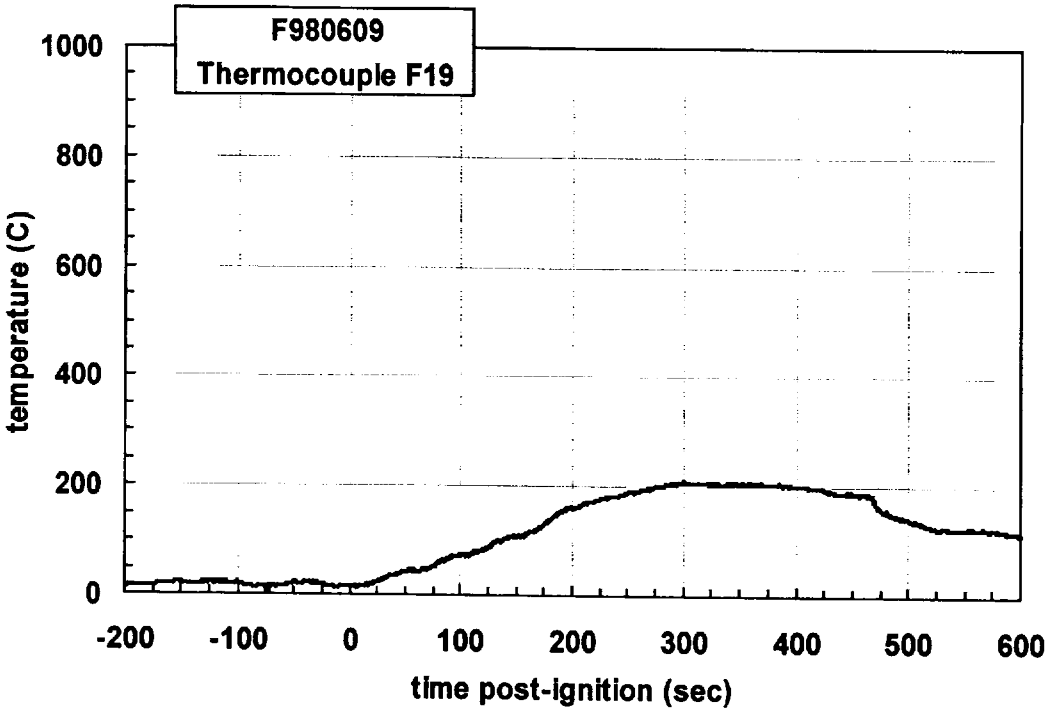

Plot C43. Fire Test F980609. Data plot from thermocouple F19.

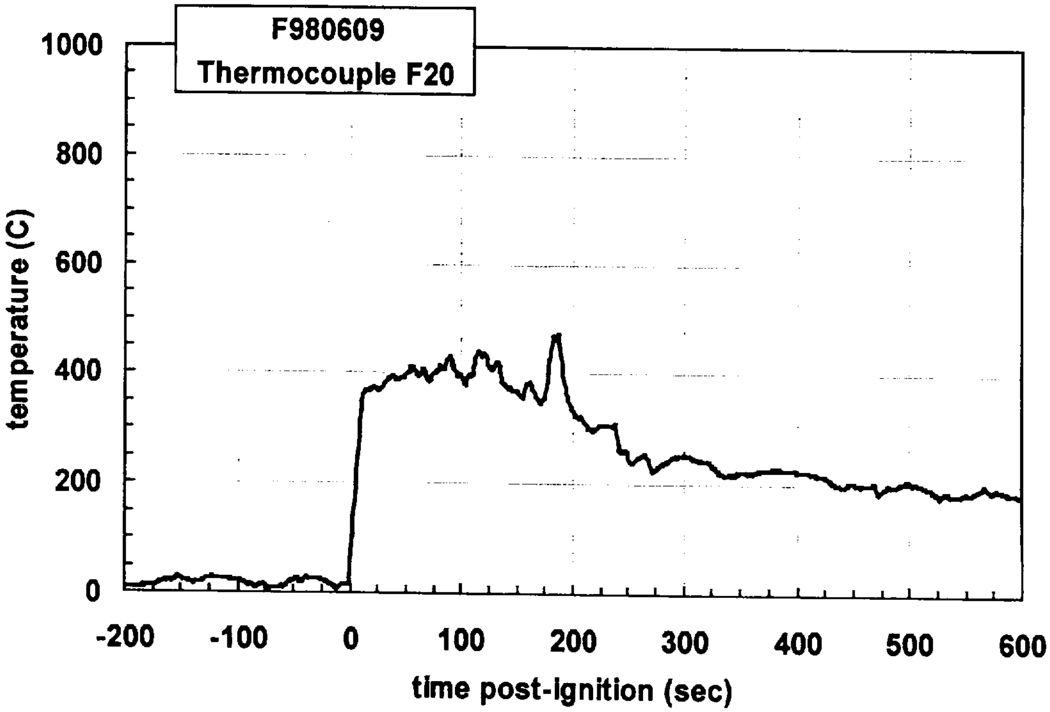

Plot C44. Fire Test F980609. Data plot from thermocouple F20.

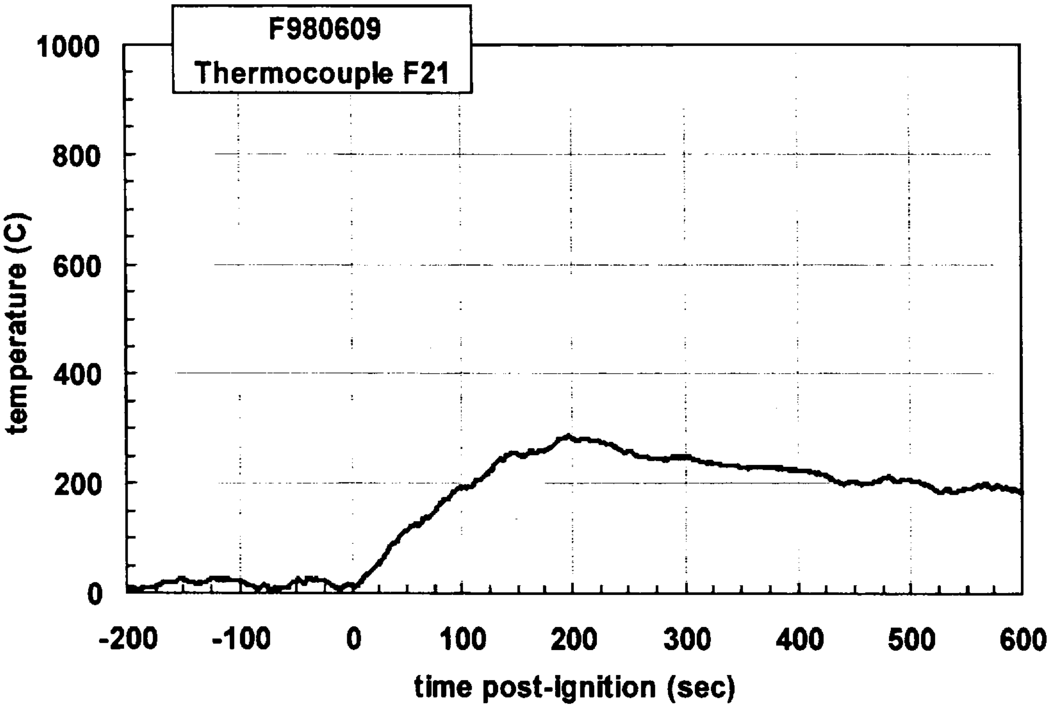

Plot C45. Fire Test F980609. Data plot from thermocouple F21.

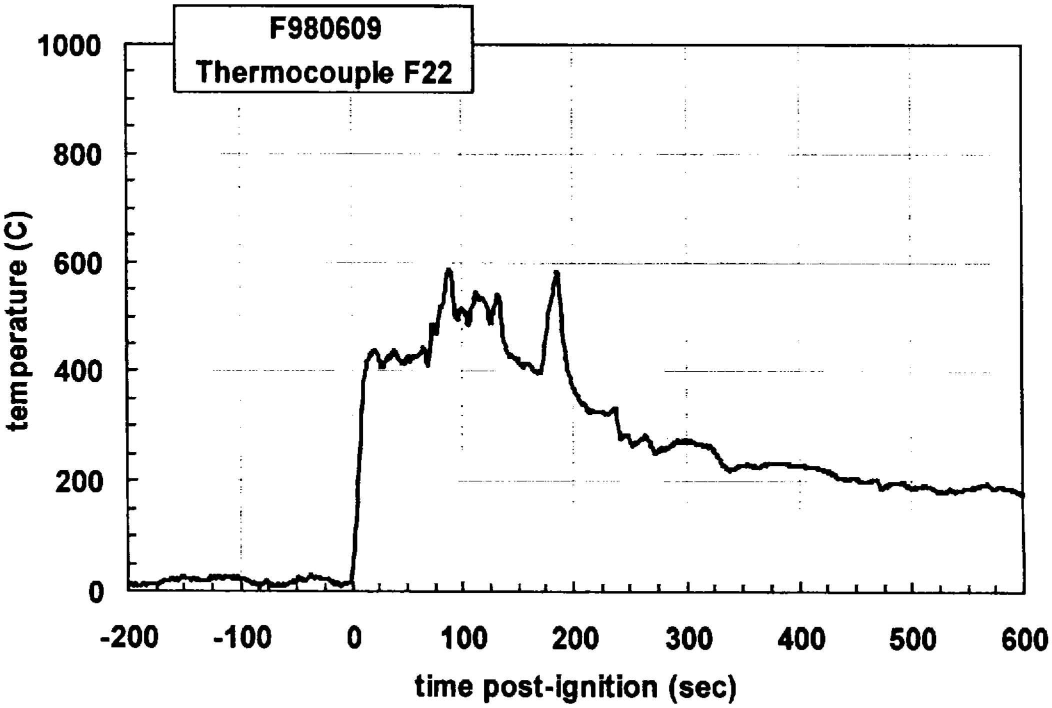

Plot C46. Fire Test F980609. Data plot from thermocouple F22.

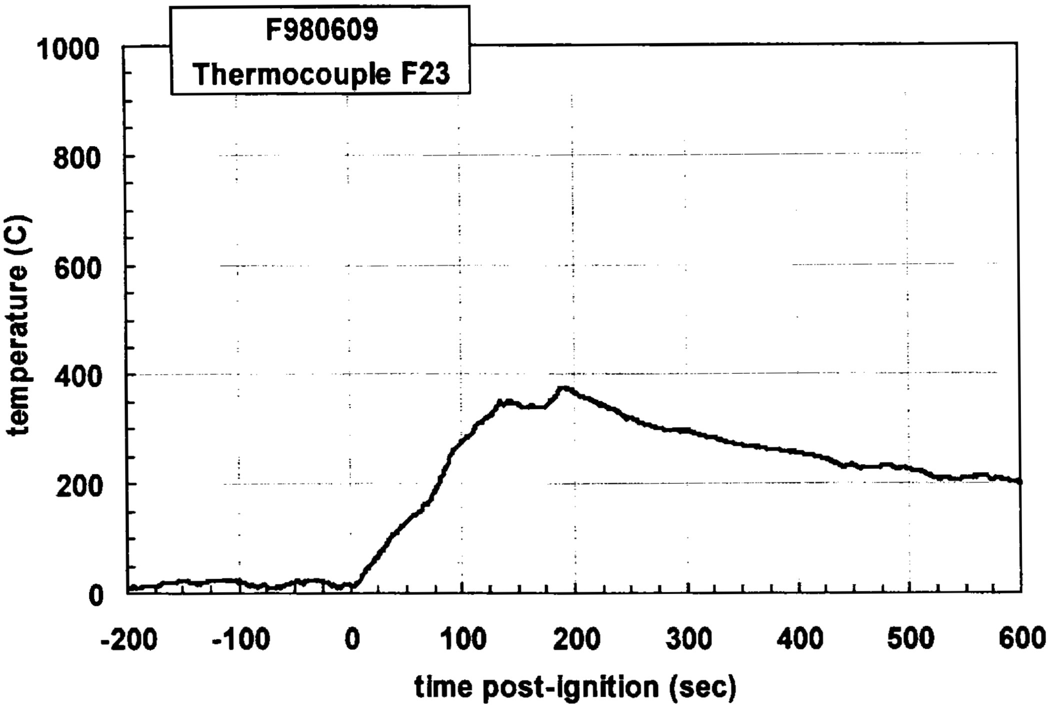

Plot C47. Fire Test F980609. Data plot from thermocouple F23.

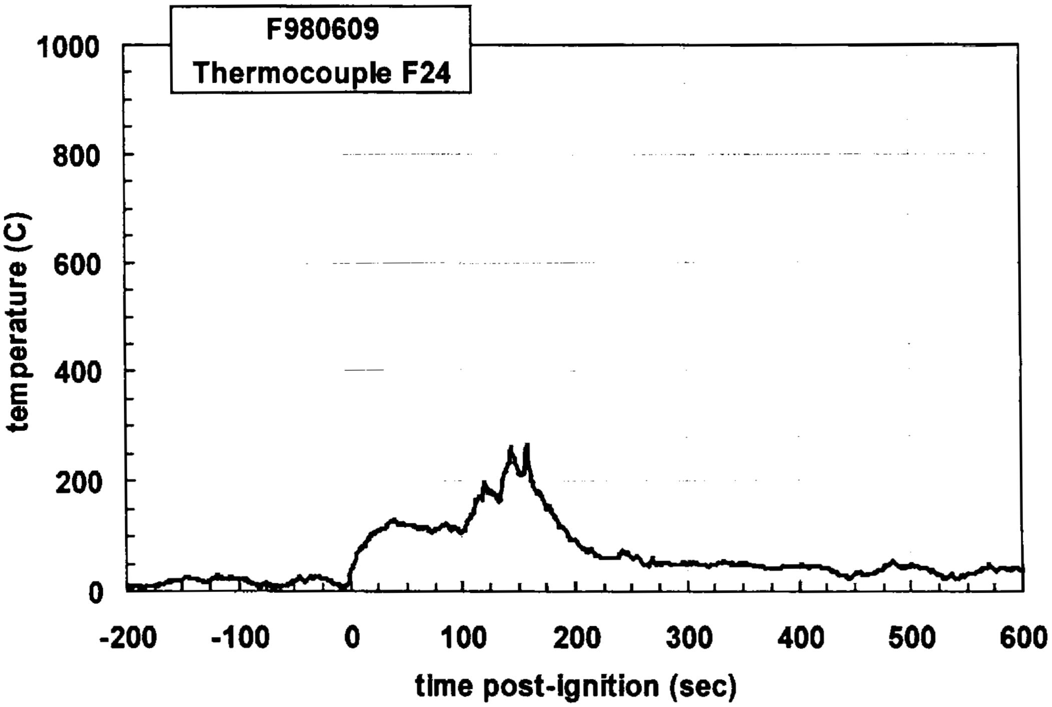

Plot C48. Fire Test F980609. Data plot from thermocouple F24.

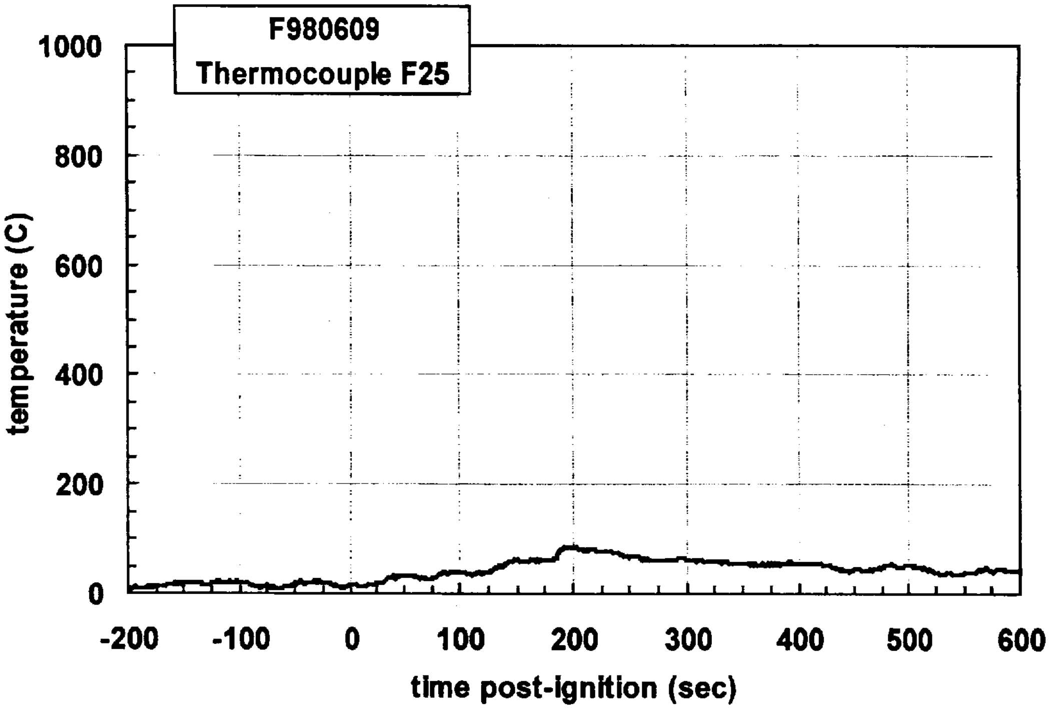

Plot C49. Fire Test F980609. Data plot from thermocouple F25.

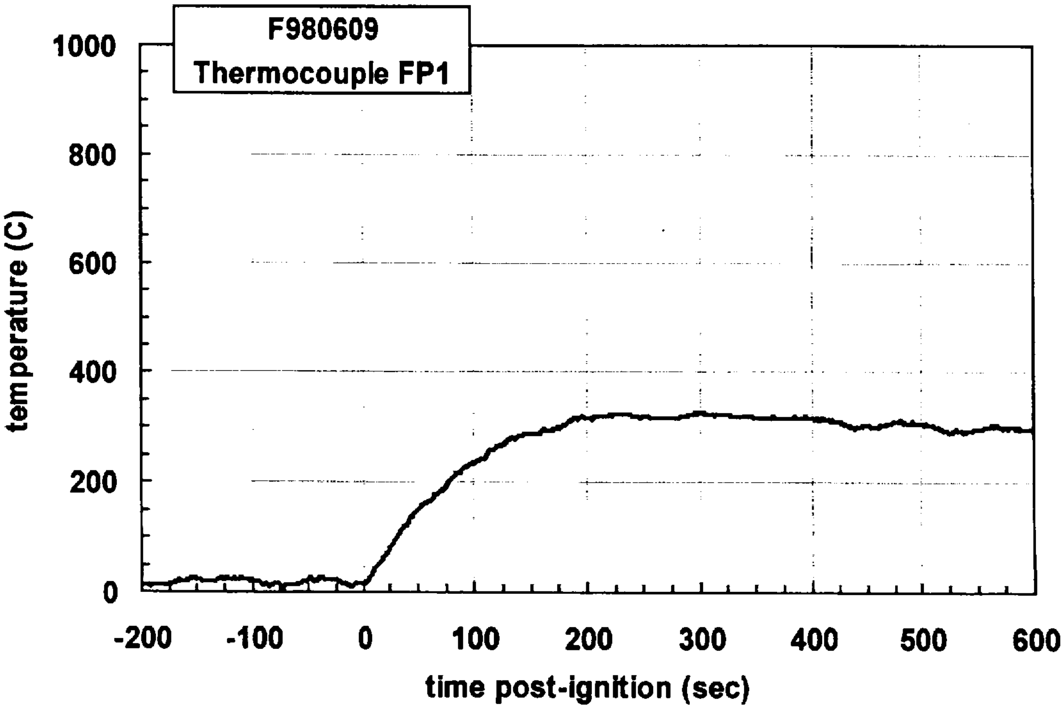

Plot C50. Fire Test F980609. Data plot from thermocouple FP1.

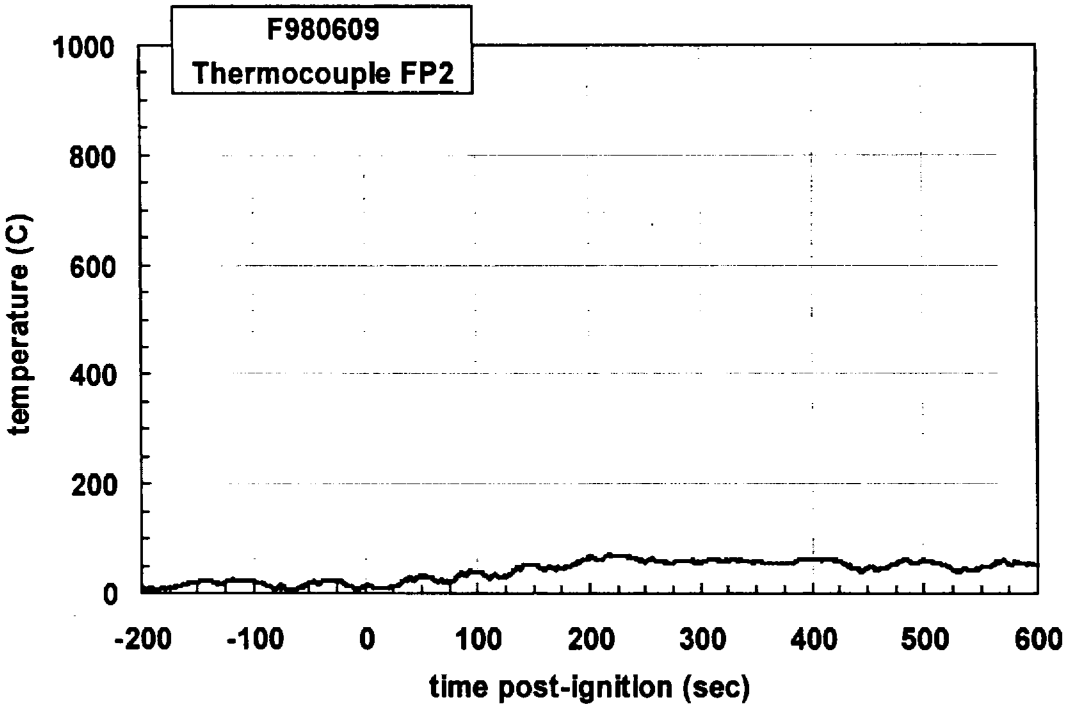

Plot C51. Fire Test F980609. Data plot from thermocouple FP2.

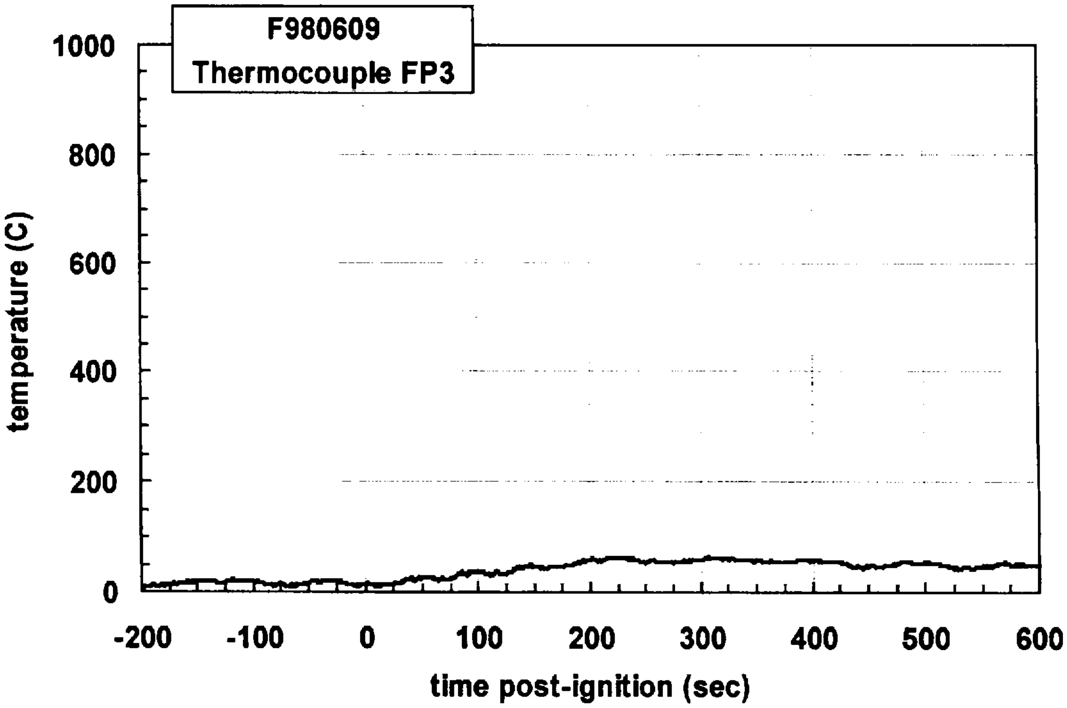

Plot C52. Fire Test F980609. Data plot from thermocouple FP3.

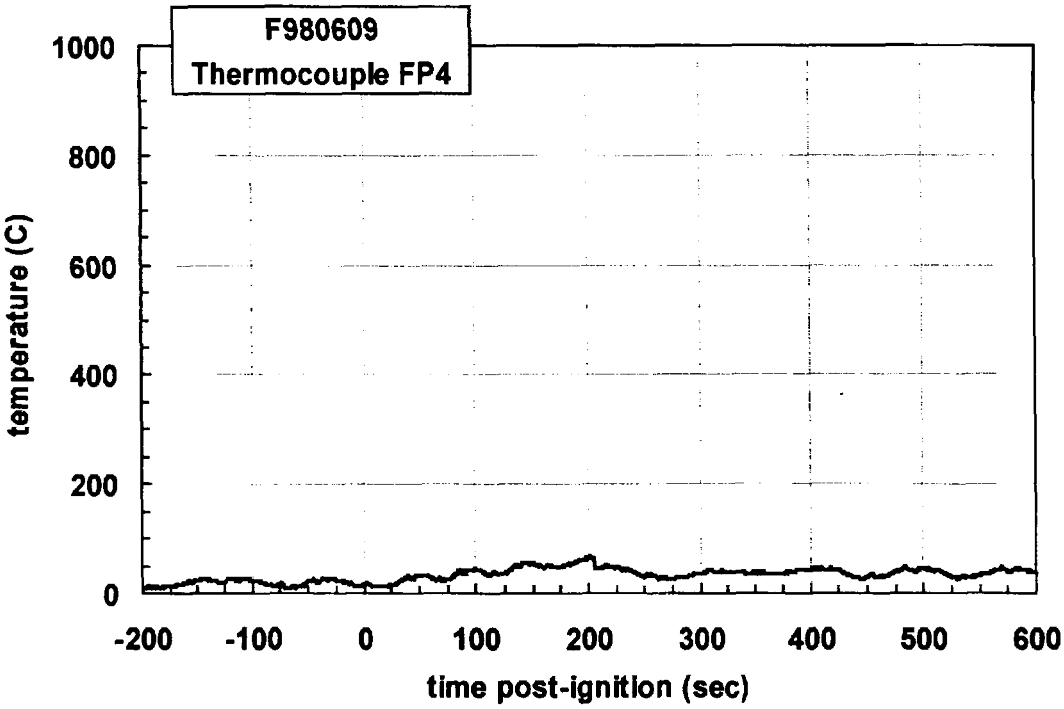

Plot C53. Fire Test F980609. Data plot from thermocouple FP4.

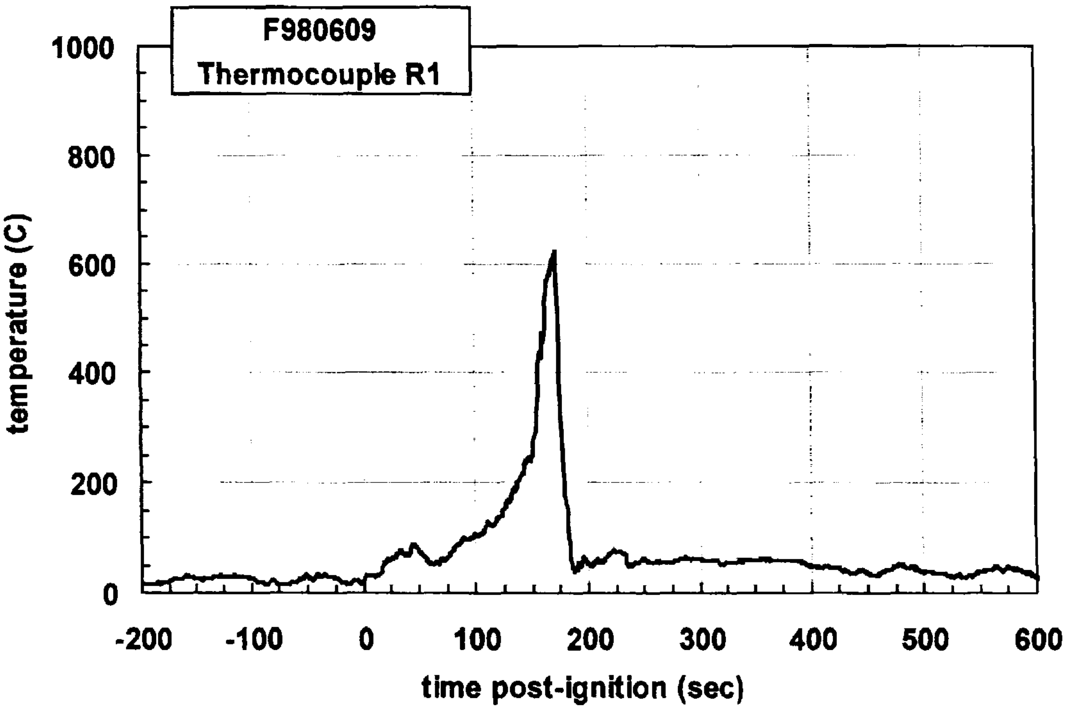

Plot C54. Fire Test F980609. Data plot from thermocouple R1.

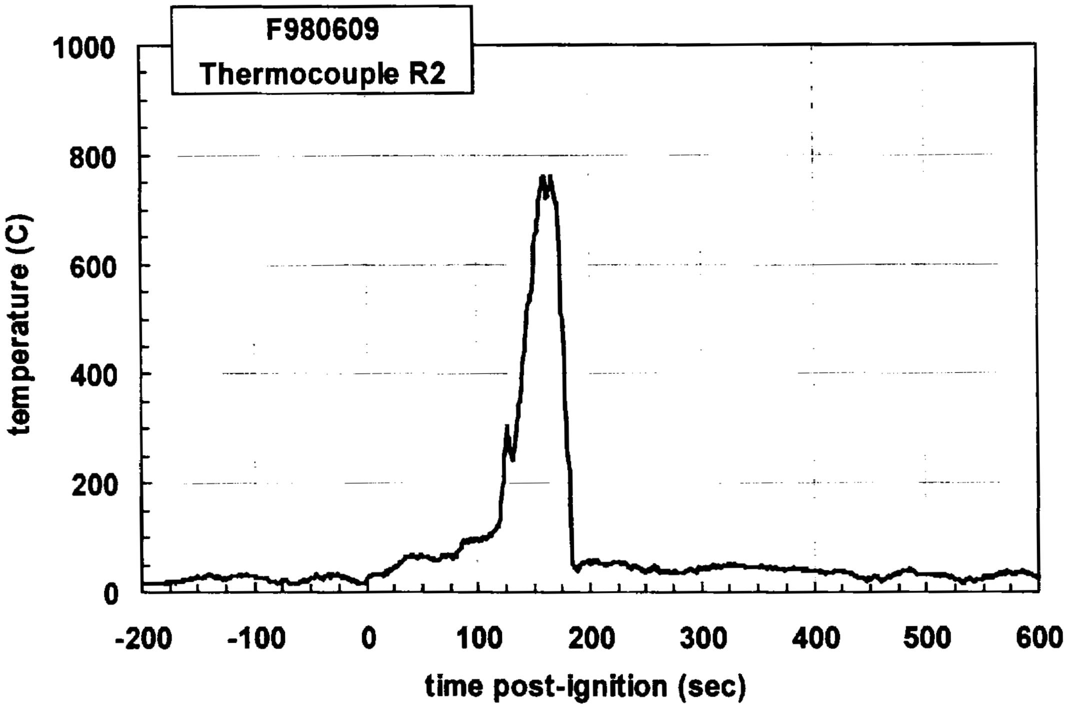

Plot C55. Fire Test F980609. Data plot from thermocouple R2.

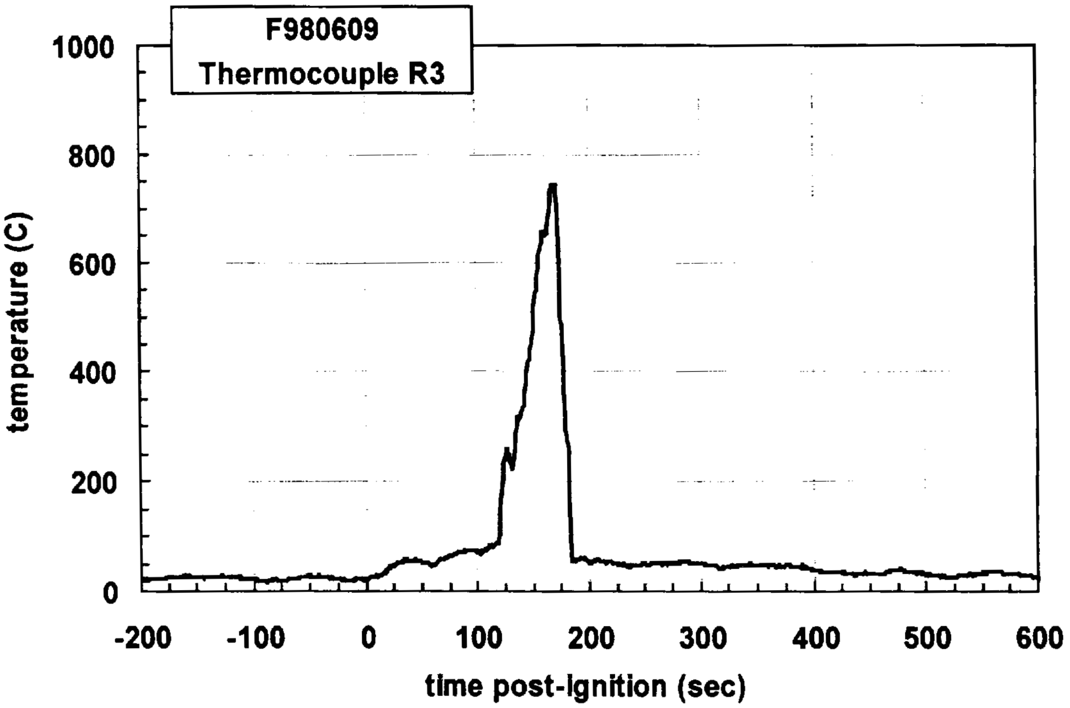

Plot C56. Fire Test F980609. Data plot from thermocouple R3.

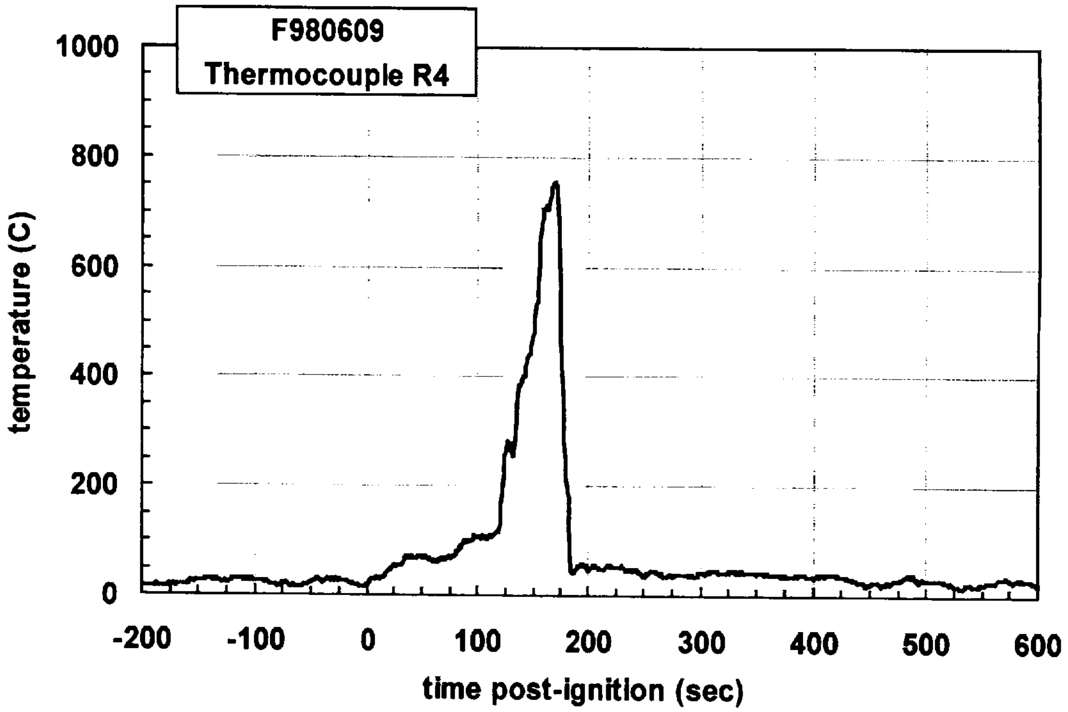

Plot C57. Fire Test F980609. Data plot from thermocouple R4.

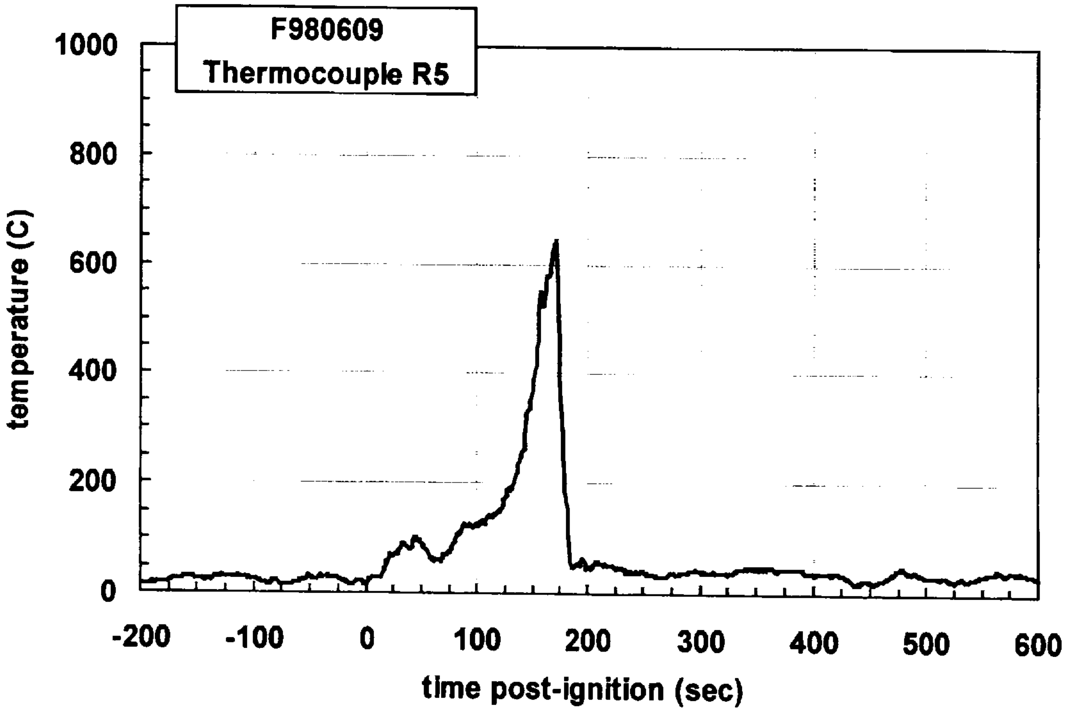

Plot C58. Fire Test F980609. Data plot from thermocouple R5.

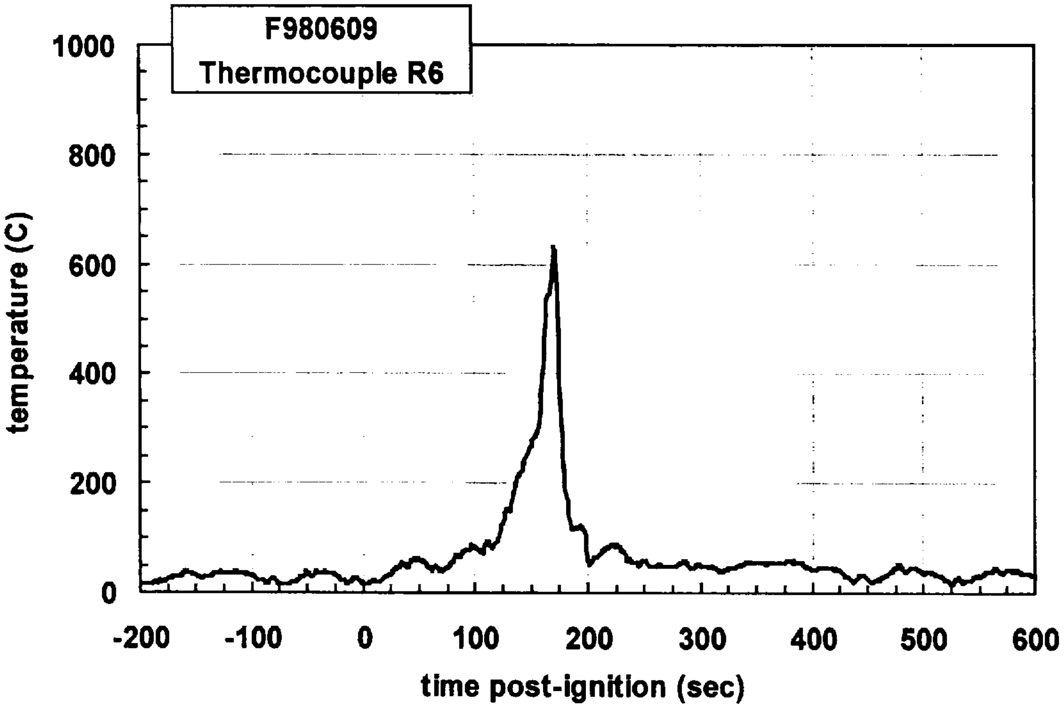

Plot C59. Fire Test F980609. Data plot from thermocouple R6.

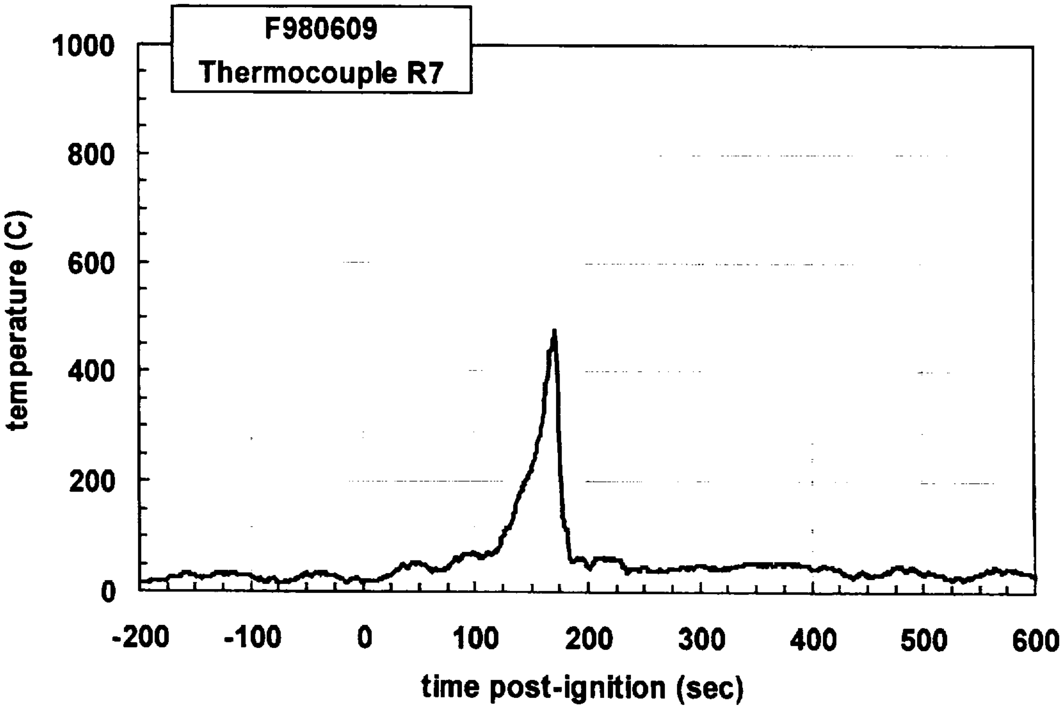

Plot C60. Fire Test F980609. Data plot from thermocouple R7.

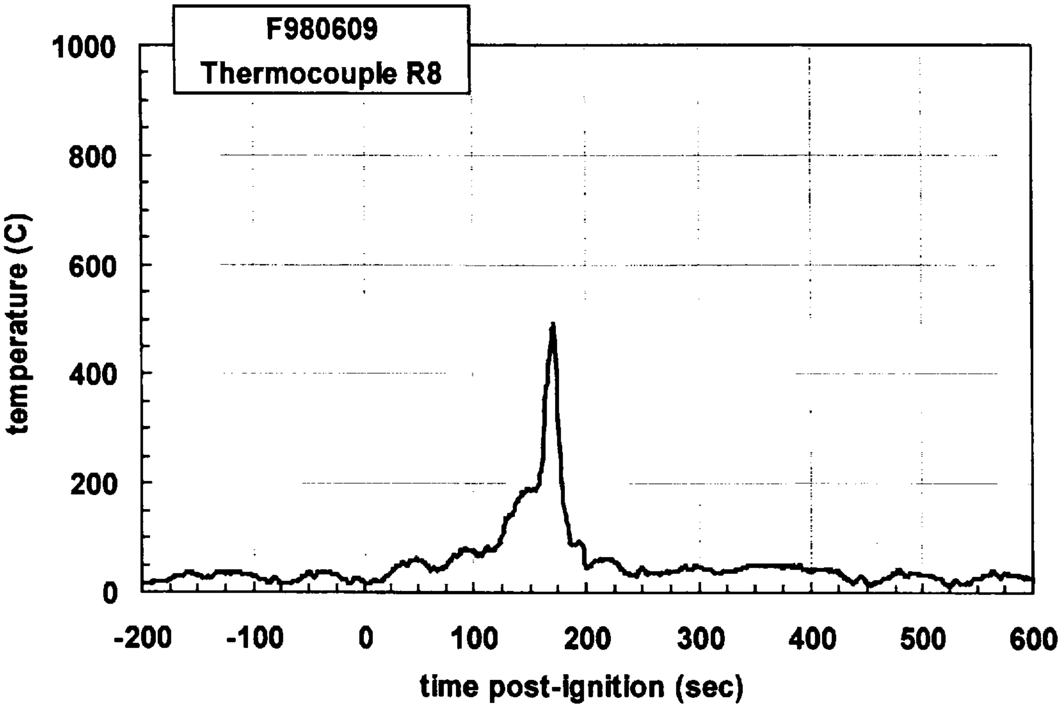

Plot C61. Fire Test F980609. Data plot from thermocouple R8.

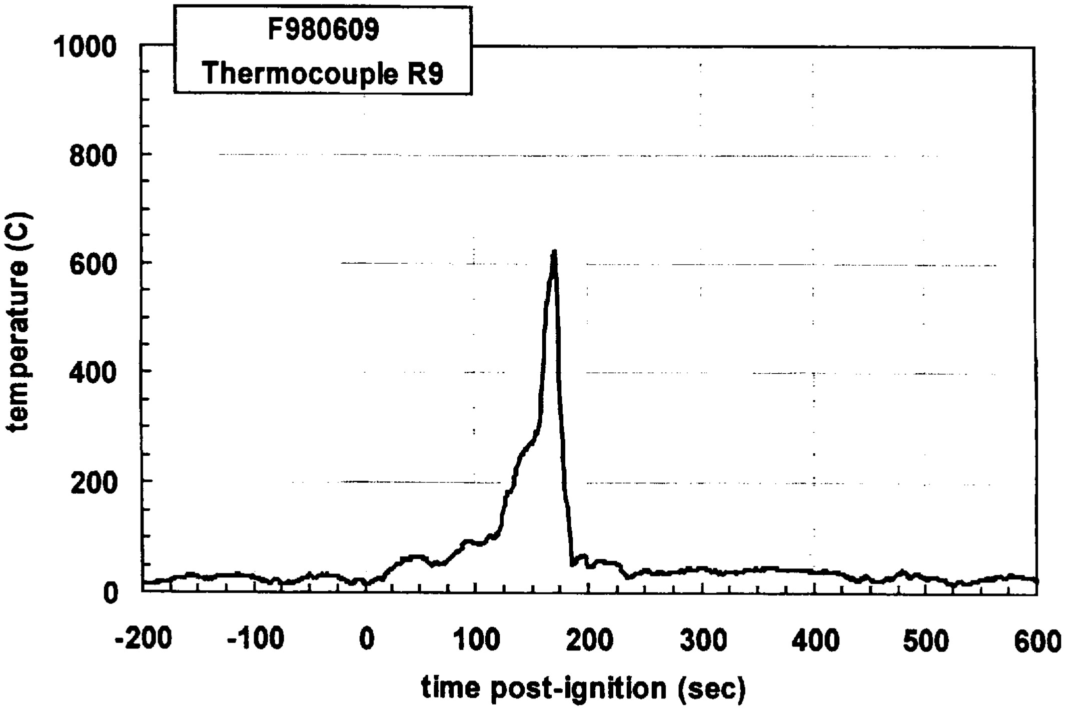

Plot C62. Fire Test F980609. Data plot from thermocouple R9.

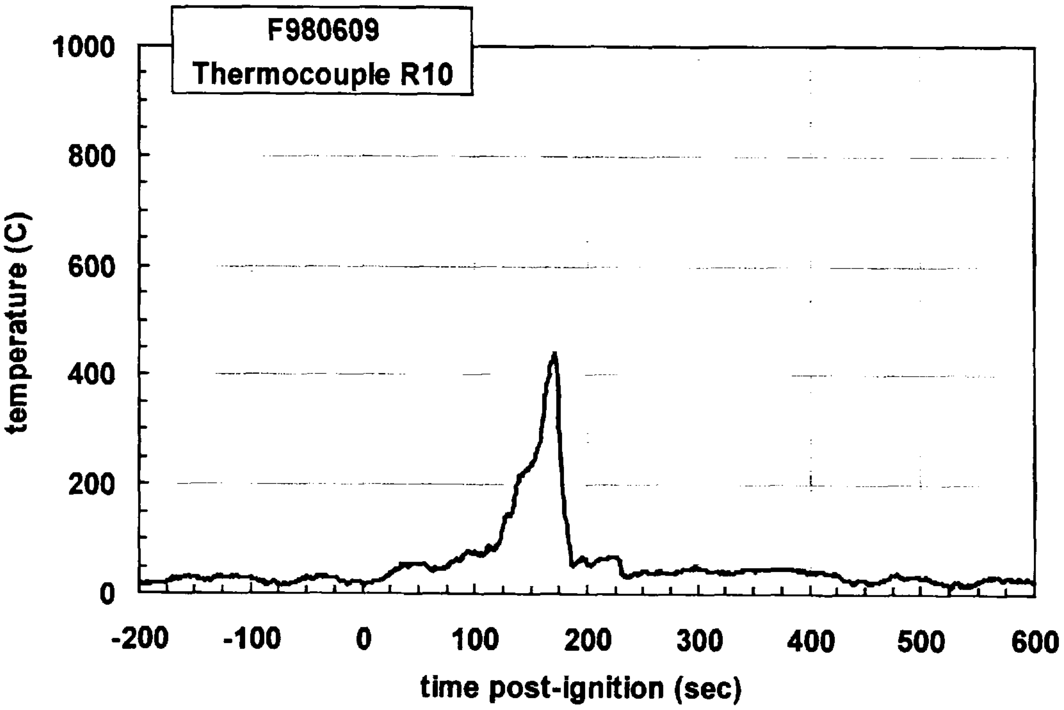

Plot C63. Fire Test F980609. Data plot from thermocouple R10.

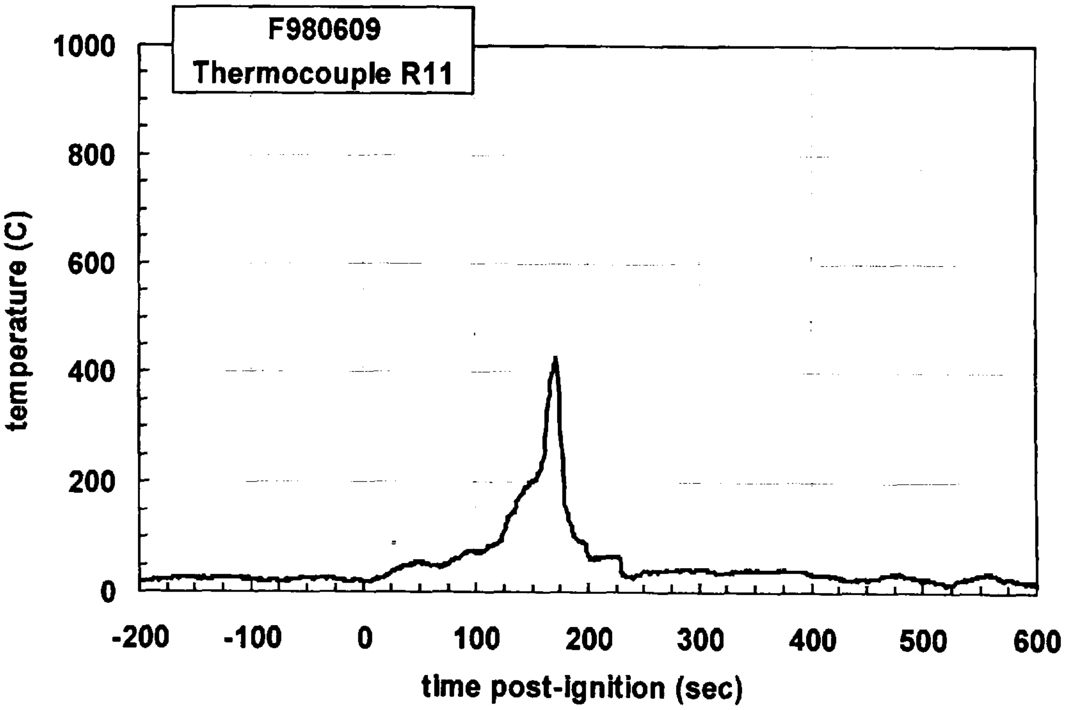

Plot C64. Fire Test F980609. Data plot from thermocouple R11.

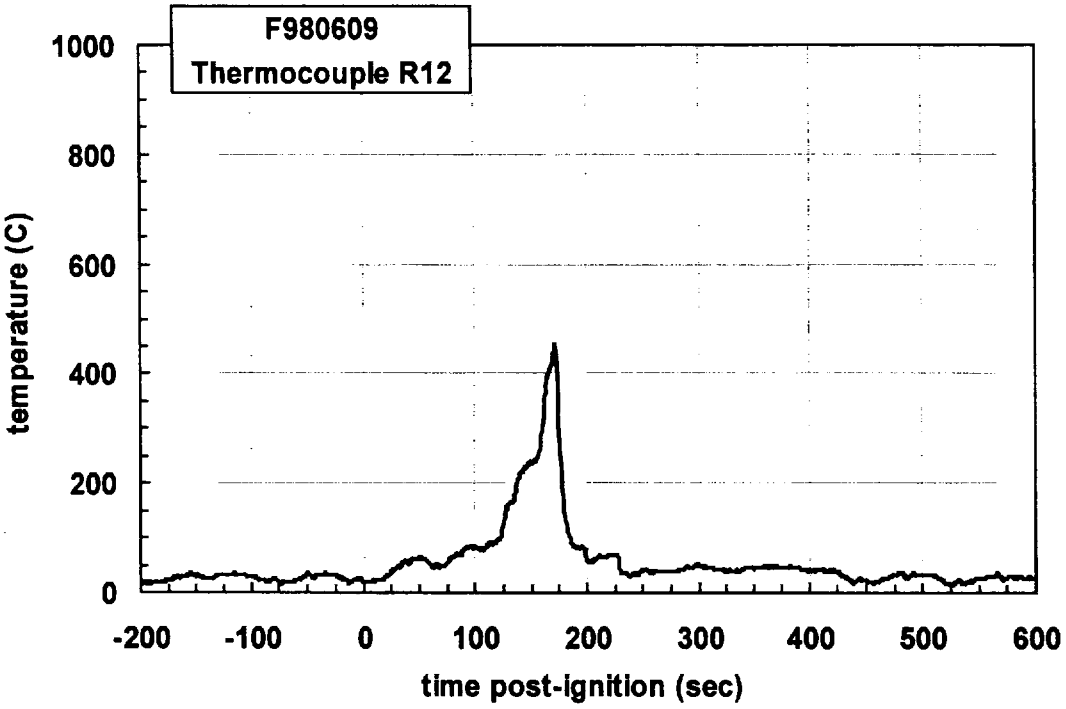

Plot C65. Fire Test F980609. Data plot from thermocouple R12.

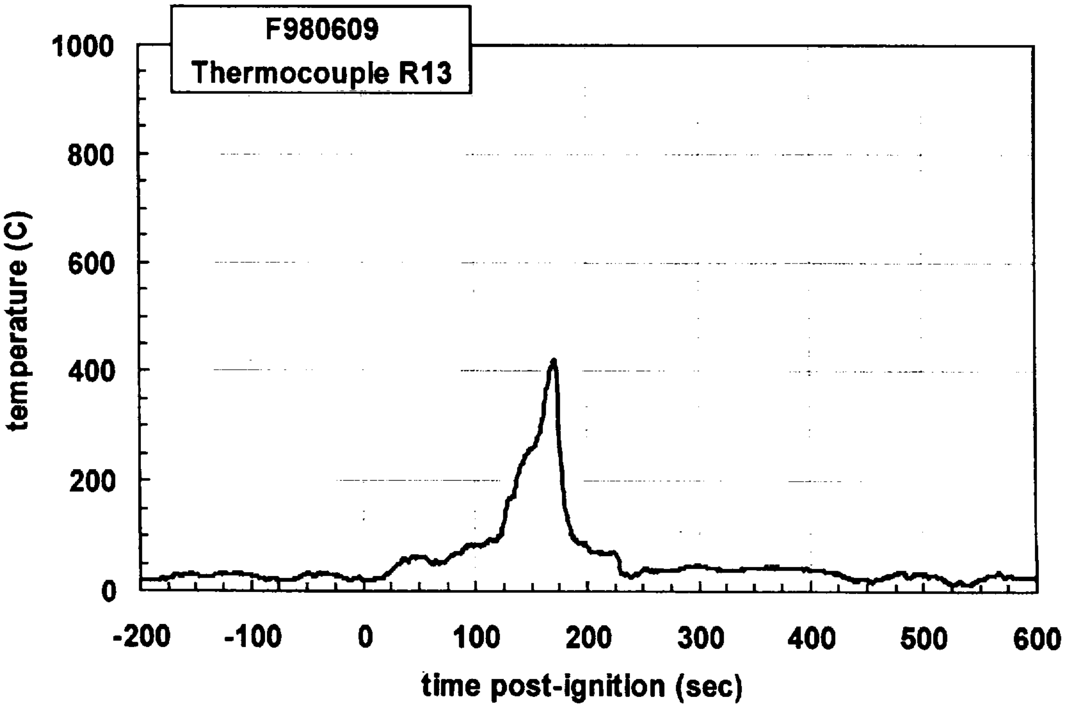

Plot C66. Fire Test F980609. Data plot from thermocouple R13.

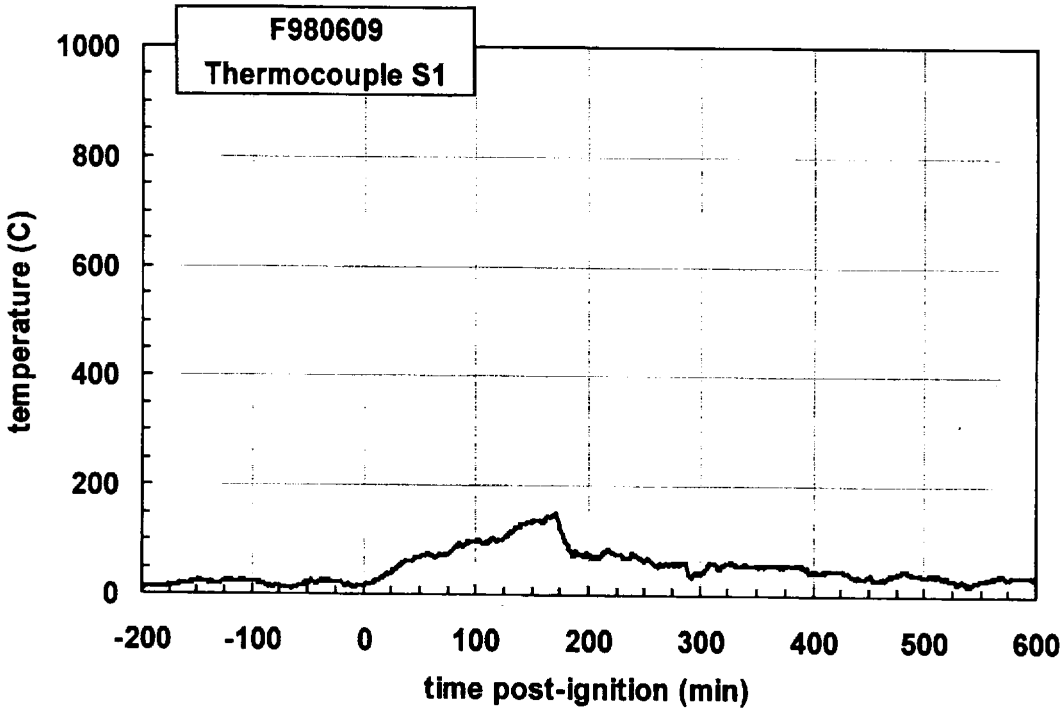

Plot C67. Fire Test F980609. Data plot from thermocouple S1.

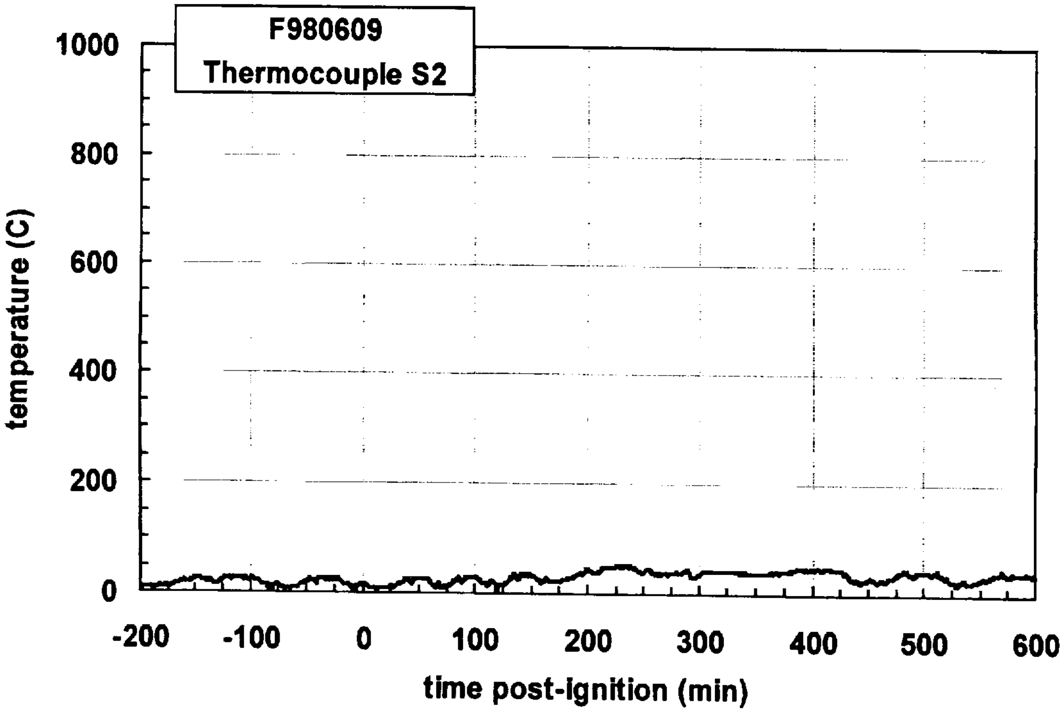

Plot C68. Fire Test F980609. Data plot from thermocouple S2.

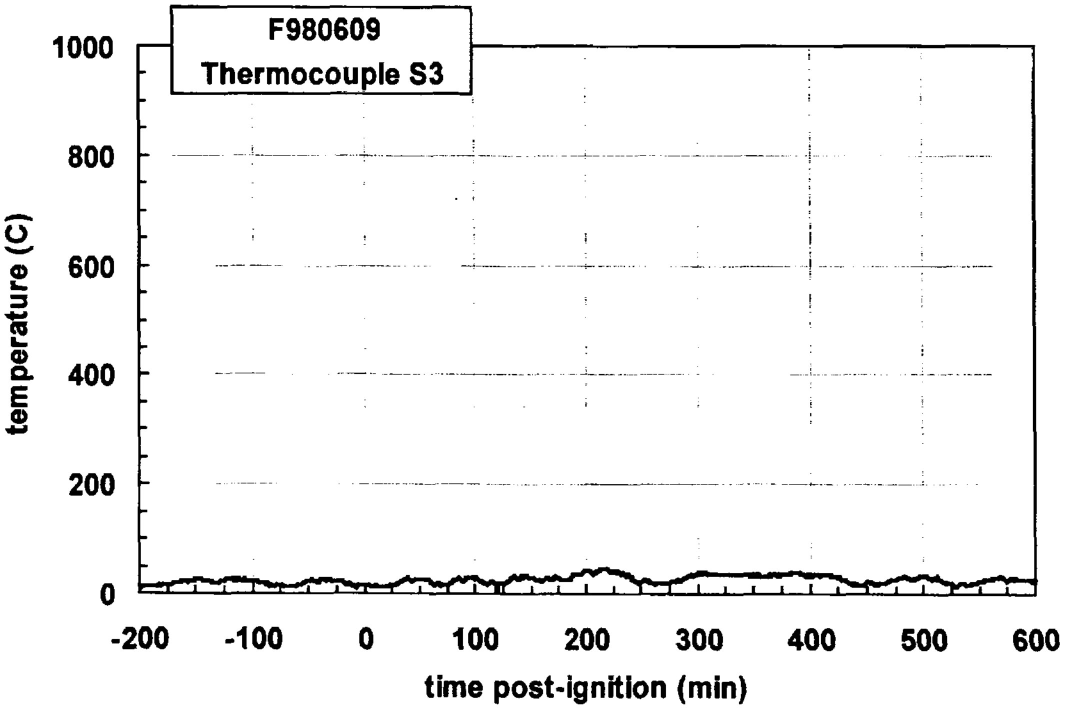

Plot C69. Fire Test F980609. Data plot from thermocouple S3.

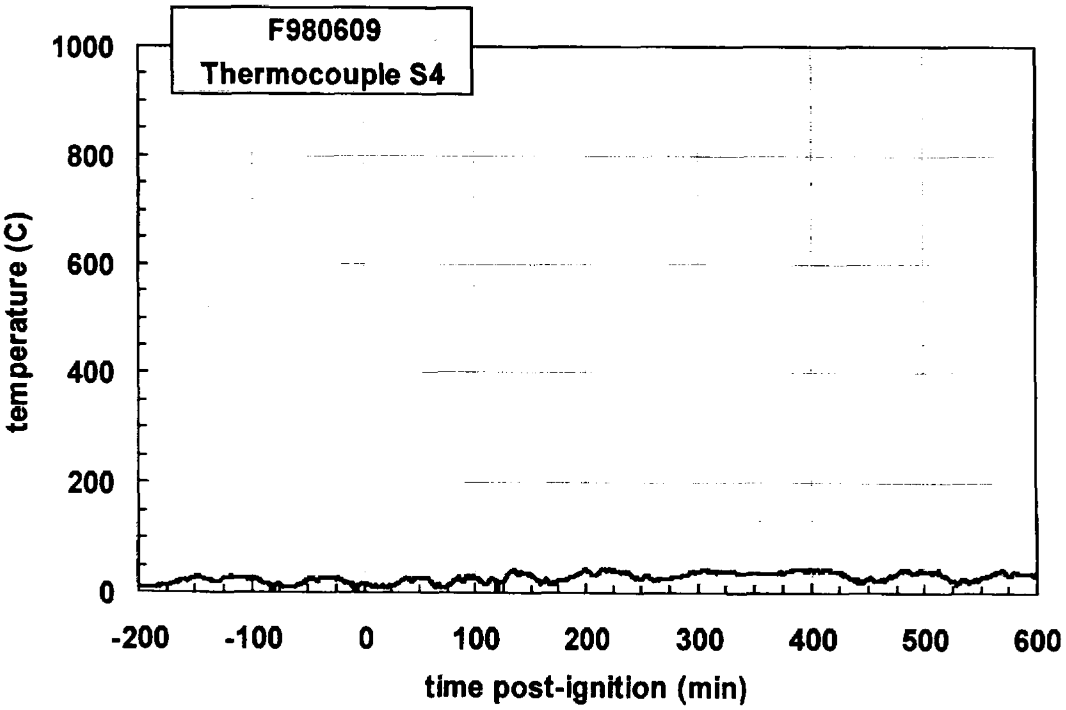

Plot C70. Fire Test F980609. Data plot from thermocouple S4.

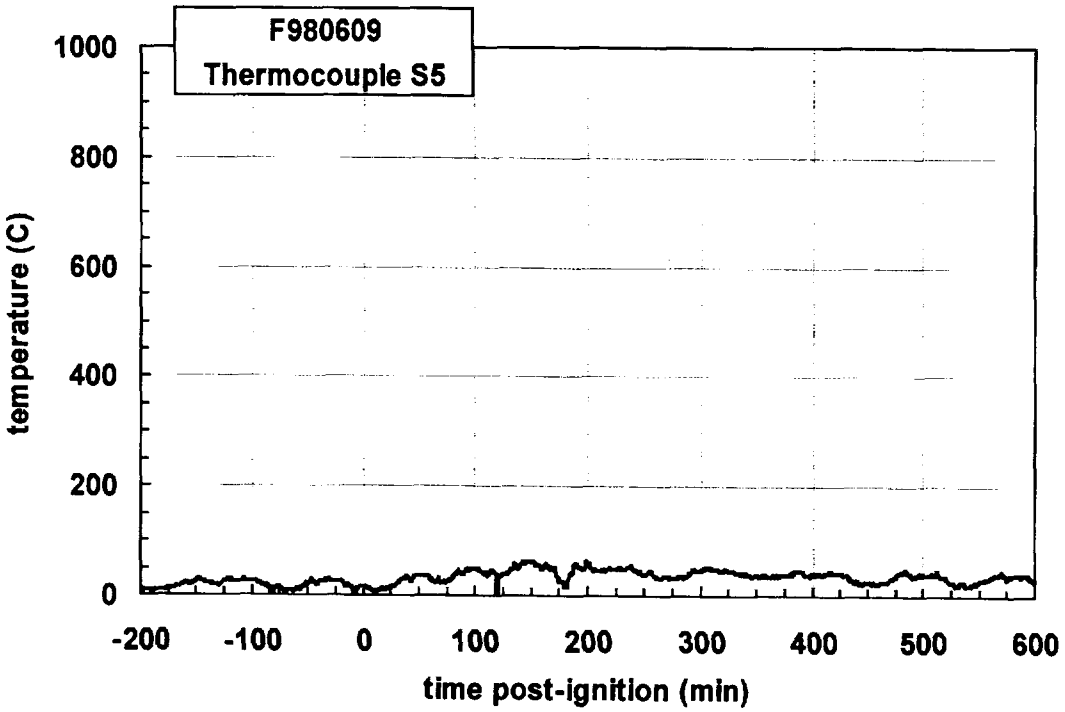

Plot C71. Fire Test F980609. Data plot from thermocouple S5.

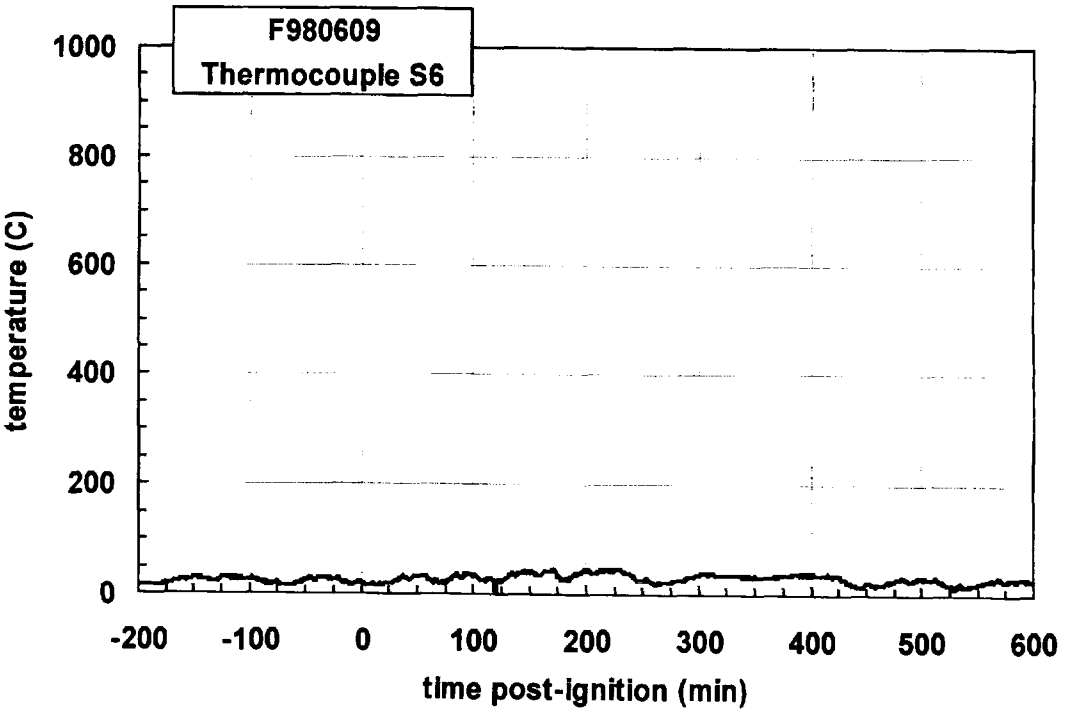

Plot C72. Fire Test F980609. Data plot from thermocouple S6.

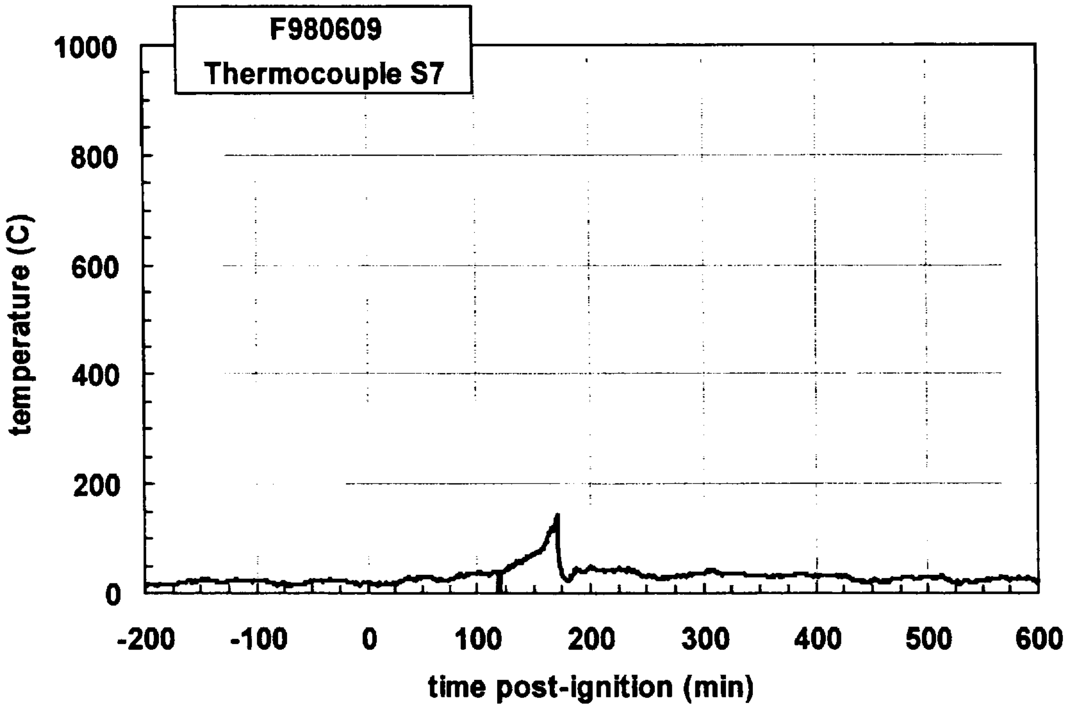

Plot C73. Fire Test F980609. Data plot from thermocouple S7.

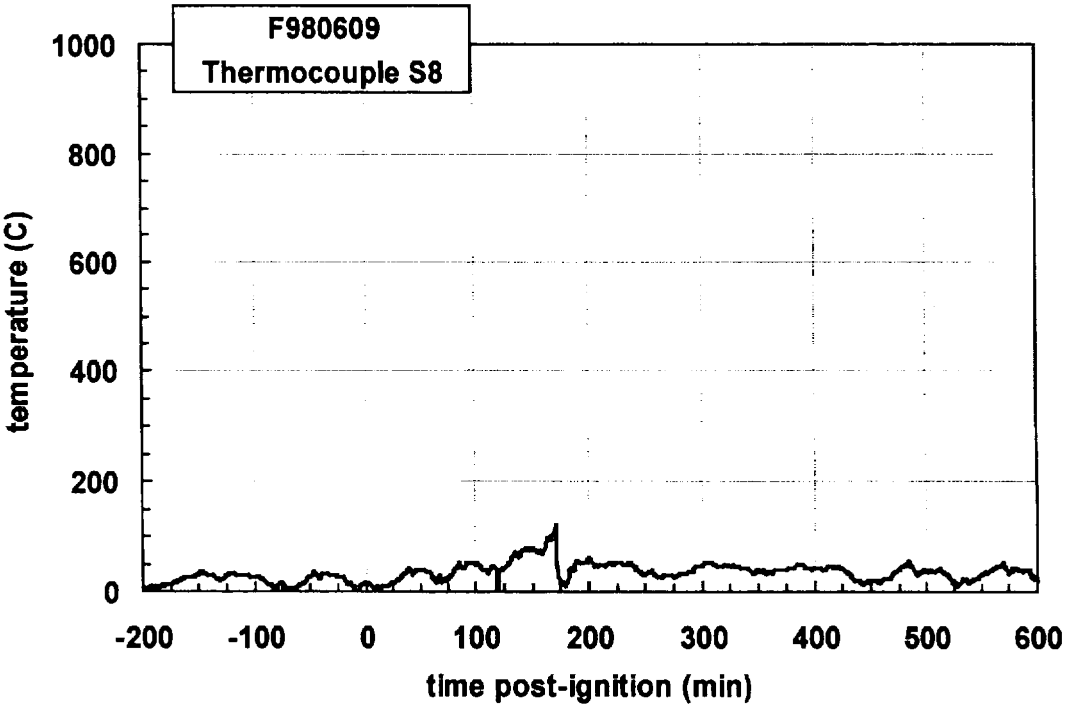

Plot C74. Fire Test F980609. Data plot from thermocouple S8.

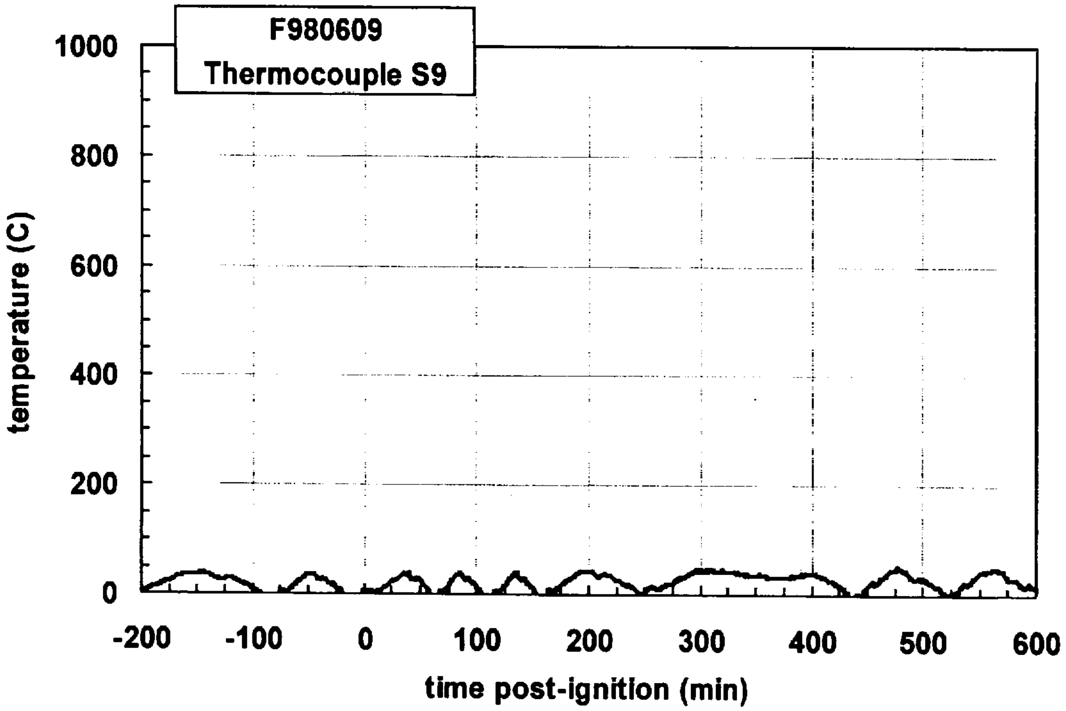

Plot C75. Fire Test F980609. Data plot from thermocouple S9.

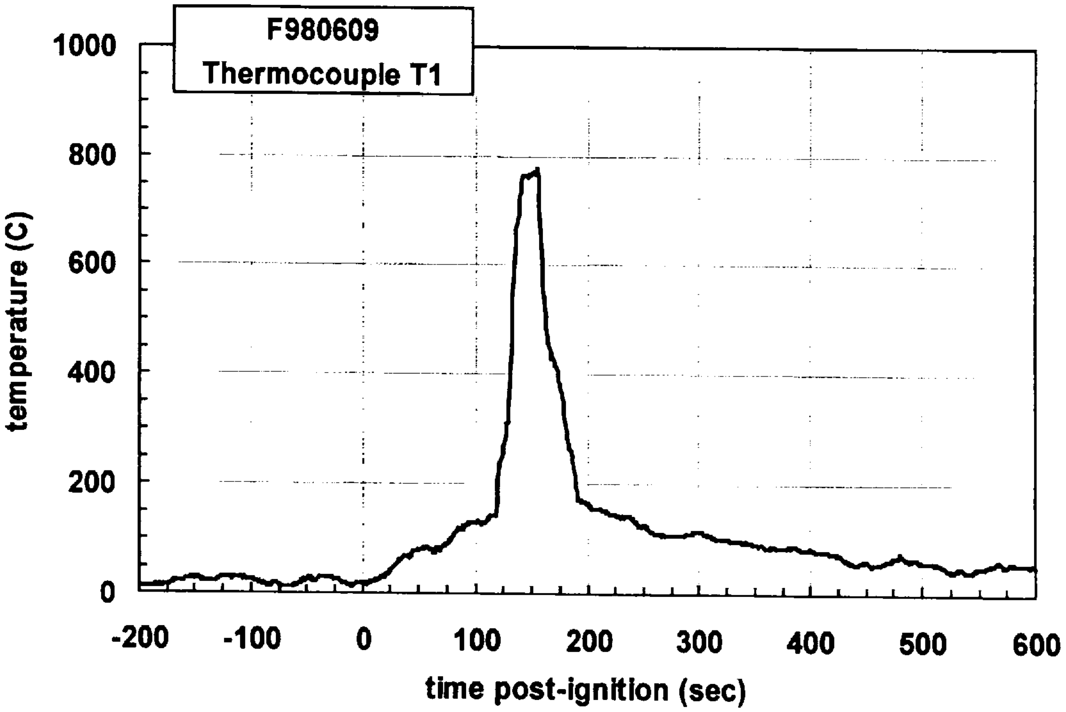

Plot C76. Fire Test F980609. Data plot from thermocouple T1.

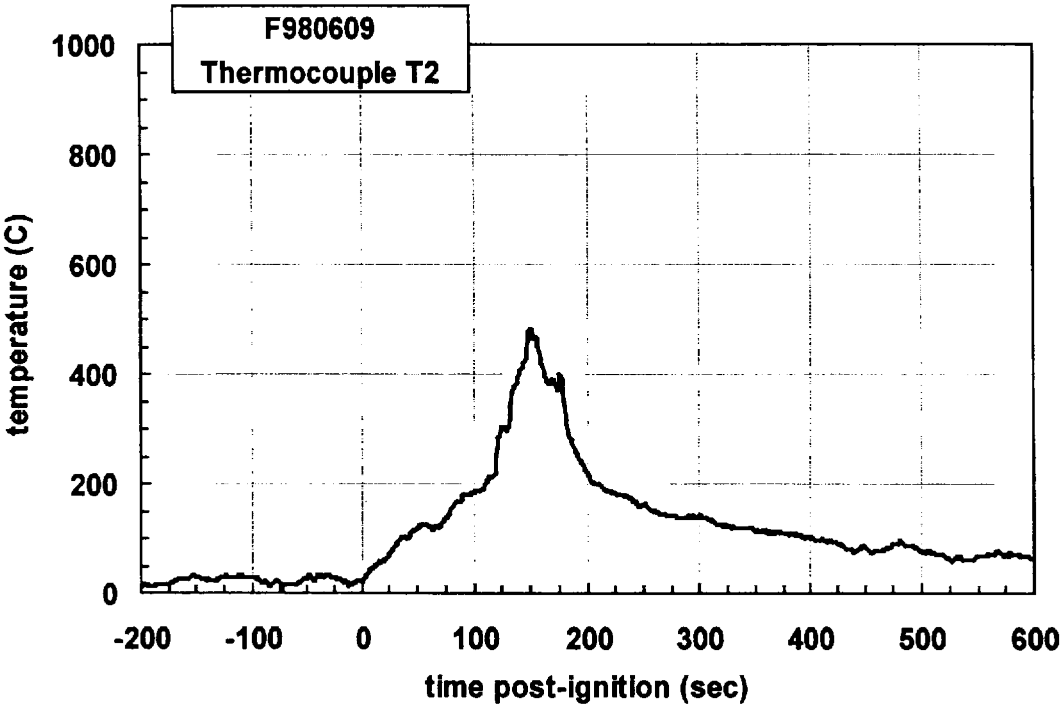

Plot C77. Fire Test F980609. Data plot from thermocouple T2.

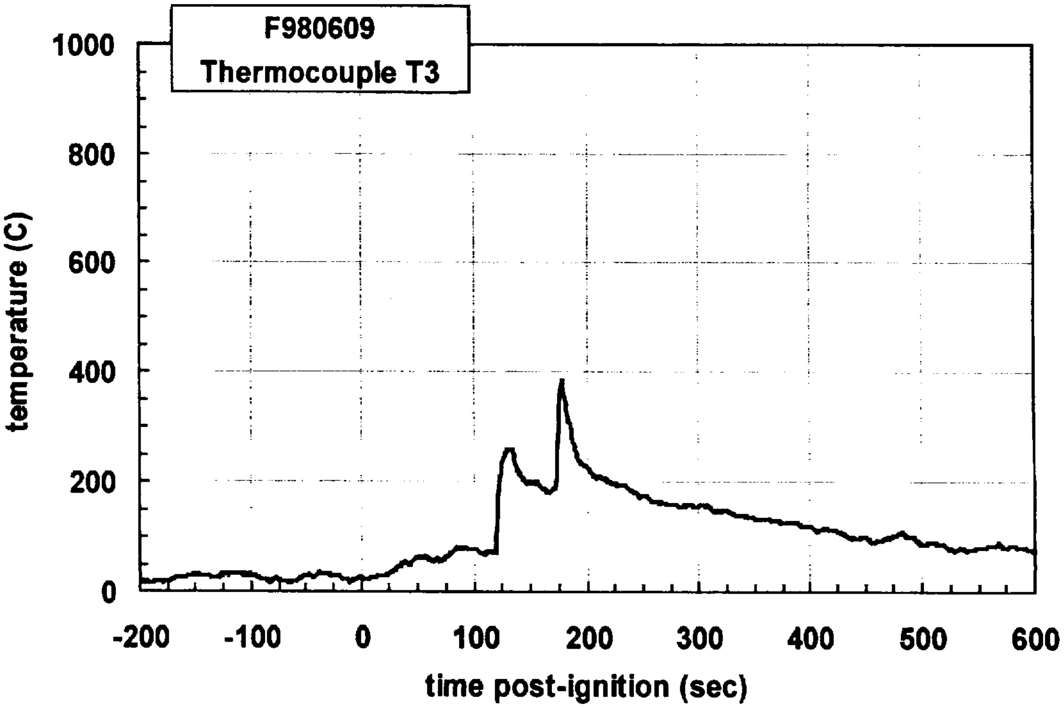

Plot C78. Fire Test F980609. Data plot from thermocouple T3.

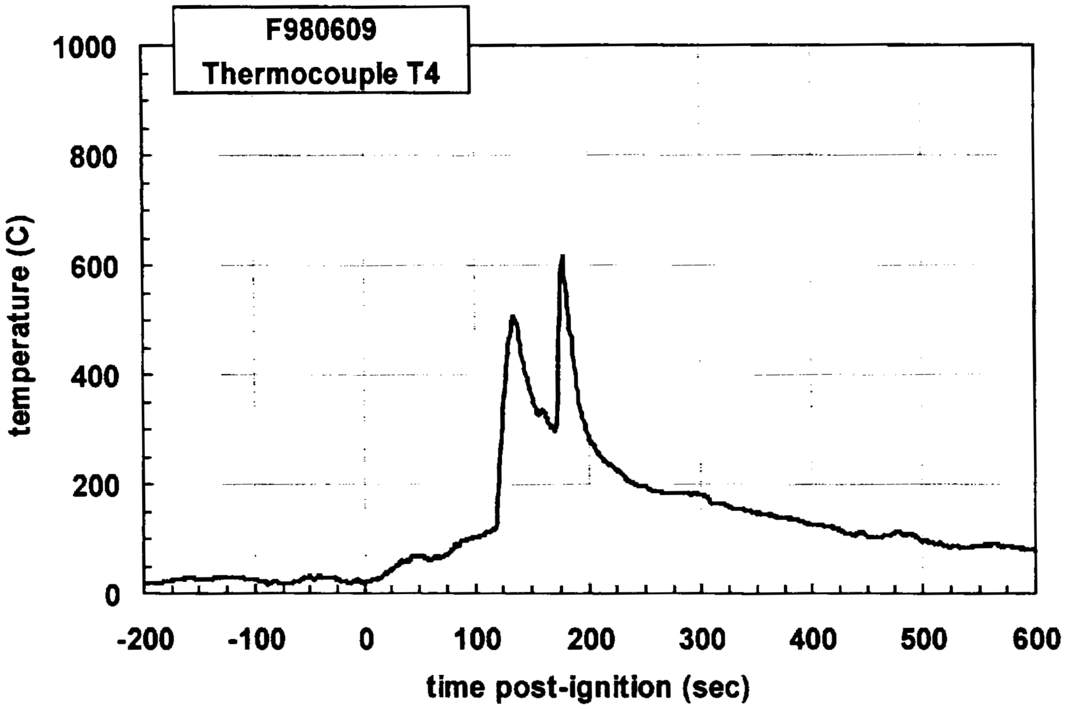

Plot C79. Fire Test F980609. Data plot from thermocouple T4.

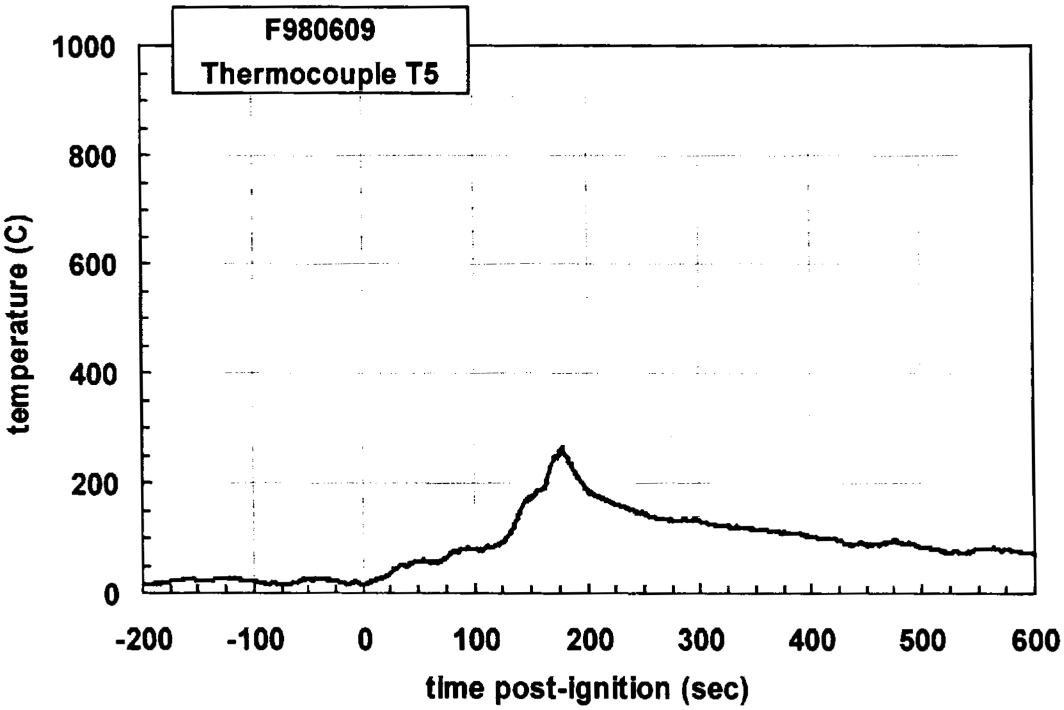

Plot C80. Fire Test F980609. Data plot from thermocouple T5.

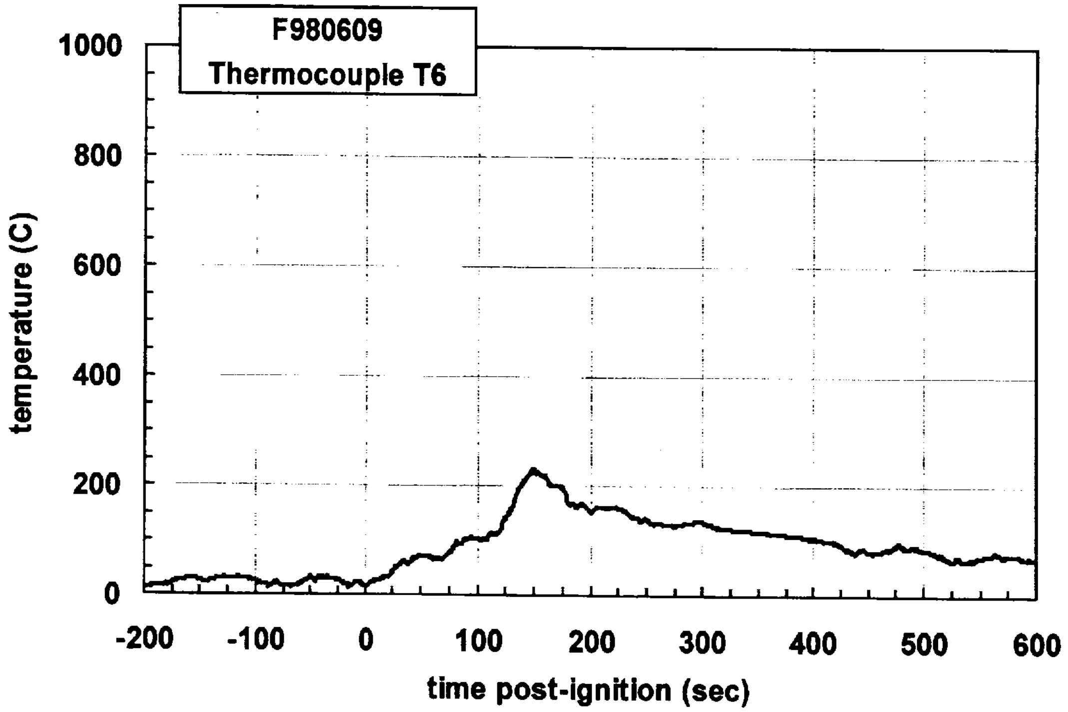

Plot C81. Fire Test F980609. Data plot from thermocouple T6.

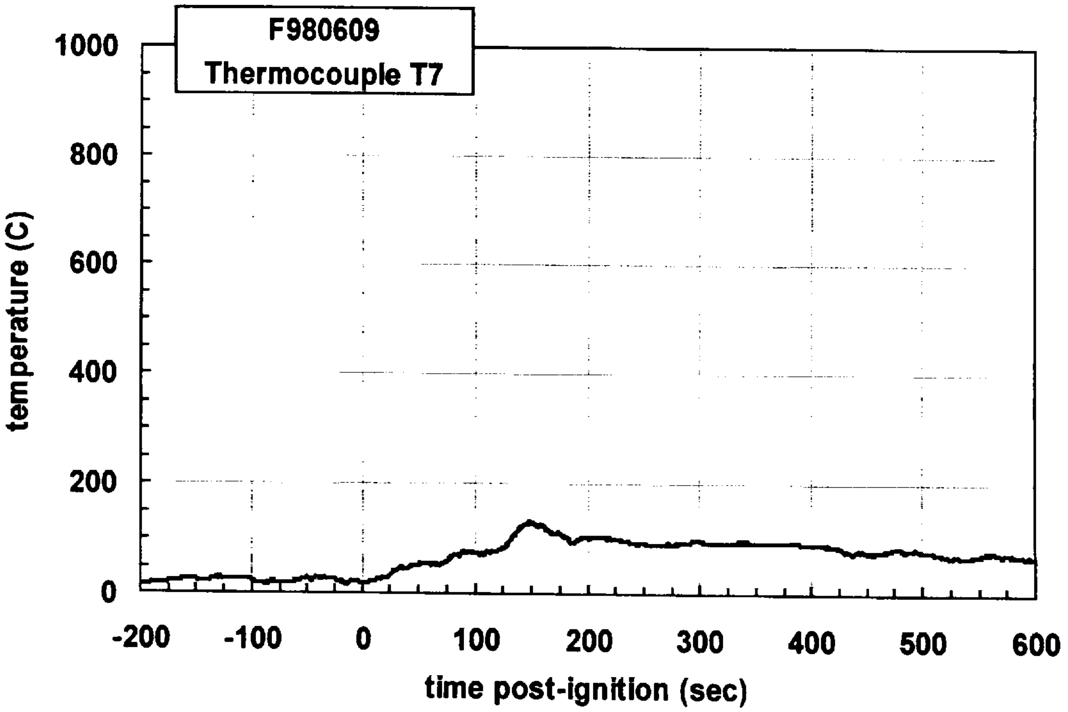

Plot C82. Fire Test F980609. Data plot from thermocouple T7.

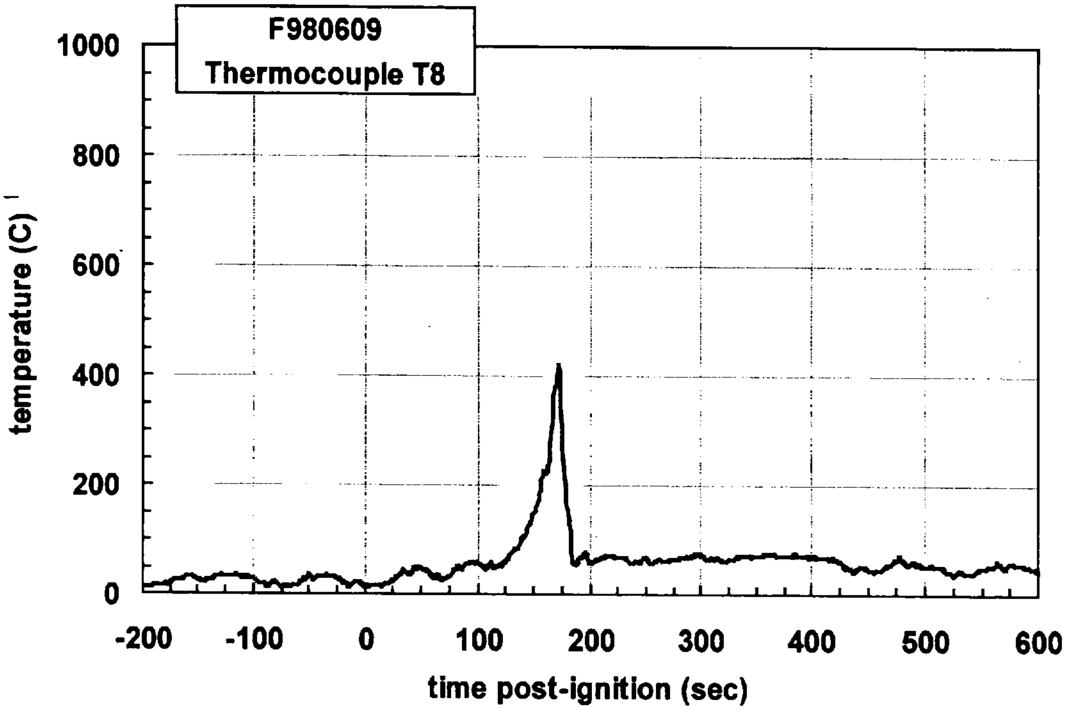

Plot C83. Fire Test F980609. Data plot from thermocouple T8.

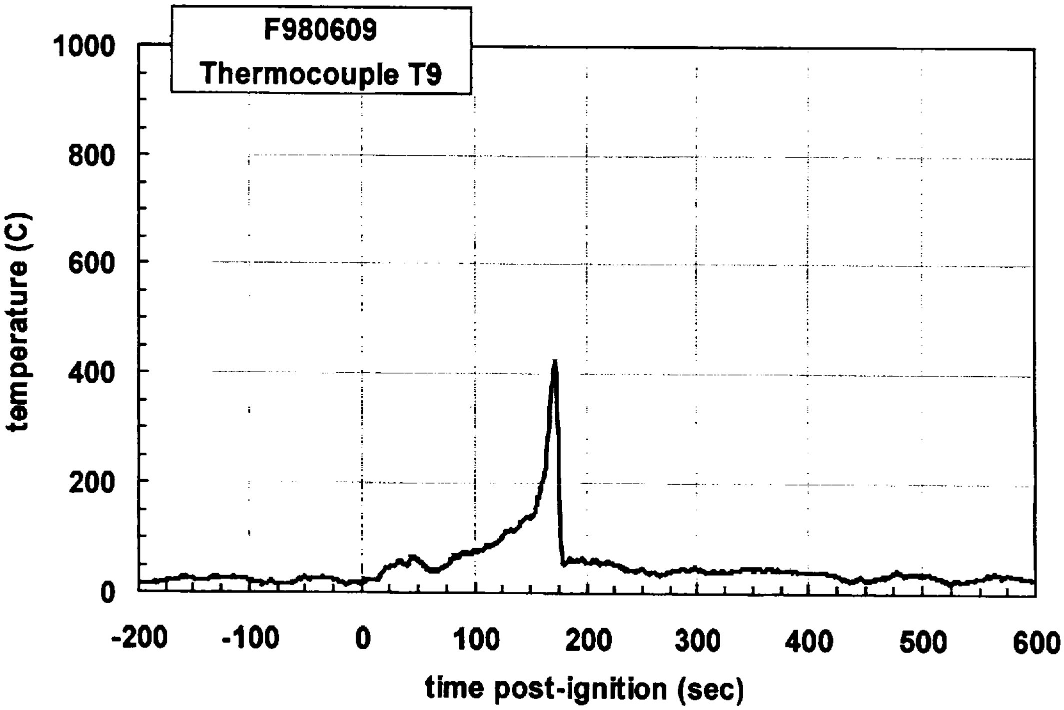

Plot C84. Fire Test F980609. Data plot from thermocouple T9.

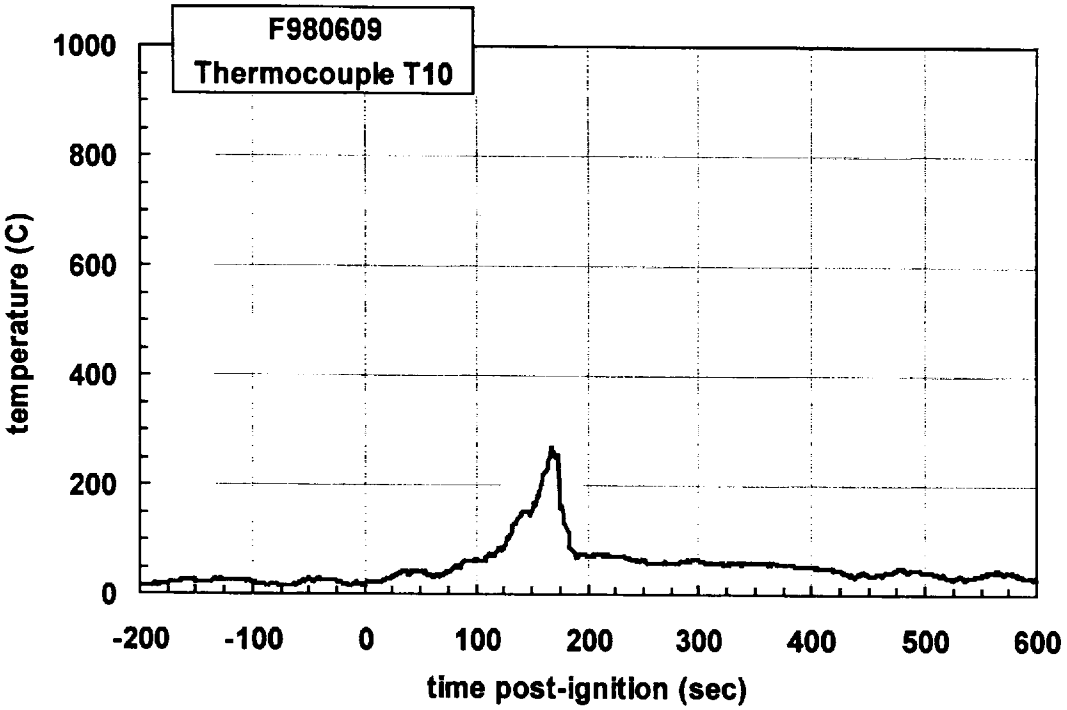

Plot C85. Fire Test F980609. Data plot from thermocouple T10.

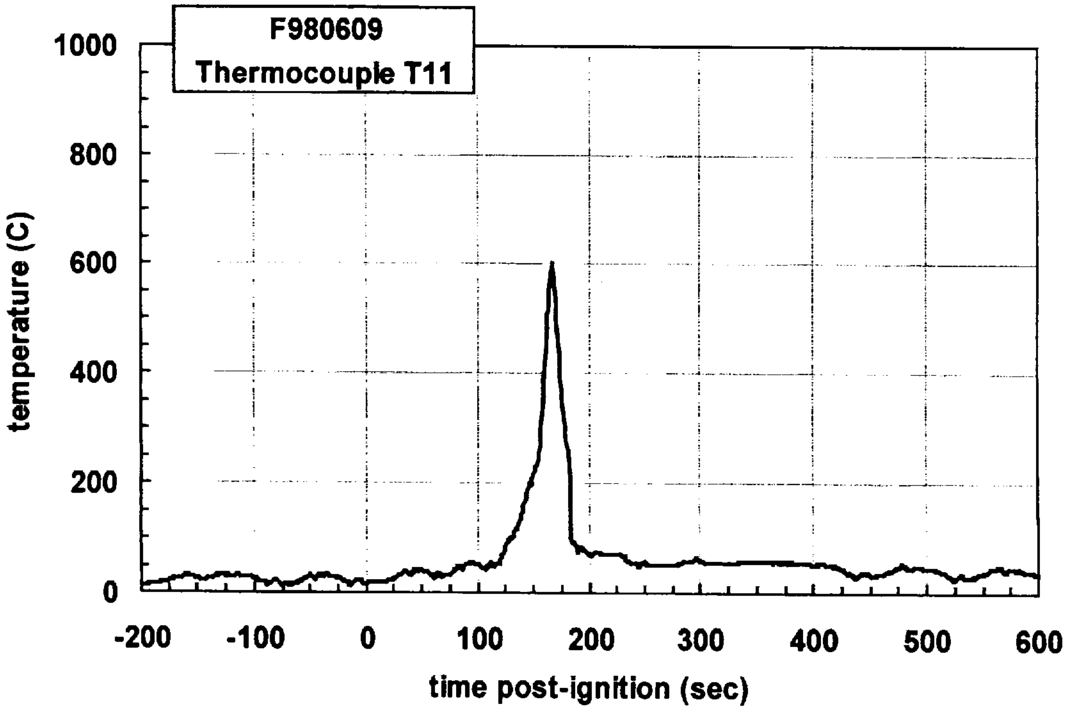

Plot C86. Fire Test F980609. Data plot from thermocouple T11.

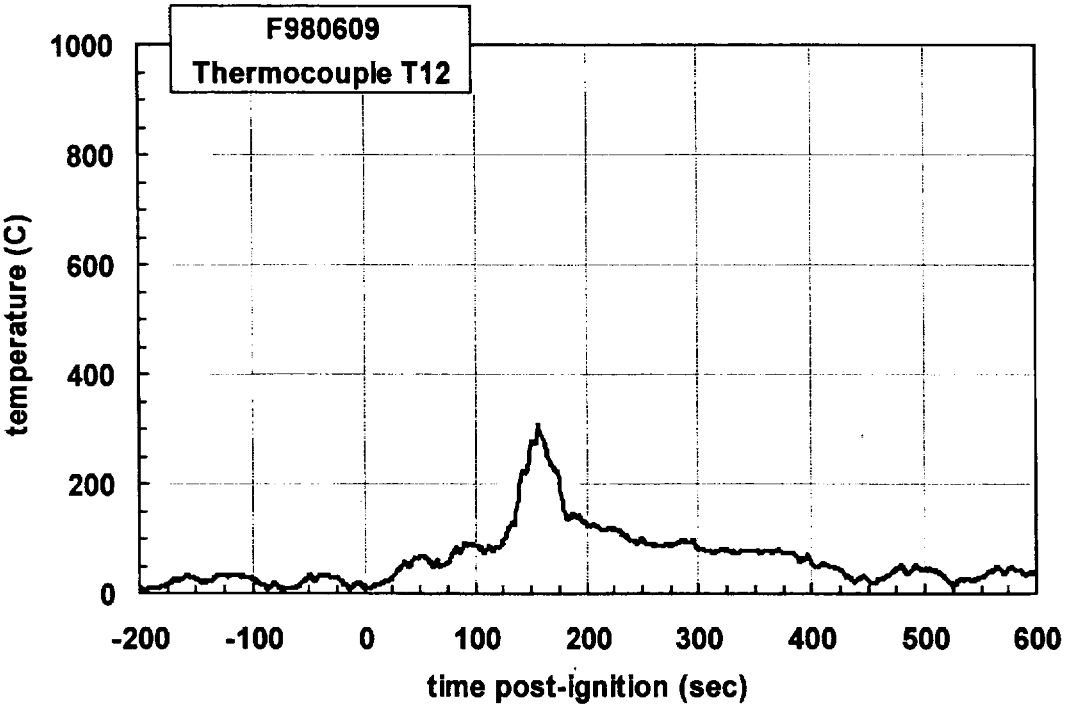

Plot C87. Fire Test F980609. Data plot from thermocouple T12.

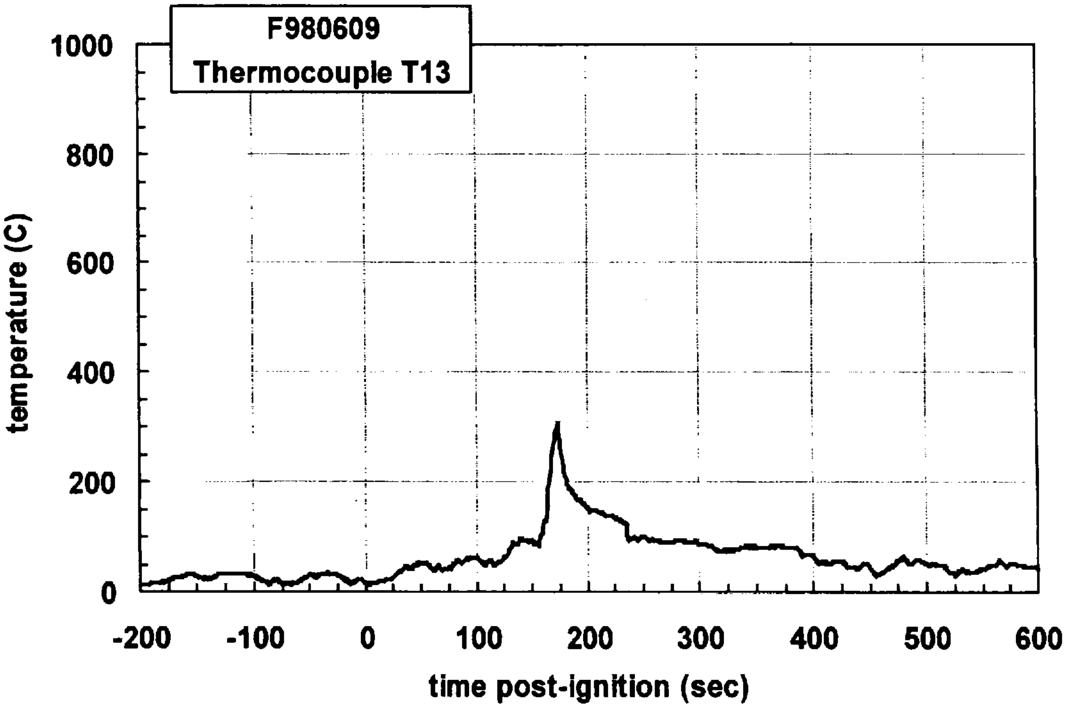

Plot C88. Fire Test F980609. Data plot from thermocouple T13.

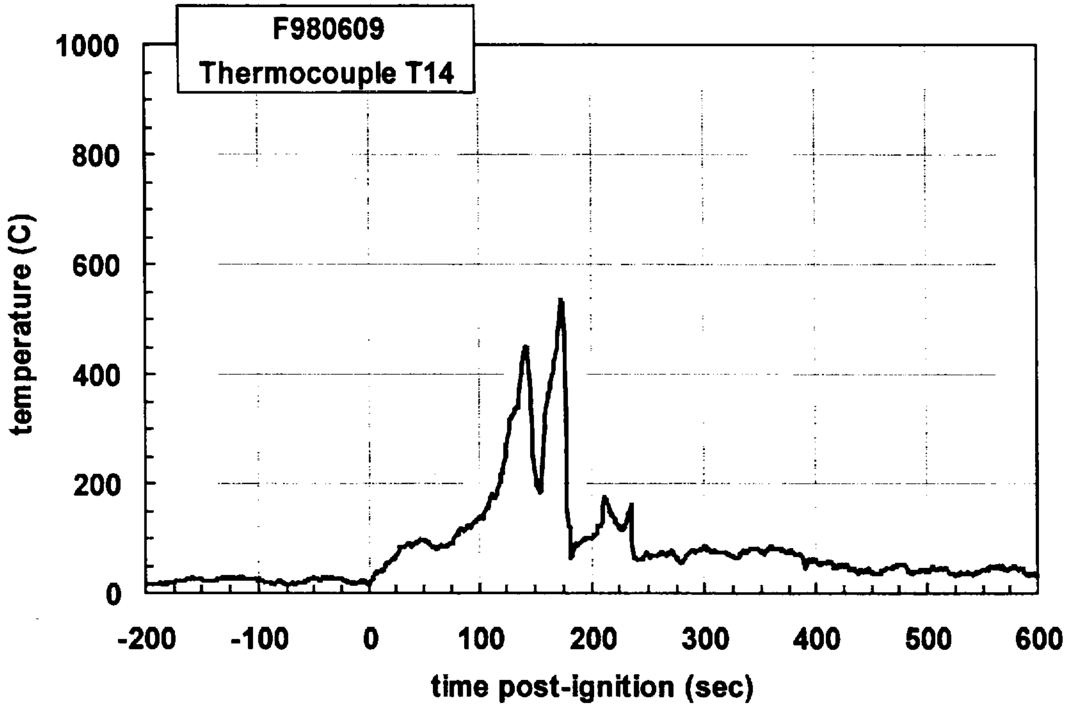

Plot C89. Fire Test F980609. Data plot from thermocouple T14.

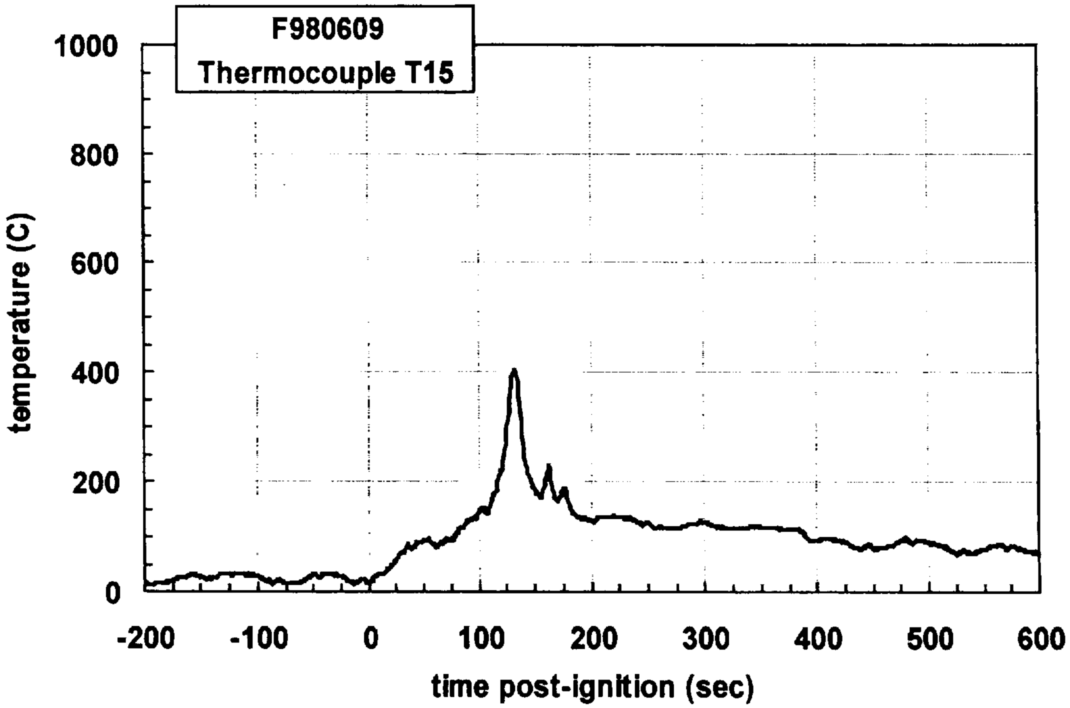

Plot C90. Fire Test F980609. Data plot from thermocouple T15.

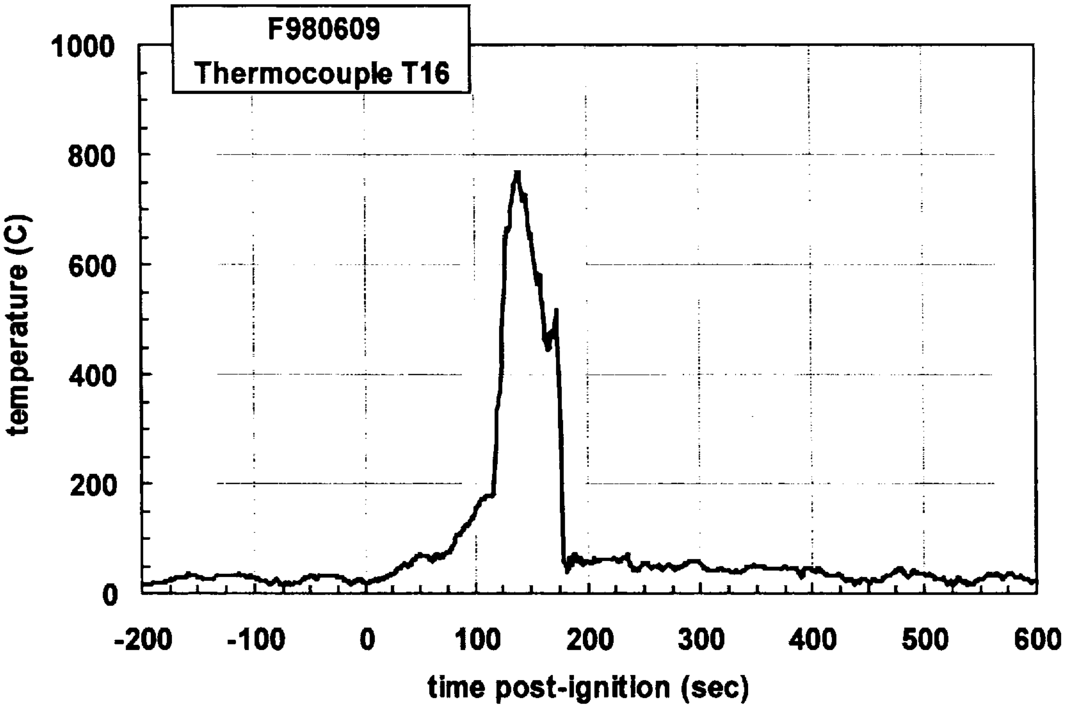

Plot C91. Fire Test F980609. Data plot from thermocouple T16.

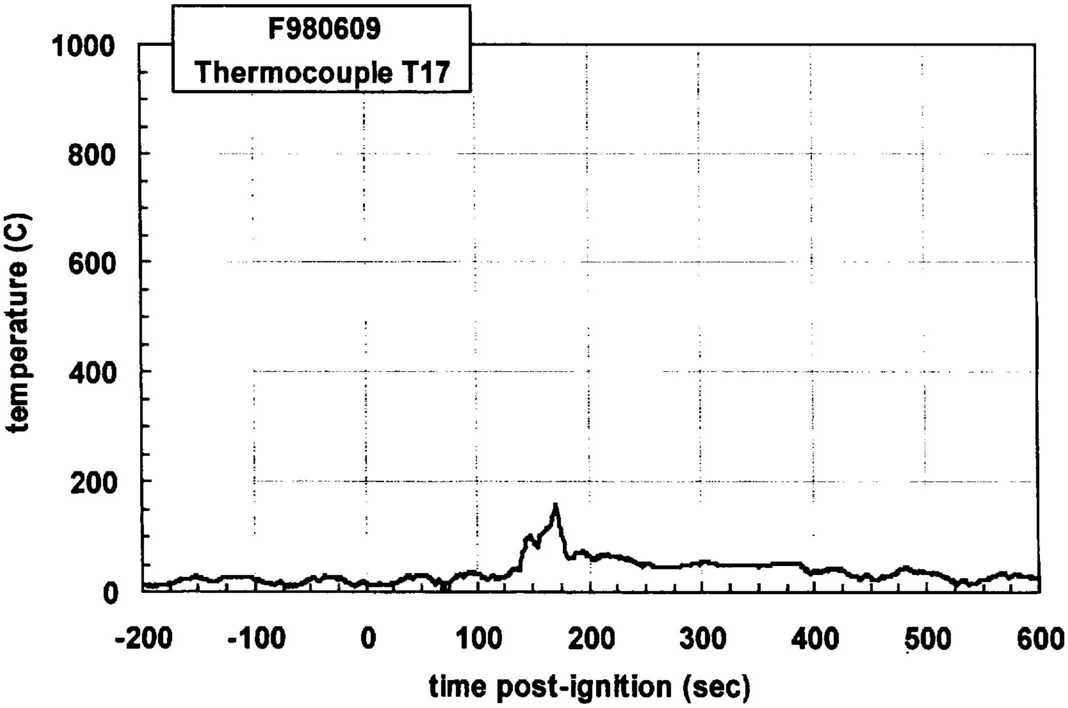

Plot C92. Fire Test F980609. Data plot from thermocouple T17.

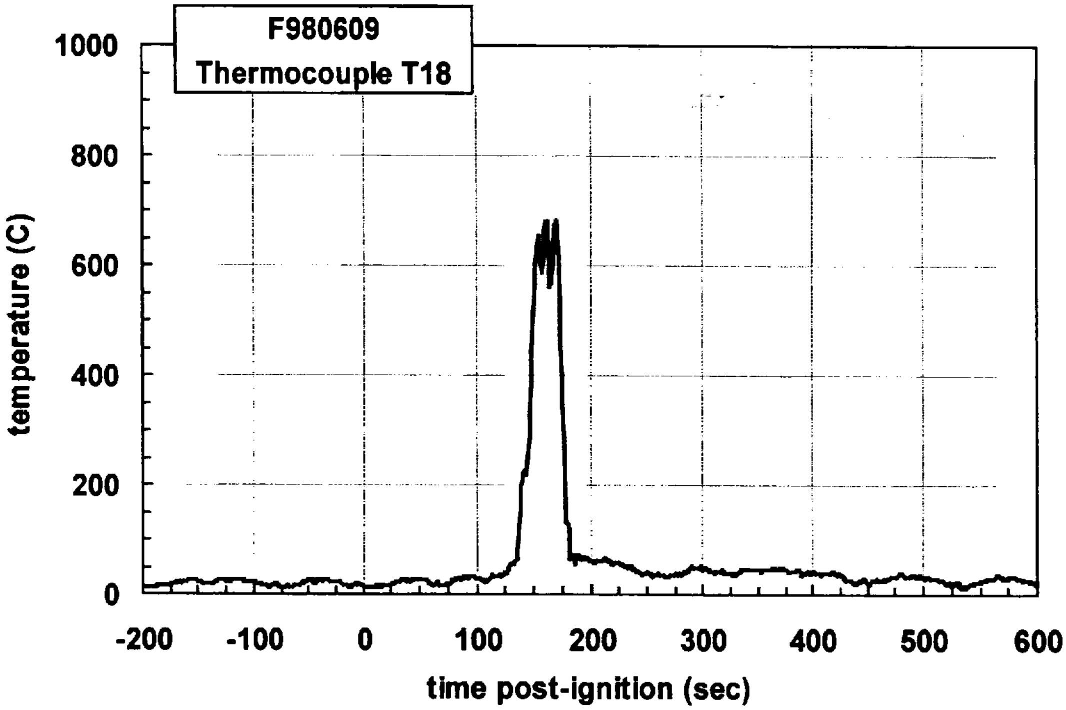

Plot C93. Fire Test F980609. Data plot from thermocouple T18.

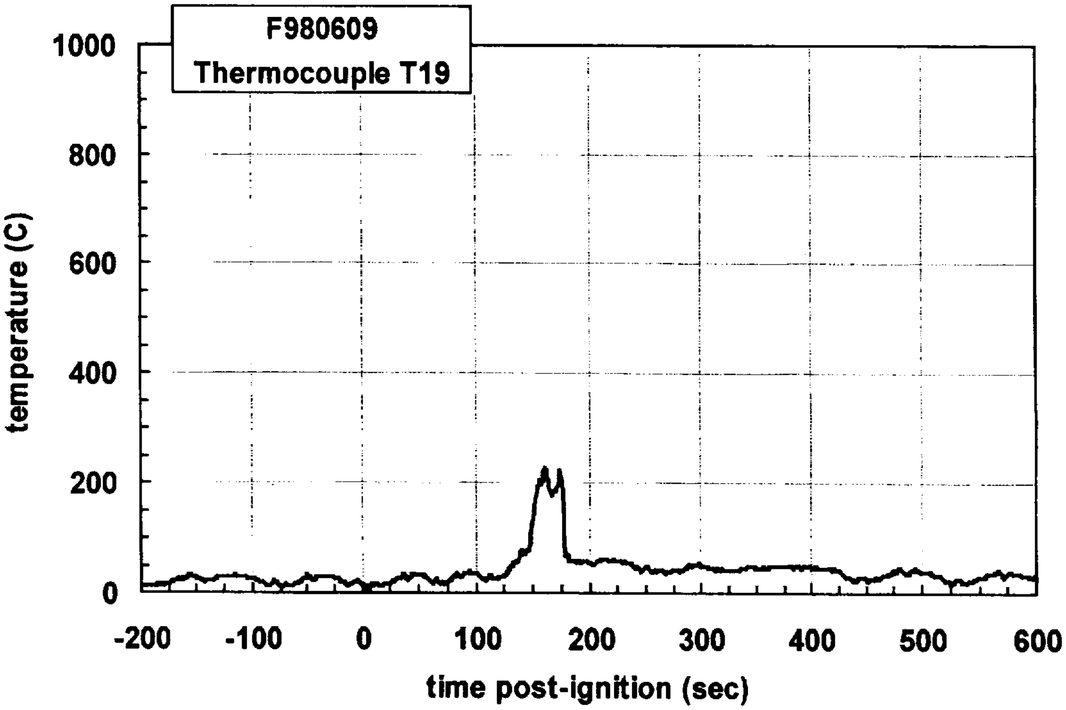

Plot C94. Fire Test F980609. Data plot from thermocouple T19.

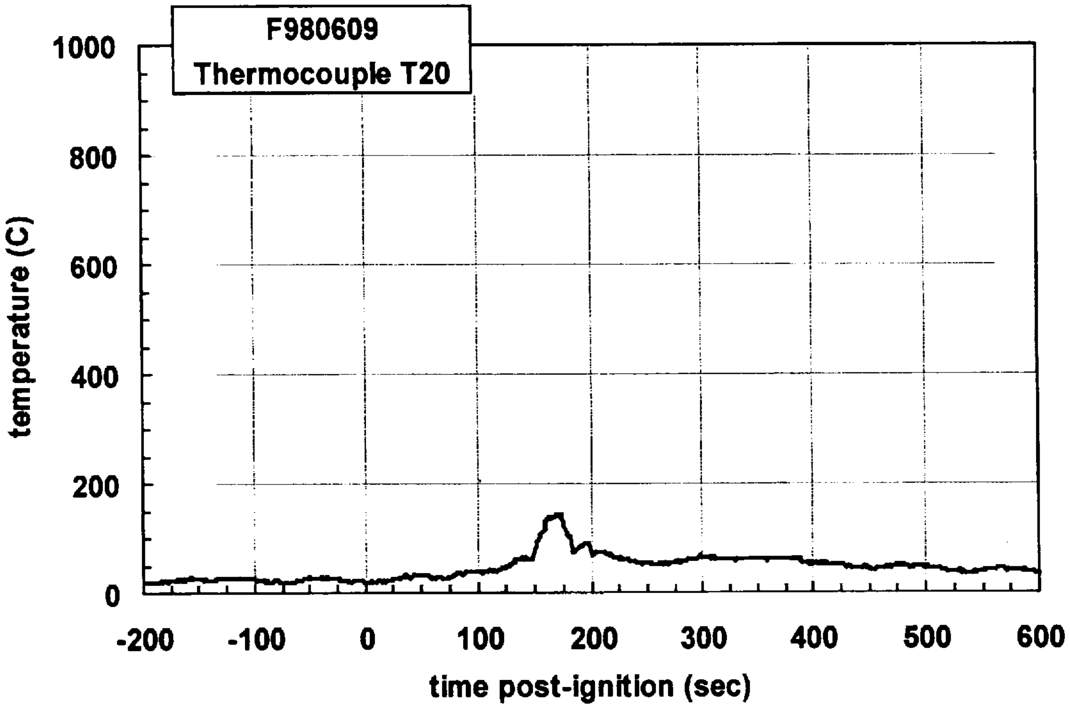

Plot C95. Fire Test F980609. Data plot from thermocouple T20.

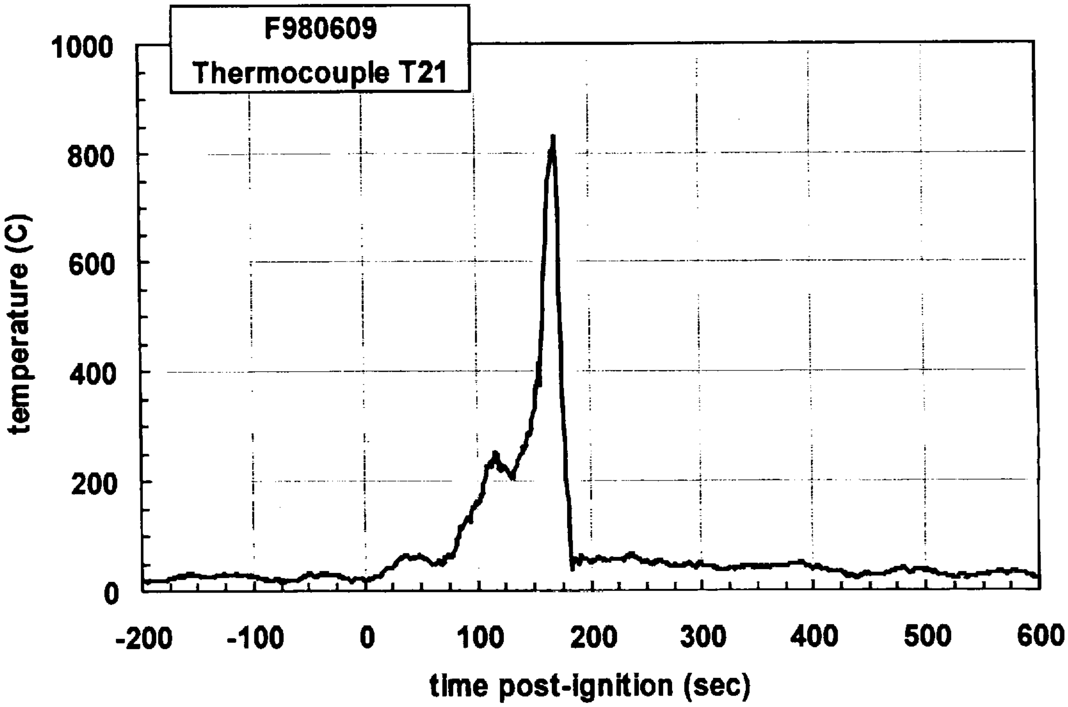

Plot C96. Fire Test F980609. Data plot from thermocouple T21.

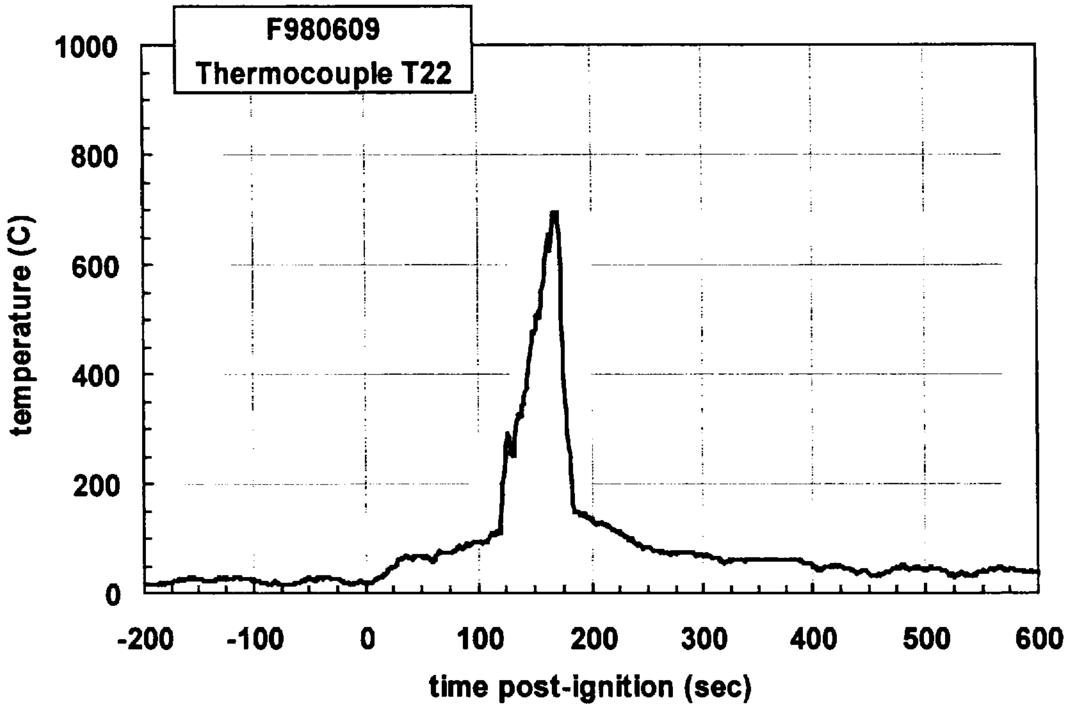

Plot C97. Fire Test F980609. Data plot from thermocouple T22.

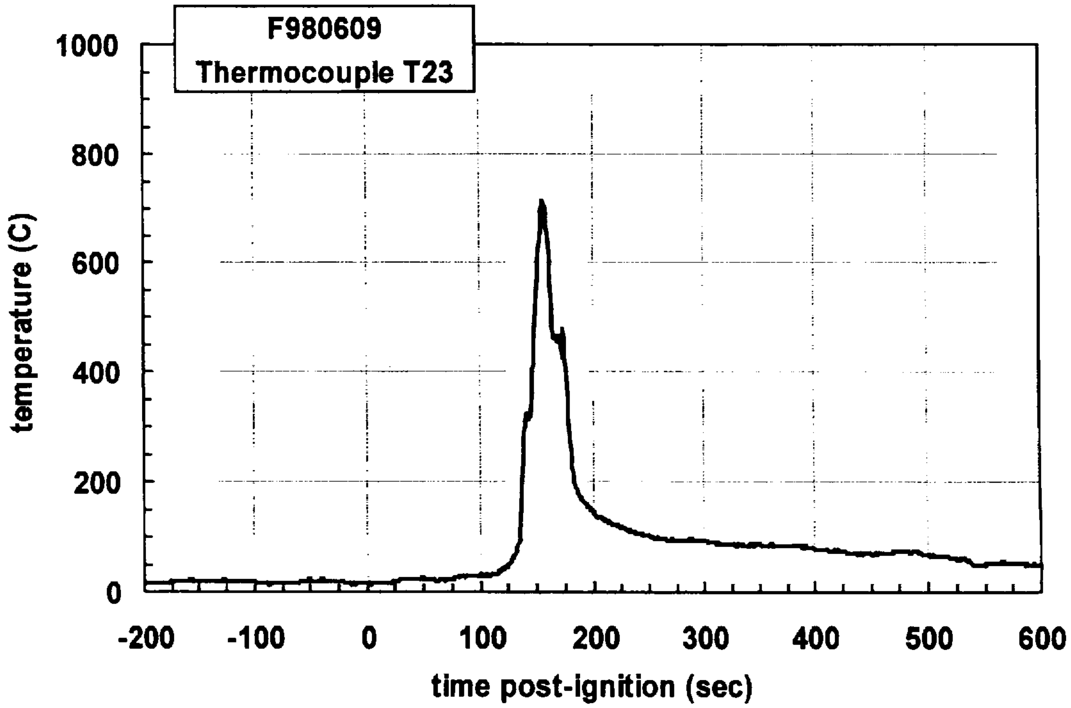

Plot C98. Fire Test F980609. Data plot from thermocouple T23.

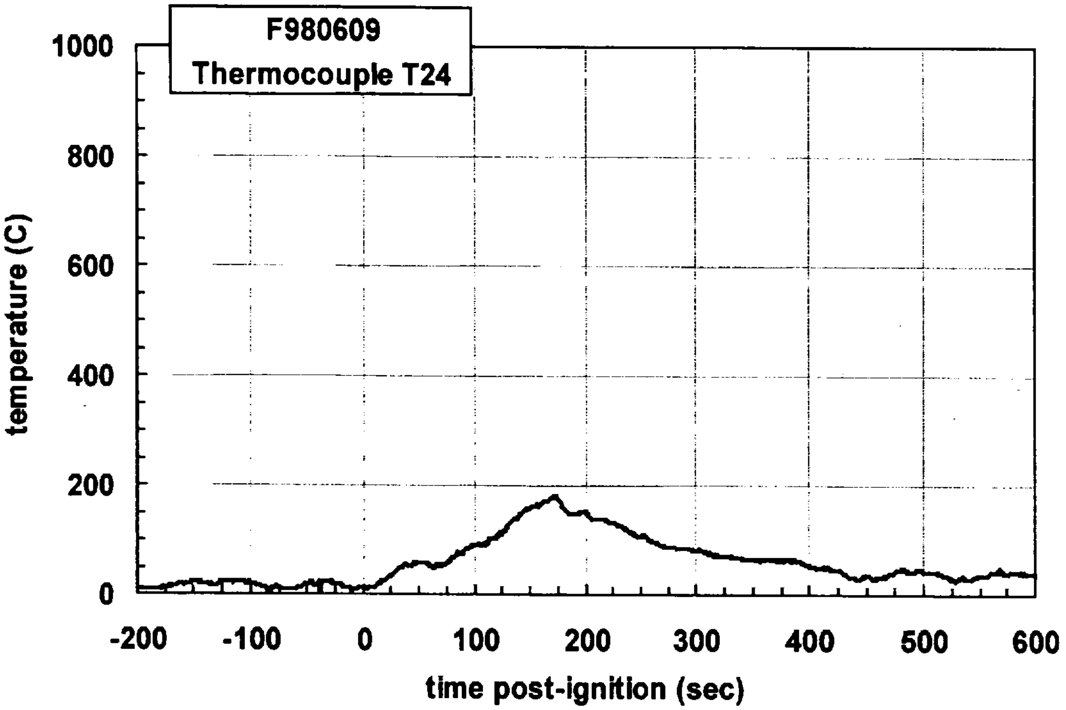

Plot C99. Fire Test F980609. Data plot from thermocouple T24.

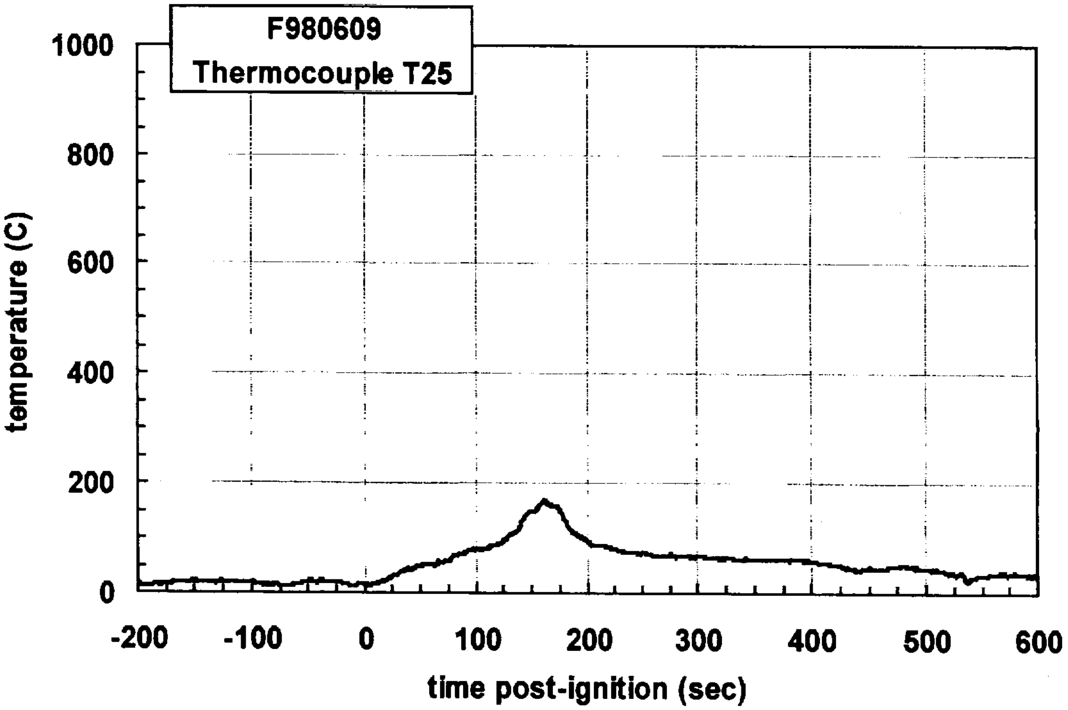

Plot C100. Fire Test F980609. Data plot from thermocouple T25.

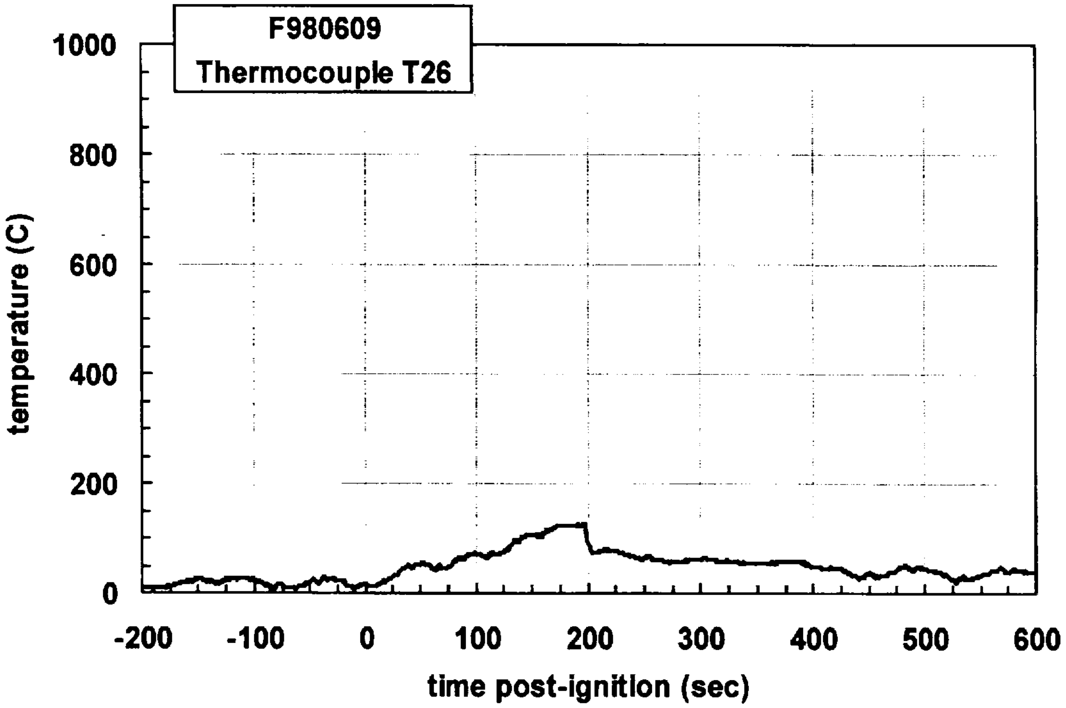

Plot C101. Fire Test F980609. Data plot from thermocouple T26.

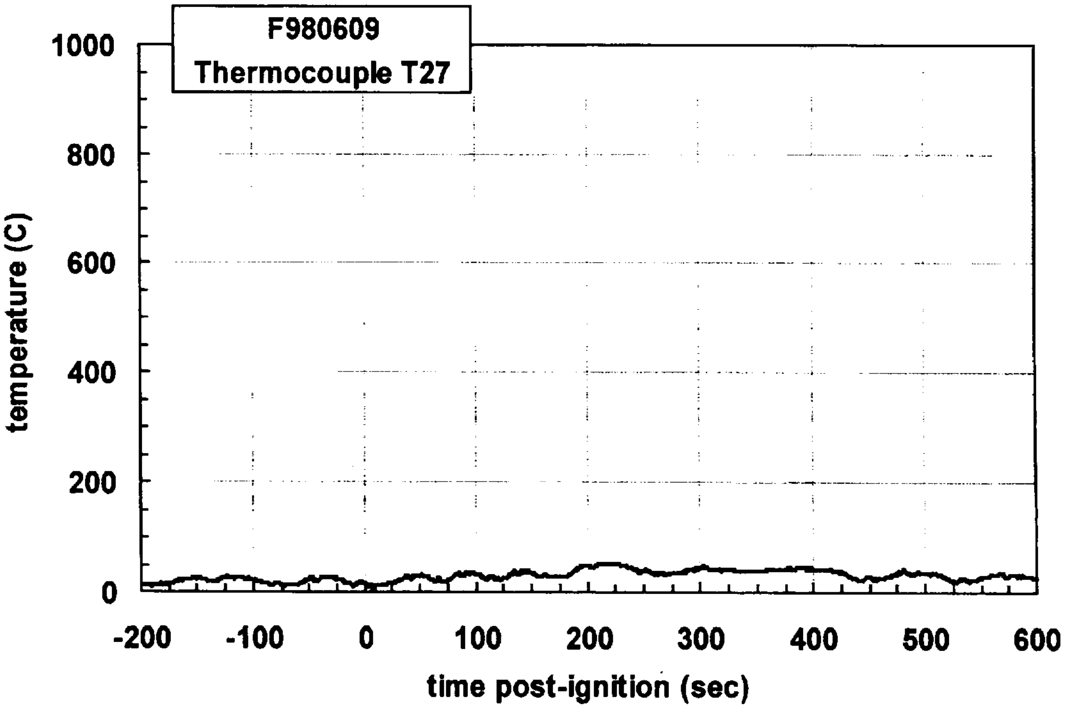

Plot C102. Fire Test F980609. Data plot from thermocouple T27.

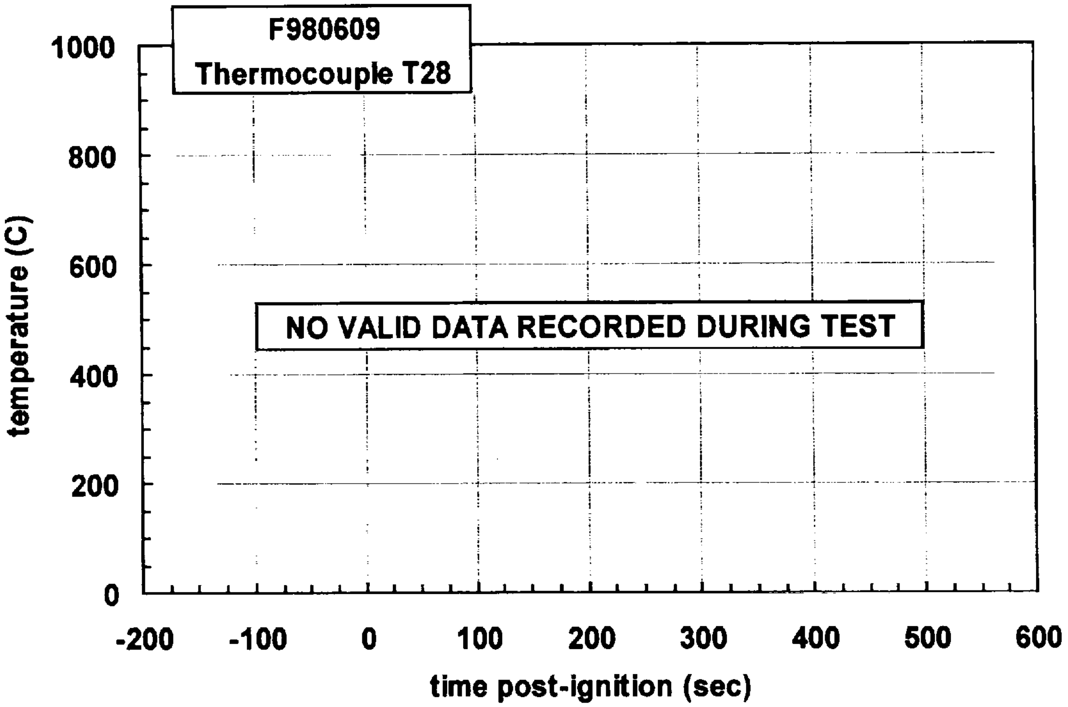

Plot C103. Fire Test F980609. Data plot from thermocouple T28.

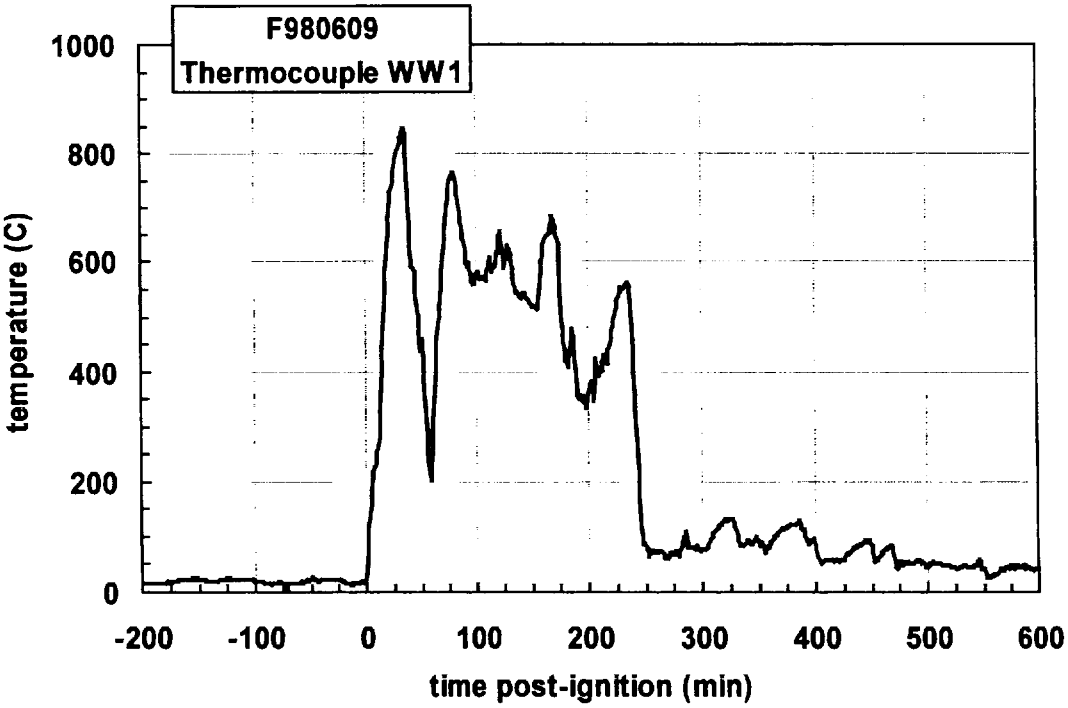

Plot C104. Fire Test F980609. Data plot from thermocouple WW1.

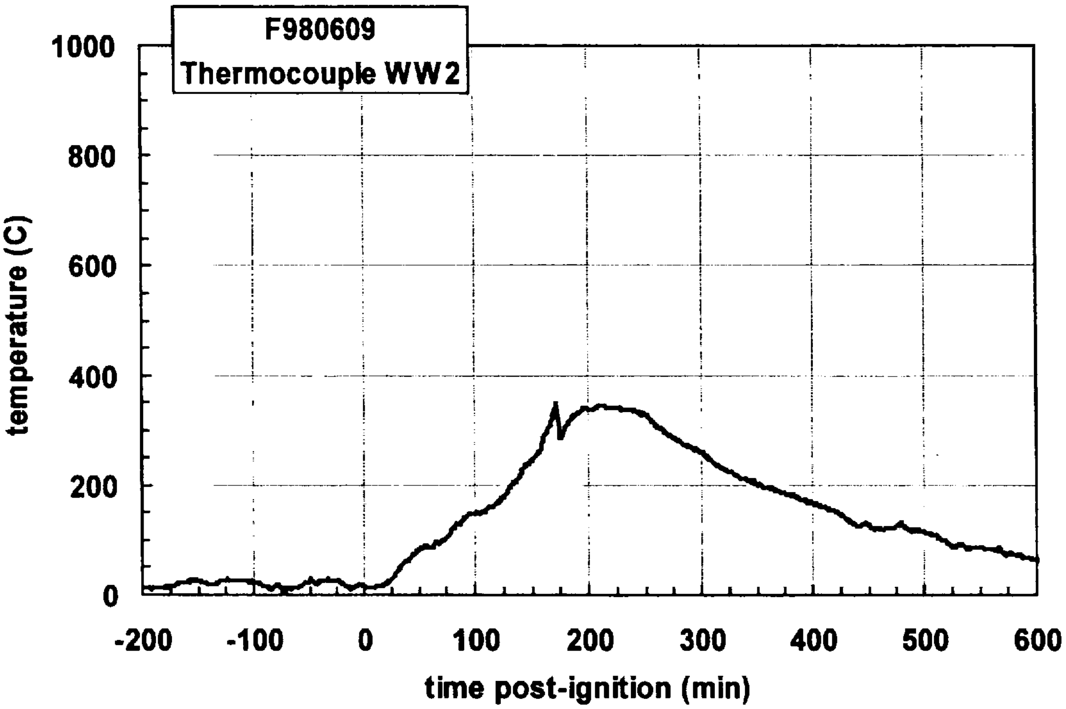

Plot C105. Fire Test F980609. Data plot from thermocouple WW2.

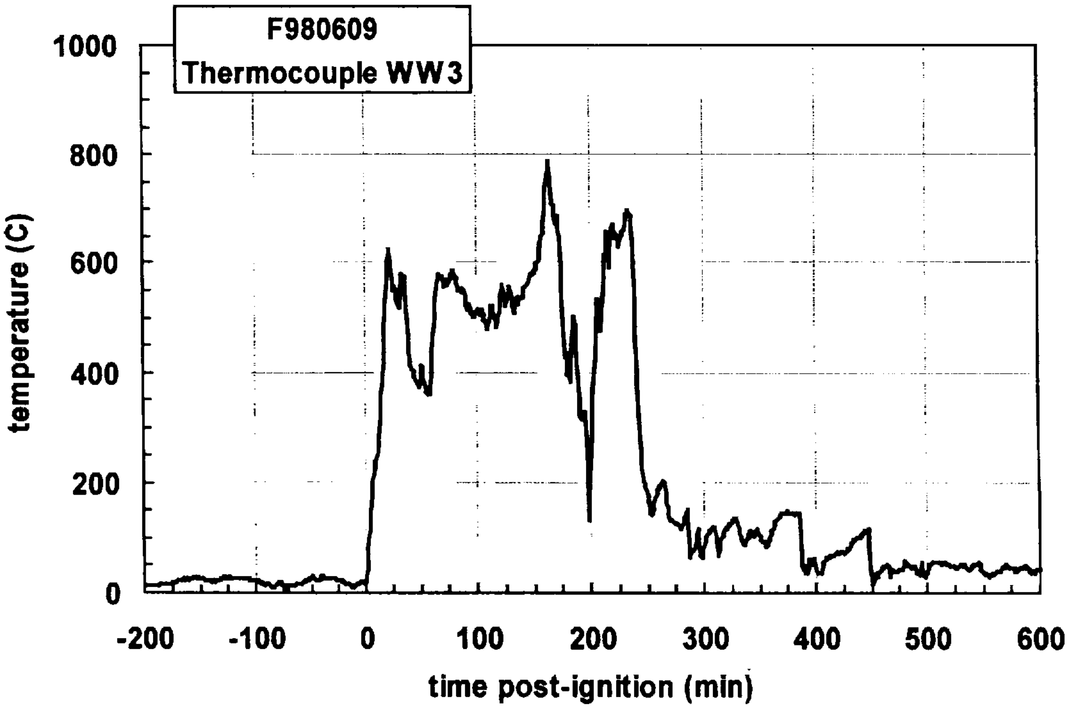

Plot C106. Fire Test F980609. Data plot from thermocouple WW3.

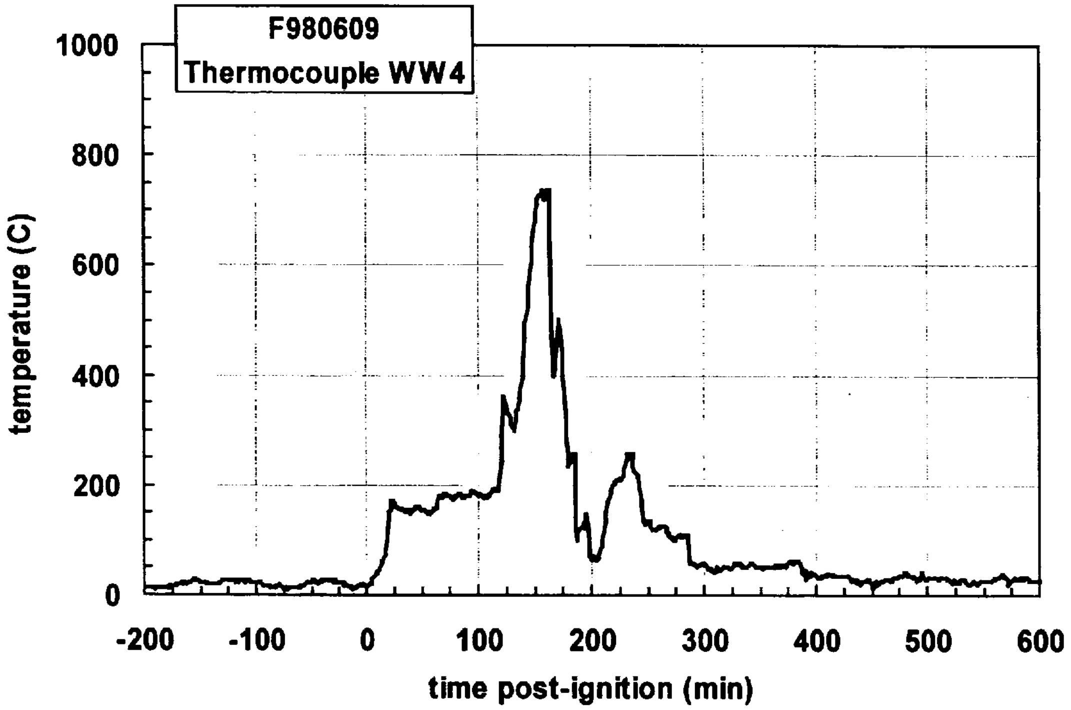

Plot C107. Fire Test F980609. Data plot from thermocouple WW4.

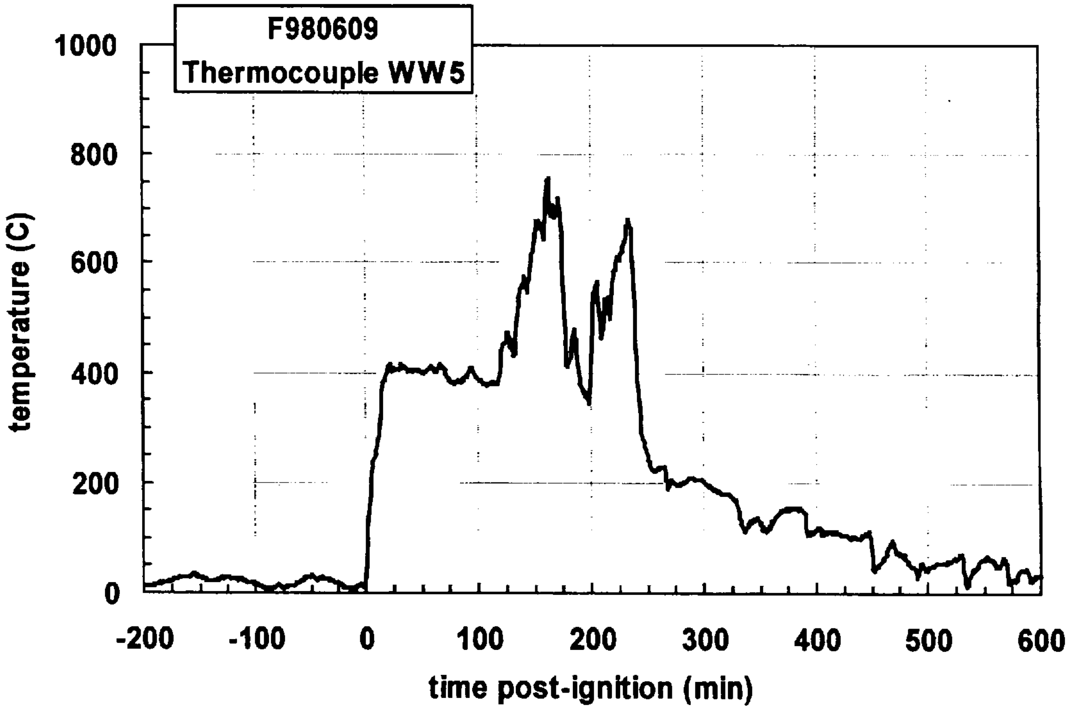

Plot C108. Fire Test F980609. Data plot from thermocouple WW5.

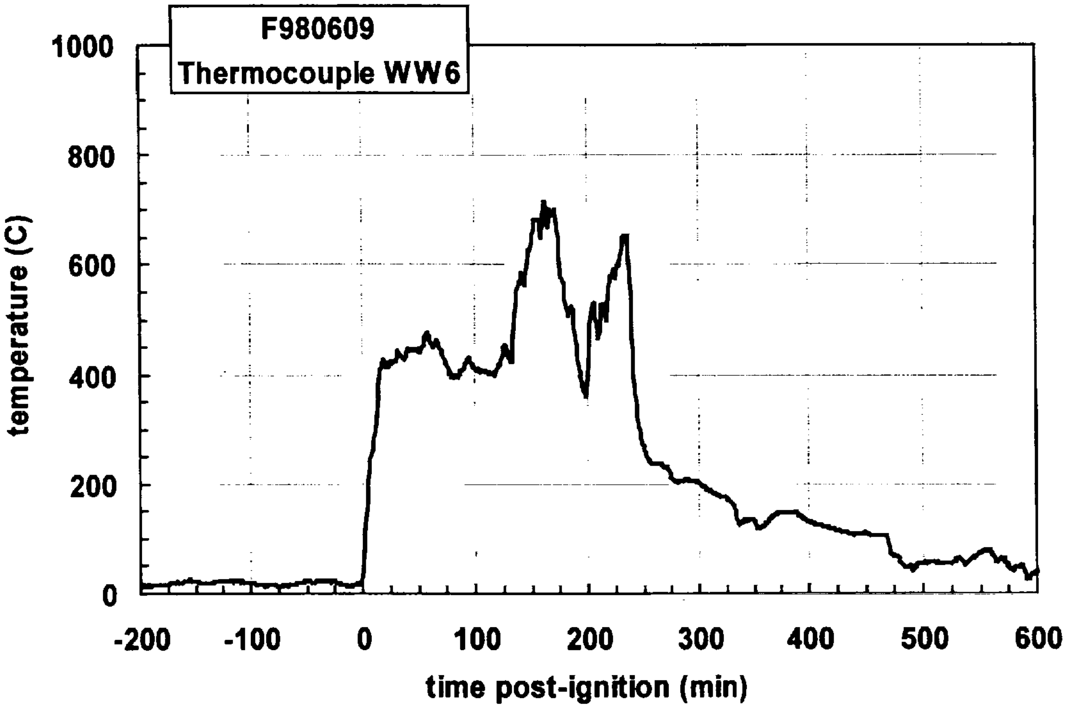

Plot C109. Fire Test F980609. Data plot from thermocouple WW6.

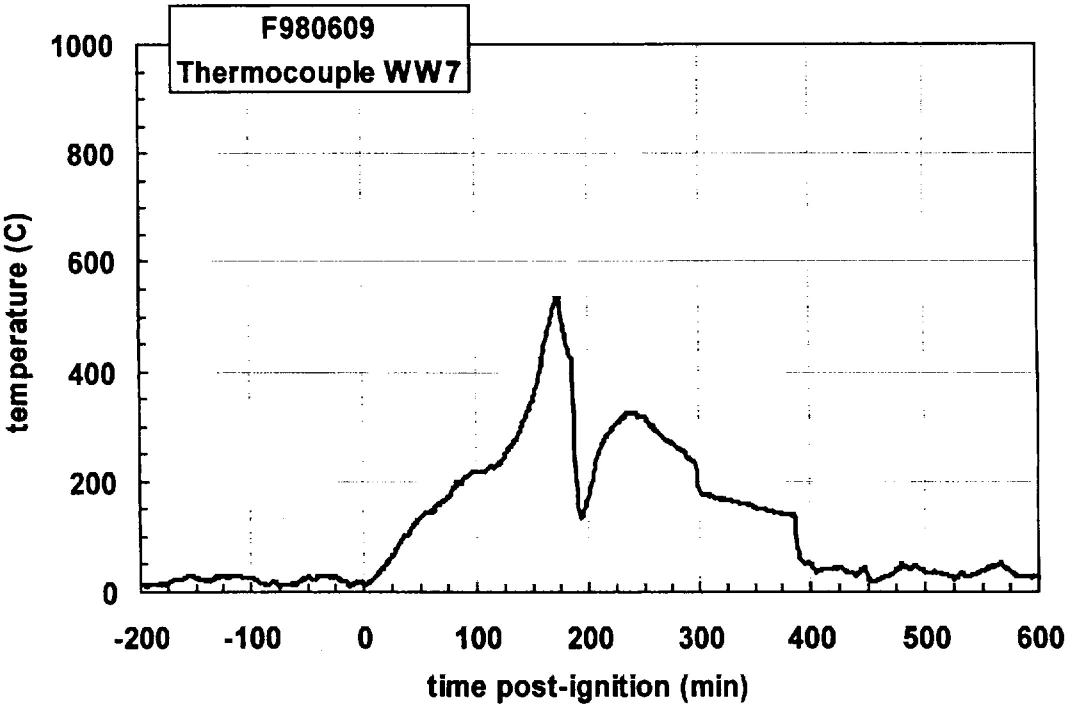

Plot C110. Fire Test F980609. Data plot from thermocouple WW7.

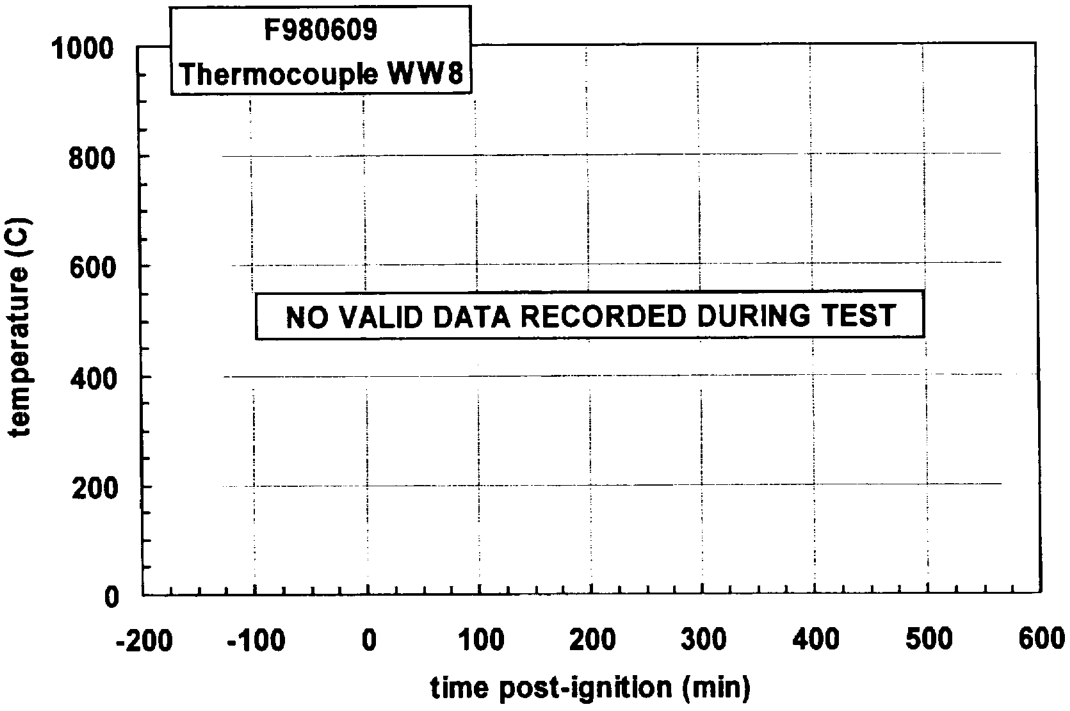

Plot C111. Fire Test F980609. Data plot from thermocouple WW8.

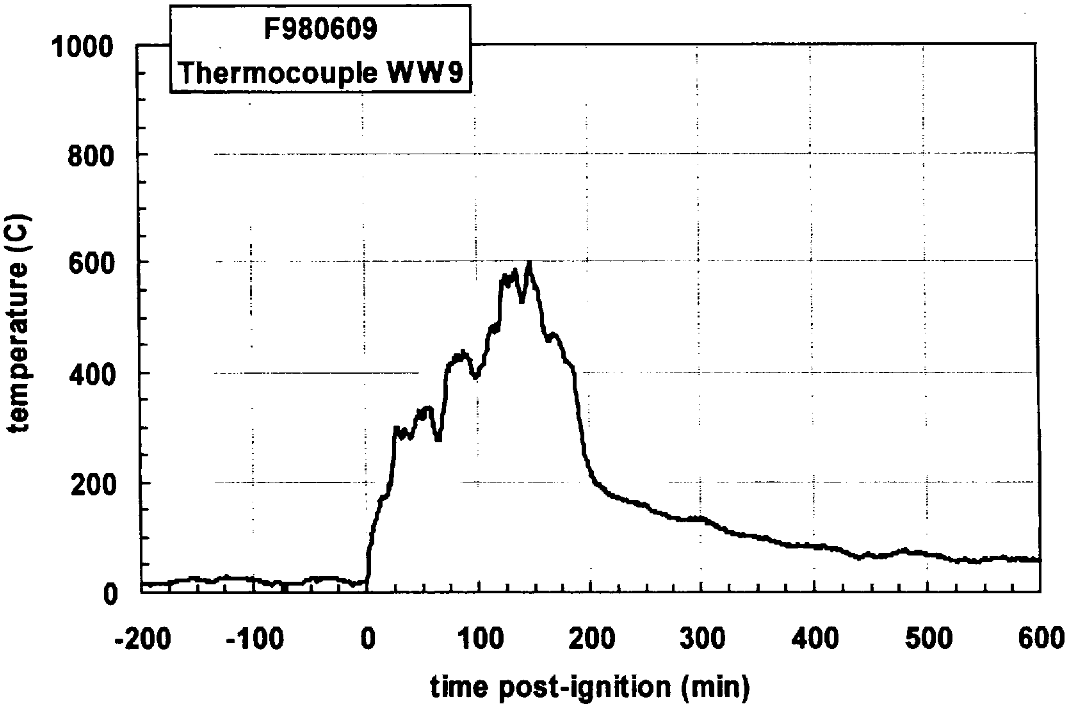

Plot C112. Fire Test F980609. Data plot from thermocouple WW9.

APPENDIX D
ASPIRATED THERMOCOUPLE DATA

Two aspirated thermocouple assembly (Medtherm Corporation) was installed in the test vehicle (Fig. D1). The aspirated thermocouple assembly was fabricated from Inconel 600 tubing. Each assembly consisted of a vertical manifold (o.d. = 0.375 in. (9.5 mm), i.d. = 0.25 in. (6.4 mm), length = 16 in. (406 mm)) with six horizontal radiation shields (o.d. = 0.25 in. (6.4 mm), i.d. = 0.19 in. (4.8 mm), length = 1.00 in. (25.4 mm)). The vertical spacing between the radiation shields along the manifold was 3 in. (75 mm). Three radial holes were drilled near the tip of each radiation shield. The holes were sized to approximately balance the airflow-rates over each thermocouple. A Type-N thermocouple inserted into each radiation shield so that the thermocouple junction was positioned approximately 0.2 in. (5.1 mm) down-stream from the inlet holes.

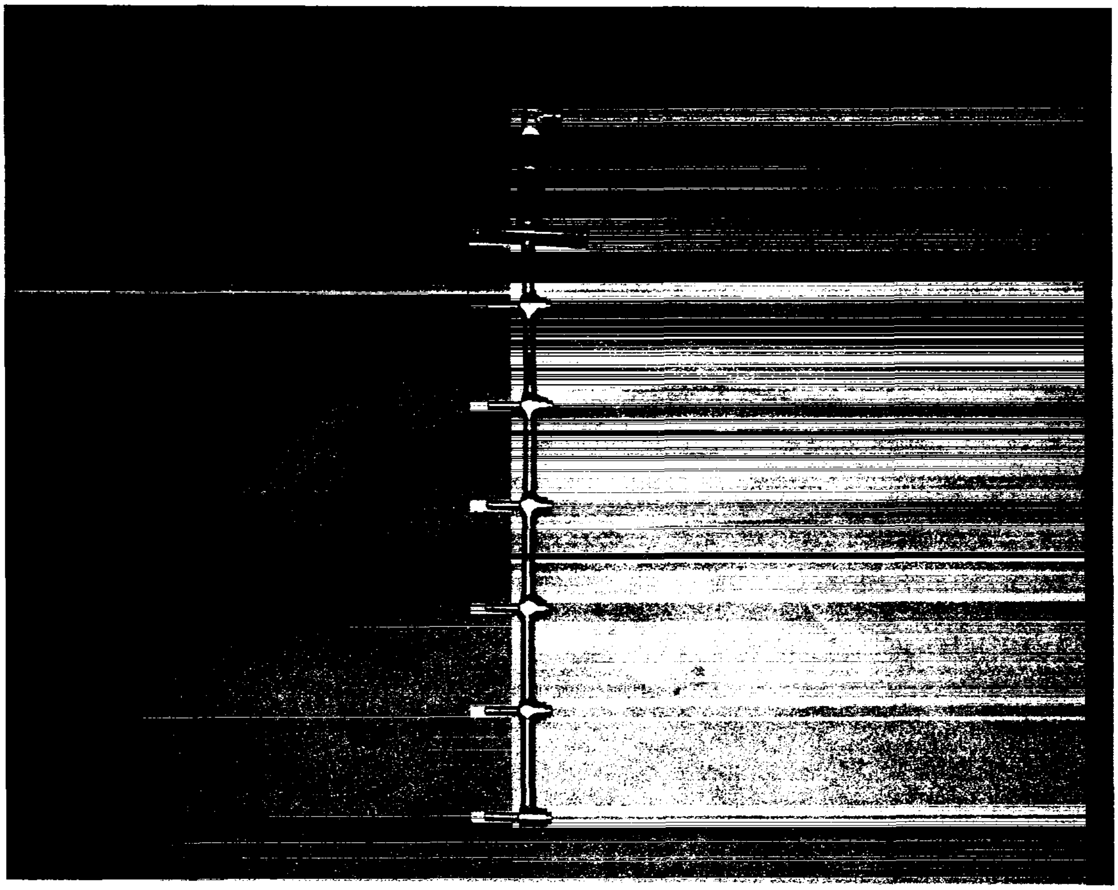

Figure D1. Fire Test F961115. Photograph of the aspirated thermocouple assembly used in the passenger compartment of the test vehicle.

The mounting flange of the aspirated thermocouple probe assembly was attached to the roof of the vehicle. The probe extended into the passenger compartment through a hole in the roof so that all 6 thermocouples were located below the headliner. The probe was vertical and located along the longitudinal mid-line of the vehicle approximately equidistant from the driver and passenger seats. The upper-most aspirated thermocouple was approximately 0.5 in. (12 mm) below the lower surface of the headliner. The manifold was connected to a rotary-vane pump with flexible copper tubing (o.d. = 0.5 in. (12 mm), length = 15 ft. (4.6 m)). The capacity of the pump was 50 L/min at atmospheric pressure.

Figures D2 and D3 show the approximate location of the aspirated thermocouple probe assembly in the test vehicle for this test.

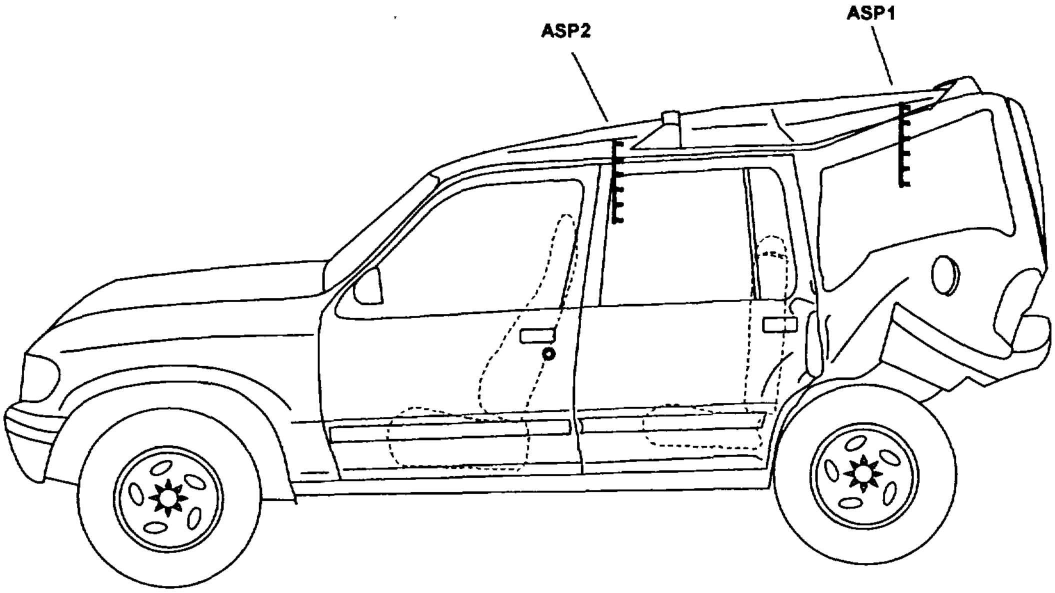

Figure D2. Fire Test F980609. Side view of the test vehicle showing the approximate location of the aspirated thermocouple probe assembly in the passenger compartment.

Electromagnetic interference of unknown origin could not be eliminated from the signals from the aspirated thermocouples. This interference rendered the temperature data from these thermocouples invalid. This electronic noise also feed-back through the grounds of the non-aspirated thermocouples installed in the test vehicle, thus rendering temperature data from the non-aspirated thermocouples invalid. The interference in the signals from the non-aspirated thermocouples was eliminated when the aspirated thermocouples were disconnected from the data system. This test was conducted with the aspirated thermocouples disconnected from the data system. Thus, no data was recorded from the aspirated thermocouples.

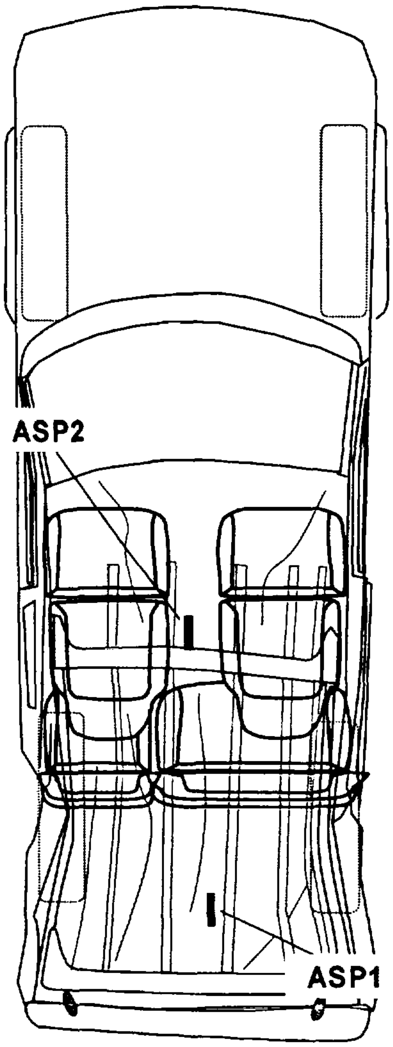

Figure D3. Fire Test F980609. Top view of the test vehicle showing the approximate location of the aspirated thermocouple probe assembly in the passenger compartment.

REFERENCES

D1. J. S. Newman and P. A. Croce. A simple aspirated thermocouple for use in fires. *J. Fire Flamm.* **10**:326-336 (1979).

D2. N. R. Keltner and K. A. Strom. Thermal Measurement Uncertainty and Compensation. Paper in preparation.

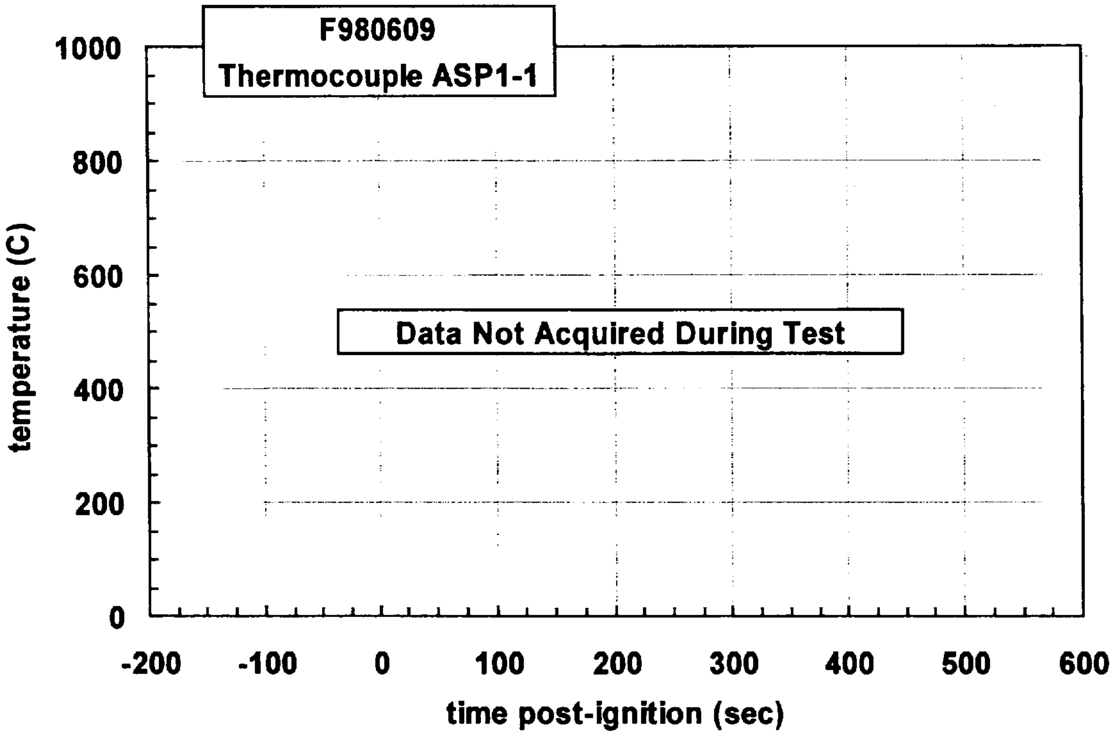

Plot D1. Fire Test F980609. Data plot from thermocouple ASP1-1.

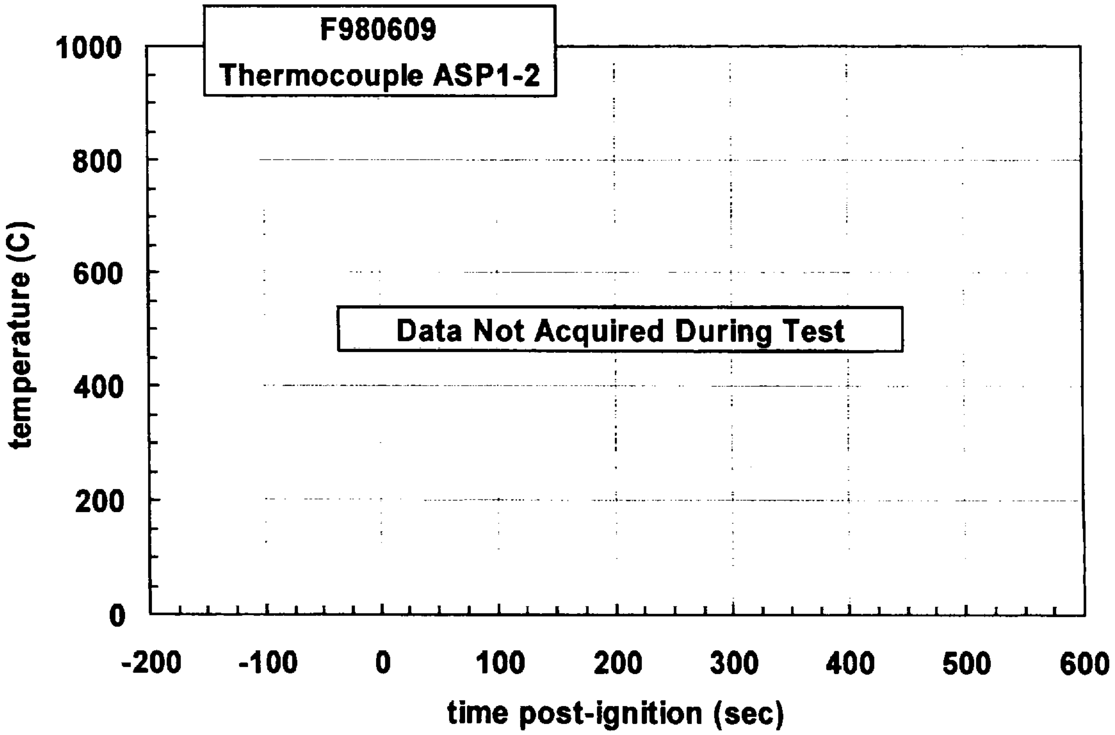

Plot D2. Fire Test F980609. Data plot from thermocouple ASP1-2.

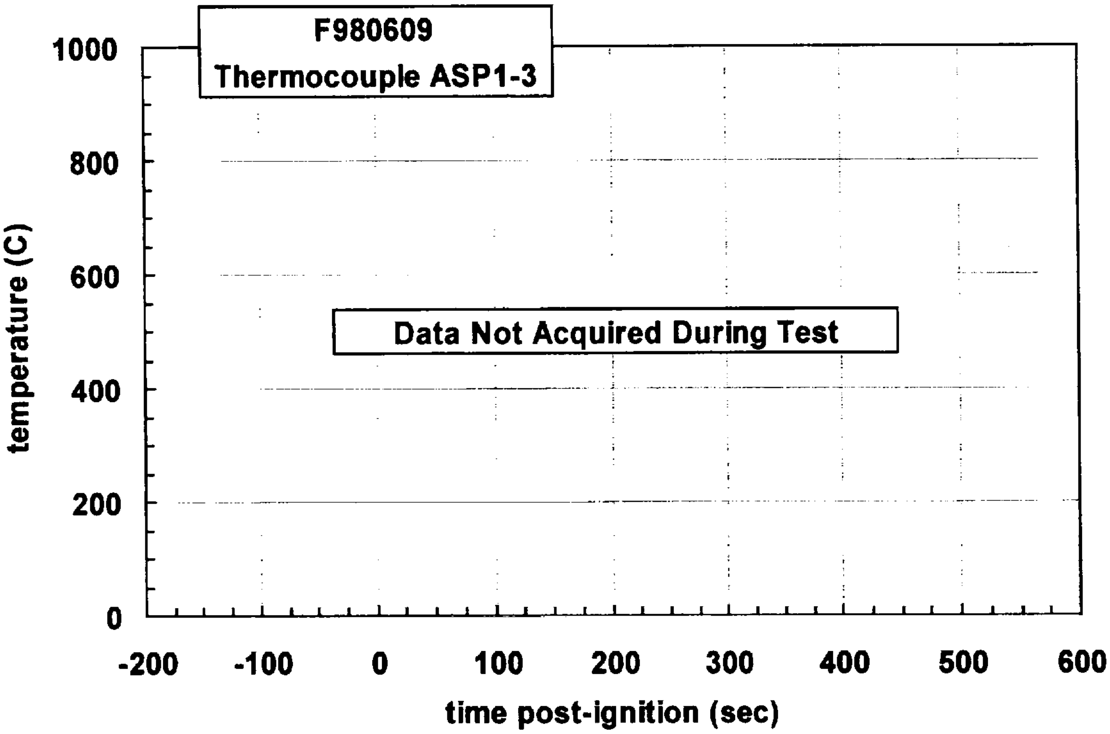

Plot D3. Fire Test F980609. Data plot from thermocouple ASP1-3.

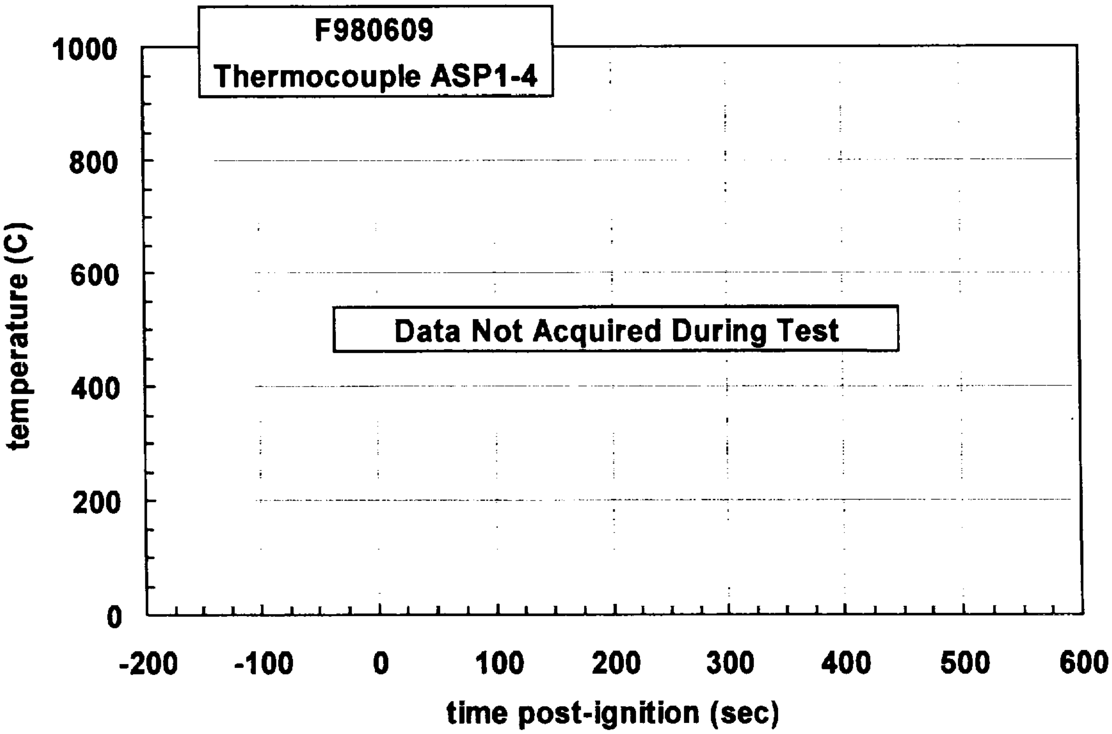

Plot D4. Fire Test F980609. Data plot from thermocouple ASP1-4.

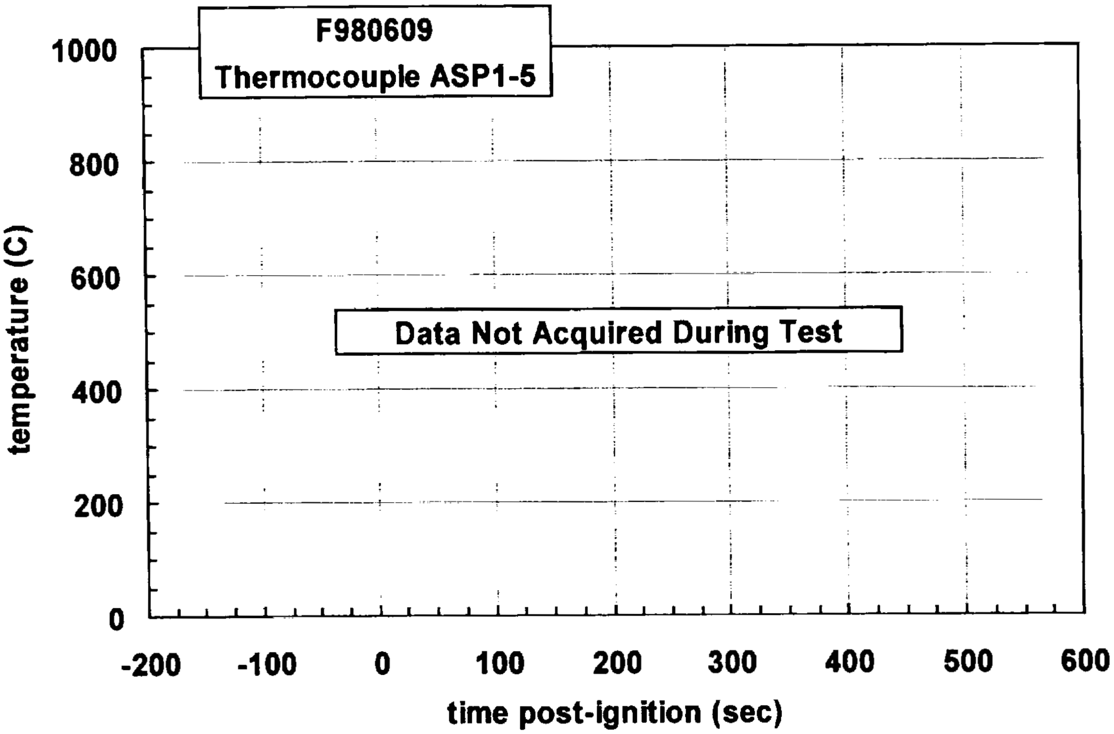

Plot D5. Fire Test F980609. Data plot from thermocouple ASP1-5.

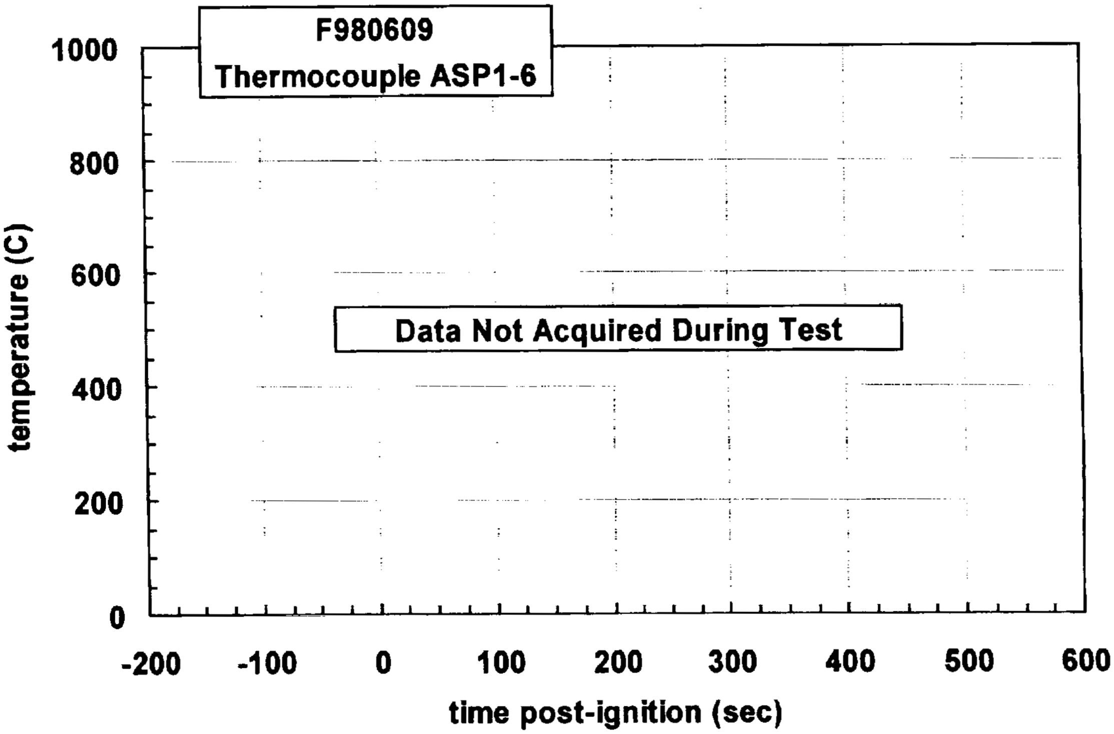

Plot D6. Fire Test F980609. Data plot from thermocouple ASP1-6.

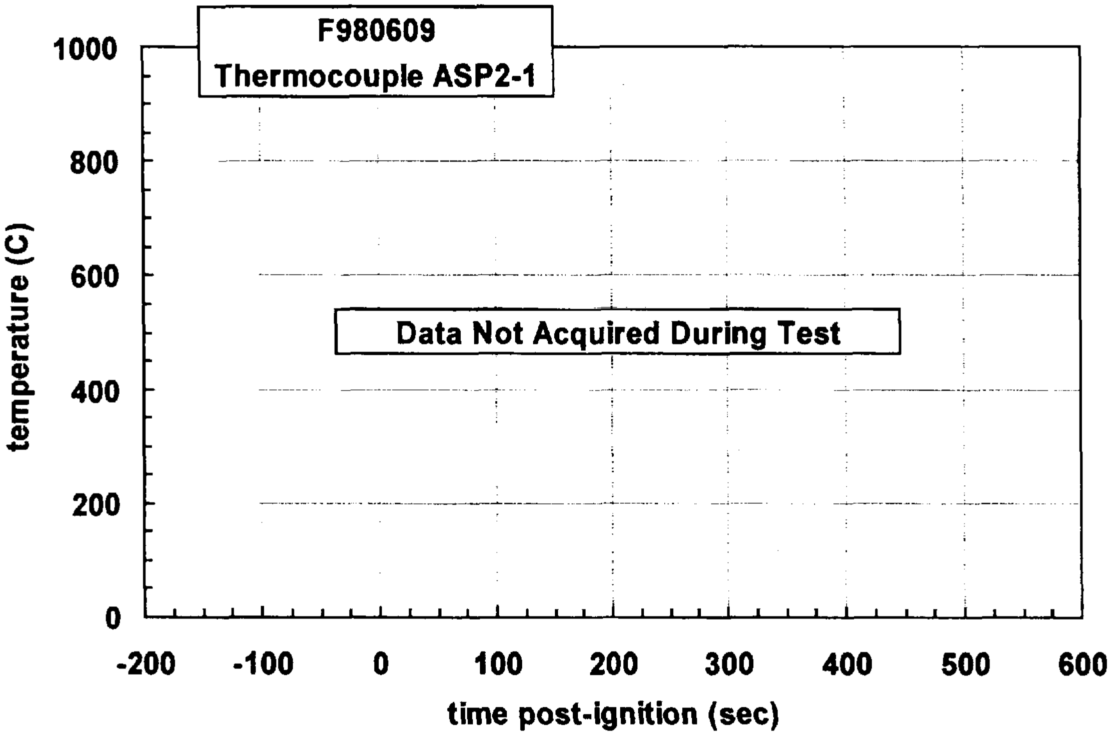

Plot D7. Fire Test F980609. Data plot from thermocouple ASP2-1.

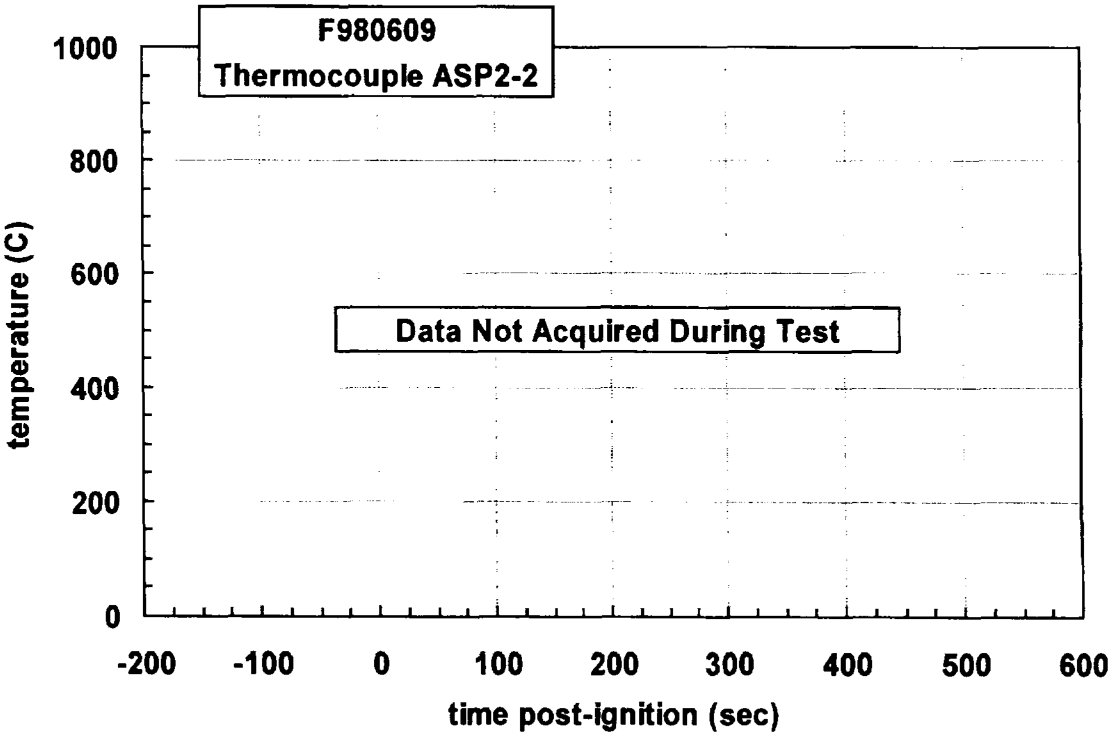

Plot D8. Fire Test F980609. Data plot from thermocouple ASP2-2.

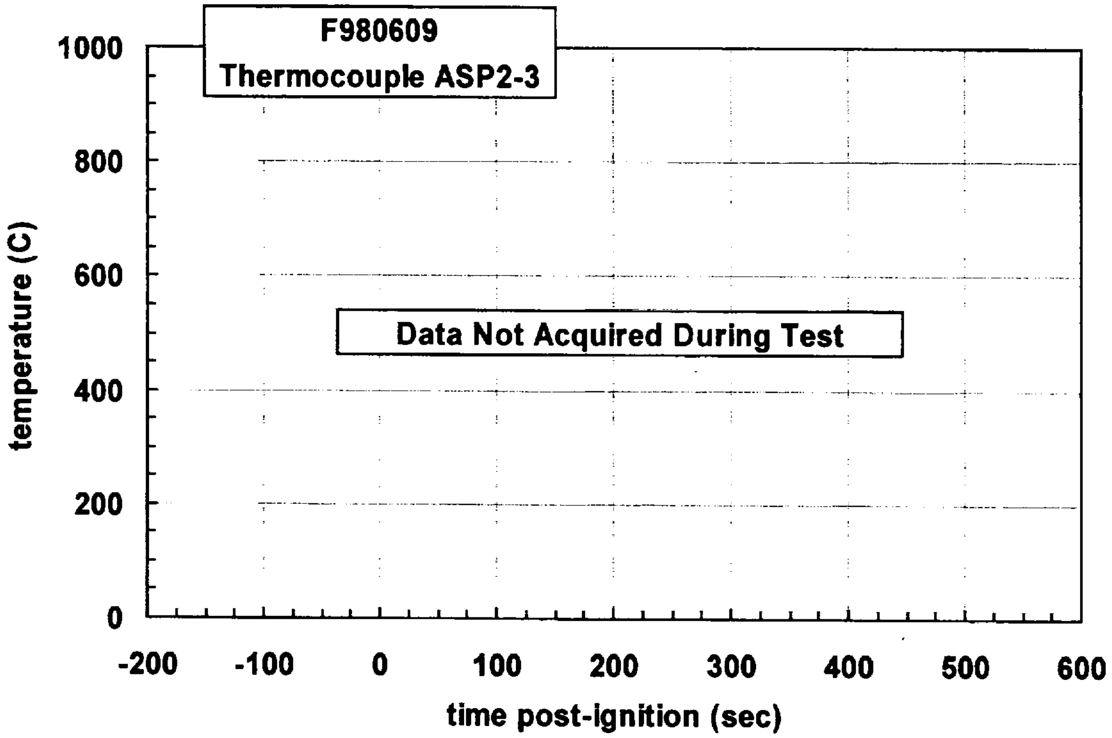

Plot D9. Fire Test F980609. Data plot from thermocouple ASP2-3.

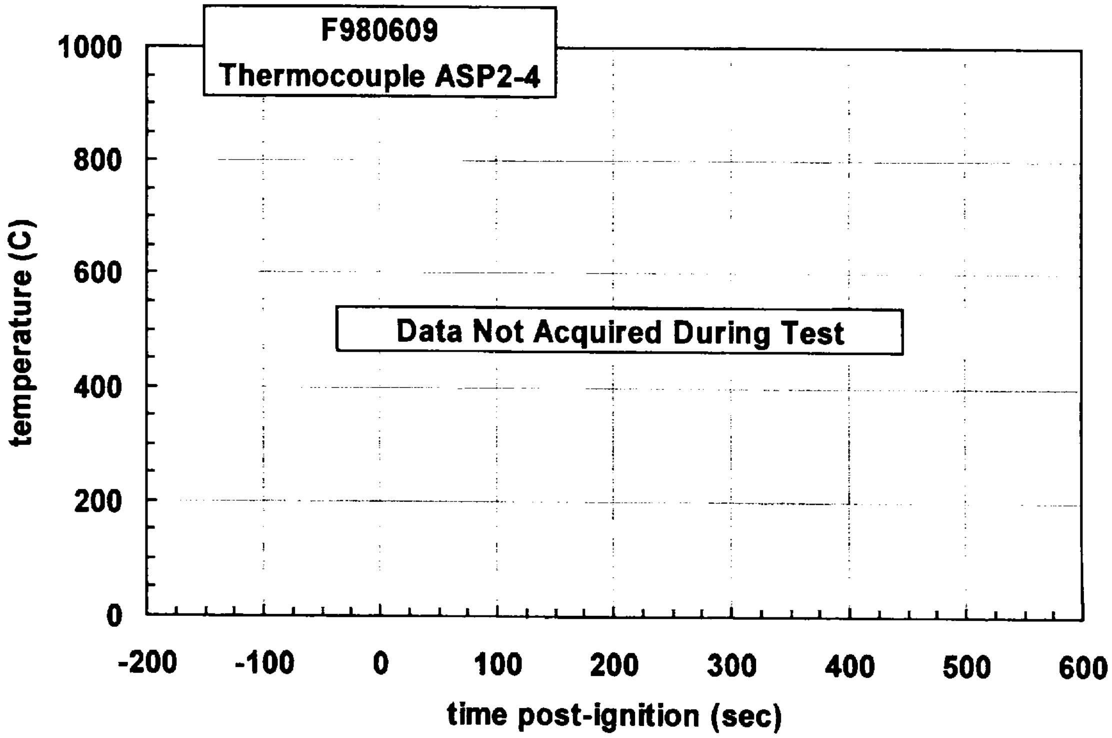

Plot D10. Fire Test F980609. Data plot from thermocouple ASP2-4.

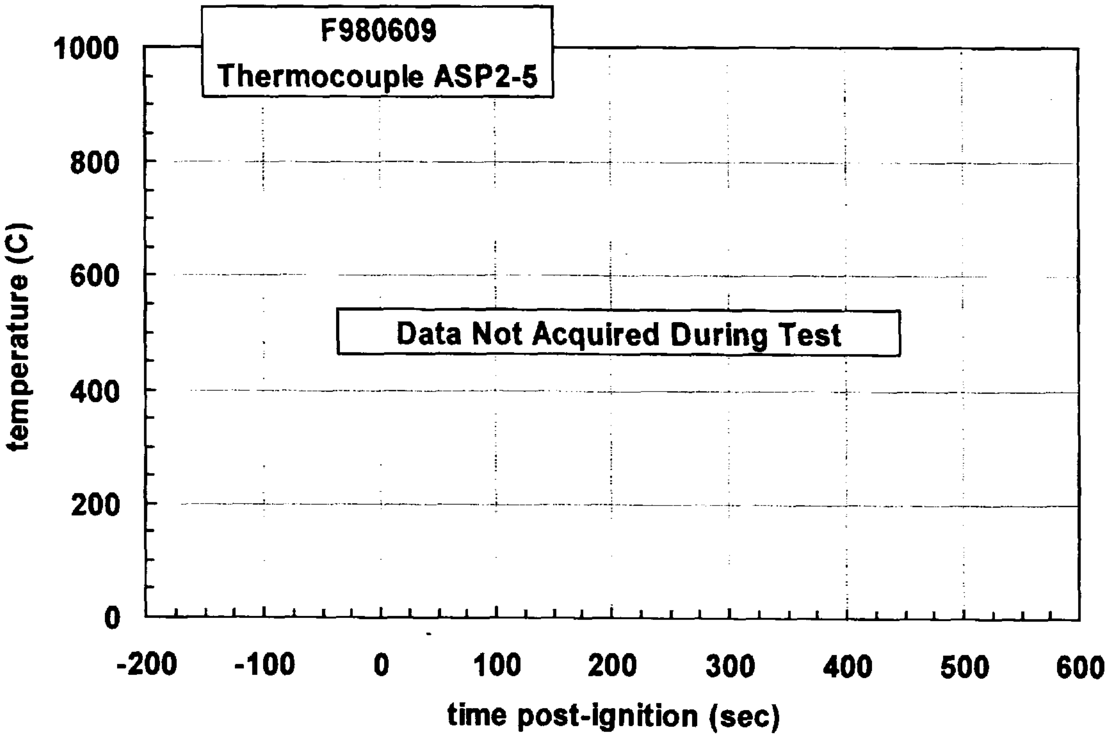

Plot D11. Fire Test F980609. Data plot from thermocouple ASP2-5.

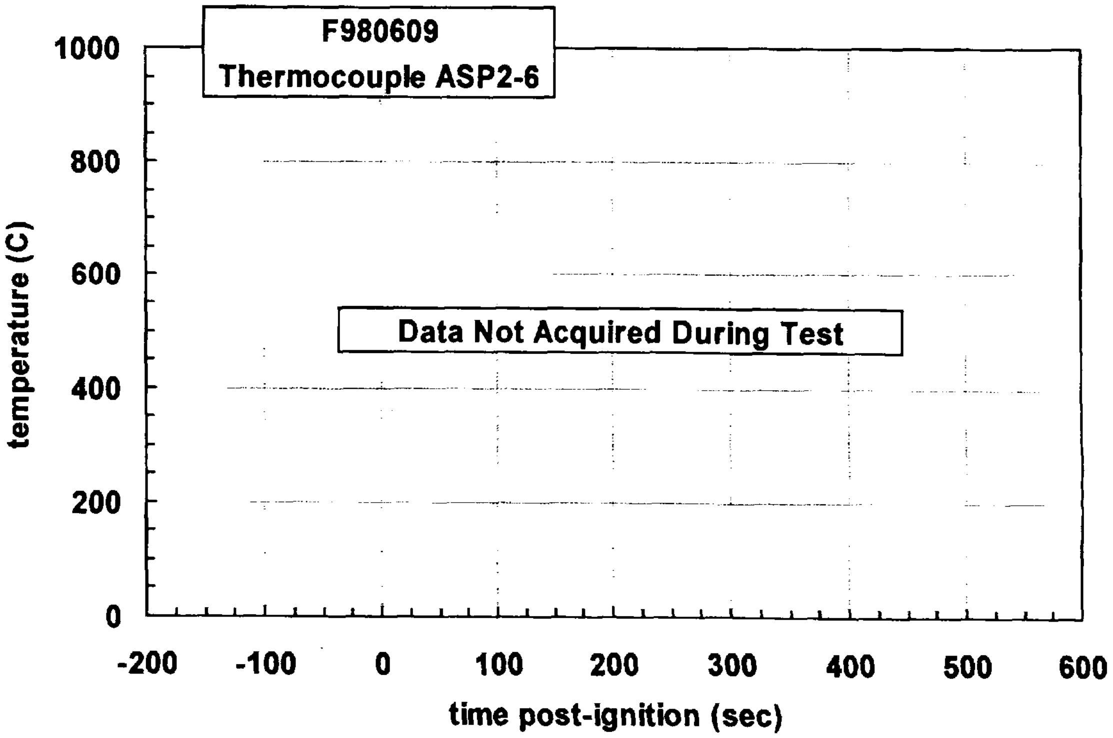

Plot D12. Fire Test F980609. Data plot from thermocouple ASP2-6.

APPENDIX E
HEAT FLUX TRANSDUCER/RADIOMETER DATA

Heat-flux transducer/radiometer assemblies (64 Series, Medtherm Corporation) were used to measure convective and radiative heat transfer to selected objects in the vehicle. Each assembly contained two Schmidt-Boelter thermopiles in a water-cooled copper body (diameter = 1 in. (25.4 mm), length = 1 in. (25.4 mm)). The faces of the heat flux transducers were coated with high-temperature optical black paint. The radiometers had permanent sapphire windows (view-angle = 150°; optical transmittance range 0.4 to 4.2 μm). Both transducers were calibrated to 100 kW/m^2 at a reference temperature of 25°C.

The PC-based data system used to acquire data from the thermocouples (**APPENDIX C**) also was used to acquire data from the heat flux transducers and radiometers. The electrical signal wires from these transducers terminated in a 5-pin circular connector (165 Series, Amphenol). Each connector was plugged into a panel-mounted jack, which was hard wired to an analog-input multiplex expansion card (DBK-12, IOTech, Inc., Cleveland, OH). As with the thermocouples, the electrical shields on the signal cables were connected to the electronic chassis grounds on the analog-input expansion cards. The data acquisition software (DASYLab) was configured to sample each channel at a rate of 10 Hz and store the data in 10-point block averages.

Figures E1 and E2 show the approximate locations of heat flux transducer/radiometer assemblies in the test vehicle.

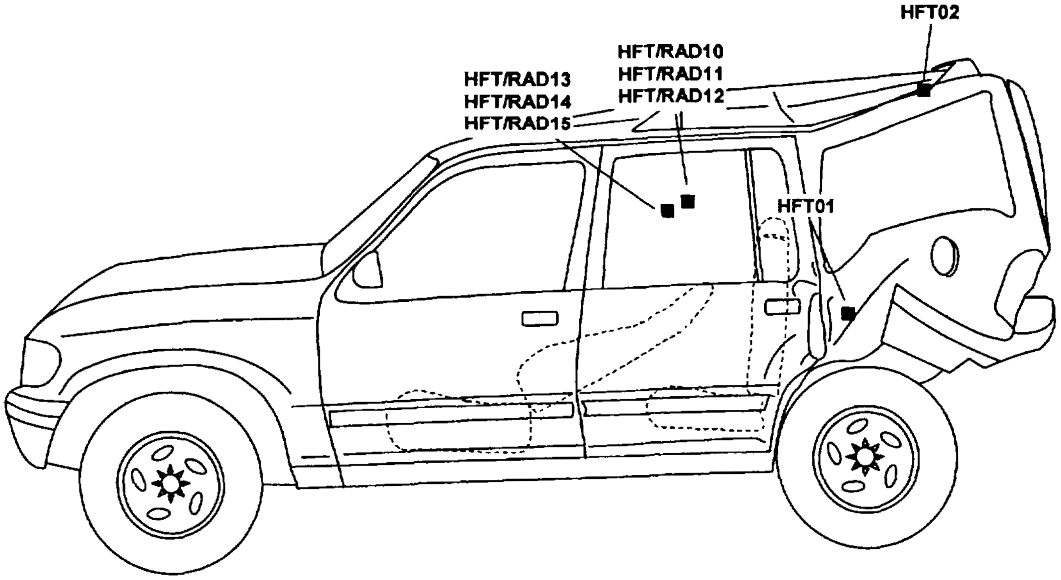

Figure E1. Fire Test F980609. Side view of the test vehicle showing the approximate locations of heat flux transducer/radiometer (HFT/RAD) assemblies in the test vehicle.

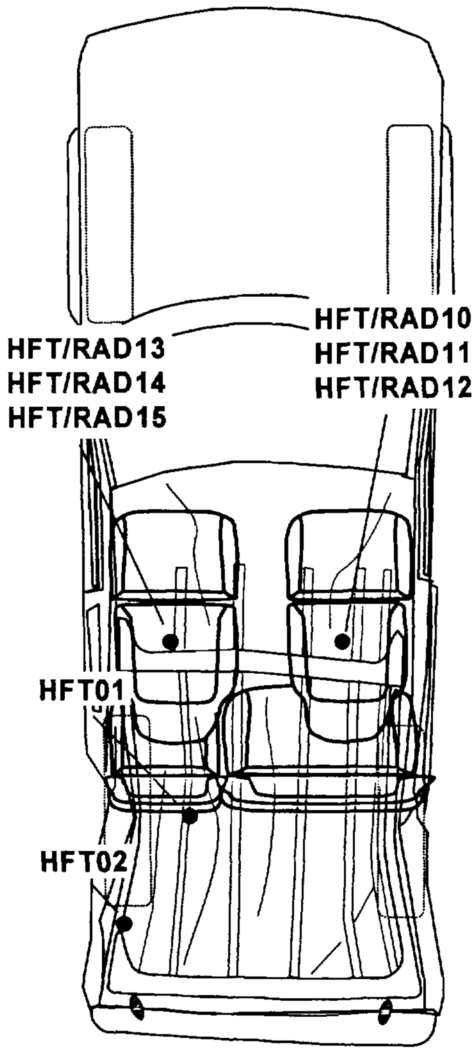

Figure E2. Fire Test F980609. Top view of the test vehicle showing the approximate locations of heat flux transducer/radiometer (HFT/RAD) assemblies mounted in the test vehicle.

HFT01 was inserted into a clearance-hole that was drilled in the floor panel in the rear compartment. The transducer was mounted on stand-offs so that the face of the transducer was flush with the exterior metal surface. HFT02 was inserted into clearance-holes drilled in the roof panel and head lining ponel in the rear compartment. The transducer was mounted on stand-offs so that the face of the transducer was flush with the lower surface of the head lining panel.

HFT/RAD10 through HFT/RAD15 were located above the front seats. These transducers were mounted to threaded rods (diameter = ½ in.) inserted through holes drilled in the roof. The lower end of each rod was secured to a seat cushion to stabilize the transducers during the test.

Copper tubing (o.d. = 0.25 in. (6.4 mm)) was used for the cooling water supply and waste lines. The temperature of the water supplied to the HFT/RAD assemblies was approximately 80°C, and the flow rate of water through each body was approximately 100 mL/min. HFT/RAD10 was located above the front passenger's seat facing upward. HFT/RAD11 was located above the front passenger's seat facing rearward. HFT/RAD12 was located above the front passenger's seat facing to the left rear door. HFT/RAD13 was located above the front passenger's seat facing upward. HFT/RAD14 was located above the front passenger's seat facing rearward. HFT/RAD15 was located above the front passenger's seat facing to the left rear door.

Thermocouples F26 and R14 were located in the bodies of each heat flux transducer or heat flux transducer/radiometer assemblies HFT01 and HFT02, respectively. Thermocouples O10, O11, O12, O13, O14, and O15 were located in the bodies of each heat flux transducer or heat flux transducer/radiometer assemblies HFT/RAD10, HFT/RAD11, HFT/RAD12, HFT/RAD13, HFT/RAD14, and HFT/RAD15, respectively.

Data recorded from these transducers is shown in Plots E1 through E12.

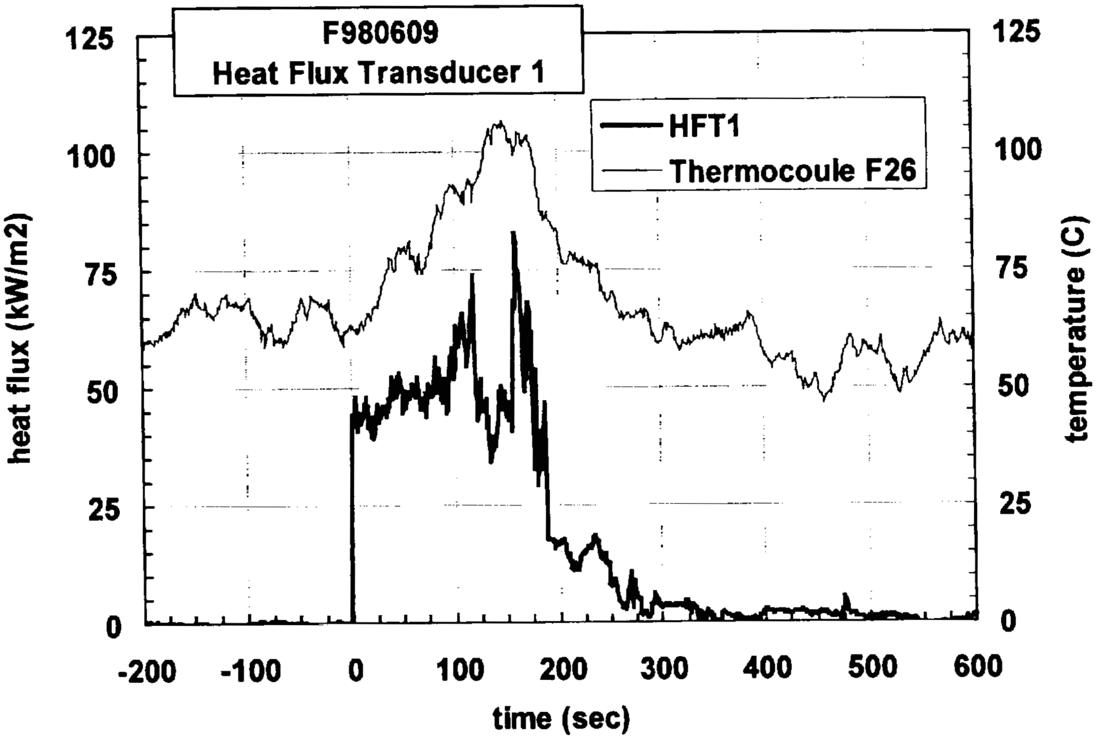

Plot E1. Fire Test F980609. Data plot from Heat Flux Transducer 01 and Thermocouple F26.

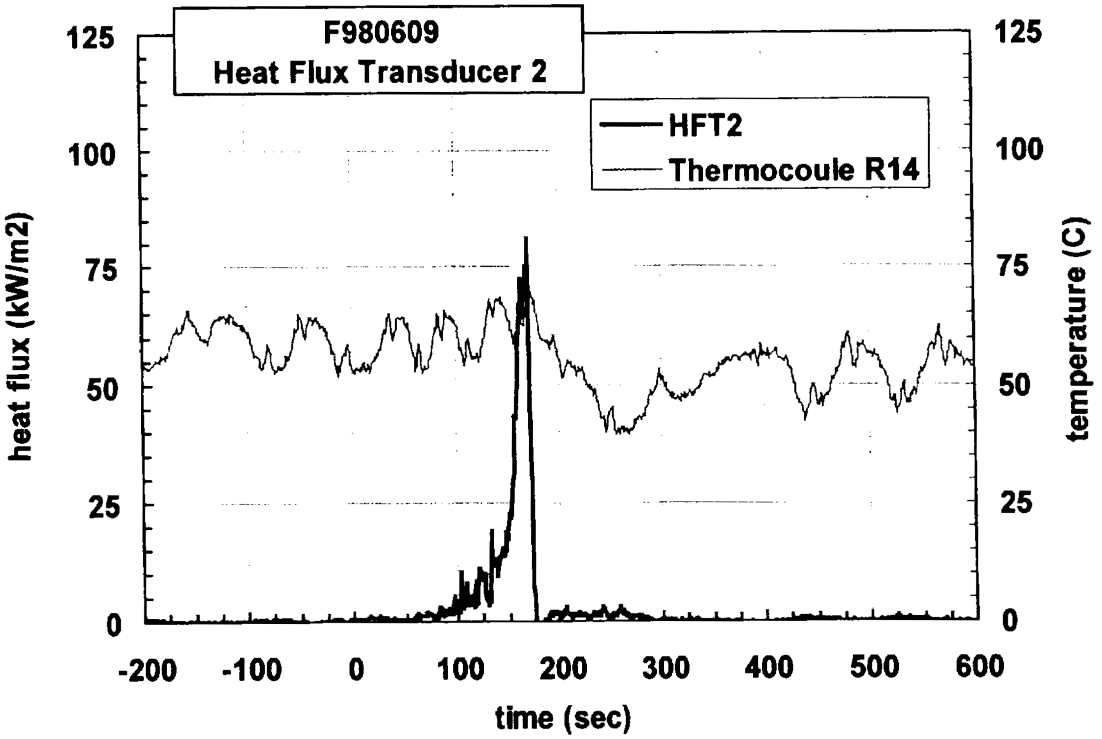

Plot E2. Fire Test F980609. Data plot from Heat Flux Transducer 02 and Thermocouple R14.

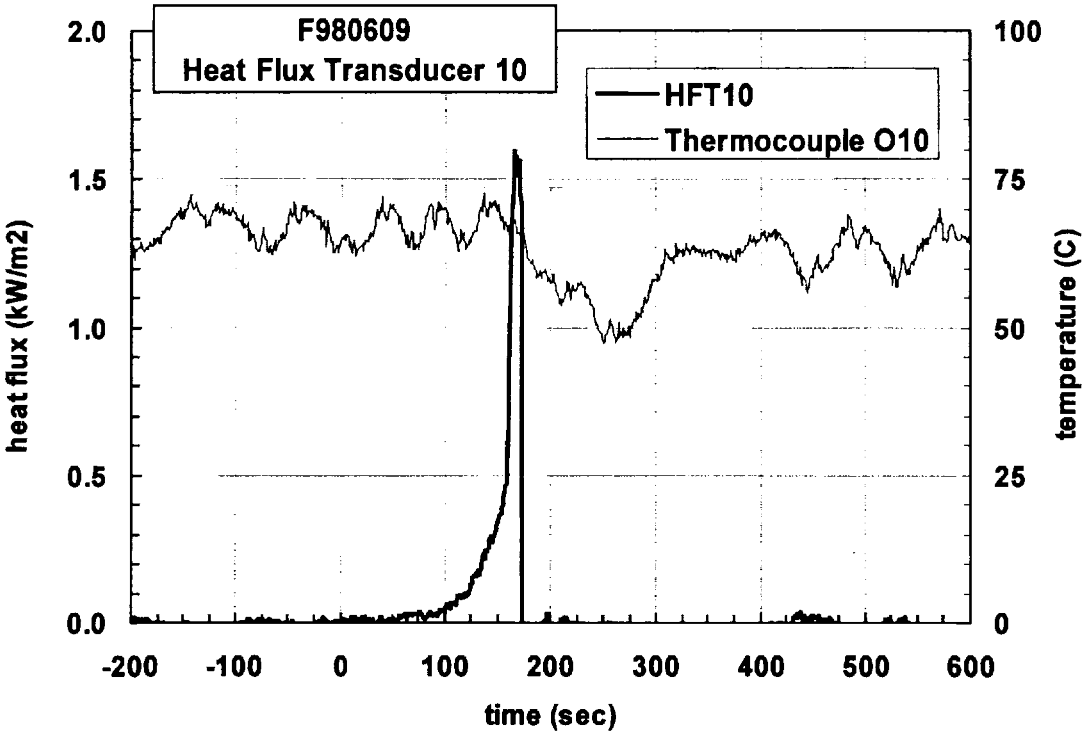

Plot E3. Fire Test F980609. Data plot from Heat Flux Transducer 10 and Thermocouple 10.

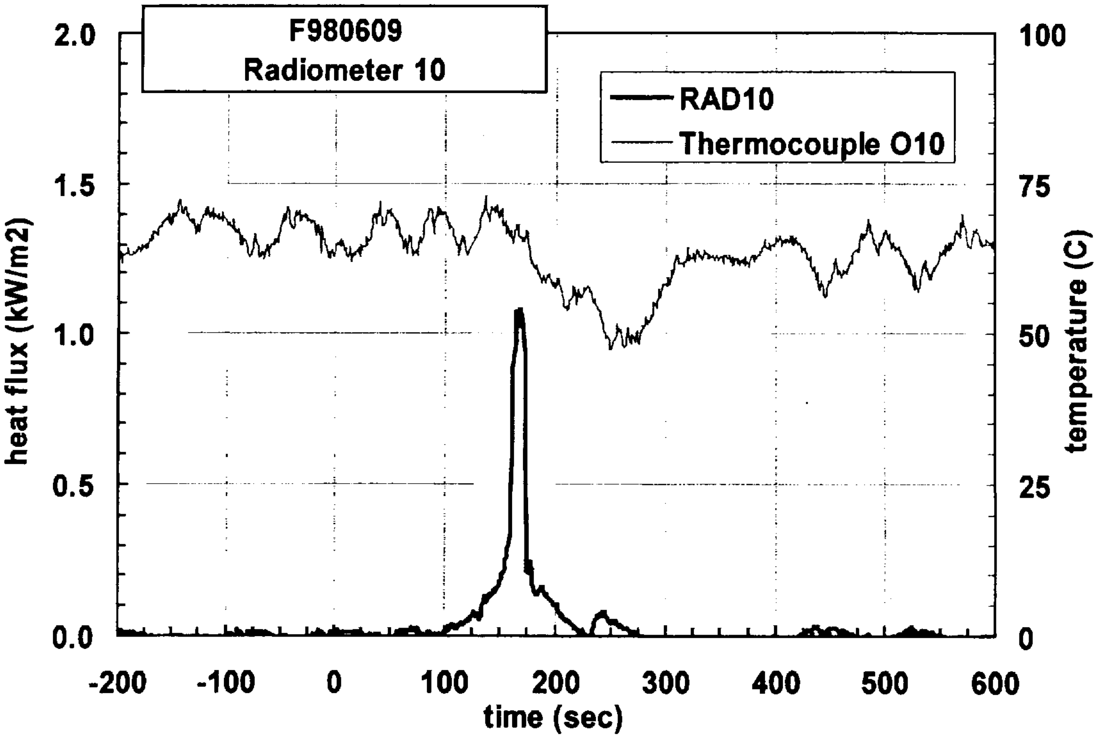

Plot E4. Fire Test F980609. Data plot from Radiometer 10 and Thermocouple O10.

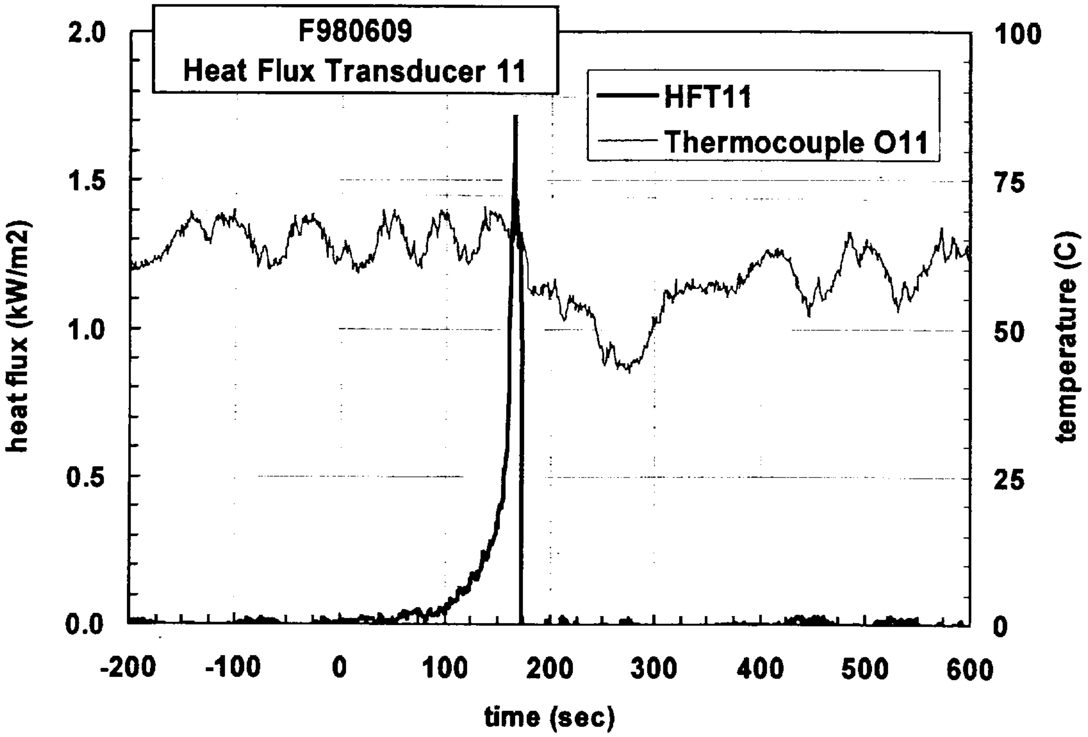

Plot E5. Fire Test F980609. Data plot from Heat Flux Transducer 11 and Thermocouple O11.

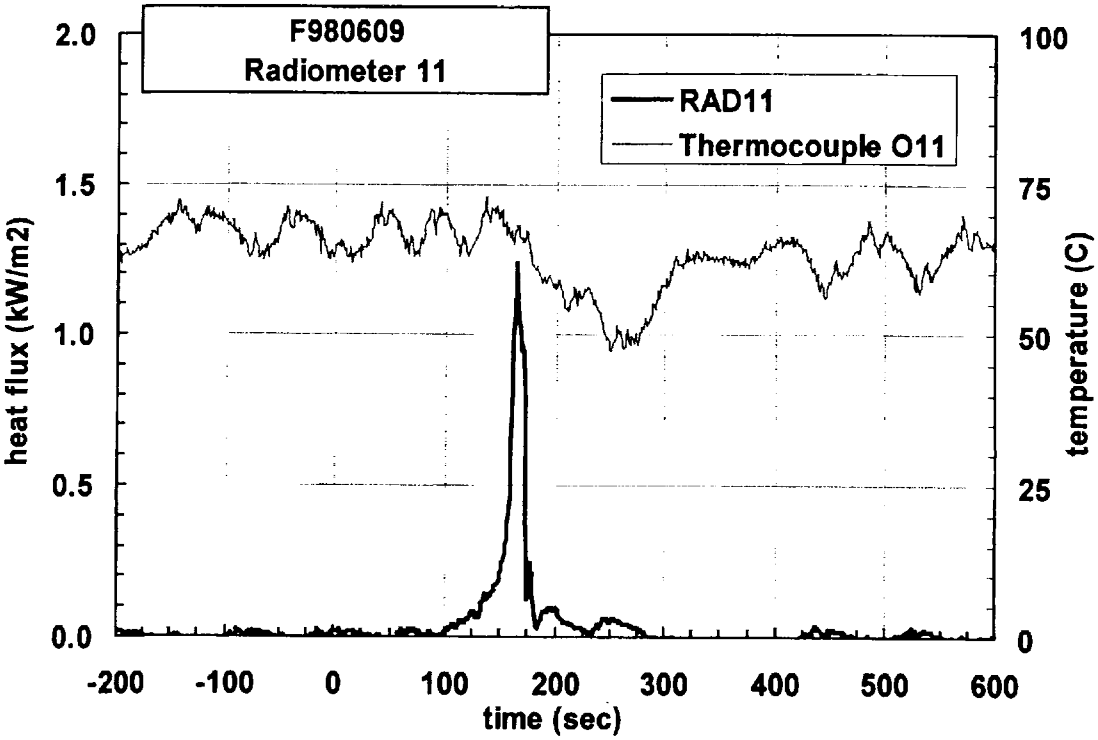

Plot E6. Fire Test F980609. Data plot from Radiometer 11 and Thermocouple O11.

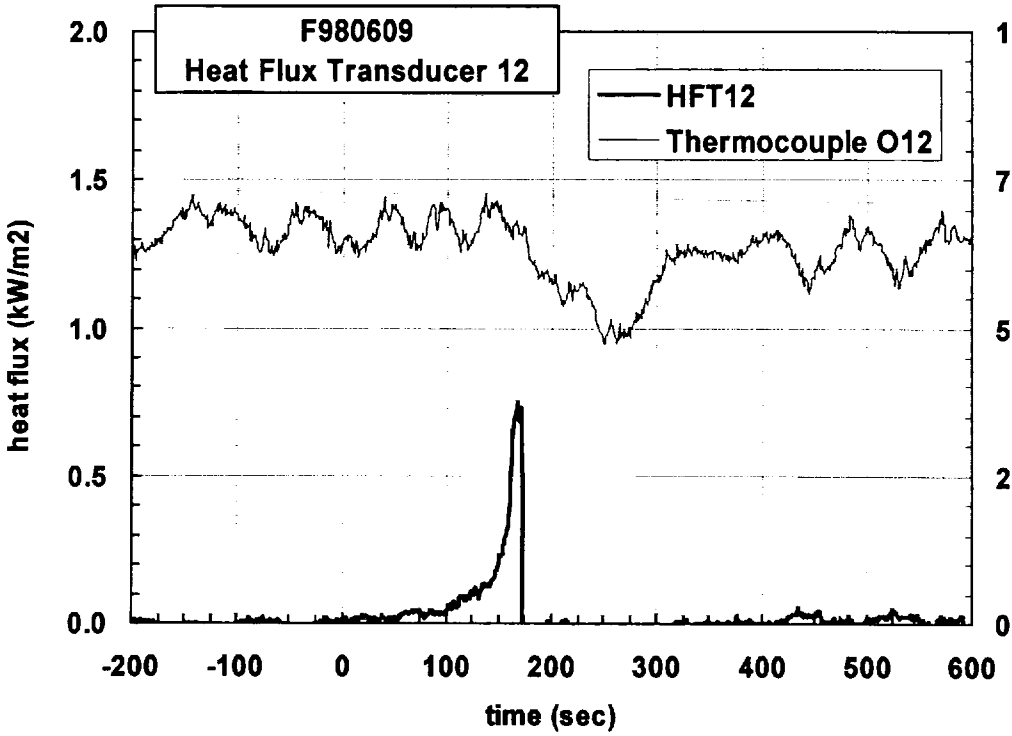

Plot E7. Fire Test F980609. Data plot from Heat Flux Transducer 12 and Thermocouple O12.

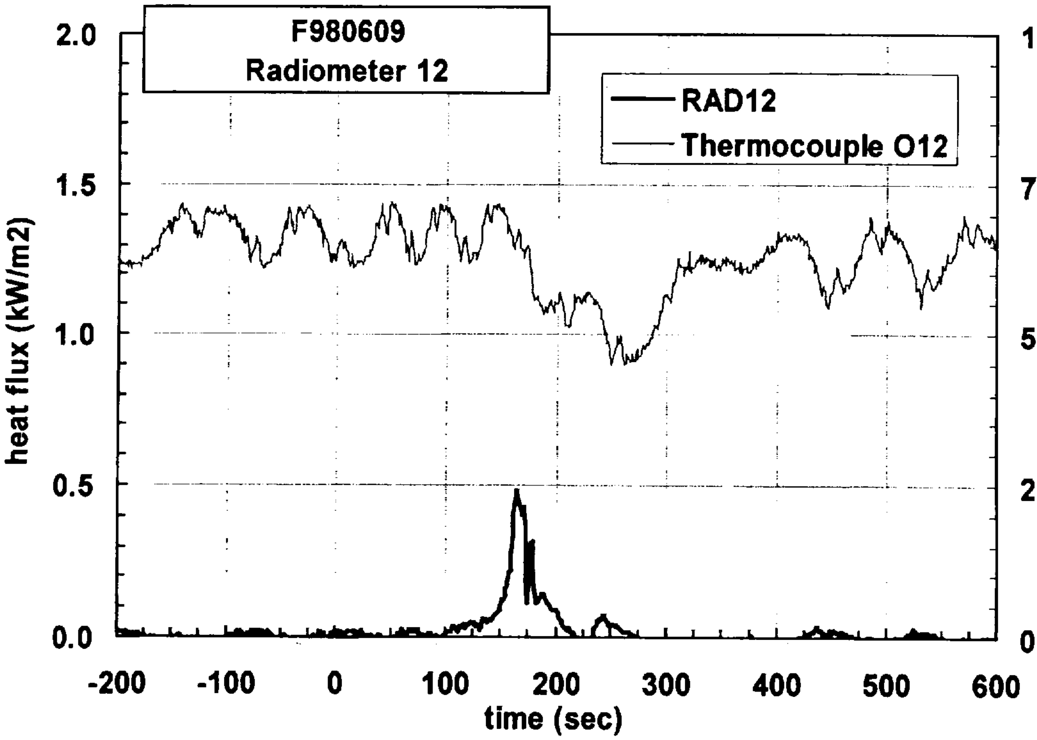

Plot E8. Fire Test F980609. Data plot from Radiometer 12 and Thermocouple O12.

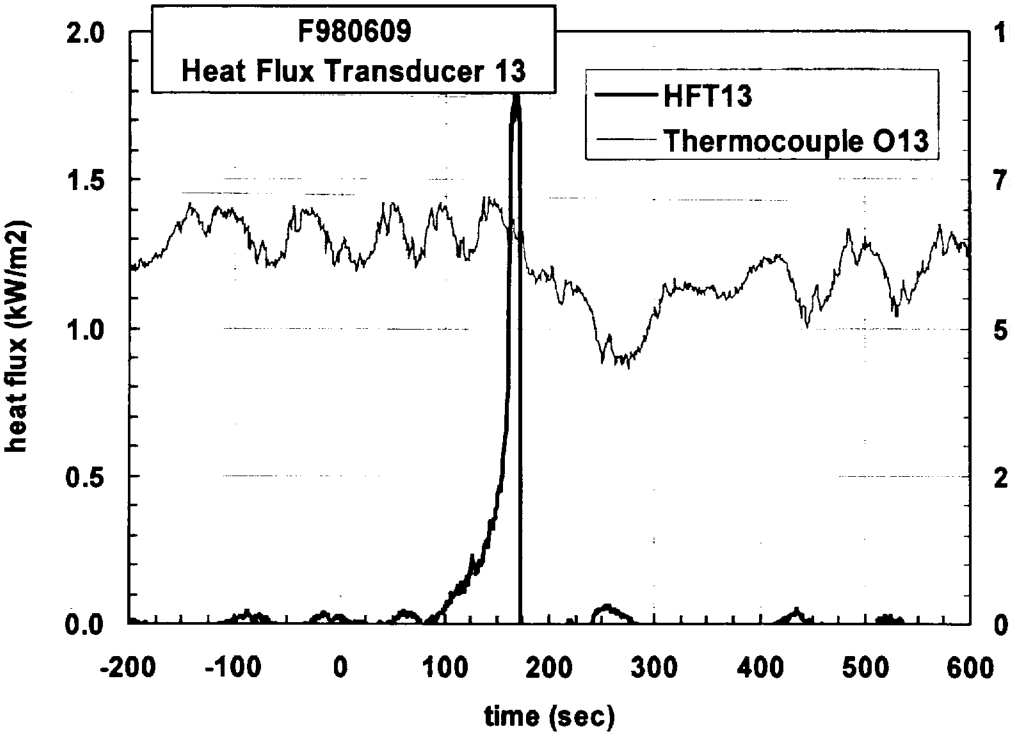

Plot E9. Fire Test F980609. Data plot from Heat Flux Transducer 13 and Thermocouple O13.

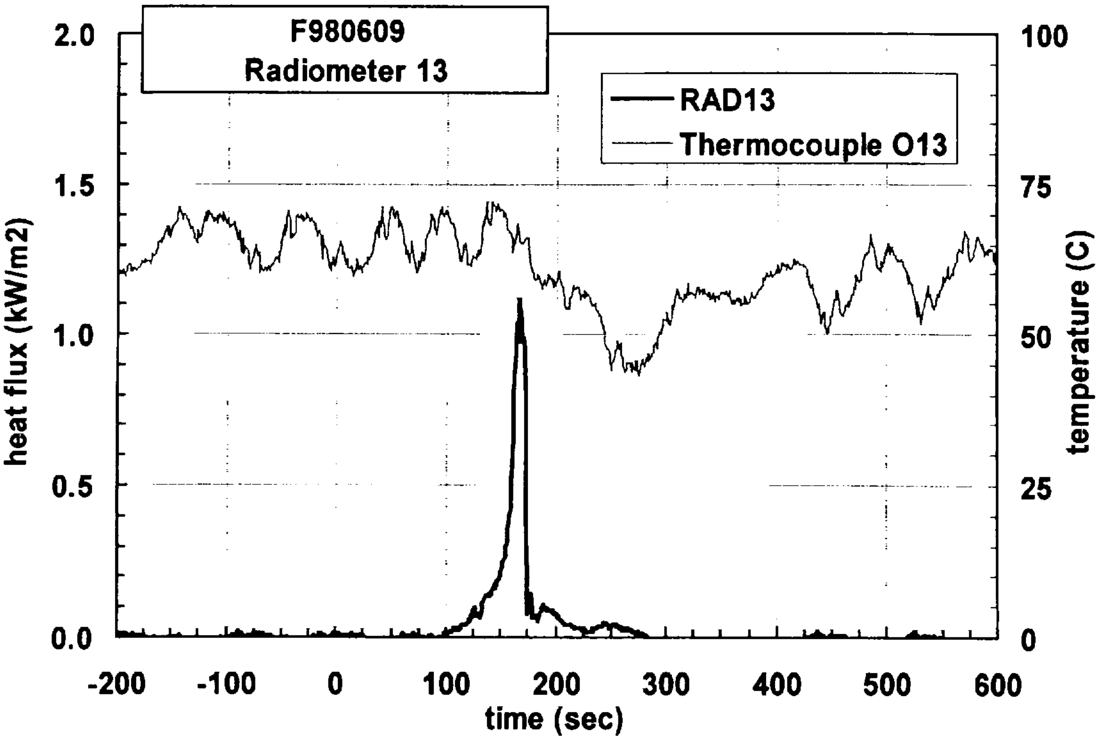

Plot E10. Fire Test F980609. Data plot from Radiometer 13 and Thermocouple O13.

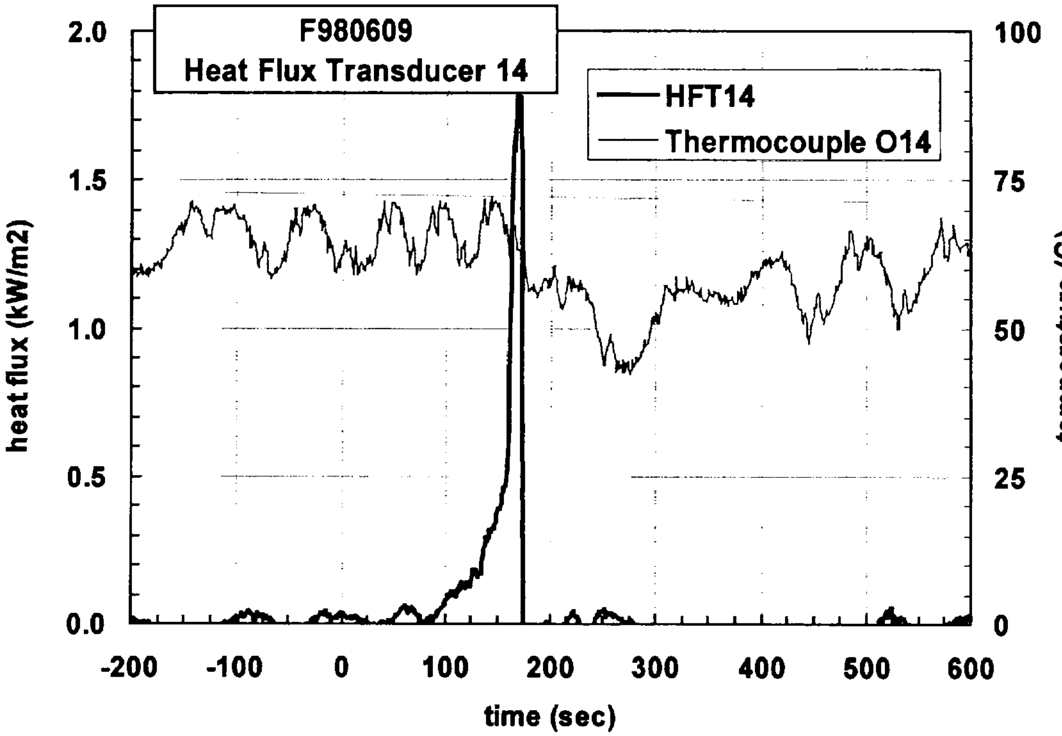

Plot E11. Fire Test F980609. Data plot from Heat Flux Transducer 14 and Thermocouple O14.

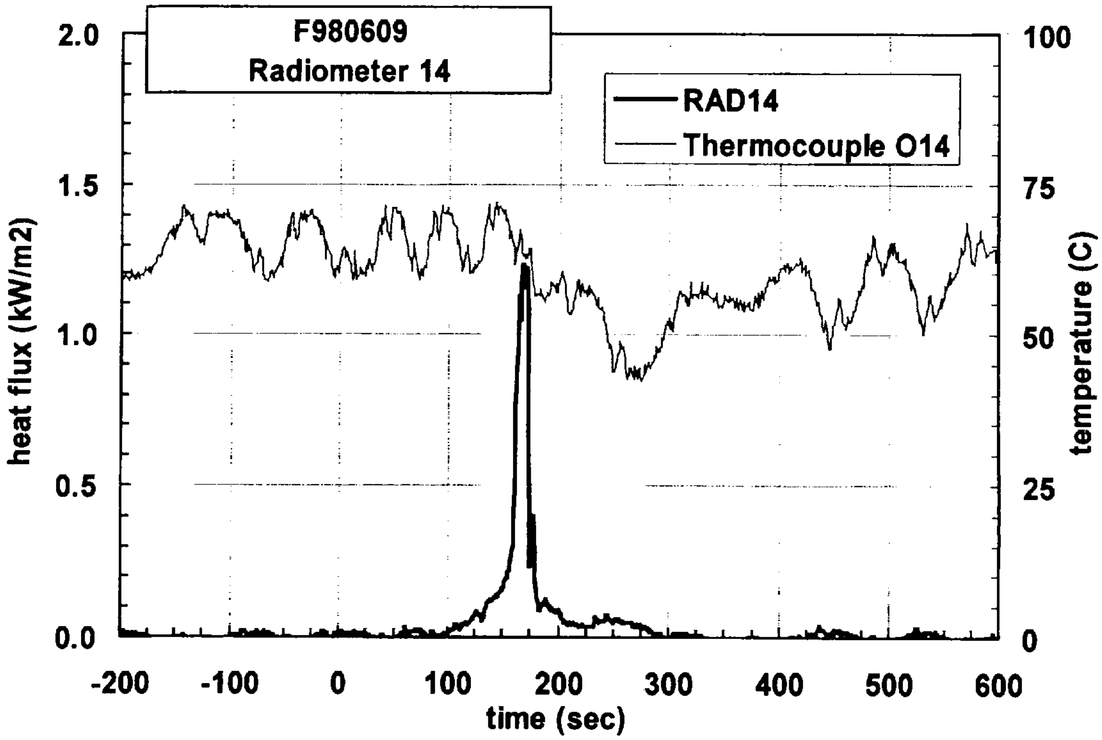

Plot E12. Fire Test F980609. Data plot from Radiometer 14 and Thermocouple O14.

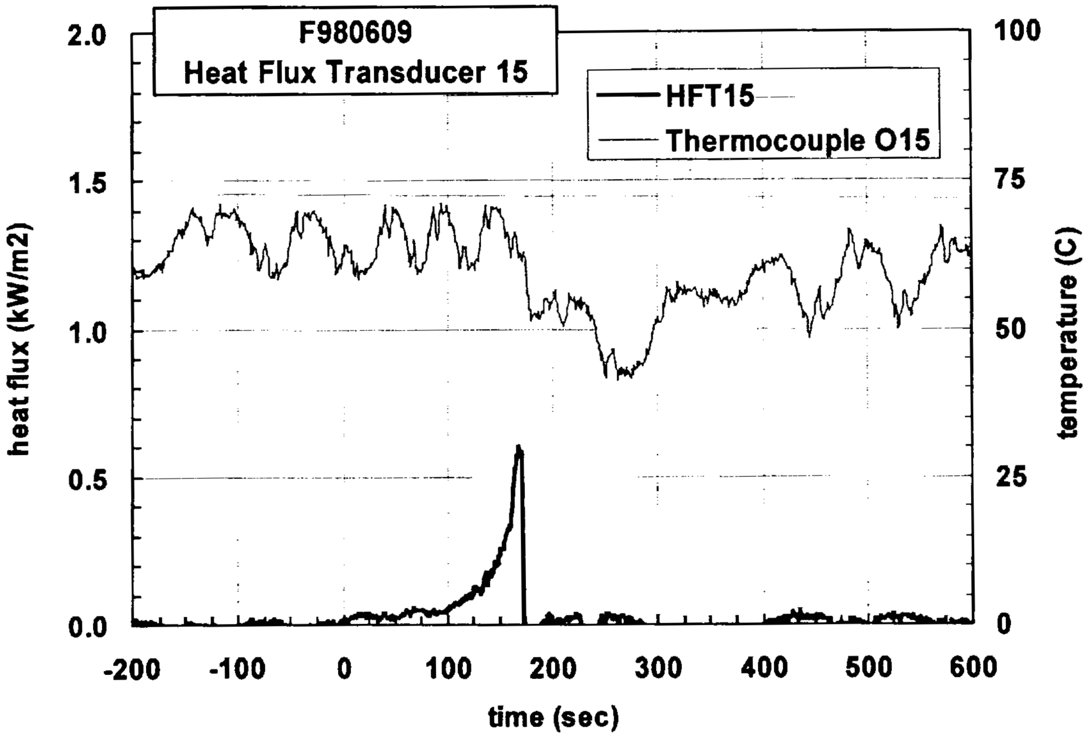

Plot E13. Fire Test F980609. Data plot from Heat Flux Transducer 15 and Thermocouple O15.

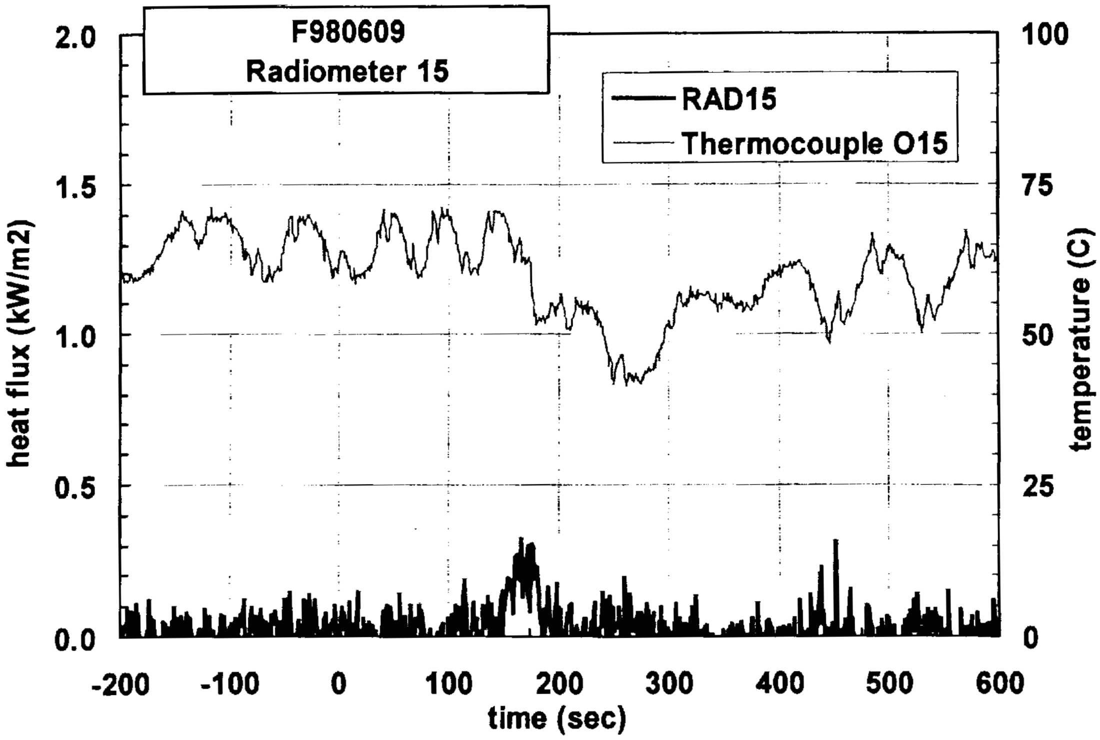

Plot E14. Fire Test F980609. Data plot from Radiometer 15 and Thermocouple O15.

APPENDIX F
PRESSURE AND AIRFLOW MEASUREMENTS

Figures F1 and F2 show the approximate locations of the pressure taps and bi-directional flow probe in the test vehicle.

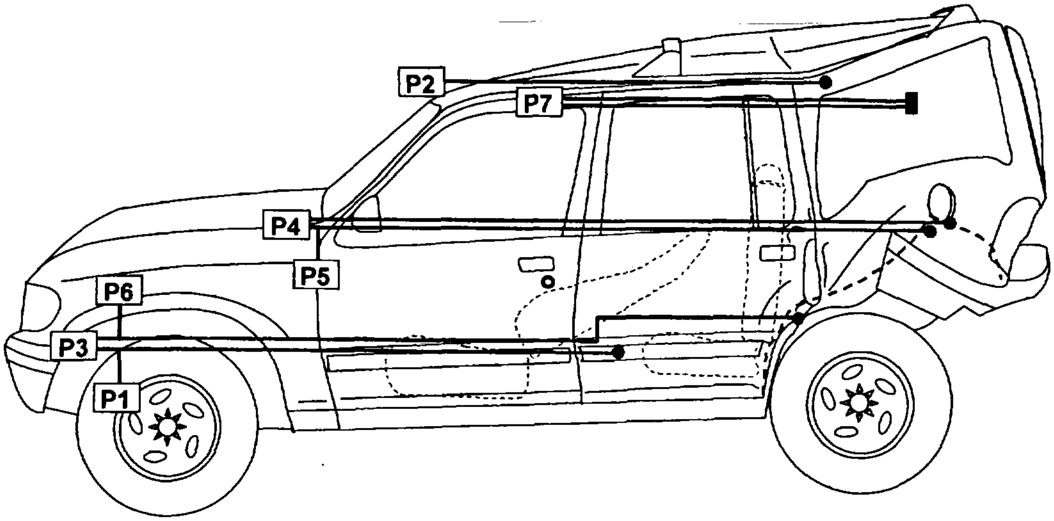

Figure F1. Fire Test F980609. Side view showing the approximate locations of the pressure taps and bi-directional flow probe in the test vehicle.

Five pressure taps were installed in the test vehicle for this test in the following locations: above the carpet in the foot area in front of the left rear seat; below the floor pan on the left side of the rear compartment, below the headlining panel in the rear compartment, in the left rear wheelhouse, and above the carpet at the rear of the rear compartment.

Each pressure tap was constructed from stainless steel tubing (o.d. = 0.250 in.). A union-T fitting with compression-type couplings (Parker) was attached to the inlet of the stainless steel tubing, with two of the three positions in the union-T fitting were left open. The other end of stainless steel tubing was connected to a pressure gauge with solvent-resistant flexible tubing (Tygon Masterflex® 6049; i.d. = 0.250 in.; o.d. = 0.438 in.). The total length of the stainless steel and flexible tubing was approximately 10 m.

A bi-directional flow probe was installed in the test vehicle so that it was located just outboard of the center of the upper edge of the left quarter opening. This probe was used to determine the velocity and direction of airflow through the window opening during the test. The stainless steel tubes leading from the flow probe were connected to pressure gauges with solvent-resistant resistant flexible tubing (Tygon Masterflex® 6049; i.d. = 0.250 in.; o.d. = 0.438 in.). The total length of tubing was approximately 10 m.

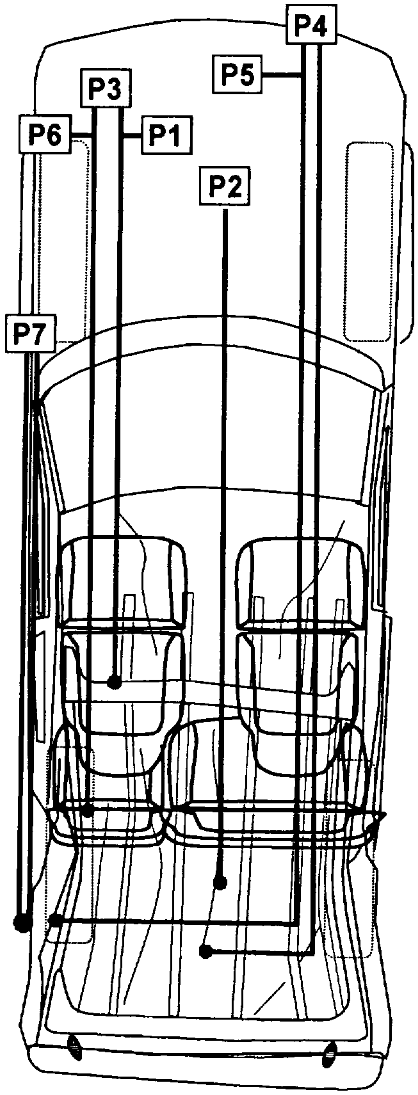

Figure F2. Fire Test F980609. Top view showing the approximate locations of pressure taps the bi-directional probe in the test vehicle.

The velocity of gas flow through the window opening in the driver's door was calculated from the pressure difference measured across the bi-directional probe using the following relationship:

$$V = 0.070\sqrt{T\Delta p} \qquad \text{(F1)}$$

where V is the gas velocity in m/s, T is the gas temperature in degrees Kelvin, and Δp is the pressure difference in Pascals (N/m^2) [F1 and F2].

Pressure gauges (Model C-264, Setra Systems, Acton, MA) with two pressure ranges were used for this test: - 0.5 to 0.5 (± 0.0013) in. W.C. (-124.5 to 124.5 Pascal) and -0.1 to 0.1 (± 0.0003) in. W.C. (-24.9 to 24.9 Pascal). Both gauges were accurate to 0.25% full scale. The gages were powered with a 24 volt non-regulated power supply (Setra Systems). The high-pressure inlet of Pressure Gauge P1 was connected to the pressure tap located above the carpet in the foot well in front of the left rear seat, and its low-pressure inlet was left open to atmosphere. The high-pressure inlet of Pressure Gauge P2 was connected to the pressure tap located below the headlining panel in the rear compartment, and its low-pressure inlet was left open to atmosphere. The high-pressure inlet of Pressure Gauge P3 was connected to the pressure tap located below the floor pan on the left side of the rear compartment, and its low-pressure inlet was connected to the pressure tap located above the carpet in the foot well in front of the left rear seat. The high-pressure inlet of Pressure Gauge P4 was connected to the pressure tap in the left rear wheelhouse, and its low-pressure inlet was connected to the pressure tap located above the carpet at the rear of the rear compartment. The high-pressure inlet of Pressure Gauge P5 was to the pressure tap in the left rear wheelhouse, and its low-pressure inlet was left open to atmosphere. The high-pressure inlet of Pressure Gauge P6 was connected to the pressure tap located below the floor pan on the left side of the rear compartment, and its low-pressure inlet was left open to atmosphere. Pressure Gauge P7 was to both sides of the bi-directional flow probe.

The PC-based data acquisition system described in **APPENDIX C** also was used to record the electronic signals from the pressure gauges during the test. The signal leads from the pressure gauges were plugged into panel-mounted connectors, which were hard-wired to a low-gain analog-input multiplex expansion card (DBK12, IOTech). The analog-input expansion card was interfaced to the main A/D card in the PC. The signal from each pressure gauge was sampled at a rate of 100 Hz. The analog data was stored to a data file in 100-point block-averages so that the effective sampling rate during the test was 1 Hz.

Plots of the pressures recorded with Pressure Gauges P1 through P7 are shown in Plots F1 through F7. Steam generated by the start of fire suppression caused the positive- and negative-going pressure deflections at about 175 seconds post-ignition.

REFERENCERS

F1. N. R. Keltner and J. L. Moya. Defining the thermal environment in fire tests. *Fire and Materials* **14**: 133-138, 1989.

F2. B. J. McCaffrey and G. A. Heskestad. Robust bidirectional low-velocity probe for flame and fire application. *Combustion and Flame* **26**: 125-127, 1976.

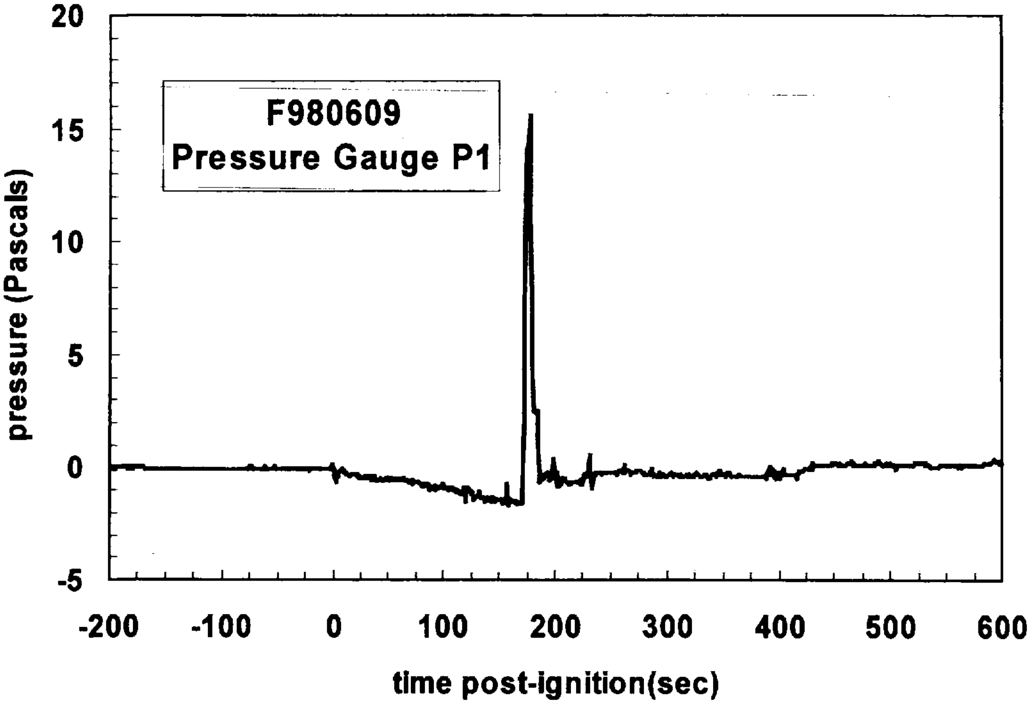

Plot F1. Fire Test F980609. Pressure above the carpet in the foot area in front of the left rear seat relative to atmospheric pressure measured with pressure gauge P1.

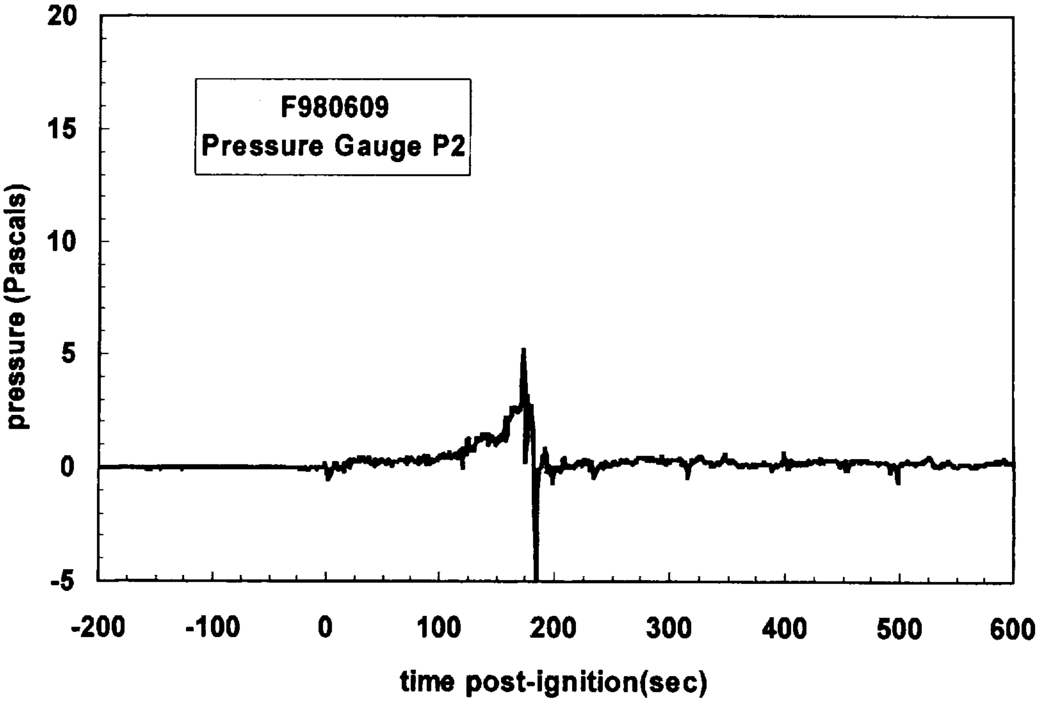

Plot F2. Fire Test F980609. Pressure below the headlining panel in the rear compartment relative to atmospheric pressure measured with pressure gauge P2.

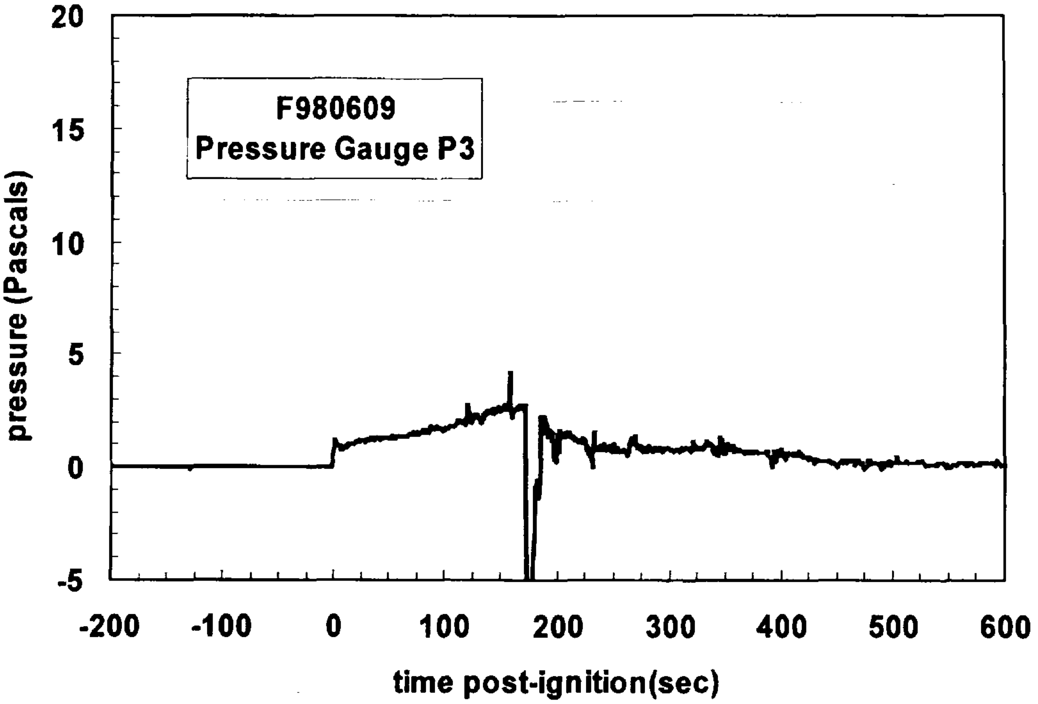

Plot F3. Fire Test F980609. Pressure difference between the foot well in front of the left rear seat and below the floor pan on the left side of the rear compartment measured with P3.

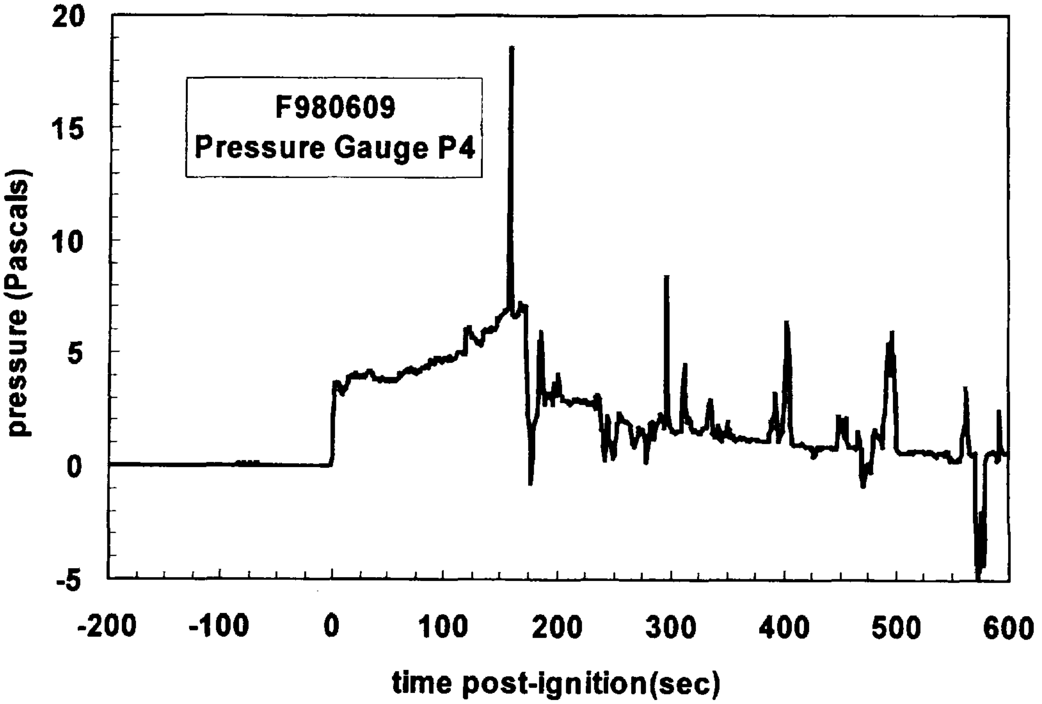

Plot F4. Fire Test F980609. Pressure difference between the left rear wheelhouse and above the carpet at the rear of the rear compartment measured with P4.

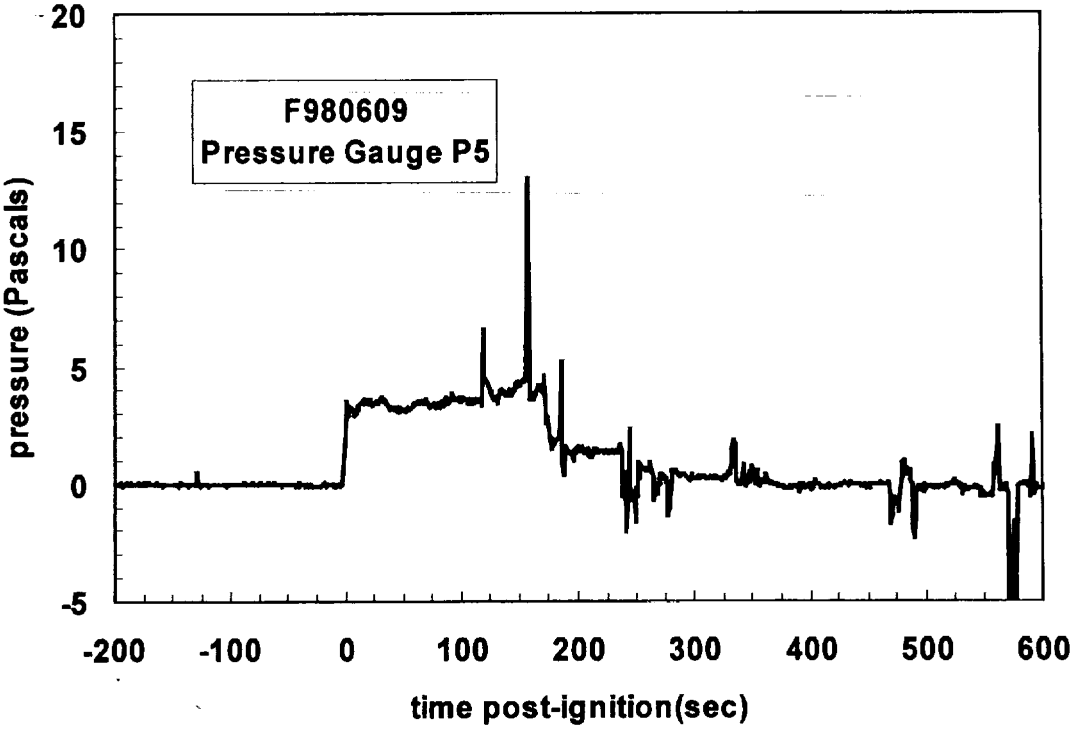

Plot F5. Fire Test F980609. Pressure in the left rear wheelhouse relative to atmospheric pressure measured with P5.

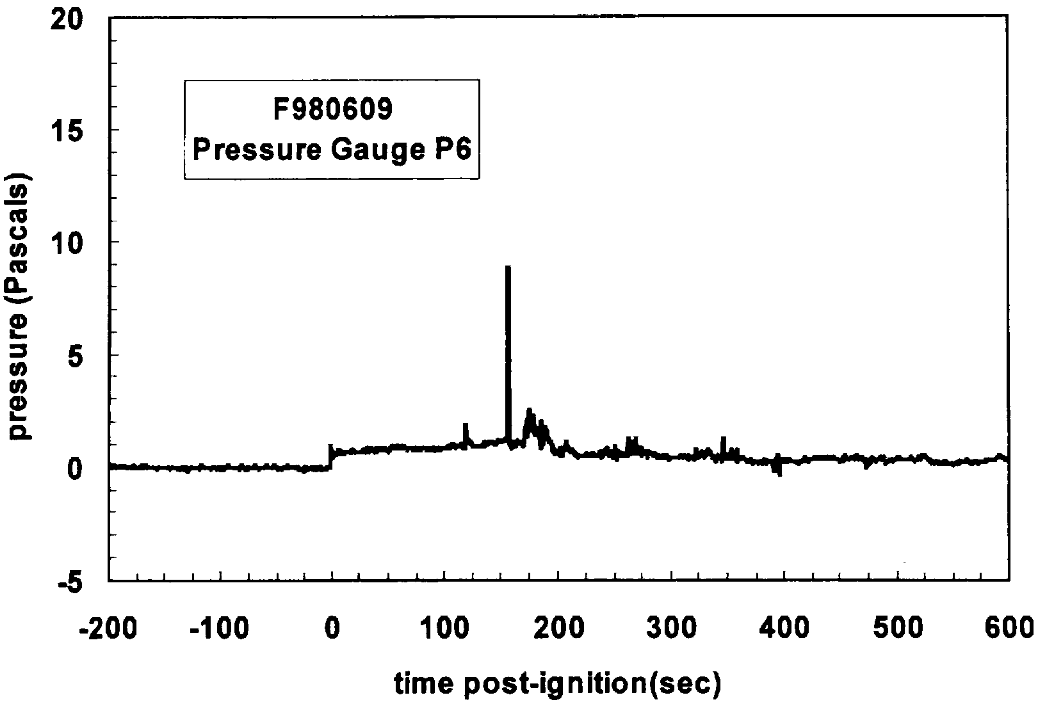

Plot F6. Fire Test F980609. Pressure below the floor pan on the left side of the rear compartment relative to atmospheric pressure measured with P6.

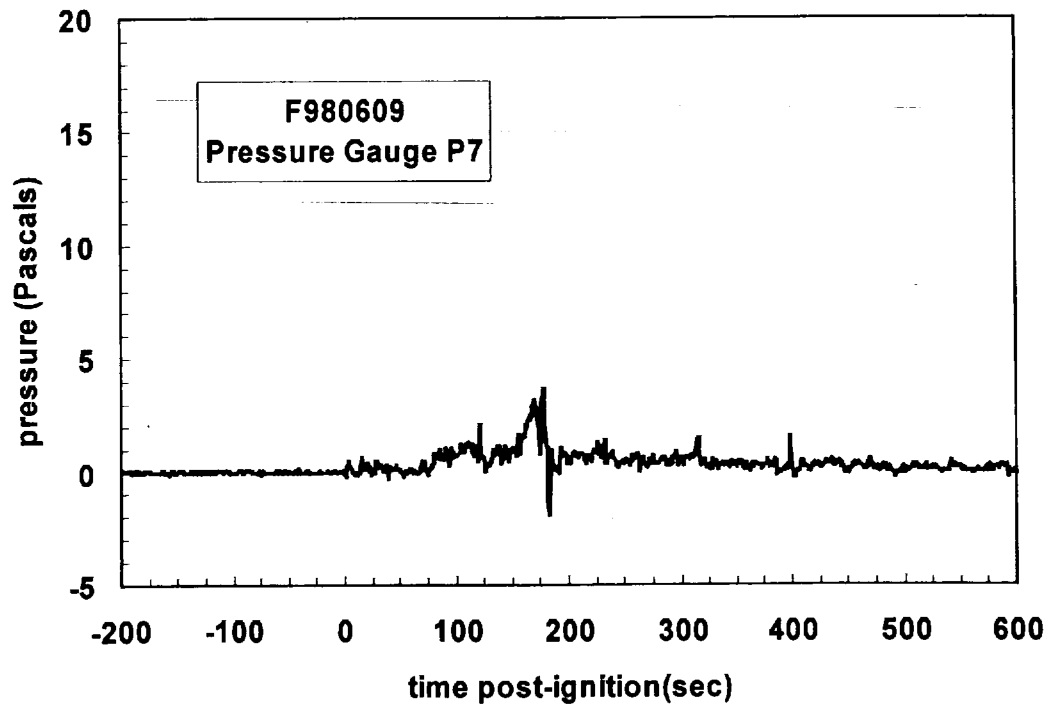

Plot F7. Fire Test F980609. Pressure difference across the bi-directional flow probe measured with P7.

APPENDIX G
FIRE PRODUCTS COLLECTOR DATA

Scientific and technical personnel from Factory Mutual Research Corporation were primarily responsible for obtaining and analyzing data from the Fire Products Collector (FPC) at the Factory Mutual Test Center.

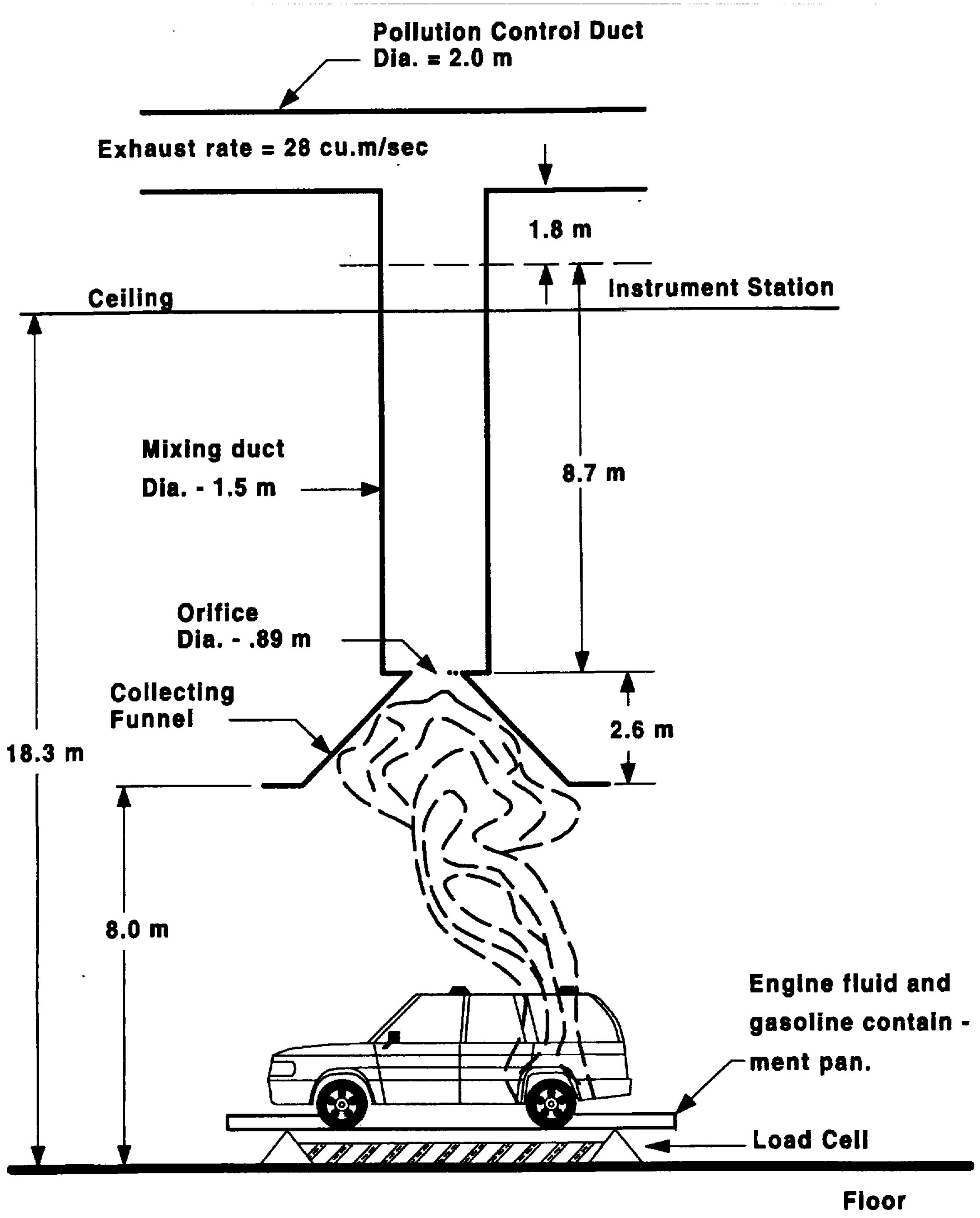

Figure G1. Fire Test F980609. Diagram of the test vehicle under the fire products collector at the Factory Mutual Test Center.

A fire products collector was used to measure heat and combustion gases generated by the burning vehicle during this test (Fig. G1). The fire products collector consisted of a collection funnel (diameter = 6.1 m), an orifice plate (hole = 0.9 m), and a vertical stainless steel sampling duct (diameter = 1.5 m). The sampling duct was connected to the air pollution control system of the Test Center. The blower of the air pollution control system induces gas flow through the sampling duct. Air enters the sampling duct via the orifice plate. The temperature, linear velocity, optical transmission, and chemical composition of the entrained gas were measured in the center of the sampling duct 8.66 m (5.7 duct diameters) downstream from the orifice plate, ensuring a flat velocity profile at the sampling location. The data acquisition system consisted of a Hewlett Packard 2313B analog-to-digital conversion sub-system interfaced to a Hewlett Packard 1000 computer.

Gas temperature in the sampling duct was measured with two Type-K thermocouples (30 gage) with exposed bead-type junctions. The thermocouple leads were housed in stainless steel tubes (o.d. = 6.4 mm). Ambient air temperature in the facility was measured by five Type-K thermocouples attached to the external surface of the duct at 2.44, 5.49, 9.14, 12.8, and 15.9 m above the floor. These thermocouples were shielded from radiation from the fire.

The linear velocity of the gas entrained in the sampling duct was measured with a Pitot ring consisting of four Pitot tubes. A static pressure tap was mounted on the inside wall of the sampling duct. The pressure difference between the Pitot ring and the static wall tap was measured with an electronic manometer (Barocel Model 1173, CGS Scientific Corporation).

The particulate concentration in the entrained air was determined from the optical transmission across the duct measured at 0.4579 μm (blue), 0.6328 μm (red), and 1.06 μm (infrared). The optical path length across the duct was 1.524 m. Gas was withdrawn from the sampling duct through a stainless steel tube (o.d. = 3.9 mm) at a flow rate of 0.17×10^{-3} m^3/s for chemical analysis. The gas flowed through a particulate filter, a water condenser, and a drying agent before entering the analyzers. Carbon dioxide (CO_2) and carbon monoxide (CO) were measured with two dedicated non-disperse infrared analyzers (Beckman Model 864 Infrared Analyzers). Oxygen (O_2) was measured with a paramagnetic oxygen analyzer (Beckman Model 755 Paramagnetic Oxygen Analyzer). Total gaseous hydrocarbons were measured with a flame ionization analyzer (Beckman Model 400 Flame Ionization Analyzer).

The rate of product release was calculated using the following relationship:

$$\left(\frac{dR_j}{dt}\right) = f_j\left(\frac{dV}{dt}\right)\rho_j = f_j\left(\frac{dW}{dt}\right)\left(\frac{\rho_j}{\rho_g}\right) \qquad \text{(G1)}$$

where d(R_j)/dt is the mass release rate of product j in kg/s; f_j is the volume fraction of product j; dV/dt is the total volume flow rate of the gas entrained in the sampling duct in m^3/s; dW/dt is the total mass flow rate of the gas entrained in the sampling duct in kg/s; ρ_j is the density of product j in g/m^3; and ρ_g is the density of the gas entrained in the concentration measurements. The rate of oxygen consumption was calculated using equation (G1), where the volume fraction of oxygen consumed was substituted for f_j.

The volume fraction of smoke particulate was calculated from the following relationship:

$$f_s = \frac{D\lambda \times 10^{-6}}{\Omega} \qquad \text{(G2)}$$

where f_s is the volume fraction of smoke, λ is the wavelength of the light source, Ω is the extinction coefficient of particulate (a value of 0.7 was used in these calculations), and D is the optical density at each of the three wavelengths at which measurements were made:

$$D = \frac{\ln\left({}^{I_0}\!/_{I}\right)}{L} \qquad \text{(G3)}$$

where I_0 is the intensity of light transmitted through clean air, I is the intensity of light transmitted through air containing smoke particulate, and L is the optical pathlength, which was equal to 1.524 m. A value of 1.1×10^6 g/m^3 was used for the density of smoke particulate (ρ_j) in equation (G1).

The convective heat release rate was calculated using the following relationship:

$$\left(\frac{dE_{conv}}{dt}\right) = \left(\frac{dW}{dt}\right) \times c_p \times \left(T_g - T_a\right) \qquad \text{(G4)}$$

where d(E_{conv})/dt is the convective heat release rate in kW; dW/dt is the mass flow rate of the gas entrained in the sampling duct in kg/s; c_p is the heat capacity of the gas entrained in the sampling duct at the gas temperature in kJ/(kg×K); T_g is the temperature of the gas entrained in the sampling duct in K; and T_a is the ambient air temperature in K.

The chemical heat release rate was calculated from the release rates of carbon dioxide and carbon monoxide as follows:

$$\left(\frac{dE_{ch}}{dt}\right) = \Delta H^{*}_{CO_2} \times \left(\frac{dR_{CO_2}}{dt}\right) + \Delta H^{*}_{CO} \times \left(\frac{dR_{CO}}{dt}\right) \tag{G5}$$

where $d(E_{ch})/dt$ is the chemical heat release rate in kW; ΔH^* is the net heat of complete combustion per unit mass of carbon dioxide or carbon monoxide released in the fire in kJ/g; and dR/dt is the mass release rate of carbon dioxide or carbon monoxide in kg/s. Values of ΔH^* for carbon dioxide and carbon monoxide were obtained from the literature [G1 and G2].

The chemical heat release rate also was calculated from the oxygen consumption rate as follows:

$$\left(\frac{dE_{ch}}{dt}\right) = \Delta H^{*}_{O}\left(\frac{dC_{O}}{dt}\right) \tag{G6}$$

where $d(E_{ch})/dt$ is the chemical heat release rate in kW; ΔH^*_O is the net heat of complete combustion per unit mass of O_2 consumed in kJ/g; and $d(C_O)/dt$ is the consumption rate of oxygen in kg/s. The value for ΔH^*_O was obtained from the literature [G1 and G2].

The radiative heat release rate was the difference between the chemical heat release rate and the convective heat release rate:

$$\left(\frac{dE_{rad}}{dt}\right) = \left(\frac{dE_{ch}}{dt}\right) - \left(\frac{dE_{conv}}{dt}\right) \tag{G7}$$

where $d(E_{rad})/dt$ is the radiative heat release rate; and $d(E_{ch})/dt$ is the average chemical heat release rate calculated using equations (G5) and (G6).

The vehicle was placed in a rectangular steel pan (length = 25 ft., width = 15 ft., height = 4 in.) to prevent spilled and leaking automotive fluids from spreading in the test facility. This fluid containment pan was fabricated from two sheets of carbon steel. Angle-braces were welded to the under-side of the pan to keep it from flexing under the weight of the vehicle. The corners of the support frame rested on load cells. Mass loss was determined from data acquired from the load cells during the test.

The fluid containment pan was lined with a layer of fiberglass-reinforced cement construction board (DuraRock, USG Corporation). A thin layer of sand was used to level the concrete board so that the grade of the surface measured from the center to the edges along the major and minor axes was no greater than 1%. The joints between boards were sealed with latex caulking.

Mass loss from the burning vehicle and any burning fluids retained by the containment pan was measured with a load cell weigh-module system. The fluid containment pan was supported by an I-beam frame a load cell weight-module (KIS Series, BLH Electronics, Inc.) at each corner. These weight-modules contain cylindrical, double cantilever strain gauge transducers that are not generally affected by changes in mass distribution. The weight-module system was calibrated before this test by placing a series of standard weights on the fluid containment pan.

Data from the fire-products collector and load cell weight-module system are shown in Plots H1 through H5. The Fire Products Collector did not detect a fire plume until approximately 15 seconds after the gasoline was ignited. After the initial increase (approximately 15 to 25 seconds post-ignition), the heat release rate increased exponentially until the fire was extinguished (Plot G1). The heat release rate reached a maximum of approximately 1200 kW at 230 seconds post-ignition. The carbon dioxide release rate curve (Plot G2) was similar to the heat release rate curve. After initially increasing between 15 and 25 seconds post-ignition, the carbon monoxide release rate curve approached a value of 1.6 to 1.7 g/s asymptotically, and decreased when the fire was extinguished (Plot G3). The smoke release rate curve was similar, approaching a value of 0.5 to 0.6 mg/s before the fire was extinguished (Plot G4). Mass loss curve indicated that the vehicle lost between 2 and 3 kg as a result of material burning during this test (Plot G5). The resolution of the load cell system used to make the weight measurement was between 0.3 and 0.4 kg (between 10 to 15% of the total mass loss during the test), and was responsible for the high degree of scatter in the mass loss curve (Plot G5).

REFERENCES

G1. G. Heskestad. A Fire Products Collector for Calorimetry into the MW Range, Technical Report J.I. OC2E1.RA. Factory Mutual Research Corporation, Norwood, MA. June, 1981.

G2. Archibald Tewarson. "Generation of Heat and Chemical Compounds in Fires" Section 3/Chapter 4, SFPE Handbook of Fire Protection Engineering, 2nd Edition, 1995, pp. 3:53-124.

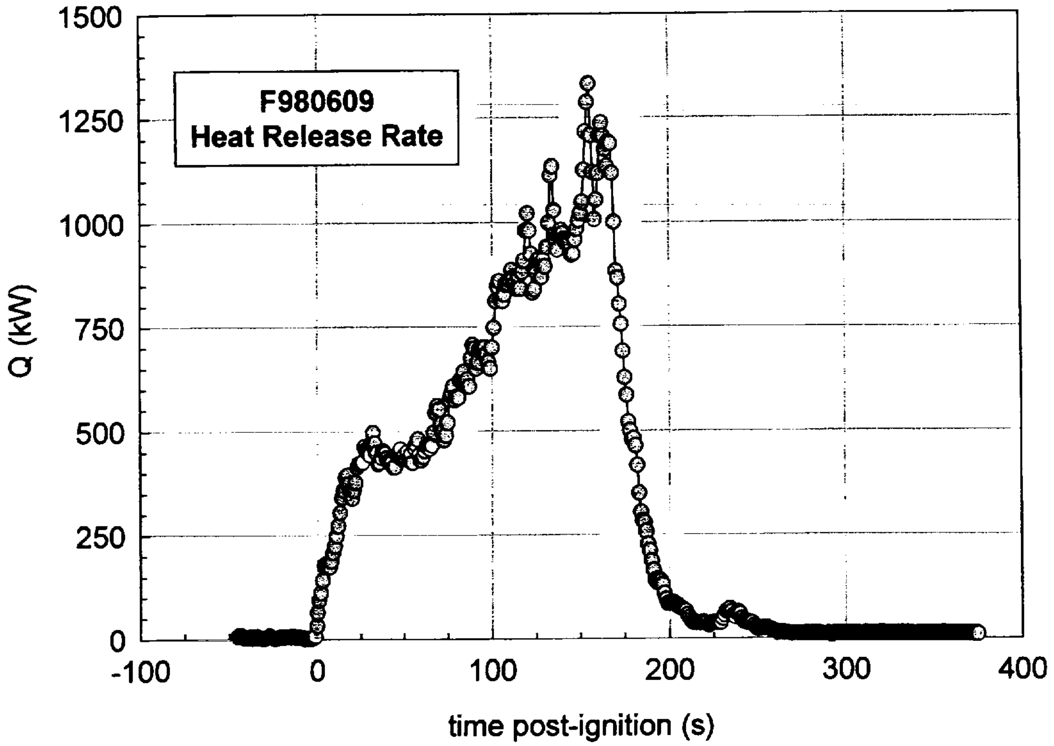

Plot G1. Fire Test F980609. Heat release rate measured using the Fire Products Collector.

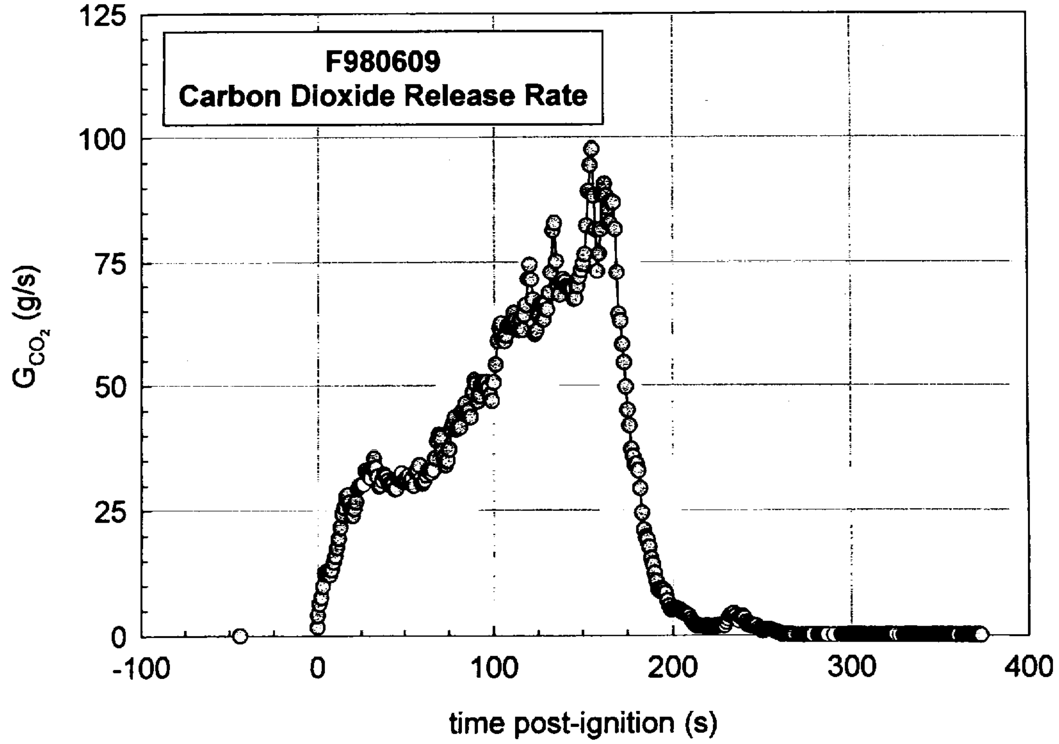

Plot G2. Fire Test F980609. Carbon dioxide release rate measured using the Fire Products Collector.

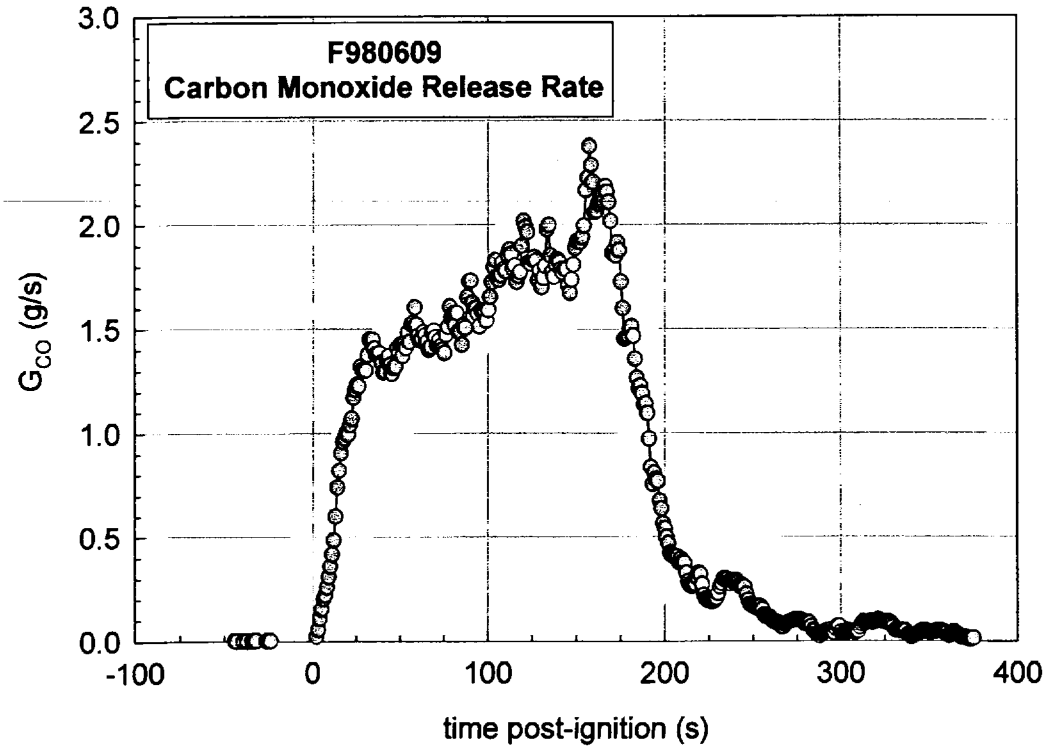

Plot G3. Fire Test F980609. Carbon monoxide release rate measured using the Fire Products Collector.

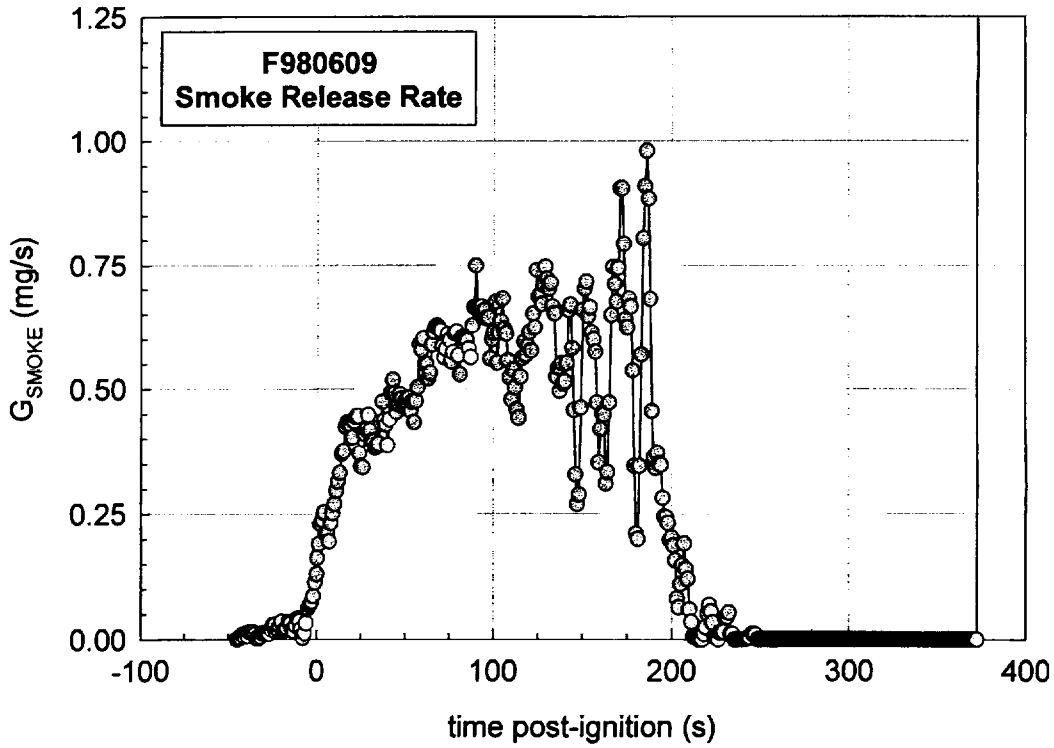

Plot G4. Fire Test F980609. Smoke release rate measured using the Fire Products Collector.

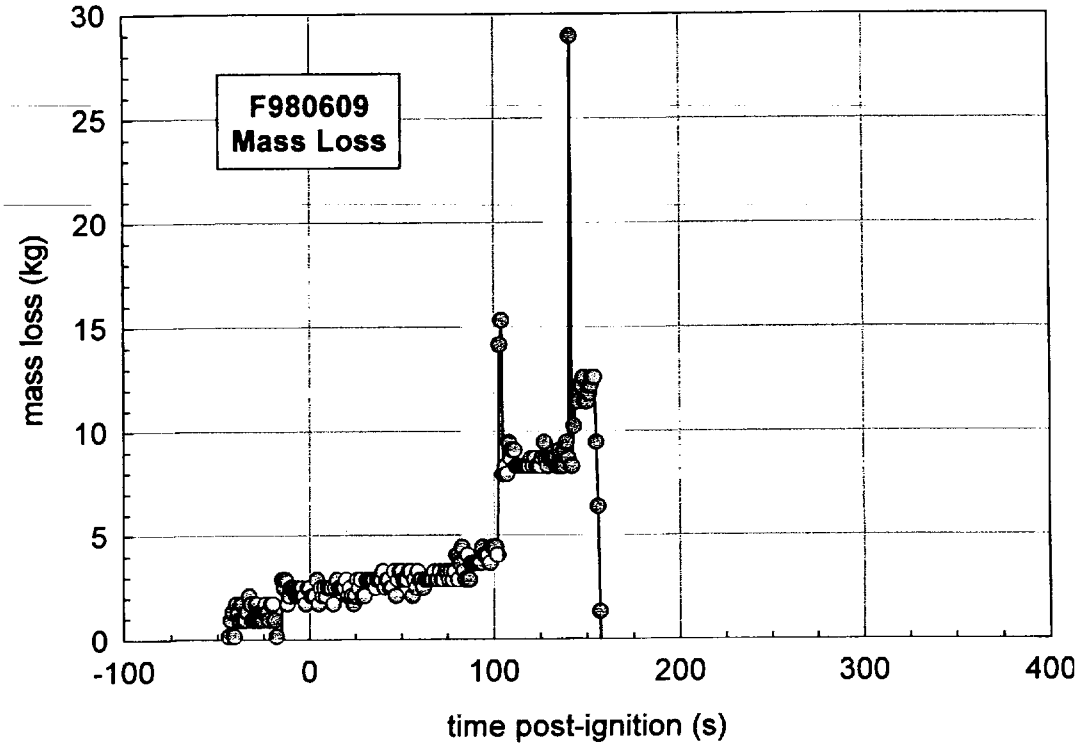

Plot G5. Fire Test F980609. Mass Loss from the test vehicle during the fire test. The mass data was not valid after 170 seconds post-ignition because test personnel stepped onto the fluid containment pan to move video equipment.

APPENDIX H
PASSENGER COMPARTMENT COMBUSTION GAS DATA
FOURIER TRANSFORM INFRARED SPECTROSCOPY

The sampling-line for FTIR analysis consisted of a stainless-steel tube (o.d. = 0.250 in. (6.4 mm), i.d. = 0.125 in. (3.2 mm), l = 20 ft (6.1 m)) inserted through the roof between the front seats along the longitudinal midline of the test vehicle (Fig.'s H1 and H2). The inlet of the sample-tube extended approximately 10 in. below the headlining. The tube was not heated. The outlet of the sample tube was connected to a heated Teflon® transfer-line (o.d. = 0.250 in. (6.4 mm), i.d. = 0.125 in. (3.2 mm), l = 75 ft. (23 m)), which was connected to the gas cell of the FTIR spectrometer. The transfer-line was heated to 105°C during the test to prevent condensation of water and water-soluble gases (*e.g.*, HCl, HCN, NO, and NO_2). An in-line stainless steel filter holder containing a quartz fiber filter (o.d. = 47 mm) was placed between the sample-tube and the transfer-line to prevent smoke particles from contaminating analytical instrumentation.

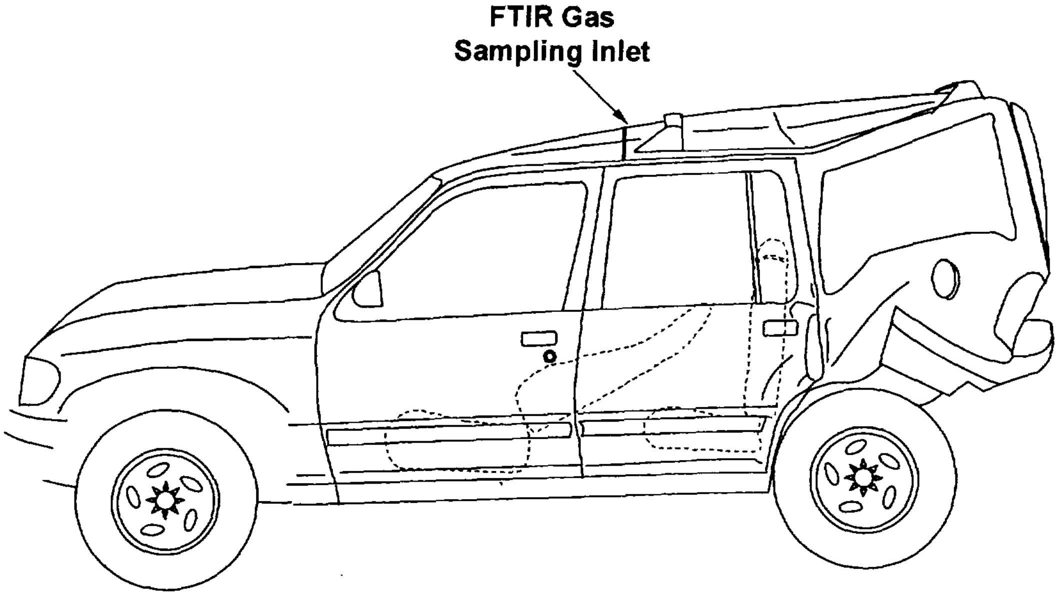

Figure H1. Fire Test F980609. Side-view of the test vehicle show the approximate location of the FTIR gas-sampling inlet in the passenger compartment.

The FTIR spectrometer was a Model I-1000 Series FTIR Spectrometer (MIDAC Corporation, Riverside, California), with a KBr beam-splitter; a liquid nitrogen-cooled Mercury-Cadmium-Telluride detector; and gold-surfaced aluminum optics. This instrument was fitted with a stainless steel, multiple-reflectance gas cell (path length = 10 m) with zinc selenide windows. The gas cell was heated to 105°C. The optical bench was filled with clean, dry argon and hermetically sealed. The usable spectral range of this instrument was approximately 7400-700 cm^{-1}. Pressure in the gas cell during the fire tests was measured with a Baratron pressure gauge (MKS Instruments, Burlington, MA). The spectrometer was operated at a spectral resolution of 0.5 cm^{-1}.

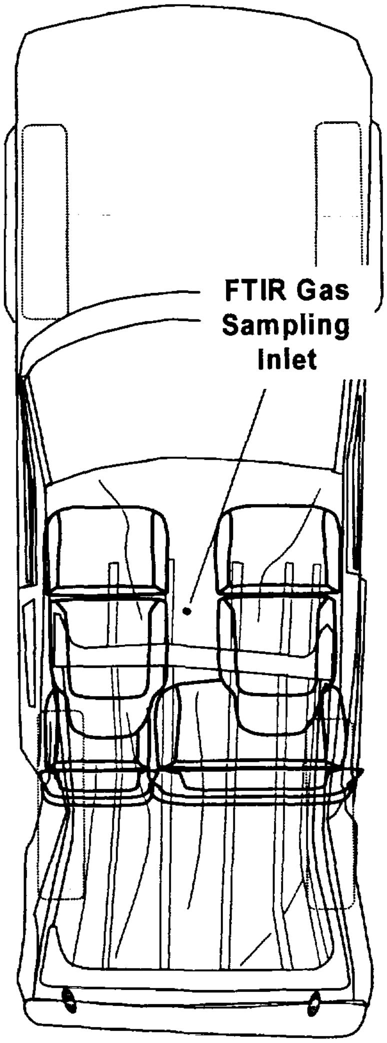

Figure H2. Fire Test F980609. Top view of the test vehicle showing the approximate location of the FTIR gas-sampling inlet in the passenger compartment.

The sampling line and gas cell were equilibrated to 105°C for at least 60 minutes before sample acquisition. A reference spectrum was acquired while the gas cell was evacuated. During the fire tests, the gas cell was purged continuously with air withdrawn from the passenger compartment at a flow rate of 7 L/min. Single-scan absorbance spectra were acquired and stored to disk at intervals of 10 s. After the test, the stored spectra were analyzed using the quantitative analysis software provided by the instrument manufacturer (AutoQuant, MIDAC). This software uses a Classical Least Squares algorithm to determine gas concentrations. The method developed for analysis of combustion gases was calibrated with gas standards (Scott Specialty

Gases, Inc., Troy, MI). The standards were either NIST-traceable or produced by a gravimetric blending process.

An electrochemical oxygen sensor (Model SE-25, FIGARO USA, Inc.) was placed in the FTIR sampling line just before the FTIR gas cell. The signal from the oxygen sensor was recorded by the data acquisition system described in **APPENDIX C**. The oxygen sensor was calibrated before this test by recording its responses when purged with room air (21% O_2) and with pure nitrogen (0% O_2).

The gaseous combustion products measured by FTIR in the passenger compartment during this test included carbon dioxide, carbon monoxide, methane, ethylene, acetylene, hydrogen cyanide, nitric oxide, and hydrogen chloride (Plots H1 through H8). Except for carbon dioxide, which has a background concentration in air of approximately 0.05%, and hydrogen chloride, the concentrations of all of these gases were less than their respective lower limits of detection before ignition. The background concentration of carbon dioxide in air is approximately 0.04%. Noise in the Infrared spectra acquired before ignition resulted in an apparent hydrogen chloride concentration of < 1 ppm.

Carbon dioxide, carbon monoxide, methane, ethylene, and acetylene started to accumulate in the passenger compartment between 50 and 75 seconds post-ignition (Plots H1 through H5). The Infrared spectra acquired during this test also contained a broad absorbance band between 2800 and 3200 cm^{-1}, indicating the presence of a mixture of aliphatic hydrocarbons in the air samples from the passenger compartment. The intensity of this absorbance band generally followed the same time-course as that of methane (Plot H3), ethylene (Plot H4), and acetylene (Plot H5). This broad band appeared to contain absorbances from ethane, propane, and butane. However, all of the gaseous species contributing to this absorbance band could not be identified or accurately quantified.

Hydrogen cyanide (Plot H7) and nitric oxide (Plot H8) started to accumulate in the passenger compartment between 50 and 100 seconds post-ignition. Hydrogen chloride (HCl) was not detected during this test (Plot H6).

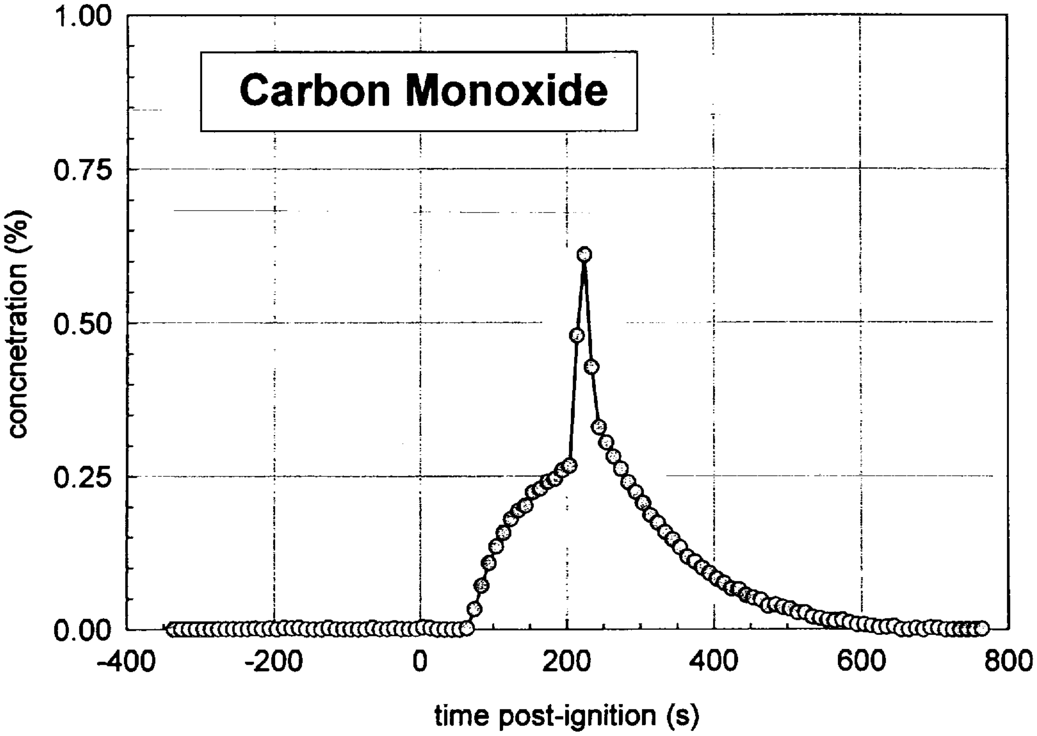

Plot H1. Fire Test F980609. Concentration of carbon monoxide (CO) in the passenger compartment determined by FTIR analysis.

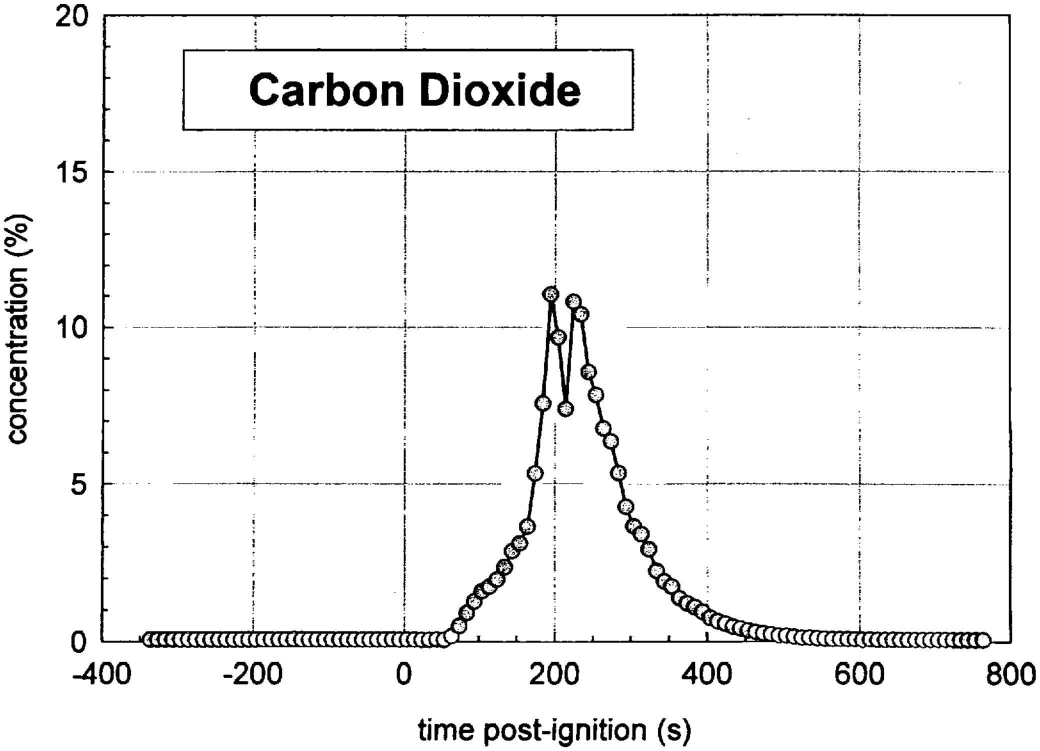

Plot H2. Fire Test F980609. Concentration of carbon dioxide (CO_2) in the passenger compartment determined by FTIR analysis.

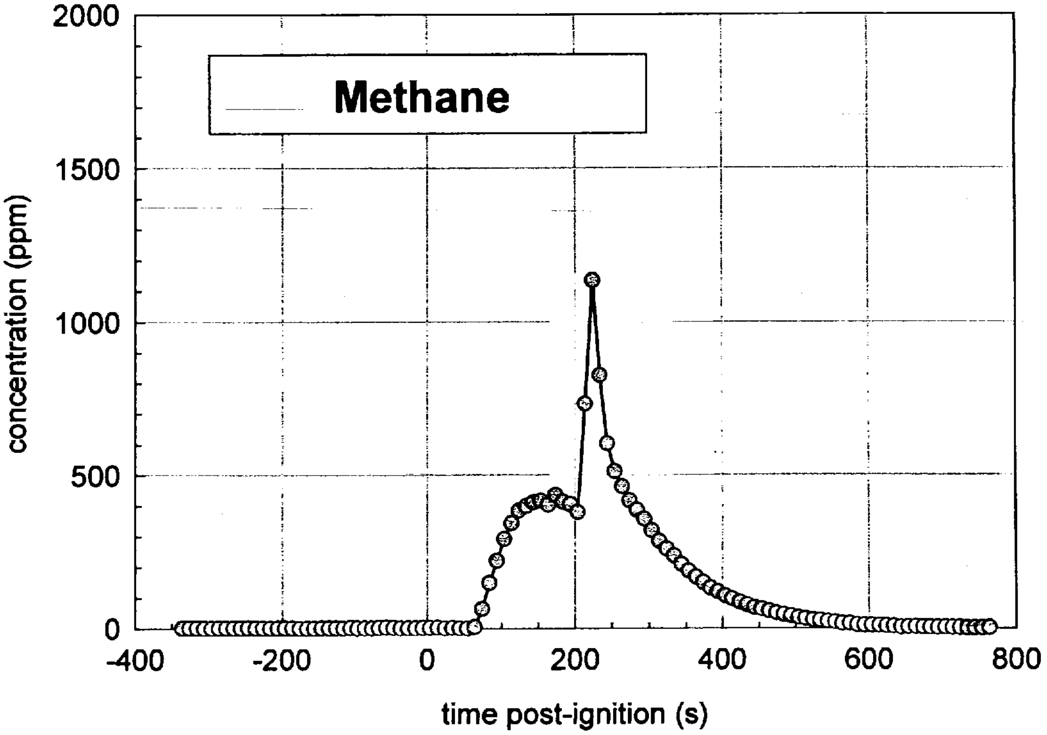

Plot H3. Fire Test F980609. Concentration of methane (CH_4) in the passenger compartment determined by FTIR analysis.

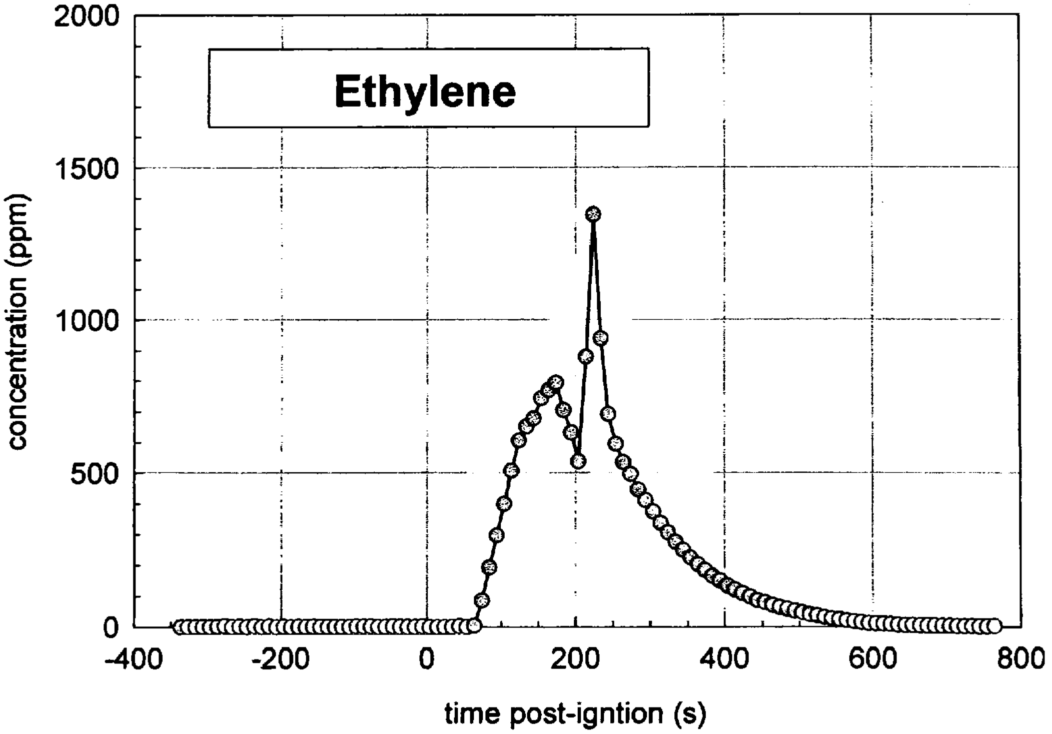

Plot H4. Fire Test F980609. Concentration of ethylene (C_2H_4) in the passenger compartment determined by FTIR analysis.

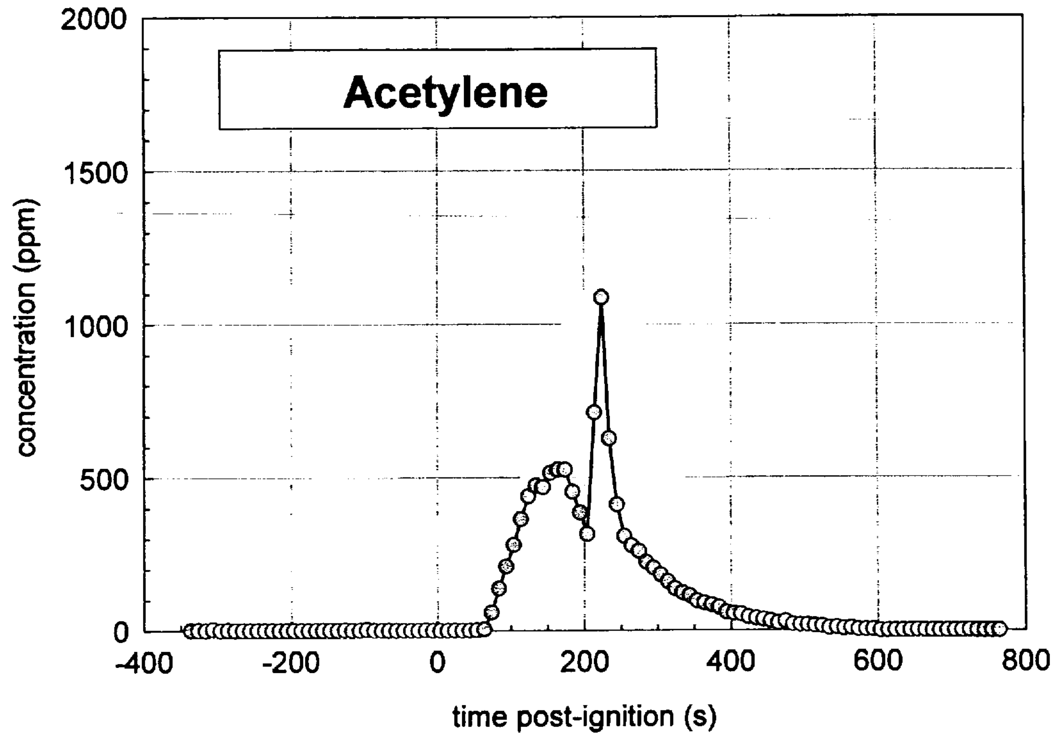

Plot H5. Fire Test F980609. Concentration of acetylene (C_2H_2) in the passenger compartment determined by FTIR analysis.

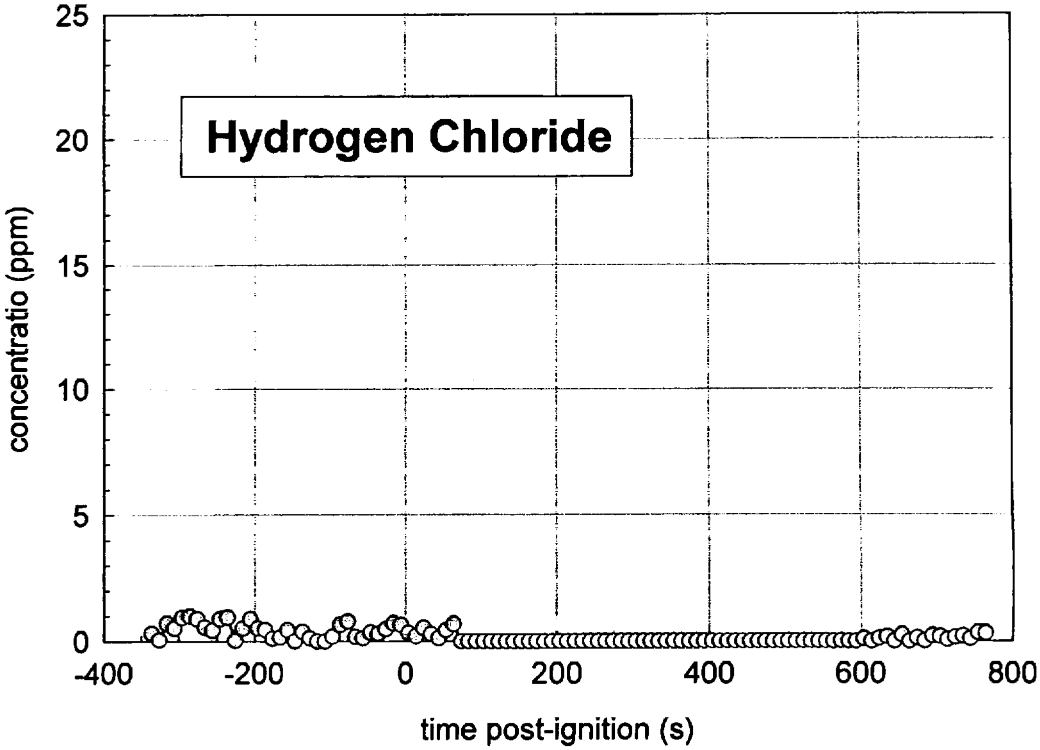

Plot H6. Fire Test F980609. Concentration of hydrogen chloride (HCl) in the passenger compartment determined by FTIR analysis.

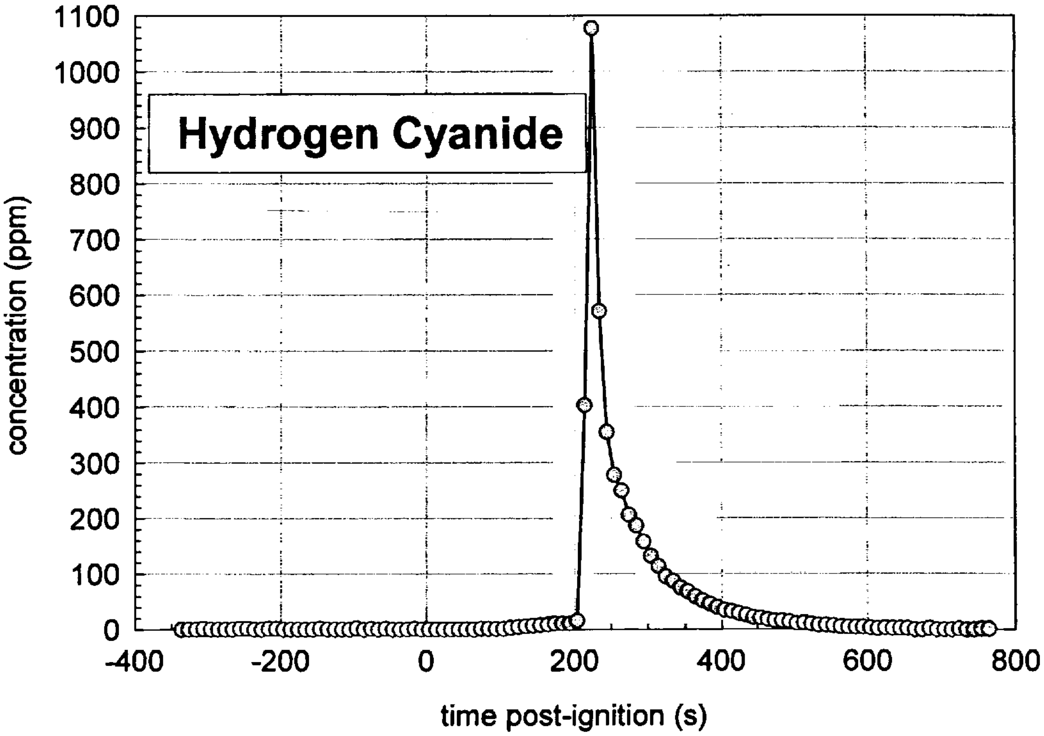

Plot H7. Fire Test F980609. Concentration of hydrogen cyanide (HCN) in the passenger compartment determined by FTIR analysis.

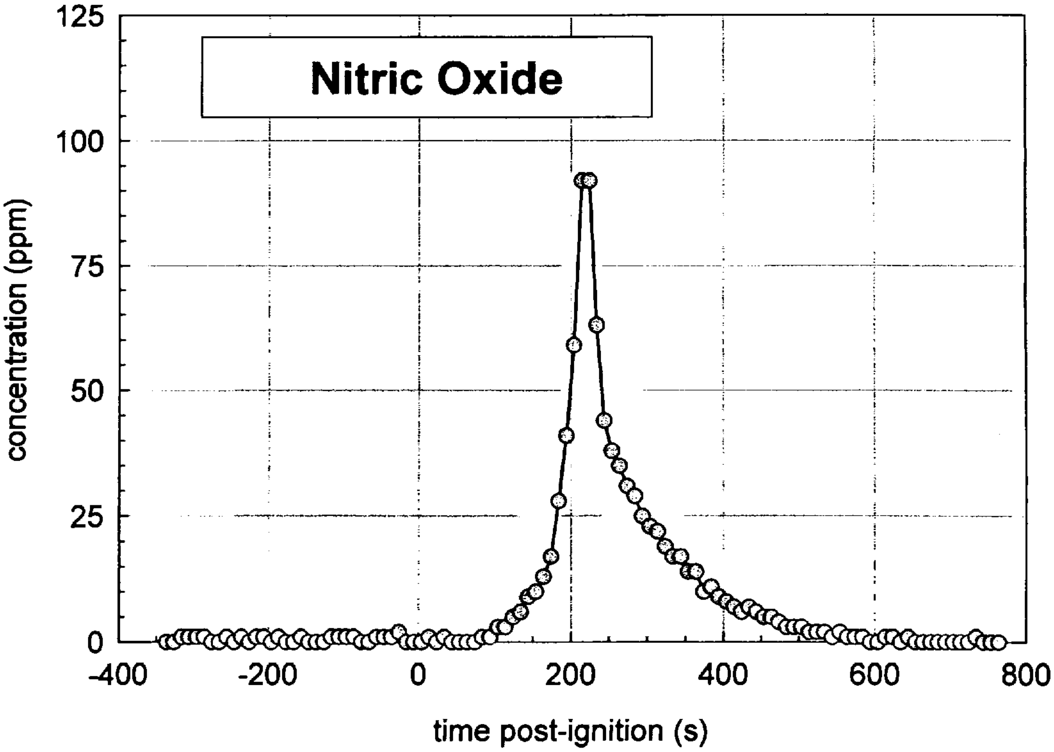

Plot H8. Fire Test F980609. Concentration of nitric oxide (NO) in the passenger compartment determined by FTIR analysis.

APPENDIX I
PASSENGER COMPARTMENT COMBUSTION GAS DATA
GAS CHROMATOGRAPHY/MASS SPECTROSCOPY GAS ANALYSIS

The sampling-line for GC/MS samples consisted of a stainless-steel tube (o.d. = 0.250 in. (6.4 mm), i.d. = 0.125 in. (3.2 mm), l = 20 ft (6.1 m)) inserted through the roof between the front seats along the longitudinal midline of the test vehicle (Fig.'s I1 and I2). The inlet of the sample-tube extended approximately 10 in. below the headlining. The outlet of the sample tube was connected to sampling manifold by a length of stainless steel sampling tube (o.d. = ¼ in., length = 25 ft.). The sampling manifold contained five sample cartridges in parallel. Airflow was directed sequentially through the sample cartridges a solenoid-actuated gas-switching manifold. The airflow rate through the cartridges during sampling was adjusted 250 cm^3/min with a rotometer. None of the components of the GC/MS sampling line were heated.

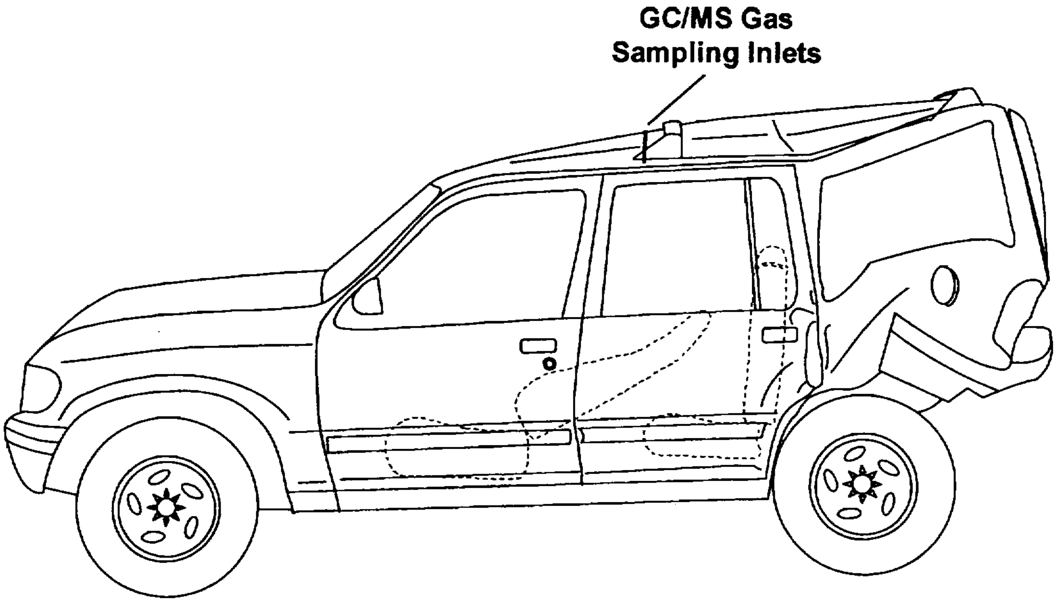

Figure I1. Fire Test F980609. Side-view of the test vehicle show the approximate locations of the GC/MS gas sampling inlets in the passenger compartment.

Each cartridge was a glass-lined stainless steel tube (i.d. = 4 mm; length = 10 cm; Scientific Instrument Services, Inc, Ringoes, NJ) packed with 25 mg of Carbotrap™ C Graphitized Carbon Black (Supelco, Inc.; Bellefonte, PA) in series with 15 mg of Carbotrap™ Graphitized Carbon Black (Supelco).

After the test, the sample cartridges were analyzed by thermal desorption/gas chromatography/mass spectrometry. Deuterated standards dissolved in deuterated methanol were added to each sorbent cartridge to monitor sample recovery. A modified purge-and-trap concentrator was used for thermal desorption (Model 600 Purge-and-Trap Concentrator, CDS Analytical, Oxford, PA). The gas chromatograph was a Model 5890 Series II Plus Gas Chromatograph (Hewlet Packard, Palo Alto, CA). The mass spectrometer was a Hewlet Packard

Model 5989B Mass Spectrometer (Hewlett Packard). The thermal desorption unit was interfaced directly to the split/splitless injector of the gas chromatograph through a cryo-focusing unit. The injector was operated in the split mode with a split of approximately 10 mL/min. The chromatographic column was a fused silica capillary column coated with 100% methyl silicone (HP-1 ; length = 30 m; i.d. = 0.25 mm; film thickness = 0.25 μm).

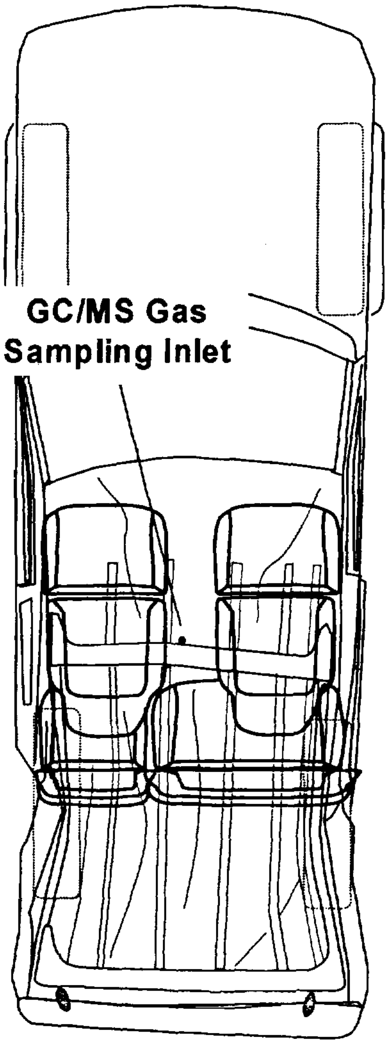

Figure I2. Fire Test F980609. Top view of the test vehicle showing the approximate locations of the GC/MS gas sampling inlet in the passenger compartment.

The sample was desorbed at 320°C for 10 min, and cryofocused onto the head of the chromatographic column -80°C. The temperature of the analytical column was maintained at 0°C while the sample was desorbed and cryo-focused. To start the chromatographic analysis, the

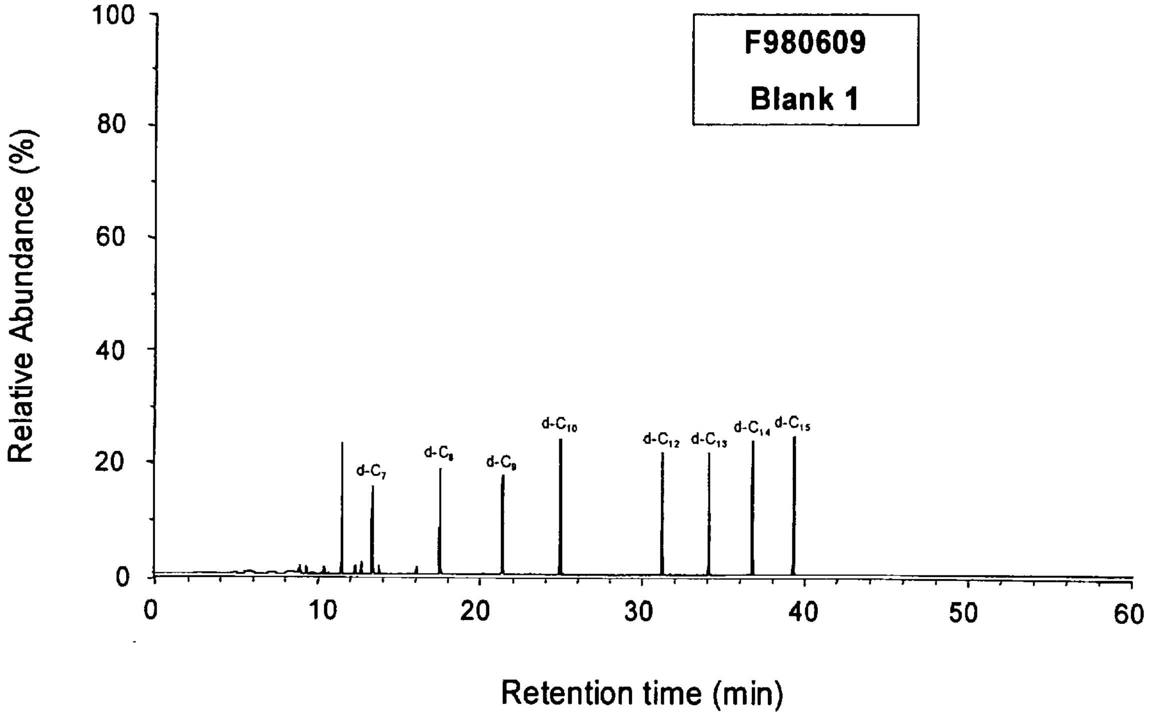

Plot I1. Fire Test F980609. Mass chromatogram from GC/MS analysis of Blank 1 acquired before the test.

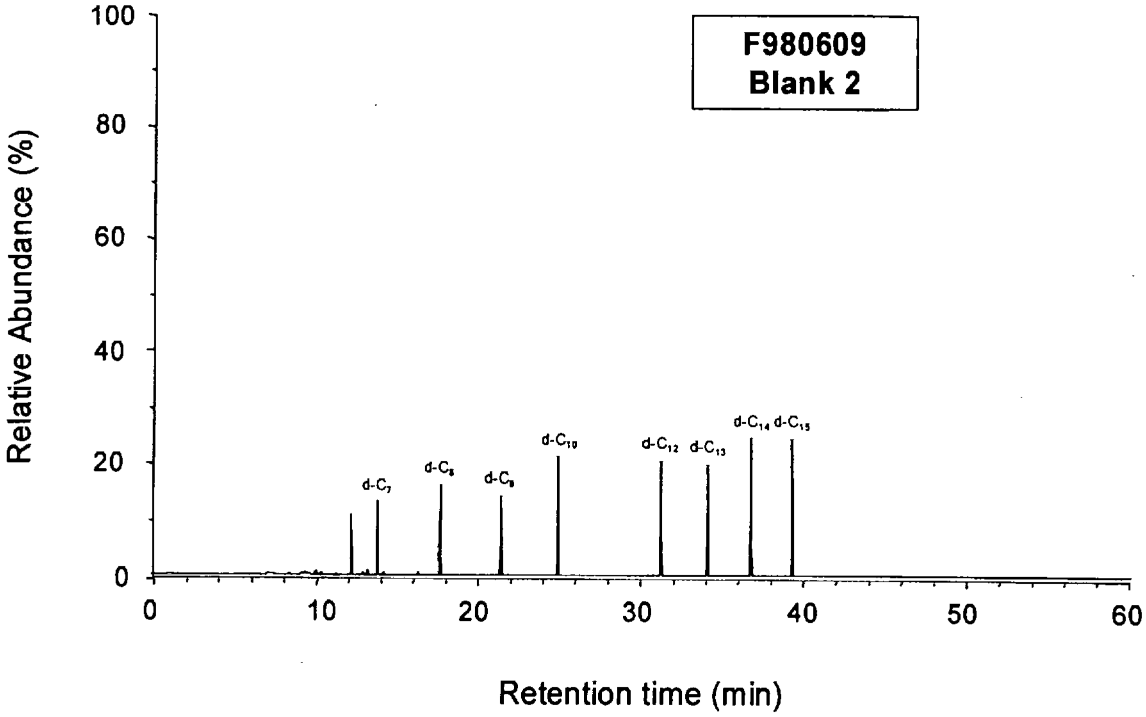

Plot I2. Fire Test F980609. Mass chromatogram from GC/MS analysis of Blank 2 acquired before the test.

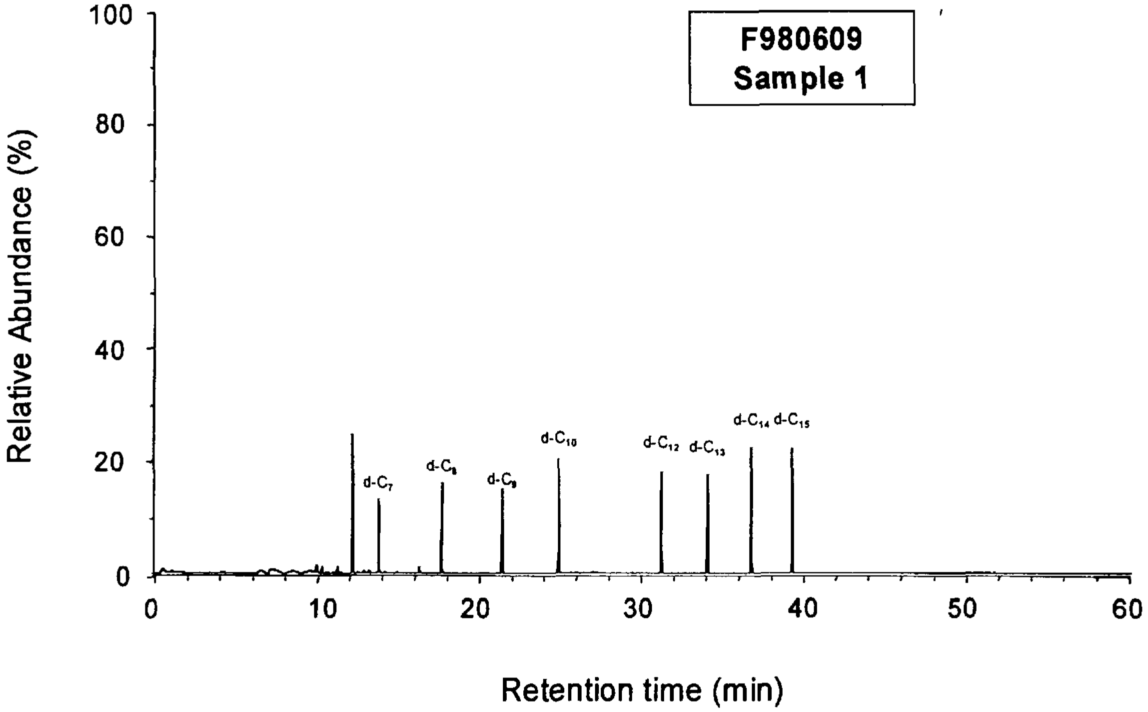

Plot I3. Fire Test F980609. Mass Chromatogram of Sample 1 acquired from -30 to +00 seconds post-ignition.

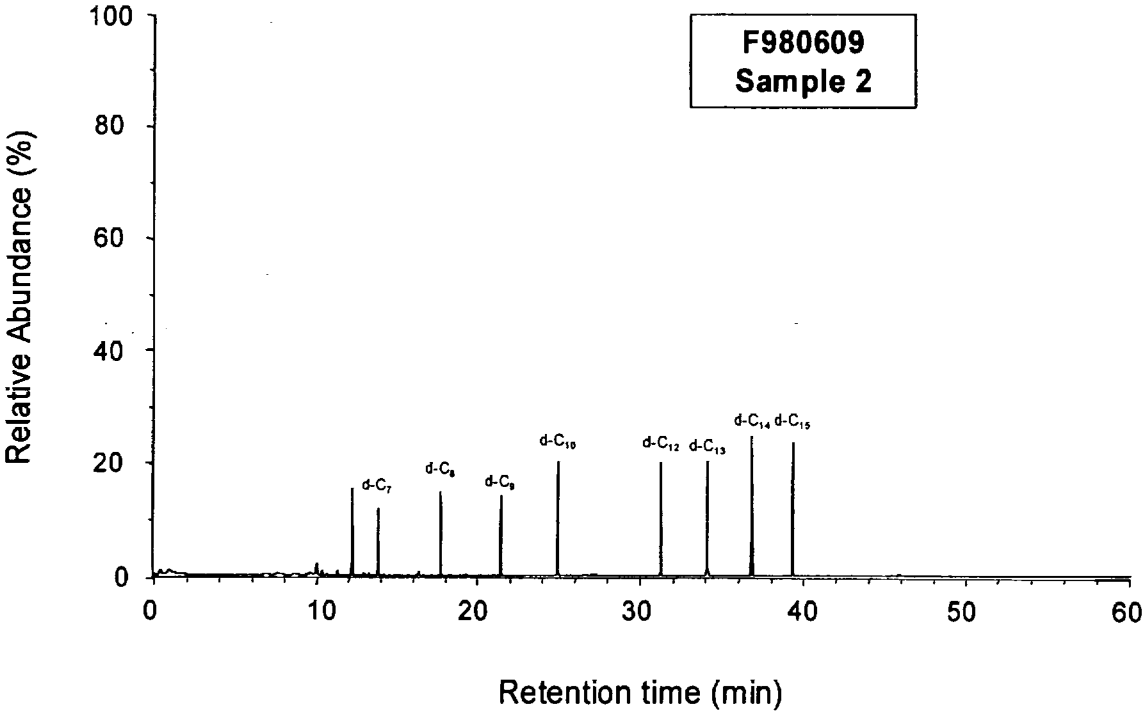

Plot I4. Fire Test F980609. Mass Chromatogram of Sample 2 acquired from +00 to +60 seconds post-ignition.

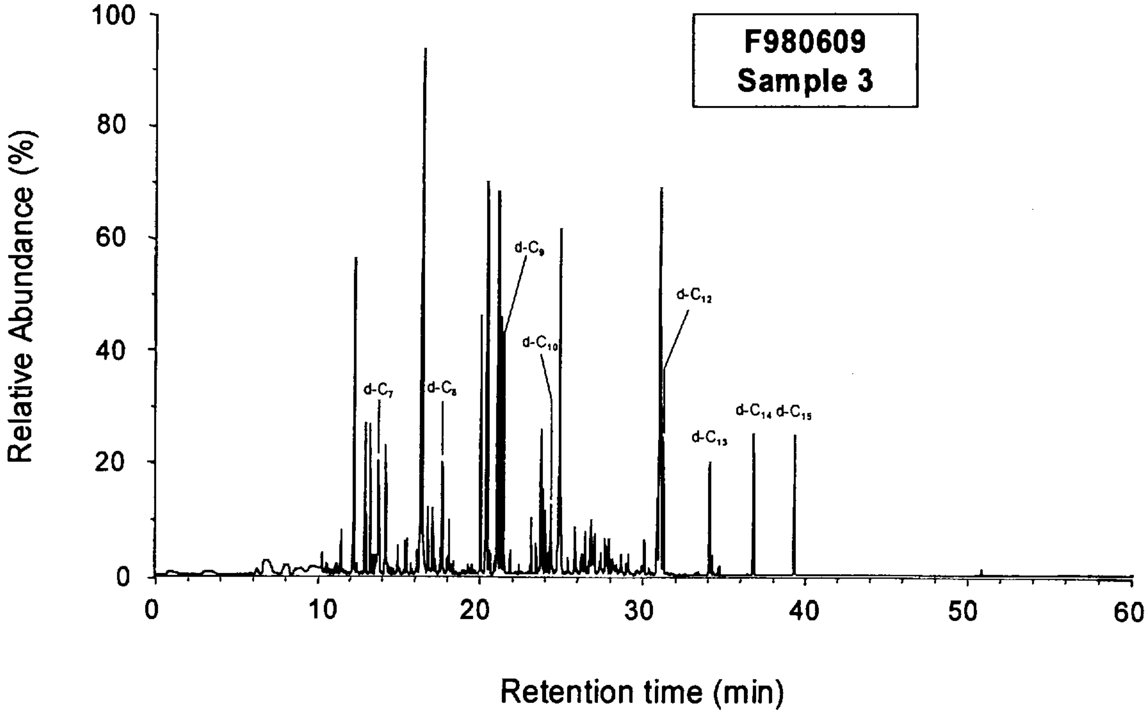

Plot 15. Fire Test F980609. Mass Chromatogram of Sample 3 acquired from +60 to +120 seconds post-ignition.

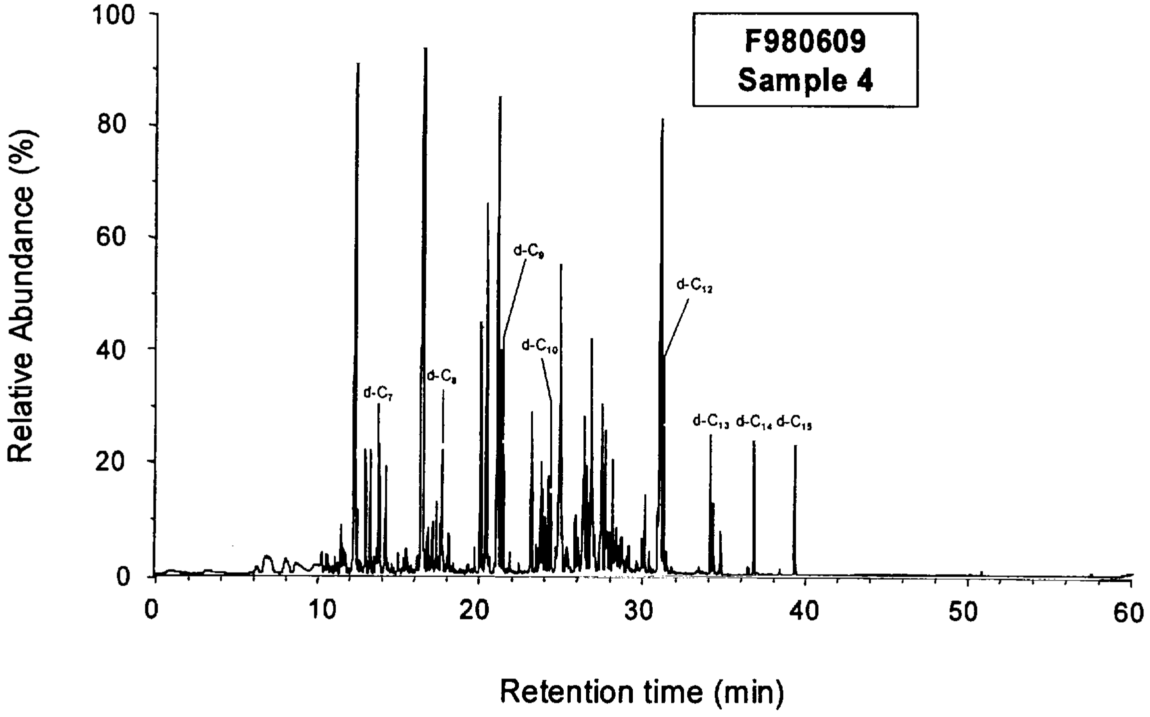

Plot I6. Fire Test F980609. Mass Chromatogram of Sample 4 acquired from +120 to +165 seconds post-ignition.

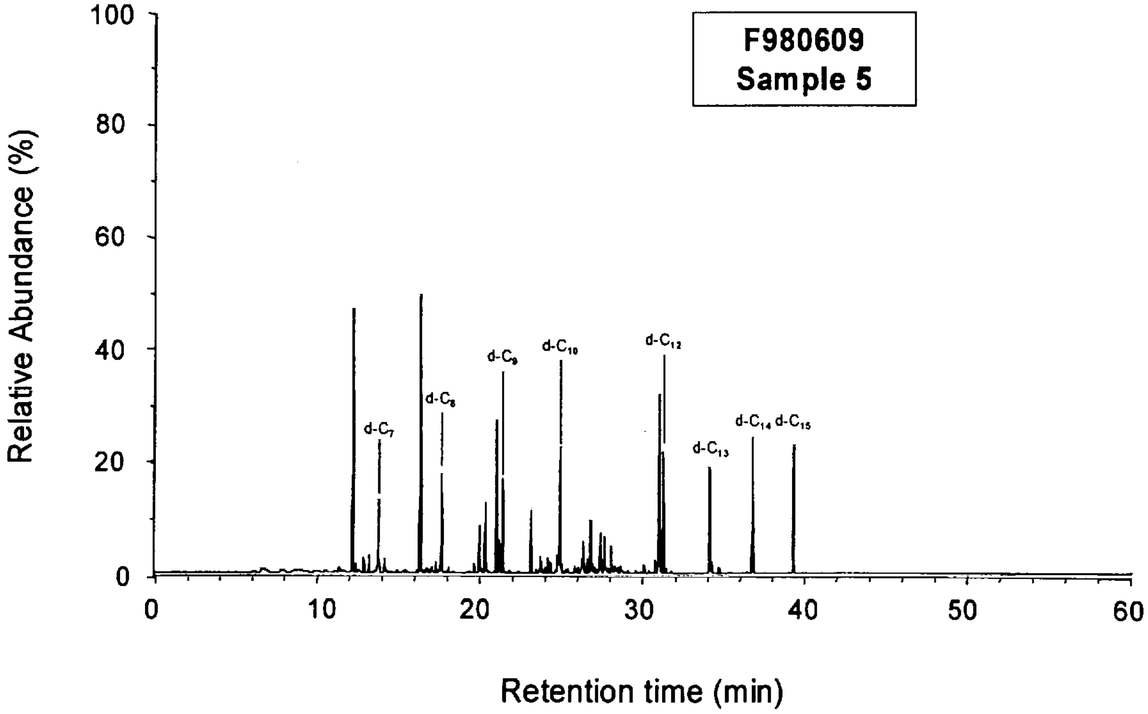

Plot I7. Fire Test F980609. Mass Chromatogram of Sample 5 acquired from +165 to +210 seconds post-ignition.

Table I1
GC/MS Peak Identification

t_R	Compound	CAS	Relative Abundance[1]						
			Blank 1	**Blank 2**	**Sample 1**	**Sample 2**	**Sample 3**	**Sample 4**	**Sample 5**
12.40	benzene	000071-43-2	0.08	0.53	1.28	0.73	3.32	5.45	3.06
13.02	2-methylhexane	000591-76-4	0.00	0.00	0.00	0.00	1.56	0.76	0.17
13.35	3-methylhexane	000589-34-4	0.00	0.00	0.00	0.00	1.19	0.61	0.14
13.85	1-heptene	000592-76-7	0.00	0.00	0.00	0.00	1.00	0.70	0.17
13.92	d_{16}-n-heptane (d-C_7)	33838-52-7	0.06	0.63	0.66	0.59	0.67	0.46	0.63
14.29	n-heptane	000142-82-5	0.00	0.00	0.00	0.00	0.98	0.75	0.16
16.59	methylbenzene	002037-26-5	0.00	0.00	0.00	0.00	10.74	7.14	2.97
16.89	2-methylheptane	000592-27-8	0.00	0.00	0.00	0.00	0.17	0.31	0.05
17.18	3-methylheptane	000589-81-1	0.00	0.00	0.00	0.00	0.58	0.31	0.08
17.75	d_{18}-n-octane (d-C_8)	017252-77-6	0.83	0.75	0.76	0.69	0.20	0.22	0.05
18.19	n-octane	000111-65-9	0.00	0.00	0.00	0.00	0.38	0.19	0.04
19.77	2,4-dimethyl-1-heptene	019549-87-2	0.00	0.00	0.00	0.00	0.05	0.12	0.07
20.13	ethylbenzene	000100-41-1	0.00	0.00	0.00	0.00	2.38	1.44	0.38
20.49	1,4-dimethylbenzene 1,3-diemthylbenzene	000106-42-3 000108-38-3	0.00	0.00	0.00	0.00	1.99	1.00	0.28
20.52	ethynylbenzene	000536-74-3	0.00	0.00	0.00	0.00	0.39	0.00	0.11
20.68	2-methyloctene	003221-61-2	0.00	0.00	0.00	0.00	0.29	0.12	0.03

Table I1, continued
GC/MS Peak Identification

t_R	Compound	CAS	Relative Abundance[1]						
			Blank 1	Blank 2	Sample 1	Sample 2	Sample 3	Sample 4	Sample 5
21.02	3-methyloctene	002216-33-3	0.00	0.00	0.00	0.00	0.16	0.07	0.02
21.22	ethenylbenzene	000100-42-5	0.00	0.00	0.00	0.00	5.26	4.64	1.43
21.37	1,2-diemthylbenzene	000095-47-6	0.00	0.00	0.00	0.00	2.26	1.11	0.29
21.44	d_{20}-n-nonane (d-C_9)	121578-11-8	0.95	0.86	0.87	0.81	1.16	0.96	1.01
21.95	n-nonane	000111-84-2	0.00	0.00	0.00	0.00	0.15	0.11	0.03
22.47	1-methylethylbenzene	000098-82-8	0.00	0.00	0.00	0.00	0.07	0.05	0.01
23.28	benzaldehyde	000100-52-7	0.00	0.00	0.00	0.00	0.50	1.28	0.63
23.54	propylbenzene	000103-65-1	0.00	0.00	0.00	0.00	0.22	0.16	0.62
23.74	2,2-dimethyl-3-methylene-bicyclo[2.2.1]heptane	000079-92-5	0.00	0.00	0.00	0.00	0.05	0.13	0.04
23.83	1-methyl-2-ethylbenzene	000611-14-3	0.00	0.00	0.00	0.00	1.99	1.14	0.27
23.99	1-methyl-4-ethylbenzene	000622-96-8	0.00	0.00	0.00	0.00	0.53	0.28	0.05
24.41	1-methylethylbenzene	000298-82-8	0.00	0.00	0.00	0.00	0.66	0.56	0.12
25.00	d_{22}-n-decane (d-C_{10})	016416-29-8	1.09	1.00	1.00	0.95	1.15	3.15	1.44
25.47	n-decane	000124-18-5	0.00	0.00	0.00	0.00	0.14	0.35	0.07
26.56	indene	000095-13-6	0.00	0.00	0.00	0.00	0.36	0.63	0.00
29.99	1-methyl-1H-indene	000767-59-9	0.00	0.00	0.00	0.00	0.12	0.26	0.00

Table I1, continued
GC/MS Peak Identification

t_R	Compound	CAS	Relative Abundance[1]						
			Blank 1	Blank 2	Sample 1	Sample 2	Sample 3	Sample 4	Sample 5
30.16	azulene	000275-51-4	0.00	0.00	0.00	0.00	0.29	0.43	0.07
31.16	naphthalene	000091-20-3	0.00	0.00	0.00	0.00	6.10	5.32	1.91
31.31	d_{26}-n-dodecane (d-C_{12})	121578-12-9	1.19	1.08	1.08	1.10	1.26	0.88	1.24
34.15	d_{28}-n-tridecane (d-C_{13})	121578-12-9	1.27	1.14	1.13	1.22	1.11	0.86	1.15
34.31	2-methylnaphthalene	000091-57-6	0.00	0.00	0.00	0.00	0.15	0.42	0.13
34.76	1-methylnaphthalene	000090-12-0	0.00	0.00	0.00	0.00	0.07	0.24	0.06
36.44	biphenyl	000092-52-4	0.00	0.00	0.00	0.00	0.00	0.04	0.02
36.82	d_{30}-n-tetradecane (d-C_{14})		1.30	1.27	1.24	1.34	1.26	0.76	1.23
39.32	d_{32}-n-pentadecane (d-C_{15})	036340-20-2	1.31	1.27	1.26	1.31	1.19	0.71	1.25

[1] The abundance values shown in this table are the ratio of the peak area of the compound of interest to the average peak area of the deuterated n-alkanes (internal standards) in each sample.

APPENDIX J
PASSENGER COMPARTMENT AIRBORNE PARTICULATE ANALYSIS

Five samples of airborne particulate were samples from the passenger compartment during this test. The approximate locations of the inlets particulate samplers are shown in Figures J1 and J2.

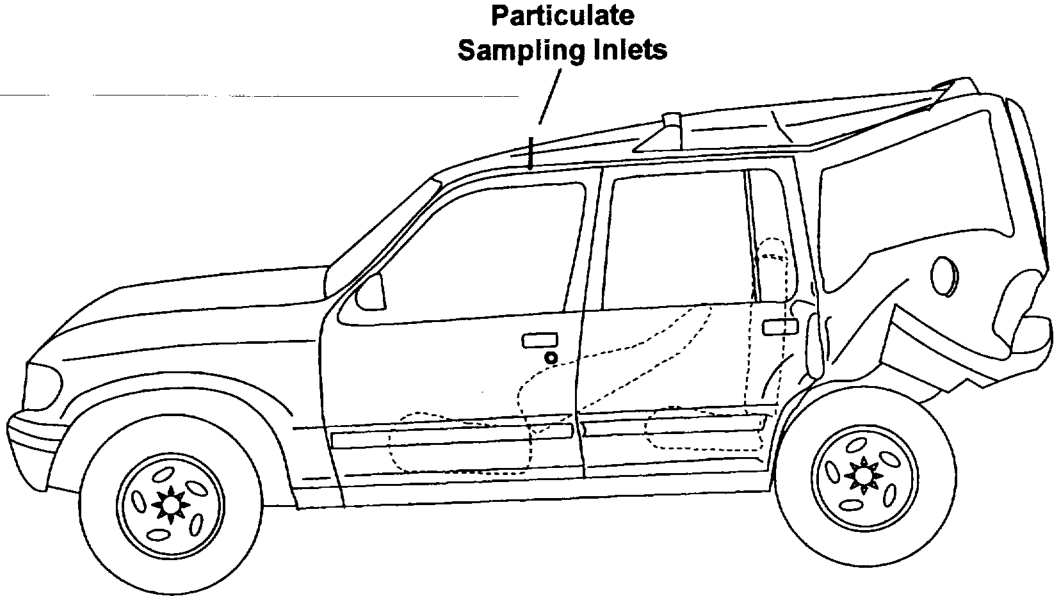

Figure J1. Fire Test F980609. Side-view of the test vehicle showing the approximate locations of the particulate sampling inlets in the passenger compartment.

Each particulate sampling apparatus consisted of an in-line stainless steel filter holder (filter diameter = 47 mm, Gelman Scientific). The inlet of each filter holder was fitted with a straight length of stainless steel tubing (o.d. = ¼ in., o.d. = $^{5}/_{16}$ in., length = 12 in.) using a compression fitting (¼ in., Swagelok). The inlet tube was inserted through the roof of the test vehicle so that it extended below the headlining approximately 10 in.. The outlet of each filer holder was connected to a vacuum manifold using flexible copper tubing (o.d. = $^{5}/_{16}$ in., length = 25 ft.). The vacuum manifold was connected to a pumping system configured to maintain constant flow through the filter holder as the pressure drop across the filter increased due to particulate loading. Qartz-fiber filters were used to collect particulate from the passenger compartment. The filters were placed in an electric furnace at 650°C in air overnight and pre-weighed. The pumping system was adjusted to maintain a volume flow rate of 30 L/min. through a single filter holder. This produced a linear velocity of approximately 29 cm/sec. of airflow perpendicular the face of the filter.

Two blanks were collected for 10 minutes before the test. Samples were collected during the test. In-line solenoid valves fitted to each port of the vacuum manifold and were actuated manually during the test to direct flow through the filter holders sequentially. The time intervals for sample acquisition were the same as those for acquiring GC/MS samples.

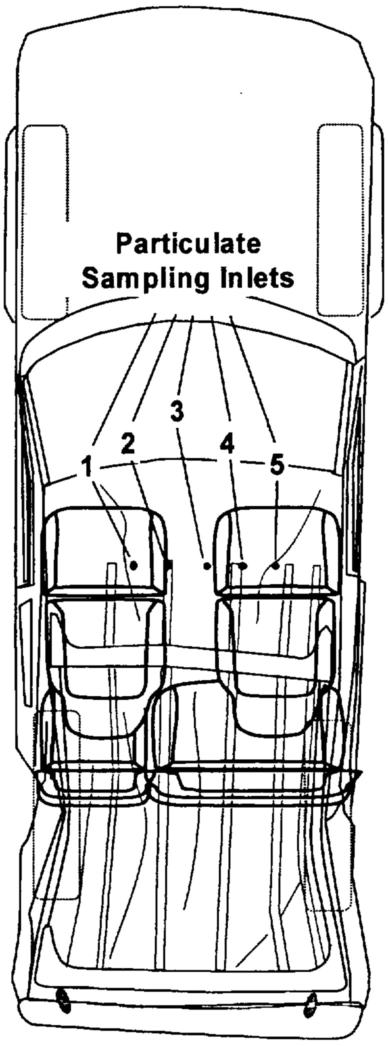

Figure J2. Fire Test F980609. Top-view of the test vehicle showing the approximate locations of the particulate sampling inlets in the passenger compartment.

After the test, the filters placed in a dissector cabinet overnight to remove water absorbed by the filter media and particulate. The weight of each filter was recorded only after constant weight was achieved. The average concentrations of airborne particulate during each sample interval were determined from the mass of particulate collected, the volume flow rate, and the elapsed time.

A quarter was cut from each filter, weighted, and extracted for quantitative ion chromatographic analysis. The extracting solution was the mobile phase buffer. The chromatography column was an IC-Pak A HC column (Waters, Milford, MA). The mobile phase was a sodium borate/gluconate buffer at a flow rate of 1.8 mL/min [J1]. The chromatographic system consisted of a Model 616 Pump, a Model 717 Autosampler, and a Model 431 Conductivity Detector (Waters). The following anions were measured in the ion chromatographic analysis: fluoride (F^-), bicarbonate (HCO_3^-), chloride (Cl^-), nitrite (NO_2^-), bromide (Br^-), hypochlorite ($HClO_3^-$), nitrate (NO_3^-), phosphate (HPO_4^-), sulfate (SO_4^-), and oxalate ($C_2O_4^-$).

Table JI shows the concentration of airborne particulate in the passenger compartment during this test.

Table J1
Average Airborne Particulate Concentration

Sample	Sampling Interval (sec.)	Sampling Time (sec.)	Airborne Concentration (mg/m^3)
Blank	n/a	600	0
Sample 1	-30 to 0	30	27
Sample 2	0 to +60	60	247
Sample 3	+60 to +120	60	1168
Sample 4	+120 to +165	45	1575
Sample 5	+165 to +210	45	1209

Table J2 shows the results of the average anion concentration in the airborne particulate. The results shown in Table J2 were corrected for bicarbonate, nitrate, phosphate, sulfate, and oxalate detected in the blanks. All samples contained chloride. Sample 4 contained fluoride. Samples 2, 3,4, and 5 contained phosphate and sulfate.

Table J2

Average Anion Concentration in the Airborne Particulate

Sample	Anion Concentration in Airborne Particulate (µg/mg)[1]									
	F^-	HCO_3^-	Cl^-	NO_2^-	Br^-	$HClO_3^-$	NO_3^-	HPO_4^-	SO_4^-	$C_2O_4^-$
Sample 1	n/d[1]	n/d	n/d	n/d	n/d	n/d	n/d	n/d	n/d	n/d
Sample 2	n/d	n/d	44	n/d	n/d	n/d	n/d	18	23	n/d
Sample 3	n/d	n/d	34	n/d	n/d	n/d	n/d	0.4	2	n/d
Sample 4	1.8	n/d	46	n/d	n/d	n/d	n/d	2	2	n/d
Sample 5	n/d	n/d	81	n/d	n/d	n/d	n/d	6	7	n/d

[1] n/d = not detected

REFERENCES FOR APPENDIX J

J1. Method A-102, Waters Innovative Methods for Ion Analysis, Manual Number 22340, Waters Corporation, Milford, MA.